

Disorder Trapping in Rapidly Solidified Intermetallic Compounds

Nafis Ul Haque

Submitted in accordance with the requirements for the degree of Doctor of
Philosophy

The University of Leeds
Institute for Materials Research (IMR)
School of Chemical and Process Engineering

July, 2018

The candidate confirms that the work submitted is his own, except where work which has formed part of jointly-authored publications has been included. The contribution of the candidate and the other authors to this work has been explicitly indicated below. The candidate confirms that appropriate credit has been given within the thesis where reference has been made to the work of others.

The following publications have been made based on materials contained in Chapter 4 and 5 of this thesis. The citations for these publications are as follows:

List of Article Publications and Presentations:

(From February 2014 to date)

- N. Haque, R.F. Cochrane, A.M. Mullis, Rapid solidification morphologies in Ni₃Ge: Spherulites, dendrites and dense-branched fractal structures, *Intermetallics*, 76 (2016) 70-77. <https://doi.org/10.1016/j.intermet.2016.06.012>
- N. Haque, R.F. Cochrane, A.M. Mullis, Disorder-order morphologies in drop-tube processed Ni₃Ge: Dendritic and seaweed growth, *Journal of Alloys and Compounds*, 707 (2017) 327-331. <https://doi.org/10.1016/j.jallcom.2016.11.080>
- N. Haque, R.F. Cochrane, A.M. Mullis, Morphology of Order-Disorder Structures in Rapidly Solidified L₁₂ Intermetallics, Springer, 2017, pp. 729-736. https://link.springer.com/chapter/10.1007/978-3-319-51493-2_70
- N. Haque, R.F. Cochrane, A.M. Mullis, Morphology of Spherulites in Rapidly Solidified Ni₃Ge Droplets, *Crystals*, 7 (2017) 100. <http://dx.doi.org/10.3390/cryst7040100>
- N. Haque, R.F. Cochrane, A.M. Mullis, The Role of Recrystallization in Spontaneous Grain Refinement of Rapidly Solidified Ni₃Ge, *Metallurgical and Materials Transactions A*, 48 (2017) 5424-5431. <https://link.springer.com/article/10.1007/s11661-017-4290-8>
- N. Haque, R.F. Cochrane, A.M. Mullis, Order-disorder morphologies in rapidly solidified ε/ε'-Ni₅Ge₃ intermetallic, *Journal of Alloys and Compounds*, (2017). <https://doi.org/10.1016/j.jallcom.2017.12.253>
- N. Haque, R. Cochrane, A. Mullis, Mechanical properties of rapidly solidified Ni₅Ge₃ intermetallic, Springer, 2017. https://link.springer.com/chapter/10.1007/978-3-319-72526-0_66

Conference Presentation:

- National Student Conference in Metallic Materials, Sheffield, UK, 23th June 2014.
- National Student Conference in Metallic Materials, Manchester, UK, 23th June 2015.
- The 6th annual University of Leeds Postgraduate Research Conference (SHOWCASE 2015), Leeds, UK, 8th December 2015.
- 22nd International Symposium on Metastable, Amorphous and Nanostructured Materials, Paris, France, 15th July 2015.
- 23rd International Symposium on Metastable, Amorphous and Nanostructured Materials, Nara city, Japan, 5th July 2016.
- TMS 2017 (The Minerals Materials and Metals Society) 146th Annual Meeting and Exhibition, San Diego, USA, 27th February 2017.
- 24th International Symposium on Metastable, Amorphous and Nanostructured Materials, San Sabastian, Spain, 20th June 2017.
- 25th International Symposium on Metastable, Amorphous and Nanostructured Materials, Rome, Italy, 6 July 2018.
- FEMS Junior EUROMAT, Budapest, Hungary, 9 July 2018.

This copy has been supplied on the understanding that it is copyright material and that no quotation from the thesis may be published without proper acknowledgement.

The right of Nafis Ul Haque to be identified as Author of this work has been asserted by him in accordance with the Copyright, Designs and Patents Act 1988.

Dedication

This humble work is dedicated to my beloved

Father & Mother,

*Whose affection, love, encouragement and prays make me able to get such success
and honour,*

Along with all hard working and respected

Teachers,

And above all,

To the Almighty God!

Acknowledgements

With gratitude to God, I would first and foremost like to express thanks to my supervisors, Professor Andrew M. Mullis and Dr Robert F. Cochrane who have been an unequivocal resource of guidance and academic support, as well as excellent supervision of this research project. This work will not have been possible without your knowledge, guidance and patience. Also, special thanks to HEC and NED University of Engineering and Technology for granting me scholarship and sponsorship for this study.

I would like to thank Diane Cochrane, Robert Simpson, Timothy Bigg, Mike Ward, John Harrington, Zabeada Aslam, Richard Walshaw, Stuart Micklethwaite, Mohammed Javed, Duncan Hedges for their extended help during Arc-melting, Drop-tube processing, Metallography, XRD, SEM, TEM, EBSD samples preparation and operations.

It is important to also thank my few friends, Salman, Rizwan, Junaid and my colleagues (Toyin, Lekan and Frank), for their love and kind support. I would love to thank my parents, my sisters, brothers (Rais & Rameez) and teachers (especially Dr Muhammad Tufail). Thank you very much for your unwavering support through the whole adventure. I could not have done it without you. Finally, but most importantly, I want to say thank you Almighty God. I give all glory to You.

Abstract

The congruently melting, single phase, intermetallic compounds β -Ni₃Ge and ϵ -Ni₅Ge₃ were produced by arc melt. Each was subject to rapid solidification via drop-tube processing. Each compound remained fully single phase β -Ni₃Ge/ ϵ -Ni₅Ge₃, irrespective of the imposed cooling rate. In the investigation of β -Ni₃Ge compound, droplets spanning the size range ≥ 850 to ≤ 38 μm diameter particles, with corresponding cooling rates of ≤ 700 to > 54500 K s^{-1} , were subject to microstructural investigation using SEM. Six dominant solidification morphologies were identified with increasing cooling rate, namely; (i) spherulites, (ii) mixed spherulites and dendrites, (iii) dendrites - orthogonal, (iv) dendrites - non-orthogonal, (v) recrystallised, and (vi) dendritic seaweed, are observed imbedded within a featureless matrix. Selected area diffraction (SAD) in the TEM analysis confirmed that it is only the spherulite microstructure that is partially ordered amongst the above listed microstructures, which are disordered. However, SAD analysis indicated that the featureless background material of all above microstructures is chemically ordered.

While, in the examination of ϵ -Ni₅Ge₃ compound, four dominant solidification morphologies were observed, namely; (i) Partial plate and lath, (ii) plate and lath microstructure (iii) isolated hexagonal crystallites, and (iv) single crystal imbedded within a featureless matrix. SAD analysis in the TEM reveals that the partial plate and laths and plate and laths are partial ordered variant of ϵ -Ni₅Ge₃ and ϵ -Ni₅Ge₃ respectively, whilst the featureless matrix of both microstructures are the ordered variant of the same compound. However, isolated hexagonal crystallites are a disordered variant of ϵ -Ni₅Ge₃, although featureless matrix are the ordered variant of the same compound. SAD analysis in the TEM also indicated that, at the highest cooling rates, single crystal structure along with featureless matrix is the completely disordered variant of the same compound. Thermal analysis and in situ heating in the TEM indicate a reversible solid-state order-disorder transformation between 470 – 485 °C. The micro-Vickers hardness results confirmed that the ϵ -Ni₅Ge₃ (1021 Hv_{0.01}) is significantly harder than the β -Ni₃Ge (526 Hv_{0.01}) compound.

Table of Contents

DEDICATION.....	I
ACKNOWLEDGEMENTS.....	II
ABSTRACT	III
TABLE OF CONTENT	IV
LIST OF FIGURES	VI
LIST OF TABLES	XVI
ABBREVIATIONS	XVII
CHAPTER 1 INTRODUCTION	1
CHAPTER 2 LITERATURE REVIEW	5
2.1 FUNDAMENTALS	5
2.1.0 Crystal System and Chemical Ordering	5
2.1.1 Phase Diagram of Ge – Ni System.....	6
2.1.2 Intermetallic Compounds	6
2.1.3 Fundamental of Ordering Structure	6
2.1.4 Rapid Solidification and Disorder Trapping of of Intermetallic Compounds	9
2.2 RECENT PROGRESSES	12
2.2.0 Spherulites Microstructure	15
2.3.0 Departure from normal Dendritic Growth during Rapid Solidifications	19
2.4.0 Spontaneous grain refine (SGR) microstructure	21
2.5.0 Plate and Lath microstructure	23
CHAPTER 3 EQUIPMENT AND METHODOLOGY	29
3.1 ARC-MELTER.....	29
3.2 SELECTION OF MATERIALS/COMPOUND FOR DROP-TUBE PROCESS	32
3.3 DROP-TUBE PROCESS	33
3.3.1 Drop-tube Cooling Rate Calculation Method	36
3.4 SAMPLE ANALYSIS AND MICROSTRUCTURAL CHARACTERISATION	38
3.4.1 Metallography: Specimen Preparation and Etching.....	39
3.5 CHARACTERISATION TECHNIQUES EMPLOYED.....	41
3.5.1 X-ray Diffraction (XRD).....	41
3.5.2 Optical Microscopy (OM).....	44
3.5.3 Scanning Electron Microscope (SEM).....	44

3.5.4	Energy Dispersive X-Ray Spectrometry and Line-scan Techniques	47
3.5.5	Electron Backscatter Diffraction (EBSD)	48
3.5.6	TEM	50
3.5.7	FIB	57
3.5.8	Differential Scanning Calorimetry (DSC)	59
3.5.9	Micro-hardness Measurements	60
CHAPTER 4 EXPERIMENTAL RESULTS		62
4.1	PREPARATION OF INGOT - Ni_3Ge	62
4.2	RAPIDLY SOLIDIFIED DROP-TUBE SAMPLE - Ni_3Ge	63
4.2.1	Microstructural Characterisation	70
4.2.2	EBSD Analysis	72
4.2.3	TEM Analysis	95
4.3	PREPARATION OF INGOT – Ni_5Ge_3	112
4.4	RAPIDLY SOLIDIFIED DROP-TUBE SAMPLE – Ni_5Ge_3	113
4.4.1	Microstructural Characterisation	118
4.4.2	EBSD Analysis	119
4.4.3	TEM and Thermal Analysis	132
4.4.4	DSC and In-situ TEM analysis	133
4.5	MICROHARDNESS	139
CHAPTER 5 DISCUSSION		141
5.1	Ni_3Ge COMPOUND	141
5.1.1	Spherulites Morphology	142
5.1.2	Dendrites Morphologies (orthogonal and non-orthogonal and seaweed)	150
5.1.3	Recrystallised Morphology	155
5.2	Ni_5Ge_3 COMPOUND	160
5.3	MICRO-VICKERS HARDNESS	164
CHAPTER 6 CONCLUSION		168
FUTURE WORK		173
REFERENCES		175
APPENDIX		186

List of Figures

Figure 2.1 Shows L1 ₂ crystal structure of Ge-Ni (a) chemical ordered (b) chemical disordered crystal structure.....	24
Figure 2.2a Ge - Ni phase diagram [19]	24
Figure 2.2b Ni – Si phase diagram [45] and (c) Fe – Ge Phase diagram [51].....	25
Figure 2.3 The thermodynamic characteristics of (a) first order and (b) second order phase transformation [25].....	26
Figure 2.4 Here, η is a function of dimensionless growth velocity, V/V_D , at the interface of growing solid for congruently melting stoichiometric compound. This figure shows prediction of long range order parameter by (a) second order, (b) first order [33].....	26
Figure 2.5 This figure shows parallel growth of order domains resulting in formation of antiphase boundary (APB) [35].....	27
Figure 2.6 A diagram representing different stages of rapid solidification in which an intermetallic compound becomes disordered as a result of increase in the cooling rate [36].	27
Figure 2.7 (a) Mixed variety of spherulites with positively birefringent centers and (b) mixed spherulites of nylon with ringed centers.....	28
Figure 3.1 Arc-melter furnace setup [University of Leeds].....	31
Figure 3.2 Arc melted samples of Ni-Ge (a) inhomogeneous and (b) and homogeneous.....	31
Figure 3.3 Internal shape of chamber (tungsten striker stub, longitudinal and round shapes of moulds).....	32
Figure 3.4 Schematic diagram of the drop-tube apparatus used in this research.	35
Figure 3.5 Estimated cooling rate of droplets cooled in N ₂ as a function of their diameter.	38
Figure 3.6 Diffraction X-rays on parallel atomic planes satisfying Bragg's law [112].	43
Figure 3.7 (a) Picture – PANalytical X'pert Pro XRD (University of Leeds) and, (b) drop-tube sample.....	43
Figure 3.8 Signals from the interaction of an electron beam with a sample [113].	46
Figure 3.9 Picture (Carl Zeiss EVO® MA 15 SEM – University of Leeds).....	46
Figure 3.10 The basic components of an EBSD (FEI Quanta 650 FEGSEM with Oxford/HKL Nordlys EBSD - University of Leeds).	49

Figure 3.11 TEM operating modes (a) diffraction mode which produce DP and (b) image mode [115].	54
Figure 3.12 Imaging mode of TEM - (a) Bright field image and (b) dark-field image.	54
Figure 3.13 Geometry of construction of an electron diffraction pattern. On the film, the diffracted spot A occurs at a distance R_0 from the central spot, O in a direction perpendicular to the planes. L_0 is known as the camera length [116].	55
Figure 3.14 Geometry of the construction of an electron diffraction pattern from a single crystal in TEM. The beam is parallel to a zone axis including two planes (1 and 2). The included angle ϕ is equal to the angle between the normal directions of the planes [116].	55
Figure 3.15 Transmission electron microscope - (FEI Tecnai TF20 - TEM with Oxford control instruments - University of Leeds).	56
Figure 3.16 FIB process technique for TEM sample preparation.	58
Figure 3.17 Differential Scanning Calorimetry - Perkin Elmer STA 8000 and Lauda Alpha RA 8 Chiller unit (University of Leeds).	61
Figure 3.18 (a) TUKONTM 1202 Wilson Vickers micro-hardness analyser with resultant measurement and (b) an example of micro-Vickers hardness indentation in a drop-tube sample (Ni_5Ge_3).	61
Figure 4.1a X-ray diffraction analysis of as cast (arc-melted, on-stoichiometry) sample prior to drop-tube process. Vertical black lines indicate peak position for the single-phase ($\beta\text{-Ni}_3\text{Ge}$ reference pattern, and vertical red lines indicate peak position of $\text{Ni}_{1.88}\text{Ge}$, Ge and Ni_2Ge .	65
Figure 4.2a SEM (SEI) micrograph of HF etched of as cast (arc-melted, on-stoichiometry) sample prior to drop-tube process, showing eutectic phase with a single phase. The region (i) eutectic phase and region (ii) single phase selected for EDX area analysis.	66
Figure 4.3 Electron backscatter diffraction (EBSD) result of phase map (arc-melted, Ni-enhanced sample).	68
Figure 4.4 Average EDX compositions of Ni and Ge of the Ni-23.8 at.% Ge drop-tube particles. At least 10 particles were analysed in each size range.	68
Figure 4.5 X-ray diffraction analysis of rapidly solidified drop-tube processed samples, ranges from ($\geq 850 \mu\text{m}$ to $\leq 38 \mu\text{m}$). Vertical black lines indicate peaks position for the single-phase $\beta\text{-Ni}_3\text{Ge}$ reference pattern and different colours represents XRD patterns of particle sizes from $\geq 850 \mu\text{m}$ to $\leq 38 \mu\text{m}$.	69

Figure 4.6 Electron backscatter diffraction (EBSD) result of phase map (drop-tube, 75 – 53 μm sample).	69
Figure 4.7 SEM (SEI) micrograph of an HF etched $\beta\text{-Ni}_3\text{Ge}$ drop-tube particle from the ≥ 850 μm size fraction. Numerous spherulite structures are evident in a more-or- less featureless matrix.	74
Figure 4.8 SEM (SEI) micrograph of an HF etched $\beta\text{-Ni}_3\text{Ge}$ drop-tube particle from the 850 – 500 μm size fraction. Numerous spherulite structures are evident in a more-or-less featureless matrix.	74
Figure 4.9 SEM (SEI) micrograph of an HF etched $\beta\text{-Ni}_3\text{Ge}$ drop-tube particle from the 500 – 300 μm size fraction. Shows co-existence of spherulites with dendritic microstructure.	75
Figure 4.10 SEM (SEI) micrograph of an HF etched $\beta\text{-Ni}_3\text{Ge}$ drop-tube particle from the 300 – 212 μm size fraction. Shows co-existence of spherulites with dendritic microstructure.	75
Figure 4.11 SEM (SEI) micrograph of an HF etched $\beta\text{-Ni}_3\text{Ge}$ drop-tube particle from the 212 – 150 μm size fraction showing dendritic structures in a featureless matrix.	76
Figure 4.12 SEM (SEI) micrograph of an HF etched $\beta\text{-Ni}_3\text{Ge}$ drop-tube particle from the 150 – 106 μm size fraction showing dendritic structures in a featureless matrix.	76
Figure 4.13 SEM (SEI) micrograph of an HF etched $\beta\text{-Ni}_3\text{Ge}$ drop-tube particle from the 106 – 75 μm size fraction, showing dendritic structure with non-orthogonal side branching. Two dendrites in particular are indicated with side-branches at angles of (i) 60° and (ii) 45° and 30°	77
Figure 4.14 SEM (SEI) micrograph of an HF etched $\beta\text{-Ni}_3\text{Ge}$ drop-tube particle from the 75-53 μm size fraction showing crack-like relief (recrystallised microstructure).	77
Figure 4.15 (a) SEM (SEI) micrograph of an HF etched $\beta\text{-Ni}_3\text{Ge}$ drop-tube particle from the 53 - 38 μm size fraction showing dendritic seaweed structure and (b) dendritic seaweed structure, dendrites, crack-like relief (recrystallised-microstructure) along with featureless matrix; within the same size of drop-tube particle (a).	78
Figure 4.16 SEM (SEI) micrograph of an HF etched $\beta\text{-Ni}_3\text{Ge}$ drop-tube particle from the ≤ 38 μm size fraction showing dense branched fractal or ‘dendritic seaweed’ structure.	79
Figure 4.17 (a) EDX line scan across a spherulite trunk (b) dendrite trunk and (c) seaweed trunk, showing that the contrast revealed by etching is not the result of solute partitioning.	80

Figure 4.18 (a) Electron backscatter diffraction (EBSD) result of Euler texture map of unetched β-Ni₃Ge drop-tube particle size $\geq 850 \mu\text{m}$; (b) Histogram of the correlated misorientation angle distribution across grain boundaries for the image shown in (a).	81
Figure 4.19 (a) Electron backscatter diffraction (EBSD) result of Euler texture map of unetched β-Ni₃Ge drop-tube particle size $850 - 500 \mu\text{m}$ (arrow indicates presence of spherulite); (b) Histogram of the correlated misorientation angle distribution across grain boundaries for the image shown in (a).	82
Figure 4.20 (a) Electron backscatter diffraction (EBSD) result of Euler texture map of unetched β-Ni₃Ge drop-tube particle size $500 - 300 \mu\text{m}$; (b) Histogram of the correlated misorientation angle distribution across grain boundaries for the image shown in (a).	83
Figure 4.21 (a) Electron backscatter diffraction (EBSD) result of Euler texture map of unetched β-Ni₃Ge drop-tube particle size $300 - 212 \mu\text{m}$; (b) Histogram of the correlated misorientation angle distribution across grain boundaries for the image shown in (a).	84
Figure 4.22 (a) Electron backscatter diffraction (EBSD) result of Euler texture map of unetched β-Ni₃Ge drop-tube particle size $212 - 150 \mu\text{m}$; (b) Histogram of the correlated misorientation angle distribution across grain boundaries for the image shown in (a).	85
Figure 4.23 (a) Electron backscatter diffraction (EBSD) result of Euler texture map of unetched β-Ni₃Ge drop-tube particle size $150 - 106 \mu\text{m}$; (b) Histogram of the correlated misorientation angle distribution across grain boundaries for the image shown in (a).	86
Figure 4.24 (a) Electron backscatter diffraction (EBSD) result of Euler texture map of unetched β-Ni₃Ge drop-tube particle size $106 - 75 \mu\text{m}$; (b) Histogram of the correlated misorientation angle distribution across grain boundaries for the image shown in (a).	87
Figure 4.25 (a) Electron backscatter diffraction (EBSD) result of Euler texture map of unetched β-Ni₃Ge drop-tube particle size $75 - 53 \mu\text{m}$; (b) Histogram of the correlated misorientation angle distribution across grain boundaries for the image shown in (a).	88
Figure 4.26 (a) Electron backscatter diffraction (EBSD) result of Euler texture map of unetched β-Ni₃Ge drop-tube particle size $53 - 38 \mu\text{m}$; (b) Histogram of the correlated misorientation angle distribution across grain boundaries for the image shown in (a).	89

Figure 4.27 (a) Electron backscatter diffraction (EBSD) result of Euler texture map of unetched β -Ni ₃ Ge drop-tube particle size $\leq 38 \mu\text{m}$; (b) Histogram of the correlated misorientation angle distribution across grain boundaries for the image shown in (a).	90
Figure 4.28 (a) shows EBSD results of grain orientation spread (GOS) map of unetched β -Ni ₃ Ge drop-tube particle size $\geq 850 \mu\text{m}$. Grains are outlined with white boundaries and were constructed presuming a 5 deg tolerance angle (success rate of indexing is 99.5 pct) ; (b) Histograms for the image shown in (a), where colour indicates the range of orientation angle.....	91
Figure 4.29 (a) shows EBSD results of grain orientation spread (GOS) map of unetched β -Ni ₃ Ge drop-tube particle size 106 – 75 μm . Grains are outlined with white boundaries and were constructed presuming a 5 deg tolerance angle (success rate of indexing is 99.5 pct) ; (b) Histograms for the image shown in (a), where colour indicates the range of orientation angle.....	92
Figure 4.30 (a) shows EBSD results of grain orientation spread (GOS) map of unetched β -Ni ₃ Ge drop-tube particle size 75 – 53 μm . Grains are outlined with white boundaries and were constructed presuming a 5 deg tolerance angle (success rate of indexing is 99.5 pct) ; (b) Histograms for the image shown in (a), where colour indicates the range of orientation angle.....	93
Figure 4.31 (a) shows EBSD results of grain orientation spread (GOS) map of unetched β -Ni ₃ Ge drop-tube particle size 53 – 38 μm . Grains are outlined with white boundaries and were constructed presuming a 5 deg tolerance angle (success rate of indexing is 99.5 pct) ; (b) Histograms for the image shown in (a), where colour indicates the range of orientation angle.....	94
Figure 4.32 TEM bright field image of a spherulite (i) and surrounding matrix material (ii) in a β -Ni ₃ Ge drop-tube particle $\geq 850 \mu\text{m}$ particle.	99
Figure 4.33 TEM bright field image of a spherulite (i) and surrounding matrix material (ii) in a β -Ni ₃ Ge drop-tube particle 850 – 500 μm particle.	99
Figure 4.34 TEM bright field image of a spherulite (i) and surrounding matrix material (ii) in a β -Ni ₃ Ge drop-tube particle 500 – 300 μm particle.	100
Figure 4.35 TEM bright field image of a spherulite and surrounding matrix material in a β -Ni ₃ Ge drop-tube particle 300 – 212 μm particle.	100
Figure 4.36 (a) Selected area diffraction patterns from Figure 4.35 at region (i) spherulite, and (b) from the featureless matrix well away from the spherulite at region (ii).....	101
Figure 4.37 (a) TEM bright field image of a spherulite, (b) selected area diffraction patterns obtained from the initial core of the spherulite at	

region (i), c from the region (ii) - spherulites and (d) from the featureless matrix well away from the spherulite at the region (iii).	102
Figure 4.38 TEM dark-field image of HF etched drop-tube processed β -Ni ₃ Ge droplets obtained from one of the superlattice spots within the diffraction pattern of drop-tube particles (a) $\geq 850 \mu\text{m}$ (b) $850 - 500 \mu\text{m}$, (c) $500 - 300 \mu\text{m}$, and (d) $300 - 212 \mu\text{m}$ respectively.	103
Figure 4.39 Average spherulite lamellar width as a function of cooling rate... ..	104
Figure 4.40 (a) TEM bright field image of a dendrite (orthogonal) and surrounding matrix material in a $212 - 150 \mu\text{m}$ drop-tube sample, (b) selected area diffraction patterns obtained from the region (i) dendrite and (c) from the region (ii) matrix material.....	105
Figure 4.41 (a) TEM bright field image of a dendrite (non-orthogonal) in a $106 - 75 \mu\text{m}$ drop-tube sample, (b) selected area diffraction patterns obtained from the dendrites (as shown by a circle on Figure a).....	106
Figure 4.42 (a) TEM bright field image of a recrystallised structure in a $75 - 53 \mu\text{m}$ drop-tube sample, (b) selected area diffraction patterns obtained from the large blocky areas between the cracks-like features as shown in Figure (a). Arrow shows the specification of the spot from which the dark-field image shown in Figure 4.43 (b).	107
Figure 4.43 (a) : Transmission electron microscope (TEM) bright-field image of the blocky region occurring between the ‘cracks’ in the $75 - 53 \mu\text{m}$ size fraction and (b) TEM dark-field image of same region obtained from one of the super-lattice spots within the diffraction pattern (Figure 4.42b).	108
Figure 4.44 (a) TEM bright field image of a dendritic seaweed in a $53 - 38 \mu\text{m}$ drop-tube sample, (b) selected area diffraction patterns obtained from the region (circle) at dendritic seaweed.	109
Figure 4.45 (a) TEM bright field image of a dendritic seaweed and surrounding crack-like features in a $53 - 38 \mu\text{m}$ drop-tube sample, (b) selected area diffraction patterns obtained from the region (i) crack-like features, (c) from the region (ii) featureless matrix and (d) from the region (iii) dendritic seaweed.....	110
Figure 4.46 (a) TEM bright field image of a dendritic seaweed and surrounding matrix material in a $\leq 38 \mu\text{m}$ drop-tube sample, (b) selected area diffraction patterns obtained from the region (i) dendritic seaweed and (c) from the region (ii) matrix material.	111
Figure 4.47 X-ray diffraction analysis of as cast (arc-melted, Ni-enhanced) sample prior to drop-tube process. Vertical black lines indicate peak position for the single-phase (ϵ -Ni ₅ Ge ₃ reference pattern).	114

Figure 4.48 SEM micrograph of HF etched of as cast (arc-melted, Ni-enhanced) sample prior to drop-tube process, showing sample has completely single phase (featureless matrix). The regions (square blocks) selected from different regions of sample for EDX area analysis.	115
Figure 4.49 Electron backscatter diffraction (EBSD) result of phase map (arc-melted, Ni-enhanced sample).	116
Figure 4.50 Average EDX compositions of Ni and Ge of the Ni – 37.2 at. % Ge drop-tube particles. At least 10 particles were analysed in each size range.	116
Figure 4.51 X-ray diffraction analysis of rapidly solidified drop-tube processed samples, ranges from ($\geq 850 \mu\text{m}$ to $\leq 38 \mu\text{m}$). Vertical black lines indicate peak positions for the single-phase $\epsilon\text{-Ni}_5\text{Ge}_3$ / $\epsilon'\text{-Ni}_5\text{Ge}_3$ reference pattern and different colours represents XRD patterns of particle sizes from $\geq 850 \mu\text{m}$ to $\leq 38 \mu\text{m}$	117
Figure 4.52 Electron backscatter diffraction (EBSD) result of phase map (drop-tube, $850 - 500 \mu\text{m}$ sample).	117
Figure 4.53 SEM (SEI) micrograph of HF etched Ni_5Ge_3 drop-tube particle from the $\geq 850 \mu\text{m}$ size fraction showing numerous plate and lath structures in a more-or-less featureless matrix.	121
Figure 4.54 SEM (SEI) micrograph of HF etched Ni_5Ge_3 drop-tube particle from the $850 - 500 \mu\text{m}$ size fraction showing numerous plate and lath structures in a more-or-less featureless matrix.	121
Figure 4.55 SEM (SEI) micrograph of HF etched Ni_5Ge_3 drop-tube particle from the $500 - 300 \mu\text{m}$ size fraction showing numerous plate and lath structures in a more-or-less featureless matrix.	122
Figure 4.56 SEM (SEI) micrograph of HF etched Ni_5Ge_3 drop-tube particle from the $300 - 212 \mu\text{m}$ size fraction showing numerous plate and lath structures in a more-or-less featureless matrix.	122
Figure 4.57 SEM (SEI) micrograph of HF etched Ni_5Ge_3 drop-tube particle from the $212 - 150 \mu\text{m}$ size fraction showing numerous plate and lath structures in a more-or-less featureless matrix.	123
Figure 4.58 SEM (SEI) micrograph of HF etched Ni_5Ge_3 drop-tube particle from the $150 - 106 \mu\text{m}$ size fraction showing isolated faceted crystallites.	123
Figure 4.59 SEM (SEI) micrograph of HF etched Ni_5Ge_3 drop-tube particle from the $106 - 75 \mu\text{m}$ size fraction showing isolated faceted crystallites..	124
Figure 4.60 SEM (SEI) micrograph of HF etched Ni_5Ge_3 drop-tube particle from the $75 - 53 \mu\text{m}$ size fraction showing isolated faceted crystallites....	124

Figure 4.61 SEM (SEI) micrograph of HF etched Ni₅Ge₃ drop-tube particle from the , 53 – 38 μm size fraction showing featureless matrix (single crystal).	125
Figure 4.62 SEM (SEI) micrograph of HF etched Ni₅Ge₃ drop-tube particle from the , ≤ 38 μm size fraction showing featureless matrix (single crystal).	125
Figure 4.63 (a) EDX line scan across a lath and plate trunk and (b) isolated faceted crystallites trunk, showing that the contrast revealed by etching is not the result of solute partitioning.	126
Figure 4.64 (a) Electron backscatter diffraction (EBSD) result of Euler texture map of unetched Ni₅Ge₃ drop-tube particle size 500 – 300 μm; (b) Histogram of the correlated misorientation angle distribution across grain boundaries for the image shown in (a).	127
Figure 4.65 (a) Electron backscatter diffraction (EBSD) result of Euler texture map of unetched Ni₅Ge₃ drop-tube particle size 300 – 212 μm; (b) Histogram of the correlated misorientation angle distribution across grain boundaries for the image shown in (a).	128
Figure 4.66 (a) Electron backscatter diffraction (EBSD) result of Euler texture map of unetched Ni₅Ge₃ drop-tube particle size 212 – 150 μm; (b) Histogram of the correlated misorientation angle distribution across grain boundaries for the image shown in (a).	129
Figure 4.67 (a) Electron backscatter diffraction (EBSD) result of Euler texture map of unetched Ni₅Ge₃ drop-tube particle size 150 – 106 μm; (b) Histogram of the correlated misorientation angle distribution across grain boundaries for the image shown in (a).	130
Figure 4.68 (a) Electron backscatter diffraction (EBSD) result of Euler texture map of unetched Ni₅Ge₃ drop-tube particle size 53 – 38 μm; (b) Histogram of the correlated misorientation angle distribution across grain boundaries for the image shown in (a).	131
Figure 4.69 (a) TEM bright field image of a partially plate and lath structure (ε) and surrounding matrix material in a ≥ 850 μm size fraction, (b and c) selected area diffraction patterns from regions (i) and (ii) identified in the bright field image (i) matrix materials well away from the plate and lath structure, (ii) inside the structure.	134
Figure 4.70 (a) TEM bright field image of a plate and lath structure and surrounding matrix material in a 500 – 300 μm size fraction, (b and c) selected area diffraction patterns from regions (i) and (ii) identified in the	

bright field image (i) matrix materials well away from the plate and lath structure, (ii) inside the structure.	135
Figure 4.71 (a) TEM bright field image of a plate and lath structure and surrounding matrix material in a 150 – 106 μm size fraction, (b and c) selected area diffraction patterns from regions (i) and (ii) identified in the bright field image (i) matrix materials well away from the isolated faceted hexagonal crystallites microstructure, (ii) inside the isolated faceted hexagonal crystallites microstructure.	136
Figure 4.72 (a) TEM bright field image of a plate and lath structure and surrounding matrix material in a 53 – 38 μm size fraction, (bandc) selected area diffraction patterns from regions (i) and (ii) identified in the bright field image, two different regions of matrix materials.....	137
Figure 4.73 (a) DSC trace from a Ni_5Ge_3 drop-tube particle from the 150 – 106 μm size fraction, 1st and 2nd cycle indicated by green and blue respectively, two vertical black line shows the transition temperature at 320 to 460 $^\circ\text{C}$ and (b) TEM (In-situ) SAD pattern taken from Figure 4.58 at room temperature (ordered) and (c) SAD of the same area but at 485 $^\circ\text{C}$ (disordered).....	138
Figure 4.74 Micro-hardness value of Ni_3Ge compound as a function of droplet diameter ranges from $\geq 850 \mu\text{m}$ to $\leq 38 \mu\text{m}$.....	140
Figure 4.75 Micro-hardness value of Ni_5Ge_3 compound as a function of droplet diameter ranges from $\geq 850 \mu\text{m}$ to $\leq 38 \mu\text{m}$.....	140
Figure 5.1 Schematic diagram showing proposed model for spherulite formation in $\beta\text{-Ni}_3\text{Ge}$ with initial growth to the disordered phase during the recalescence phase of solidification followed by partial reordering during the plateau phase.	149
Figure 5.2 (a) SEM micrographs of HF etched $\beta\text{-Ni}_3\text{Ge}$ drop-tube particles from the 106 – 75 μm size fraction showing dendritic structure with non-orthogonal side-branching and (b) sketch of same highlighting two bent dendrites with non-orthogonal side-branching.	154
Figure 5.3 EBSD band contrast image of unetched $\beta\text{-Ni}_3\text{Ge}$ drop-tube particles from the 75 – 53 μm size fraction showing highly grain refined structure.	159
Figure 5.4 Solidification sequence as a function of increasing cooling rate with arrow showing placement of (Figure 3.5) in the sequence. (a) 150 – 106 μm, 8,000 – 13,000 K s^{-1} and (b) 106 – 75 μm, 13,000 – 23,000 K s^{-1}) showing dendritic growth with orthogonal and non-orthogonal side-branching	

respectively, (c) 53 – 38 μm , 42,000 – 62,000 K s^{-1} showing development of dendritic seaweed. 159

Figure 5.5 Micro-hardness value of Ni_3Ge (diamond symbol) and Ni_5Ge_3 (square symbol) compounds as a function of droplet diameter ranges from ≥ 850 μm to ≤ 38 μm 167

List of Tables

Table 3.1 Thermophysical properties of N₂ and Ni₃Ge compound.....	37
Table 4.1a Shows the calculation of Ni and Ge composition (on-stoichiometry), at atomic percentage.	64
Table 4.2a Shows the results of EDX area analysis of Ni and Ge composition (on – stoichiometry) at their atomic percentages. The regions (i) and (ii) have been taken from the Figure 4.2a.	67
Table 4.3 Shows the calculation of Ni and Ge composition (Ni-enhanced) at their atomic percentage.....	114
Table 4.4 (i) shows the average result of EDX area analysis of Ni and Ge composition at. % from the larger area, (ii) and (iii) shows results of EDX area analysis of Ni and Ge composition at. % from the two smaller regions of Figure 4.2b.....	115

Abbreviations

BS – British Standard

BSD – Backscatter Detector

D – Droplet diameter

DSC – Differential Scanning Calorimetry

EBSD – Electron Back Scattered Diffraction

EDX – Energy Dispersive X-ray

FIB – Focused Ion beam

OM – Optical Microscope

R – Cooling Rate

SADP – Selected Area Diffraction Pattern

SE – Secondary Electron

SEM – Scanning Electron Microscopy

TEM – Transmission Electron Microscopy

XRD – X-Ray Diffraction

Chapter 1 Introduction

Intermetallic compounds have been of widespread and enduring interest within Materials Science over the last 30 years or so. Such compounds are characterised by strong order and mixed covalent/ionic and metallic bonding, which gives rise to mechanical behaviour intermediate between ceramics and metals. Due to these characteristics they can display desirable magnetic, superconducting and chemical properties [1]. They also have a range of potential applications as high temperature structural materials due to good chemical stability and high hardness at elevated temperatures. Despite these strengths and wide range of applications of Intermetallic compounds including Ni-Ge intermetallic system, they have poor room temperature ductility. Therefore, the formability of these compounds has restricted industrial uptake of these materials. However, these kinds of limitations can be surpassed through the control of the degree of chemical ordering present within the intermetallic, with the disordered form will typically show behaviour that is mechanically more metallic relatively to the fully ordered form (higher ductility, lower hardness, and lower chemical resistance). Rapid solidification of intermetallics is therefore an important area of research as high cooling rates are one means of suppressing ordering. Annealing of the formed part, which occurs afterwards, can then be used to restore chemical ordering, and hence the properties of the intermetallic that are desirable.

Ni-base superalloys using two-phase γ/γ' have been used for many decades for structural material at high temperature because of their high melting points, relatively low densities, high strength, as well as good corrosion and oxidation resistance [2]. Since the 1980s, there has also been interest in using monolithic Ni_3Al (i.e. single phase γ'). On account of their exceptional high-temperature properties, Ni_3Al (γ') are also used as heat shields for combustion chambers. They are also used in industrial gas turbines [3]. However, researchers have found that Ni_3Ge is in many ways comparable to Ni_3Al (γ'). Both intermetallic compounds have the ordered L1_2 crystal structure. Ni_3Ge is brittle at room temperature but can be deformed plastically at higher temperatures [4].

Moreover, another well-established intermetallic compound $\gamma\text{-TiAl}$ has been studied and used for high temperature applications. The intermetallic compound $\gamma\text{-TiAl}$ has

significant capacity for being used in high temperature applications. This is due to the compound's low density, high strength and excellent capacity to resist oxidation [5]. Nonetheless, one of the main issues with alloy compounds that are single-phase is that they are not very ductile [6]. It has been demonstrated that two-phase (γ -TiAl + α_2 -Ti₃Al) alloys, which have a structure that is lamellar, tend to be comparatively stronger and more ductile [7, 8]. This could be caused by the gettering of interstitials from the γ -phase by the α_2 [9]. However, the structure of the interfaces may also have a significant role in this. It is supposed that the defects, which produce plastic deformations through their motion, are brought into being at interfacial features. Furthermore, the character and/or defect content of the interfaces that must be penetrated [10-13] also influences their transmission between different lamellas.

The α_2 -Ti₃Al phase has the characteristic of exhibiting the hexagonal DO₁₉ Ni₃Si-type structure that has a P6₃/mmc space group. α_2 -Ti₃Al can be explained as an ordered form of the hcp structure. In every close-packed (0002), a quarter of the sites plane is occupied by Al atoms at the stoichiometric composition. The γ -TiAl phase exhibits the tetragonal L1₀ CuAu-type structure. γ -TiAl is understood to be an ordered form of a fcc structure. In this structure, alternate (002) planes consisting of Ti and Al atoms are only present at the stoichiometric composition [14]. The lamellar structure forms from prior grains of α -phase. This α -phase is an hcp solid solution made of Al in Ti. It happens upon the cooling process, through the precipitation of γ -lamellae. It is followed by the ordering of the α -phase to α_2 [5].

The aim of this project is to study the solidification morphologies which are associated with disorder trapping at high growth rate, using drop-tube processing. Two congruently melting, intermetallic compounds β -Ni₃Ge and ϵ -Ni₅Ge₃ were selected for this project. The reason for selecting these compounds is that they are analogous to commercial high temperature intermetallics. Ni₃Ge is similar to Ni₃Al inasmuch it shares with the latter the L1₂ crystal structure. Ni₅Ge₃ shares with Ti₃Al the P6₃/mmc crystal structure. The rationale for concentrating on Ge-based analogues is that the Ge based compounds (β -Ni₃Ge and ϵ -Ni₅Ge₃) are congruently melting. In contrast, Ni₃Al and Ti₃Al are not. The reason why congruently melting compounds are particularly interesting for studying the various effects of disorder trapping in intermetallics is that with the correct stoichiometry (a fixed ratio of chemical composition) for the given

compound, the melt will be solidified without any form of solute partition. This solidification without partition occurs even during equilibrium solidification. Consequently, it is possible to study disorder trapping without having to consider solute trapping that are simultaneous, which would otherwise make the process more complicated. Since there is no solute partitioning, these results from the congruently melting compound are only made possible by order-disorder type reactions. In turn, these order-disorder type reactions are only made possible by a rapid solidification process. While there is not much work reported for the compound Ni_5Ge_3 , $\beta\text{-Ni}_3\text{Ge}$ compound has been examined before by Ahmed *et al* [15], who performed the undercooling experiments on the Ni-24 at% Ge alloy. In this experiment, a maximum undercooling of 362 K was observed using a melt-fluxing technique. They observed a discontinuous break in the curve at the onset of fully disordered development. For $\beta\text{-Ni}_3\text{Ge}$, this condition was met with an undercooling of 168 K and with a critical growth velocity of 0.22 m s^{-1} . Nonetheless, in flux undercooling experiments ($\sim 10 \text{ K s}^{-1}$) the post-recalescence cooling rate is extremely slow. This means that any evidence of a microstructural kind that relates to disorder trapping will have been extensively modified in the as-solidified sample. In this situation, there is no chance of examining APD's or even disordered material that have been retained.

This thesis has seven chapters. Each of the seven chapters addresses a subject of interest in a sequential manner, which will ultimately lead to an appropriate understanding of the research's aims and objectives. This project has been carried out within the scope of the two congruently, melting compounds, Ni_3Ge and Ni_5Ge_3 . The primary focus will be the morphology of the observed microstructures that is the consequence of the rapid solidification process (drop-tube). Consequently, this thesis studies the order-disordered trapping in these two compounds. It also studies the effect of the cooling rate on the microhardness and microstructures of Ni_3Ge and Ni_5Ge_3 compounds. Chapter one is a general introduction to the subject that has the function of describing the different sections as well as the function of providing an outline of the essential theme and scope of the study. Chapter two focuses on the achievements of previous researchers who have worked in this area of study. Also, we will briefly introduce some fundamentals of this project. Chapter three essentially gives details of the different experimental methods as well as details about the preparation of samples that were utilised during this study. These equipment and methods include: Arc-melt

and drop-tube process (for production of samples), Metallography technique and focused ion beam (FIB) technique (for preparation of samples), X-ray diffraction (XRD) , optical microscopy (OM), scanning electron microscope (SEM), energy-dispersive X-ray spectroscopy (SEM-EDX) and line-scan technique, electron backscatter diffraction (EBSD), transmission electron microscopy (TEM) bright field and dark field techniques, TEM selected area diffraction pattern (SADP), differential scanning calorimetry (DSC) and also Micro-Vickers hardness tester (for measurement of mechanical properties-hardness). Chapter four contains all the experimental results associated with congruent melting intermetallic compounds Ni_3Ge and Ni_5Ge_3 . Firstly, the results of the characterisation of the arc-melted produced compounds (Ni_3Ge and Ni_5Ge_3) will be presented. This chapter will also present the results of disorder – order morphologies and microstructural evolution of these two compounds (single phases) via drop-tube process. Chapter five is based around a discussion of all the results that have been presented in this thesis. It will state the principles and mechanism that underpin the observed results as well as exploring the basic science that governs such interdependence. In this chapter, all the results of our two congruently, melting compounds (Ni_3Ge and Ni_5Ge_3), will be discussed. In this discussion, the primary focus will be the morphology of the observed microstructures that is the consequence of the rapid solidification process (drop-tube). We will also discuss the effect of the cooling rate on the mechanical parameters of microhardness and microstructures of these two compounds. Finally, we will compare the microhardness results of Ni_3Ge and Ni_5Ge_3 compounds. Chapter six summarises the whole study, emphasising the findings as well as discussing what the value of this research is and its original contribution to knowledge. The chapter ends with a number of recommendations for future implementation. Chapter seven gives some suggestions for the future work. This appendixes contain additional data not included in the main body of the thesis (XRD reference pattern). All this data is referred to in an appropriate way in the main body of the work.

Chapter 2 Literature Review

In this chapter firstly we will present some fundamentals of this project, including crystal system, phase diagram of the Ge- Ni system, intermetallic compounds, fundamental of ordering structure (solute trapping, disorder trapping, antiphase domains boundaries), rapid solidification of intermetallic compounds, disorder trapping on Ge – Ni and non-germanium nickel intermetallic, and recent progress on this system. Secondly, we will present briefly a review of the observed microstructures including spherulites and dendrites (orthogonal and non-orthogonal dendrites, dendritic seaweed); spontaneous grain refine (SGR) microstructure in compound β -Ni₃Ge. Finally, in the ϵ -Ni₅Ge₃ compound the lath and plate microstructure that was observed is also briefly reviewed.

2.1 Fundamentals

2.1.0 Crystal System and Chemical Ordering

The knowledge of the crystal structure is an essential for the understanding and alteration of structure-property relationship. The nature of bonding in intermetallic compound could be partly ionic or covalent and metallic bonding, but the atoms of the individual elements commence in a preferred position within the crystal lattice, which is referred to as ordering. The chemical ordering of intermetallic compounds is referred to as having the arrangement of same element in the lattice parameter as shown in **Figure 2.1a**, otherwise chemically disordered crystal structure will formed as shown in **Figure 2.1b**. Intermetallic compounds can be classified into two categories on the basis of their chemical ordering (composition): one is stoichiometric and the other is non-stoichiometric intermetallic compounds. A stoichiometric intermetallic compound shows a fixed ratio of chemical composition, while a non-stoichiometric intermetallic compound has a range of chemical composition [16]. If there is exactly on the right composition (Ni₃Ge) all of the Ni is all of the cube of the faces and all the Ge is corner of the cubic which give exactly Ni₃Ge composition. But, if there is Ge-rich, then all of the Ge are in the Ge sites but there are some additional Ge at some of the Ni sites. They will produce anti-site defects by means Ni sites have wrong atoms because Ge atoms. In the other case, if there is Ni-rich, then all of the Ni atoms on Ni sites but rather than Ni atom on the Ge sites, some of the Ge site vacant. So there is

still 3 moles of Ni but there is less than 1 mole of Ge so means that compound is actually Ni rich. That's kind of compound produce structure vacancy.

2.1.1 Phase Diagram of the Ge – Ni System

The phase diagram for the Ni-Ge system has been studied extensively by Ellner *et al.* [17] and by Nash and Nash [18], in 1971 and 1987 respectively. More recently, further work has been also reported by Liu *et al.* [19] and by Jin *et al.* [20]. Nevertheless, it cannot be considered well established phase diagram, predominantly in the region from 20 to 50 at.% Ge. The accepted Ge- Ni phase diagram [18] is shown in **Figure 2.2a**, where 9 intermetallic compounds, i.e. β -Ni₃Ge, γ -Ni₃Ge, Ni₃Ge₂, δ -Ni₅Ge₂, Ni₂Ge, ϵ -Ni₅Ge₃, $\acute{\epsilon}$ -Ni₅Ge₃, Ni₁₉Ge₁₂ and NiGe. These listed 9 intermetallic compounds identified within the currently accepted phase diagram.

2.1.2 Intermetallic Compounds

The Intermetallic compounds, Ni₃Al, Ni₃Si, Ni₃Fe and Ni₃Ge have an ordered L1₂ (cP4) crystal structure and have a space group 221. A derivative of the face centered cubic (fcc) crystal structure is shown in **Figure 2a** in which nickel (Ni) atoms occupy face-centred positions and the aluminium (Al)/ silicon (Si)/ iron (Fe)/ germanium (Ge) occupy the corners of the unit cell. **Figure 2a** shows 6 Ni atoms on faces ($6 \times (1/2) = 3$ Ni atoms) and the 8 Al/Si/Fe/Ge atoms on edges ($8 \times (1/8) = 1$ Ge atom), which gives the expected 3:1 Ni-Ge ratio. The intermetallic compound ϵ -Ni₅Ge₃ (high temperature) has the P6₃/mmc crystal structure (hexagonal, space group 194), while $\acute{\epsilon}$ -Ni₅Ge₃ (low temperature) has the C2 crystal structure (monoclinic, space group 5) [20].

2.1.3 Fundamental of Ordering Structure

An ordered intermetallic compound belongs in a distinctive class of metallic materials that form long-range ordered crystal structures below a critical temperature, which is commonly referred to as the critical ordering temperature (T_c). These ordered intermetallics generally occur in comparatively narrow compositional ranges around simple stoichiometric ratio, such as the Ni₃Ge and Ni₃Al intermetallic compounds. The term superlattice and ordered structure are usually used interchangeably. The term

superlattice suggests the ‘superlattice is made up of sublattices’ (such as Ni_3Al , Ni_3Sn , Ni_3Ge , Ni_5Ge_3).

An ordered structure is a result of an ordering transformation of a disordered structure. In phase formation and transformation of intermetallic compounds, chemical ordering has an important function. A critical temperature, T_c , is defined for a system in question. This transition temperature is the point at which the free energies of the ordered and disordered solid phases are in equality. The solid’s equilibrium growth will at first happen in the disordered state when the relation between the transition temperature and the melting temperature (T_M) is as follows: $T_c/T_M < 1$. As the temperature goes below T_c , the solid-state is affected by a disorder-order transformation that ensues from the drop of temperature. In contrast, when the relation between the transition temperature and the melting temperature is as follows $T_c/T_M > 1$, it is directly from the liquid that the equilibrium growth will occur. This equilibrium growth leads to the ordered solid phase. Nevertheless, what is called disorder trapping can occur in these cases. By this it is understood that as a consequence of high growth rates the rapid solidification process can bring about a form of growth that is disordered. It has been demonstrated in a range of intermetallic systems [21] in relation to the B2 AlNi phase, and [22] in relation to CoSi) that growth of the ordered phase is significantly slower than that of the disordered phase, with a jump in the growth velocity being evident at the (1st order) disorder-order transition. This difference in speed of growth is marked by a rise in the velocity of the growth at the order-disorder transition.

In the development of a substitutional type of solid solution, there is no specific position for the solute atoms. The solute atoms are distributed in a random way in the solvent’s lattice structure. This kind of structural development can be considered disordered. In times when this random solid solution is cooled slowly, the atom is rearranged so that the solute atom moves into definite position in the lattice. An ordered solid solution or superlattice forms from this kind of development. Two kinds of ordering are known in substitutional solid solution. These are short range order (SRO) and long range order (LRO). The short range order denotes when the atoms have a tendency to be encircled by atoms of the opposite type. They tend to only order over some short distances. In contrast, long range order denotes when atoms have a

tendency to be encircled by atoms of the other type. LRO parameter, η , can be used for the quantification of the level of order within a structure and as a consequence for the measurement of the degree of disorder trapping as well. The LRO parameter η (for a binary compound), can be defined by following equation (2-1):

$$\eta = \frac{r_A - X_A}{1 - X_A} \quad (2-1)$$

Here, X_A is the mole fraction of atoms of species 'A', while r_A represents the probability that the correct type of atom is present on the sublattice site 'A'. In this equation, η varies from 1 (fully ordered) to 0 (completely random solid-solution) [23].

When order – disorder transformations happen, the order parameter's rate of change (especially η) with temperature fluctuates for the different superlattices. The sublattice's atomic configuration determines if, around the T_c , there is a continuous or abrupt decrease of the parameter. These order – disorder transformations can be classified, in thermodynamic terms, into two-phase transformation types. These are called first-order and second- order transformations (**Figure 2.3**).

In a first-order transformation, there is a difference in the entropy in the corresponding phases before and after. As there is a discontinuity in the first derivative of the Gibbs free energy (G) at equilibrium transformation temperature, $dG/dT = -S$ and $dG/dP = V$, first-order transformation has changes in entropy (S) and volume (V) that are discontinuous. Enthalpy (H), which corresponds to the evaluation of the latent heat of transformation, is also characterised by a similar discontinuous change. In this process, there is a discharge of a fixed amount of energy. Some of this energy cannot be progressed instantly amongst the procedure and the surrounding region. Consequently, first-order transformations are understood as forming part of a system that is mixed-phase. In contrast, a phase transition of the second-order transformation will be continuous. In latter case, the second derivatives of Gibbs free energy will be discontinuous. The enthalpy is also characterised by continues on account of the first derivative being continuous. Despite this continuity, there is no related latent heat.

Second-order transformation does not have a two phase region, even at the range of non-stoichiometric composition. In **Figure 2.3b** the order-disorder transformation is characterised by a progressive disordering of structure, which occurs over a range of

temperatures. No abrupt changes in the ordering at T_c occur here. Therefore, the internal energy and enthalpy is continuous across T_c , which shows the second-order transition. This continuity reveals the transformation of second-order. The **Figure 2.3a**, a graph of the first-order transition, shows an abrupt change in order at T_c . In comparison to states that are ordered, disordered states are characterised by internal energy that is higher as well as higher enthalpy, on account of high energy-like atoms bonds being in larger quantity. As a consequence, there is a discontinuous change in enthalpy at T_c [24].

2.1.4 Rapid Solidification and Disorder Trapping of Intermetallic Compounds

Intermetallic compounds display an attractive combination of physical and mechanical properties such as high strength, high melting point, low density, good oxidation and creep resistance. Conversely, poor room temperature ductility limits formability, although this can be increased by rapid solidification processing, wherein a reduction of the degree of chemical order and the formation of a fine pattern of antiphase domains (APD's) increases ductility [25-27]. Moreover, the high temperature properties can be restored by chemical ordering via annealing out the APD's subsequent to forming [25].

Rapid solidification of an intermetallic compound can be accomplished with a reduction in the chemical long-range order in the solid/liquid interface. The reduction in the degree of order would result in a distinctive kinetic effect, namely solute trapping and disorder trapping. Disorder trapping would occur, if the solidification velocity is increased and which resulted in loss of local interphase equilibrium leads to reduction of degree of order. However, APD's occur after rapid solidification during reordering. APD's are the boundaries between regions where chemical ordering has taken place on different sub-lattices. With the formation of APD's boundaries, the degree of order is affected at non-equilibrium by the thermodynamics of the growing phase [28, 29]. Disorder trapping may be considered analogous to the more familiar process of solute trapping, wherein a non-equilibrium solute distribution occurs at the solid-liquid interface due to rapid solidification [30].

Solute trapping, due to loosing local interface equilibrium in the course of rapid growth, occurs in a conventional, disordered solid solution. In this case, the solid's

composition approaches the composition of the liquid at the interface. For the variations that are compositional, it is through the coefficient of the partition [27] that the evaluation of the divergence is performed from thermodynamic equilibrium. In a similar way, in order to account for the disorder trapping of intermetallics in the process of rapid solidification a model has been elaborated by Boettinger and Aziz [28]. It shows that a short-range diffusion of atoms is needed for an ordered superlattice to form in the intermetallic compound. A disordered compound forms when an entrapment of disorder occurs due to the velocity of the growth approaching atomic diffusion speed. In order to measure the deviation from equilibrium due to the disorder trapping [31], the order parameter that is long range can be utilised. This is the same as when the partition coefficient's variations are utilised so as to measure quantitatively departure from equilibrium caused by the solute trapping.

Through the model discussed above (Boettinger and Aziz), it is forecast that there will be a decrease of η in the case of compounds that are congruently melting. This decrease would be due to an increase of solidification velocity, which is accompanied by steadily increasing levels of chemical disorder being trapped in the structure. In thermodynamic terms, these types of changes are either first- or second-order. In the case of first-order transitions, wherein there is a coexistence in equilibrium of phases that are ordered and disordered, there will be an uninterrupted decrease of η (see **Figure 2.4**). This is concurrent with an increase of the growth velocity V up to critical velocity (V_C) in which there is a discontinuous fall of g right down to zero for velocities that are greater than V_C , [32]. In contrast, the transitions of second-order, wherein the ordered and disordered phases are not allowed to exist together, it is regarded as likely that, with an increase in growth velocity, g will decrease repeatedly up to the point when an entirely disordered solution is secured ($\eta = 0$). For second-order transitions, V_C or the critical velocity is connected through the relationship outlined in the equation below to the velocity that is diffusive (V_D):

$$V_C = V_D \left(\frac{T_C}{T_M} - 1 \right) \quad (2-2)$$

In this equation (2-2), V_D is the characteristic velocity for interface diffusivity and we now assume $T_C/T_M > 1$, such that equilibrium growth will be direct to the ordered state. For intermediate velocities, as $V \rightarrow V_C$, partial disordered trapping can happen, with

the metastable disordered phase in competitive growth with the equilibrium phase. On account of the generally higher growth rates for disordered phases this may go faster than the growth of the partially ordered phase [32].

Assadi and Greer have established through a model of intermetallic dendritic growth [33], which considers behaviour of complex partitioning and disorder trapping, that the velocity of growth becomes greater at the moment when the solid that is growing attains a totally disordered state. This particular model seems to have emanated from Herlach's observations [22] regarding the intermetallic compound CoSi. In this intermetallic compound the velocity of the growth exhibited an abrupt gradient increase with undercooling. A critical undercooling that approximated 310 K, being consistent with a velocity of critical growth of $\approx 3.8 \text{ m s}^{-1}$. This abrupt expansion of the velocity of growth is successfully modelled because it is assumed that there is a transitioning between, on the one hand, ordered compound's diffusion limited growth that is lower than V_C and, on the other hand, the disordered compound's collision-limited growth that is higher than V_C . After the disordered solid has developed because of the high velocity growth, a certain amount of reordering can occur. This reordering would happen directly after recalescence, when the material is at an elevated temperature.

During the period that comes straight after recalescence, when the compound is at a high temperature, reordering can occur to some degree, following on from disordered solid formation. This formation of disordered solid is due to growth that occurs at high velocity. The degree of the reordering in question is dependent upon the cooling rate of the phase in post-recalescence. It should be noted that anti-phase domains can also form as a consequence of this reordering process. The transformation process from the disordered solid to the ordered form, via a nucleation process, thermally produces the results of the anti - phase domains APD's (see the **Figure 2.5**). In a specified nucleus, the locations of the atoms are specific to the sublattice. As a consequence the ordering is distinct from the adjacent nuclei. With an increase in size of the nuclei, domains grow with each other and end up touching. This leads to the creation of APB's [34]. The morphology of the APD's formed in rapid solidification is heavily dependent on the cooling rate of the solid following growth [35]. On the basis of the cooling rates, there are three possibilities in the subsequent growth of solid. First at the modest

cooling rates, columnar APD's can be formed. Second, at higher cooling rates equiaxed APD's can be formed. Finally at very high cooling rates all reordering process could be entirely suppressed (see **Figure 2.6**). Nevertheless, all steps in this sequence may not be visible in all of the materials [35]. Alternatively, some materials may experience a change to a solid that is glassy prior to the occurrence of complete disorder trapping [36].

2.2 Recent Progresses

According to the phase diagram of Nash and Nash [37], the Ni-rich portion of which is shown in **Figure 2.2a**, β -Ni₃Ge and ϵ -Ni₅Ge₃ are the congruently melting compounds with a melting point of 1405 K (1132 °C) and 1458 K (1185 °C) respectively. The β -Ni₃Ge has a homogeneity range of 22.5 to 25 at. % Ge and crystallises to the ordered fcc L1₂ structure. The ϵ -Ni₅Ge₃ has a homogeneity range of 34.6 – 44.5 at.% Ge and crystallises to the ordered hexagonal P6₃/mmc crystal structure.

Congruently melting compounds are particularly interesting for studying the various effects of disorder trapping in intermetallics. This is so because with the correct stoichiometry for the given compound, the melt will be solidified without any form of partition. This solidification without partition occurs even during equilibrium solidification. Consequently, it is possible to study disorder trapping without having to consider solute trapping that are simultaneous, which would otherwise make the process more complicated.

While there is not much work reported in the system ϵ -Ni₅Ge₃, the β -Ni₃Ge system has been examined before (Ahmed *et al.*) [15]. In this study, a maximum undercooling of 362 K was observed by utilising a technique for flux undercooling. In this particular study, the growth velocity that corresponded to the undercooling was specified to be 3.55 m s⁻¹. [15] noticed that at the start of the fully disordered process of growth, there was a break in the curve that was discontinuous in character. This finding is the same as other cases that tried to ascertain intermetallic compound velocity-undercooling curves to cross through the transformation of order-disorder. In the case of β -Ni₃Ge, it is at an undercooling of 168K that this condition was examined. The velocity of the critical growth was of 0.22 m s⁻¹. This compares with $V_c = 0.75$ m s⁻¹ in Fe-18 at. %

Ge [38] and $V_c = 3.8 \text{ m s}^{-1}$ in CoSi [22]. A change from a grained structure that is coarse at the time of the ordered phase of growth to a structure of grain that is markedly finer grained after the disordered phase of growth was revealed by the β -Ni₃Ge system microstructural analysis [15]. There appeared to be cracking patterns that were extensive on the structure with coarse grain. It is assumed that this resulted from a stress induced by shrinkage in the solid. By contrast, in the material that was disordered, these patterns (cracking) were not visible. Nonetheless, in flux undercooling experiments ($\sim 10 \text{ K s}^{-1}$) the post-recalescence cooling rate is extremely slow. This means that any evidence of a microstructural kind that relates to disorder trapping will have been extensively modified in the as-solidified sample. In this situation, there is no chance of examining APD's or even disordered material that have been retained.

The β -Ni₃Ge system has a crystal structure that is ordered fcc L1₂ (Cu₃Au). The crystal structure of the β -Ni₃Ge compound is shared with several intermetallics that have X₃Y as a composition. This is so because at the cell corners 1 atom per cell are naturally accommodated by the fcc unit cell. On the cell faces, the fcc unit cell also accommodates 3 atoms per cell. A similar L1₂ crystal structure is common to several important intermetallics that are characterised by potential structural applications at high temperature. These important intermetallics comprise γ -Ni₃Al [39] and Al₃Ti [40]. In both, adding of several dopants, which include Cr, Mn, Fe and Co, Al₃Sc [41] and Pt₃Al [42] can have the effect of changing D0₂₂ structure, which is normal, to a L1₂ structure. As a consequence, to comprehend the kinetics of the order–disorder transformation in what is a fairly uncomplicated model system could be helpful in acquiring a better understanding of the compoment of these compounds that are more complex.

Not so much research has been carried out on the solidification of Ni–Ge system. Fang and Schulson [43] studied the gas atomisation and the ensuing extrusion into bars of Ni₃Ge has previously been studied. However, in this previous study [43], the alloy was doped with 0.06 at.% of boron. Moreover, a large majority of the metallographic analysis conducted as part of the study focused on the separation of the doping agent (boron) and the nickel boride precipitates that formed subsequently. The addition of boron is usually understood to make the alloy more ductile. However, contrary to other

cases such as the Ni₃Si, Ni₃Ge tends to carry being brittle, despite the addition of boron [44].

β -Ni₃Si and Fe₃Ge are intermetallic systems that are closely related to the β -Ni₃Ge system. **Figure 2.2b** shows the equilibrium phase diagram for the Ni-rich end of the Ni-Si system [45]. Ni₃Si happens in both low (β_1) and high (β_2/β_3) temperature forms. The respective crystal structures of these are L1₂ and D0₂₂. Additionally, the high temperature phase has two forms: an ordered form and a disordered form (β_2 and β_3) that produce the three forms indicated by the phase diagram. The fields of temperature stability are $1388 \text{ K} \leq T \leq 1443 \text{ K}$ for β_3 , $1263 \text{ K} \leq T \leq 1388 \text{ K}$ for β_2 and $T \leq 1308 \text{ K}$ for β_1 . The compositional range of the two high temperature polymorphs are 25.0- 26.1 at. % Si. In contrast, the compositional range of low temperature β_1 polymorphs is 22.6- 24.5 at. % Si. However, no overlap occurs in these composition ranges. If many different undercoolings are used, this lack of overlap may make the analysis of the solidification of β -Ni₃Si from its undercooled parent melt more difficult. However, while the phase diagram suggests single phase growth of β -Ni₃Si from the Ni-25at.% Si melt should be possible for undercoolings in excess of 43 K, both flux undercooling [46] and drop-tube studies [47] have revealed that such direct growth of β from the melt appears to be inhibited at all undercoolings in favour of a α Ni- γ eutectic, γ being the phase Ni₃₁Si₁₂. Also, phase diagram shows at equilibrium is α - β eutectic but Ahead *et al.* found rapid solidification of Ni-25at.%Si did not given α - β eutectic or pure β as expected, it gave an α - γ eutectic [48].

Comprehensive studies of undercooling of the firmly similar Fe-Ge system have been conducted. These studies were conducted at compositions of Fe-25 at.% Ge [49] and Fe-18 at.% Ge [38]. Fe-25 at.% Ge is stoichiometric with the Fe₃Ge compound, whereas, the latter solidifies to the ordered α -phase. These two compositions (Fe-25 at.% Ge and Fe-18 at.% Ge) develop visibly into an ordered compound at low undercooling. Also, Fe-18 at.% Ge shows the same growth as CoSi. This growth of velocity abruptly increased above a critical undercooling temperature. This abrupt increase in velocity is consistent with a transition from diffusion to collision-limited growth. In the Fe₃Ge compound, this transition from diffusion to collision-limited growth has not been observed. However, this lack of transition may have been caused by the maximum undercooling of this system being still too low ($DT = 190 \text{ K}$).

Notwithstanding, in comparison to the simpler Ni₃Ge system, the Fe₃Ge system is significantly more complex. As a consequence, it cannot be assessed in an analogous way to β-Ni₃Ge. εFe₃Ge that has an ordered hexagonal D0₁₉ structure forms through the peritectic reaction $L + \alpha_2 \rightarrow \epsilon$, in which α_2 is an ordered B2 phase [50]. Furthermore, as shown in **Figure 2.2c** [51] ε is dimorphic undergoing a transition to ε' which, like β-Ni₃Ge, has an ordered L1₂ structure. In spite of that, ε phase should be achievable through direct solidification in the case of undercoolings that are greater than 140 K. Nevertheless, there is no evidence of an order-disorder transformation for undercoolings that went up to 198 K, in which the velocity of the growth equalled 1.3 m s⁻¹.

2.2.0 Spherulites Microstructure

The crystalline morphology termed spherulites was first observed by Talbot in 1837 during the crystallisation of borax from phosphoric acid [52]. On the basis of their morphology, spherulites are usually characterised as either Category 1 or Category 2. A spherulite of Category 1 grows radially from the site of nucleation. It branches out intermittently in order to maintain space filling. A spherulite of Category 2 grows initially as thread like fibres, forming new grains at the growth front in a successive way [53, 54]. Subsequently, Brewster gave the name of ‘circular crystals’ to the objects of Talbot’s interest [55]. Spherulite has become the generally accepted term for what Brewster called ‘circular crystals’. Example of spherulites are shown in the **Figure 2.7** [54, 56]. Spherulites are commonly found in a range of materials, including small molecule organic crystals and polymers. They are also found in other materials, including inorganic crystals, volcanic rocks and a few pure elements (e.g. graphite, sulphur and selenium). However, spherulite development is much rarer in metals that are fully crystalline, sometimes in cast iron (graphite), albeit they are noticed in partially crystalline glass forming alloys, both as residual crystals subsequent solidification and as devitrification products [56].

Spherulites are most common in polymers and small molecule organic crystals. They are especially common in high molecular weight polymers, which have been grown directly from the melt. In these, the long chain molecule reorientation is restricted by topological constraints. Spherulites are most common in systems that are unoriented.

The suppression of spherulite growth appears where there exists a strong tendency for uniform molecular orientation: for example, in the case of growth that occurs in a gradient of strong, externally imposed temperature. Polymers and metallic glasses are characterised by low diffusivity. Consequently, it is probable that kinetics dominates the development of spherulites. Additionally, the anisotropy of polymers tends to be relatively low [57]. The structure of these kinds of spherulites is characterised by multiply branched crystalline arms, which are separated by amorphous regions between the arms [56]. Typically, the amorphous regions are shorter than the molecular chains, so that one molecule can go through many such crystalline and amorphous regions [58].

The development of spherulites is also found in a number of metallic systems, including metallic glass forming alloys. In these, in particular, spherulites are observed both as residual crystals during the freezing from the melt as well as amorphous-crystalline composite structures during devitrification of the fully amorphous material. Lu *et al.* [59] observed such residual spherulite crystals forming directly from the melt during Bridgeman solidification of La-Al-Ni glass forming alloys. Spherulites between 10-30 μm in diameter were examined for pulling speeds of 2.3-2.4 mm s^{-1} . In contrast, fully amorphous materials were produced at pulling speeds higher than 2.3-2.4 mm s^{-1} . These spherulites were crystalline eutectic structures in an amorphous matrix. However, the crystalline phases containing the eutectics were not identified by Lu *et al.*

Further during the Bridgeman solidification, but in a Zr-Ti-Cu-Ni-Be glass forming alloy, Cheng *et al.* [60] identified a range of multiply branched crystalline morphologies embedded in an amorphous matrix. One of the phases present was identified as Zr_2Cu . Other phases were also present in this system. However, these could not be identified by the authors. These structures, favoured by low pulling speeds, had an elliptical outer envelope. However, the orientation of the crystalline needles within the structures had characteristic similar to Category 2 spherulites.

Aboki *et al.* reported [61] slightly larger spherulitic crystals, which were up to 120 μm in diameter, in Zr-Cu-Al-Ni glass forming alloys cast into a water cooled copper mould. This casting occurred at cooling rates estimated around 100 K s^{-1} . It can be surmised that these are crystalline, probably eutectic, structures, which are embedded

within an amorphous matrix. Through the XRD analysis of Zr-Cu-Al-Ni compound, at least 9 crystalline phases were found within this compound. However, Aboki *et al.* were not able to confirm which contributed to produce the spherulites structures.

Several authors have observed the devitrification, which takes place during the annealing process of Fe-Si-B soft magnetic metallic glasses. During this process, various morphologies, including spherulites, were found depending on the composition studied. In the case of Fe₇₅Si₁₂B₁₃, the composition of the spherulites consisted of the metastable intermetallic Fe₃B, which decomposes into Fe₂B when the samples are fully crystalline [61]. In contrast, the composition of the Fe₇₅Si₉B₁₆ compound is characterised by three discrete stages of crystallisation, which were revealed when the sample was heated [62]. However, the first stage of crystallisation during heating produces spherulites of pure Fe from the Fe₇₅Si₉B₁₆ compound.

Yano *et al* [63] used TEM and positron annihilation lifetime measurements in order to observe the formation of spherulites in a Zr₅₀Cu₄₀Al₁₀ bulk metallic glass forming alloy. After the annealing process took place at 773 K, crystallisation progressed in the form of spherical agglomerates of crystallites that develop in a radial way. These spherical agglomerates are 600 nm in diameter. In order to understand the crystallography of both the spherulites and the surrounding matrix material, selected area diffraction patterns were utilised. The selected area diffraction patterns showed that the space group for the spherulites was one of the orthorhombic groups. Additionally, the inter-spherulite region showed a two-fold symmetry and was observed to be a fcc structure.

The development of nano-crystalline spherulites during the devitrification of both binary and multicomponent metallic glass systems have been studied by numerous other researchers [63-66]. In nearly all of these studies, the spherulites are distributed in a homogeneous way in the amorphous matrix. In these cases, the spherulites are characterised by a radial growth that originates from the centre of nucleation sites. This suggests that the growth of the spherulites is initiated upon pre-existing nuclei being frozen into the metallic glass. The spherulites seem to not be sensitive to the rate of heating. Spherulite crystallisation was shown not to be inhibited even by heating rates as high as 10³ K s⁻¹ [67].

Elsewhere, Sun and Flores [68] found that in the crystallisation of $Zr_{58.5}Cu_{15.6}Ni_{12.8}Al_{10.3}Nb_{2.8}$ bulk metallic glass in DSC, high heating rates ($> 2.5 \text{ K s}^{-1}$) produced the development of spherulites. By contrast, low heating rates produced the formation of non-spherulite nano-crystalline structures. From this, Sun and Flores came to the conclusion that the activation energy needed for the growth of nano-crystalline structures is higher in comparison to the activation energy that is necessary for the growth of spherulites. They made the further observation in a laser processing study of the same alloy [69] that spherulites are able to be produced without partitioning, that is at the same composition as the amorphous matrix.

While there is controversy in the literature as to the formation mechanism for spherulitic growth, a number of common requirements for their formation have been identified. One is a tendency towards non-crystallographic, small angle branching [70]. A second is a high viscosity in the medium being crystallised. The importance of this has been demonstrated unambiguously by Morse *et al.* [71, 72] who, in a study of the crystallisation behaviour of inorganic salts, identified around 70 salts that would crystallise in spherulitic form if grown in a gel base media, but not otherwise. The requirement for a high viscosity in the melt would be consistent with the inclination for glass forming alloys, but not other metallic melts, to crystallise to spherulitic morphologies.

It has been suggested by Gránásy and co-workers that evolving a phase-field model of spherulite growth in polymers may be favoured in situations where translational diffusion may be significantly easier than rotational diffusion [73] and one can certainly imagine how this situation might arise during the crystallisation of long chain polymers, although it is less obvious how such a situation might arise in metals or other small molecular systems. Despite this, there is some evidence that similar conditions may exist in both organic [74] and metallic [75] undercooled glass forming liquids, with a decoupling of the translational diffusion coefficient from the macroscopic viscosity and a decoupling of the translational and rotational diffusion coefficients. Metal have translational diffusion means atom can move one place to another place. While, polymer is also have that but in addition polymer have rotation diffusion where the molecule is not moving to another place but they change rotation, which refer as rotational diffusion. The propensity of metallic glass formers to form spherulites is

also suggestive of the requirement for some level of structure in the non-crystalline precursor to be a prerequisite. This also appears to be true of other spherulite formers, such as pure elemental Se, which is reported to have a very unusual molecular structure, intermediate between polymeric and simple molecular liquids [76].

2.3.0 Departure from normal Dendritic Growth during Rapid Solidifications

The word dendrites derived from the Greek word, δένδρον, meaning the 'tree'. In metallurgy, a dendrite is a distinctive tree-like microstructure of crystal growing at the time that molten metal freezes, this structure results of rapid growth along firmly favourable crystallographic directions. The growth of dendrites has great effect in respect to materials properties [77]. The morphology of metal crystallization occurs during near-equilibrium solidification stage. In that stage metals exhibit a strong directionality. This strong directionality is established in the underlying crystalline anisotropy through the 'easy' growth directions. More specifically, these are directions of minimum capillary stiffness/interfacial stiffness (a quantity that represents the reduction of the melting temperature at the solid/liquid interface [78]) whereby the melting temperature is most highly depressed by the Gibbs-Thomson effect. Typically, this results in the growth of structure such as dendrites, which for metals with an underlying cubic symmetry, will display well developed side-arms orthogonal to the primary trunk. But, a number of changes will be apparent in these solidification structure with increasing departure from equilibrium. That would be either a switch in the growth direction away from these easy directions or it could be a more general loss of directionality in the solidification morphology [79].

Typically, the first of these leads to a switch from the equilibrium $\langle 100 \rangle$ growth direction, to growth along either the $\langle 110 \rangle$ or $\langle 111 \rangle$ directions. In this case, the $\langle 100 \rangle$ to $\langle 110 \rangle$ transition is directly observed in the transparent analogue casting system $\text{NH}_4\text{Cl} - \text{H}_2\text{O}$ [80]. In this kind of transition the primary solidification morphology remains dendritic. However, the transition is show by a switch to side-branches which are no longer orthogonal to the primary trunk [79, 81]. This transition can occur coincidentally with a break in the gradient of velocity-undercooling curve [82]. X-ray or EBSD pole-figure plots can be used for the confirmation of switch in growth direction within an as solidified sample [82]. This evidence can also be provide by selected area

diffraction pattern (SADP) from the TEM. This switch typically happens in an abrupt way in the growth direction, at a well-defined undercooling. This switch is also usually attributed to a competition between differently surface energy and directed kinetic anisotropies. The same mechanism is also thought to be responsible for the more general loss in directionality during rapid solidification, possibly as competing anisotropies cancel out [83]. This produces solidification morphologies such as doublons and dendritic seaweed, which have been found in the transparent analogue casting system $\text{CBr}_4 - \text{C}_2\text{Cl}_6$ [84], polymers [85] and metals [86, 87]. In comparison to well-defined switch in growth direction this transition is more diffuse. The well-defined switch can occur gradually over a range of undercoolings or with the transition being prefaced by a change in growth direction [79]. Definitely, it has been shown that in certain alloys a continuous range of growth directions can be accessed prior to a transition to seaweed type growth [88].

Within the broad class of metallic materials, the growth transition from dendritic to seaweed does not only occur in solid-solution alloys. It also happens in intermetallic compounds. Assadi *et al.* [89] have demonstrated that when close to the congruent composition the congruently melting intermetallic NiAl can experience a dendritic to seaweed transition at an undercooling around 250-265 K. The NiAl solidifies to the ordered cubic B2 crystal structure directly from the melt when close to equilibrium.

Assadi *et al.* suggest the dendritic to seaweed transition is caused by disorder trapping which happens during rapid solidification. Assadi *et al.* claim that the loss of long range order at the fast growing dendrite tip results in an extreme depression of the melting temperature. They argue that loss of long range order at the fast growing dendrite tip leads to an extreme depression of the melting temperature which can 'mask' the interfacial stiffness. Coupled with increased orientational disorder, which increases the free energy of the solid, this makes the system behave in a low anisotropy manner. The idea of orientational order parameter therefore distinct signifies the definitiveness of the crystal orientation, which can be used to interpret the influence of the orientational ordering kinetics on the growth morphology [78]. According to this model, other congruently melting intermetallics should show a dendritic to seaweed transition under rapid solidification conditions. The only other condition is that during equilibrium solidification the compound should order at the liquidus

temperature, such that disorder trapping is possible. One such intermetallic that satisfies both conditions is β -Ni₃Ge.

2.4.0 Spontaneous grain refine (SGR) microstructure

Spontaneous grain refinement (SGR) is characterised by abrupt changes in grain size. This takes place while metallic melts that have been deeply undercooled solidify. In a typical way, this change in grain size happens by at least an order of magnitude. In the case of metals that are pure, it shows as a grain size reduction, which occurs above an undercooling temperature (ΔT^*) that is critical undercooling [90-92]. By contrast, it is not rare for alloys to show a compartment that can be considered more complex. For alloys, studies have observed two transitions of grain refinement [93-95].

In alloy systems that show this behaviour, SGR is observed for undercoolings below a lower critical value, ΔT_1^* , and above an upper critical value, ΔT_2^* . Where measurement of growth velocities is taken during the deep undercooling studies required for SGR [96], a discontinuous break in the gradient of the velocity-undercooling curve is typically observed at ΔT^* (or at ΔT_2^* in alloys systems). Below ΔT^* , the growth velocity, v , depends on ΔT according to $v \propto (\Delta T)^\beta$ (typically with $\beta \approx 2$). This relationship is common to many metals undergoing dendritic growth. On the contrary, above ΔT^* the dependence of v upon ΔT is approximately linear.

The scientific community concerned with rapid solidification has taken an on-going interest in grain refinement of a spontaneous type. This is the case since Walker observed it for the first time in pure Ni in 1959 [97]. There is a some controversy about the origin of this phenomenon. Initial explanatory models were based on cavitation that was induced by shrinkage. This was understood to lead to considerable amounts of nucleation right in the solidification front [97]. Alternatively, it was understood to result from trace solute additions effects. In particular, those that took the form of dissolved gases [98]. Since these models emerged, a large majority of them have been discredited.

Several authors also proposed that recrystallization or recovery may play a role [99, 100], despite the fact that in drop-tube studies Cu-Ni and Fe-Ni alloys have difficulties

to accommodate this recovery. In these two alloy system, grain refined structures were still observed, although the cooling rate was sufficiently high to suppress recrystallization and recovery [101].

The dendritic melting and fragmentation following recalescence is considered as a 'standard model' for SGR [102]. Remelting may or may not take place in both conditions. This process is determined by the balance between two time scales, characteristic length scale and macroscopic cooling rate. The characteristic length scale used for determination of growth of melting of dendrite arms is τ_m . While the macroscopic cooling rate applicable for the co-existence of the solid and liquid is τ_s . Remelting occurs when the condition of $\tau_m < \tau_s$ is satisfied. The model of dendritic melting and fragmentation is attractive because of its ability to explain why there is one transition in pure metals and two transitions in alloys. It is relating to the predicted dependence of the dendrite tip radius, ρ , on ΔT . When there is a transfer of growth control from solute that is limited at high solute Peclet number to solute that is limited thermally at low thermal Peclet number [103], an alloy system will show a local minimum in ρ . This small ρ is given at low and high undercooling temperature. This appears to correspond with low and high undercooling SGR transitions. In the perspective of the thermal, the Peclet number is equivalent to the product of the Reynolds number (Re) and the Prandtl number (Pr).

Despite this there are a number of limitations to the model, not least that post-recalescence remelting cannot explain a break in the velocity-undercooling curve, which therefore needs to be ascribed to coincidence. Moreover, observations in deeply undercooled ultra-pure Cu by [86] seem to indicate that the break in the velocity-undercooling curve associated with SGR, observed in this system at $\Delta T = 280$ K, is actually characteristic of a switch in growth morphology from dendritic to dendritic seaweed. Frozen in seaweed structures were observed over a narrow range of undercooling > 280 K, with grain refinement by recrystallization and recovery being observed for $\Delta T = 310$ K.

At least in part, the controversy over the SGR mechanism may result from there actually being more than one mechanism operating. In two related studies on dilute Cu-Ni alloys Castle *et al.* [79, 81] identified that three separate grain refinement mechanisms were operating; recrystallization, which was observed only at the low

undercooling transition, dendritic fragmentation, which could occur at either low or high undercooling and dendritic seaweed fragmentation, which occurred only at high undercooling. Furthermore, in order for dendritic fragmentation to occur. It appeared that a switch in the growth direction was needed in the case of Cu-Ni from $\langle 100 \rangle$ at low undercooling to $\langle 111 \rangle$ at high undercooling.

2.5.0 Plate and Lath microstructure

Plate and lath structures are not unusual in intermetallic compounds [104-106]. They are also quite common in some iron alloys [107]. Plate and lath structures were observed by Hyman *et al.* in γ -TiAl [104]. These were produced by the solid-state transformation of α dendrites during cooling to a mixture of $\alpha_2 + \gamma$ laths surrounded by γ segregates. Plate and lath morphology in α_2 -Ti₃Al which, like ϵ -Ni₅Ge₃, shares the P6₃/mmc space group was also observed by McCullough *et al.* [105]. Yet, in Ti₃Al, the plate and lath morphology clearly occur because of the different phase contrasts.

In this project, the rapid solidification of the intermetallic Ni₅Ge₃ will be considered. This is an interesting model system as, being congruently melting, the ordering reaction can be examined without any complicating solute effects. By this, it is meant that solute partitioning, and consequently, also solute trapping is absent. This morphology will be discussed in the results and discussion section.

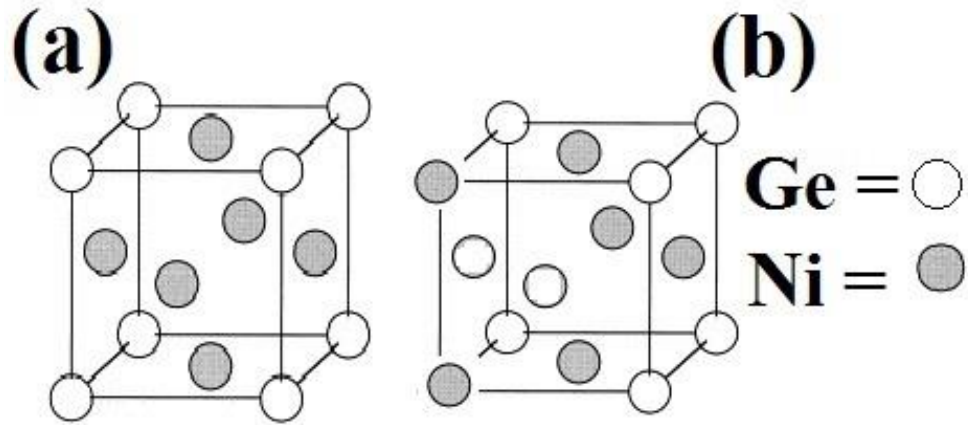


Figure 2.1 Shows L_{12} crystal structure of Ge-Ni **(a)** chemical ordered **(b)** chemical disordered crystal structure.

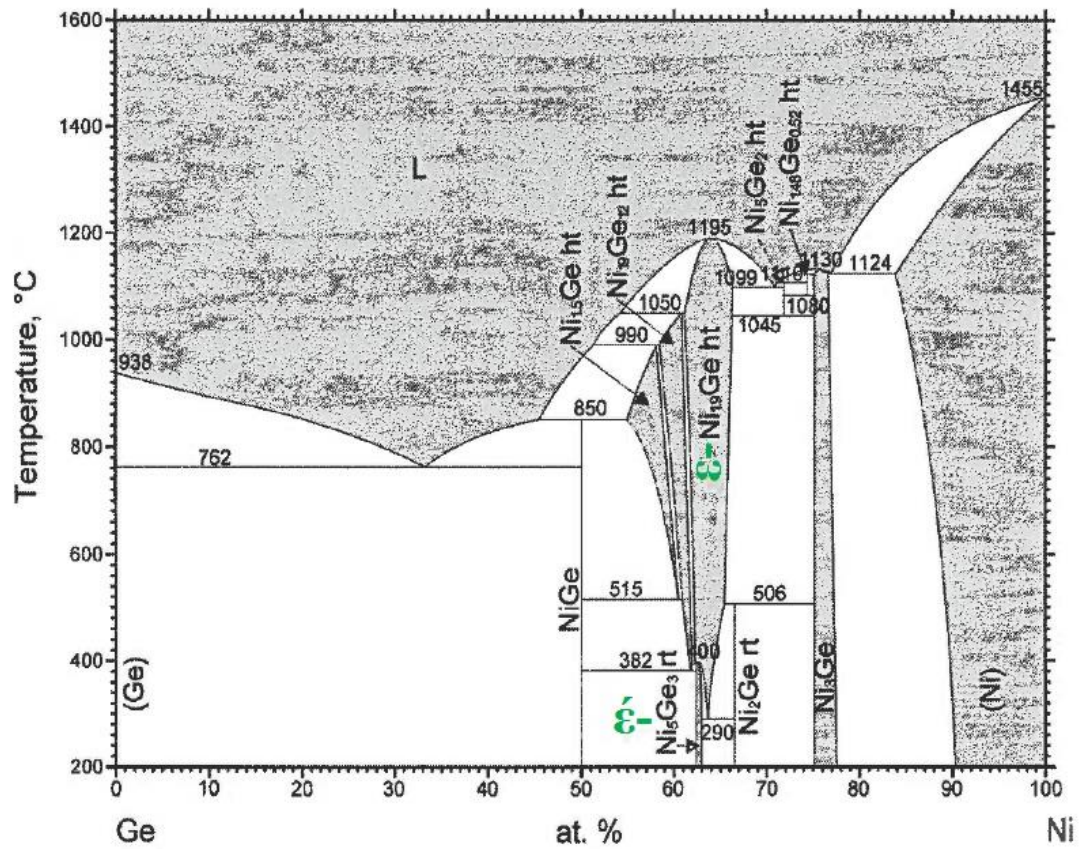


Figure 2.2a Ge - Ni phase diagram [18].

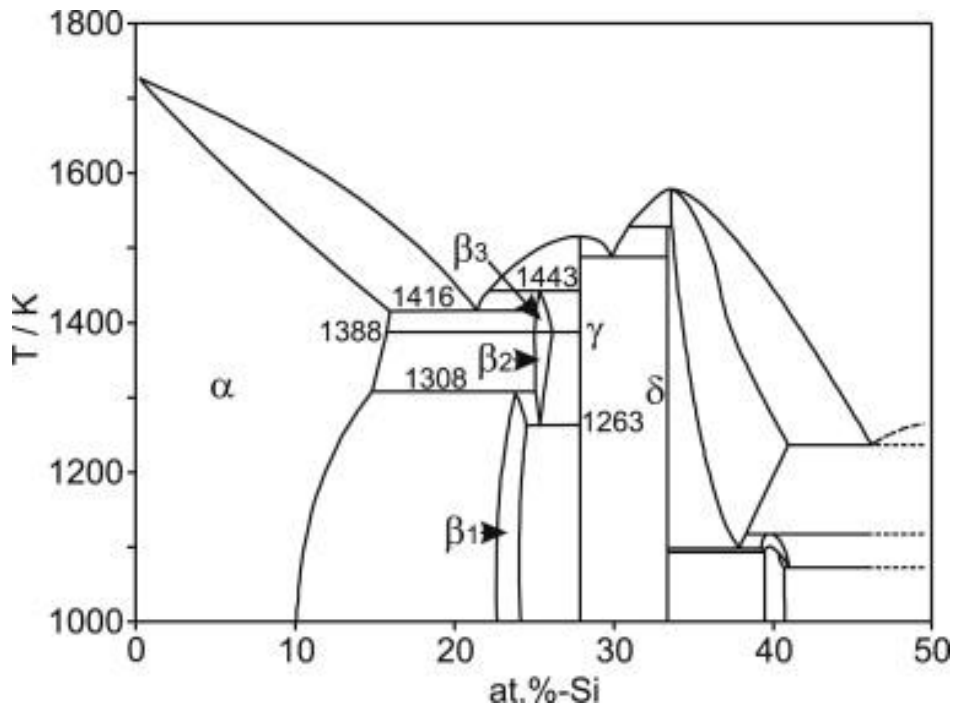


Figure: 2.2b Phase diagram for Ni-Si system [45].

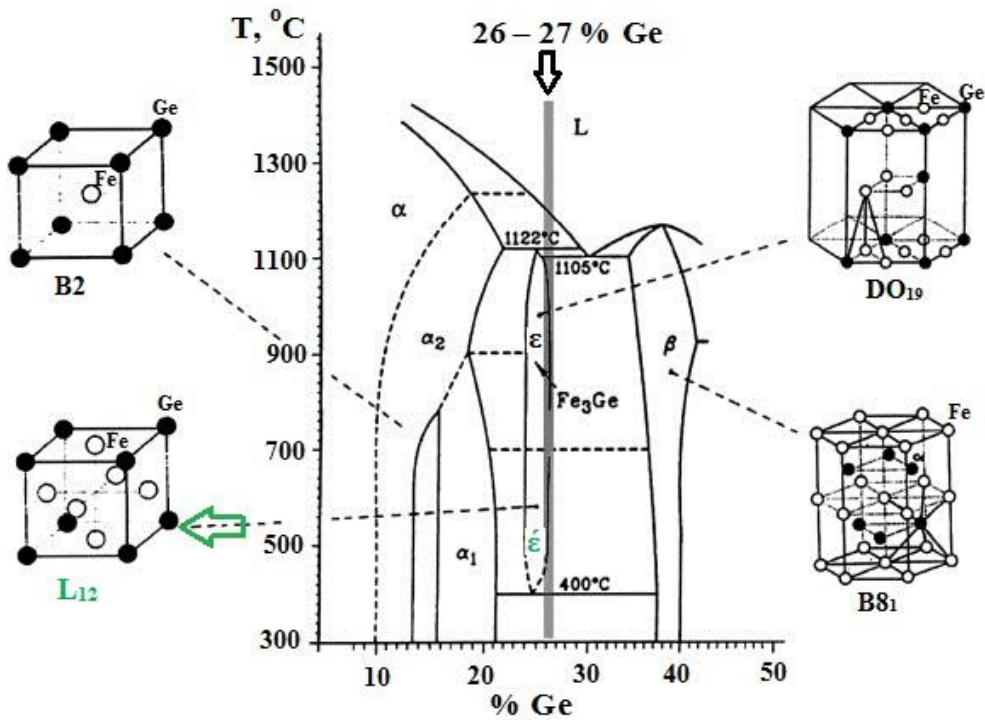


Figure: 2.2c Phase diagram for Fe-Ge system at about the Fe_3Ge composition [51].

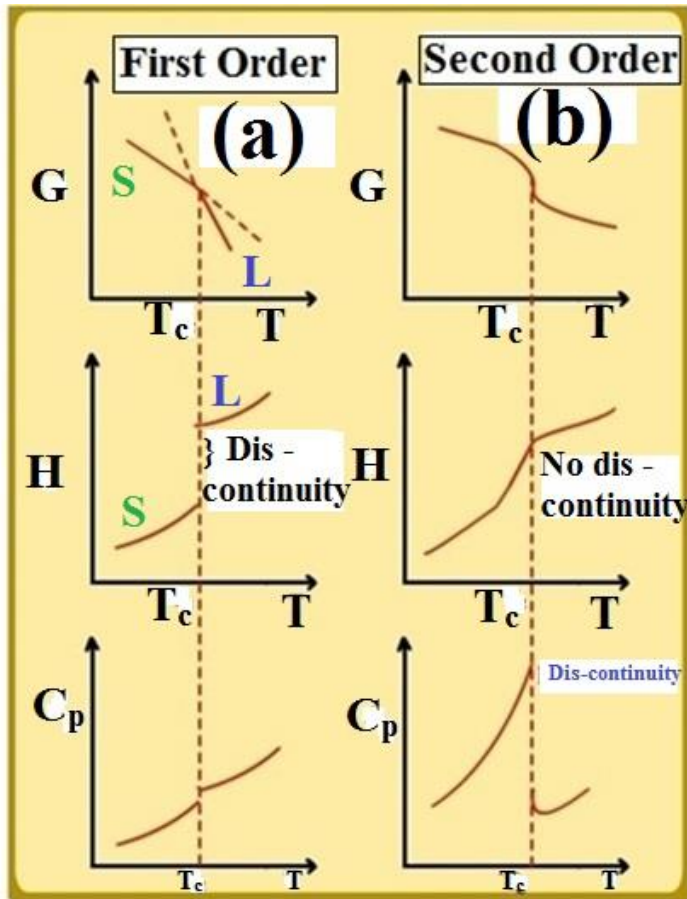


Figure 2.3 The thermodynamic characteristics of (a) first order and (b) second order phase transformation [24].

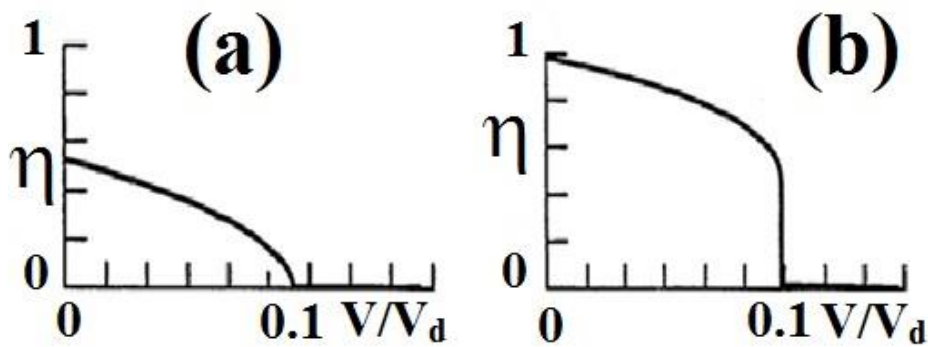


Figure 2.4 Here, η is a function of dimensionless growth velocity, V/V_D , at the interface of growing solid for congruently melting stoichiometric compound. This figure shows prediction of long range order parameter by (a) second order, (b) first order [32].

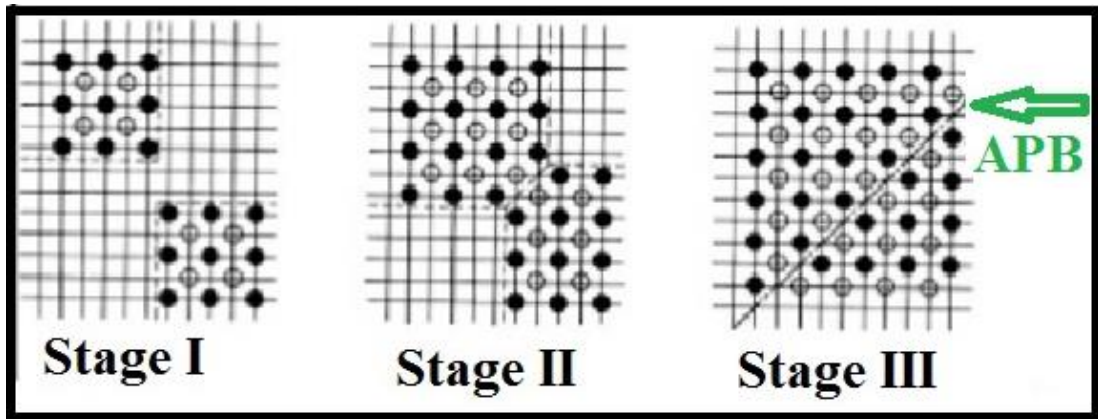


Figure 2.5 This figure shows parallel growth of order domains resulting in formation of antiphase boundary (APB) [34].

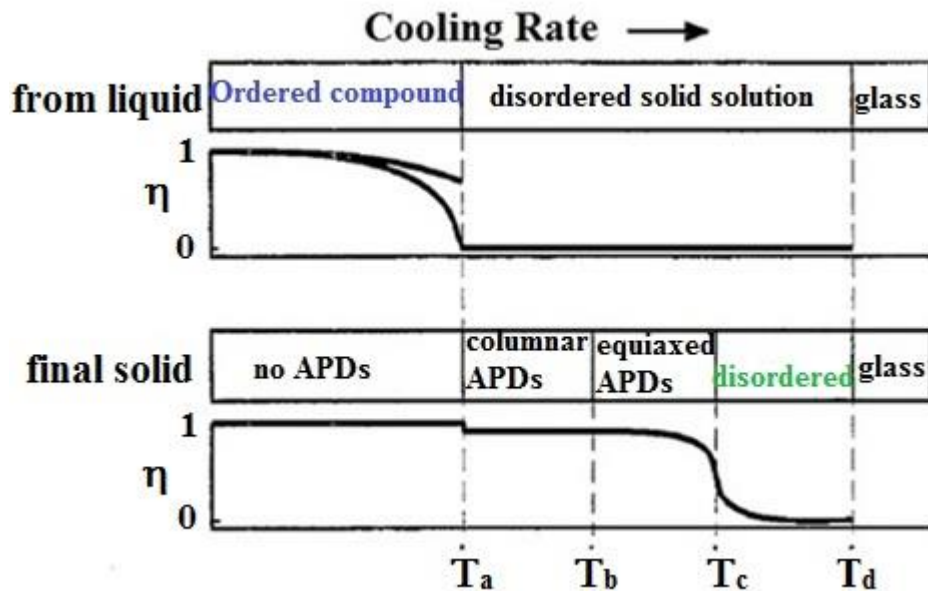


Figure 2.6 A diagram representing different stages of rapid solidification in which an intermetallic compound becomes disordered as a result of increase in the cooling rate [35].

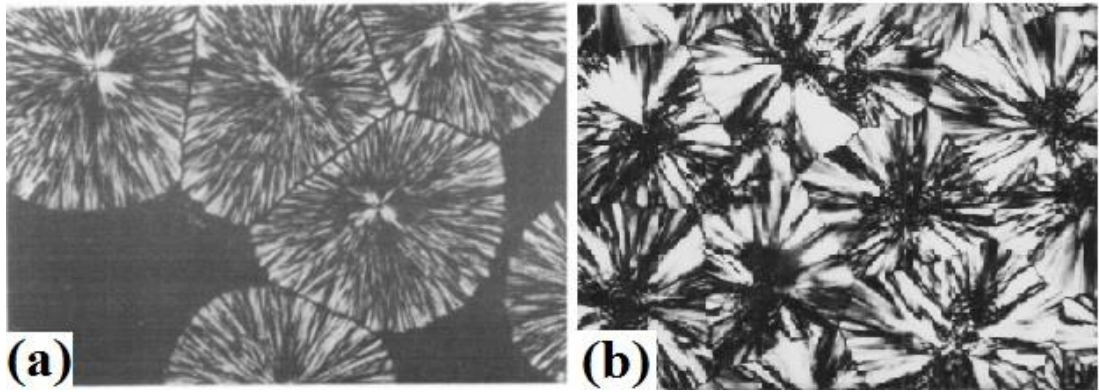


Figure 2.7 This figure shows examples of spherulites (a) mixed variety of spherulites with positively birefringent centers [54] and (b) mixed spherulites of nylon with ringed centers [56].

Chapter 3 Equipment and Methodology

This section consists of all experimental technique and equipment details, which have been used in this project. The starting point was to produce ingots of the single-phase, congruent melting β -Ni₃Ge and ε -Ni₅Ge₃ compounds for subsequent rapid solidification processing. The congruent melting compounds, β -Ni₃Ge and ε -Ni₅Ge₃ were prepared by using arc-melt technique. Sample was analysed to confirm single phase and other properties of the materials by material characterisation techniques such as optical microscopy (OM), Scanning Electron Microscopy (SEM), Energy-Dispersive X-ray (EDX) and X-ray Diffraction (XRD) analysis was performed. After confirmation of required composition of compounds, these compounds were used to non-equilibrium experiments and rapidly solidified via drop-tube processing. In addition to above mentioned characterisation techniques, Transmission Electron Microscopy (TEM), Focused Ion Beam (FIB), Electron Backscattered Diffraction (EBSD) Differential scanning calorimeter (DSC) and Vickers-micro hardness testing were also used in this project.

3.1 Arc-melter

An arc melter is used for the melting and mixing of samples. This equipment gives a low pressure and works under inert atmosphere condition. Such a furnace is particularly good for protective-atmosphere melting of easy to oxidize metals. Additionally, the furnace is purged without difficulty prior to being used for the melt of samples. This is because it has a simple structure, it is easy of access internally and it's small-scale. These features make it quick to evacuate it, as well. A simple, transition and rare earth alloy can be prepared by using this technique.

In this project, master alloys (congruently melting – single phase Ni₃Ge and Ni₅Ge₃) were prepared by using arc melter, parts of which are shown in **Figure 3.1**. There are three main parts of arc melter, (i) the melting chamber (ii) water-cooling system and (iii) the electrical power system. The melting process was completed in the chamber through a non-consumable tungsten electrode on a water-cooled copper hearth. To start the melting process, two main power-supplying steps need to be taken. The EDX analysis confirm that there is no presence of W contamination on the sample. In first

step, high electrical voltage (low current) is delivered to begin the electrical breakdown in the gaseous atmosphere between the electrode and the hearth. Secondly, it provides high current (low voltage) power for the following melting process.

In **Figure 3.1**, the chamber and upper bell jar are made from stainless steel and outer surface secured with copper cooling coils. This upper bell jar can be completely circulating behind the chamber, therefore it is easy to place and remove the sample through the chamber. Also a shaft of electrode (handle) passes through the top of the bell jar, and this handle or shaft of electrode is completely sealed from the top by a ball joint and rubbers bellows. The ball of joint permits electrode to be targeted in any desired direction and keep moving the electrode in and out of the chamber. There are also light and sliding window with small holes, which assist to observe the inside process in the chamber (hearth). Before the melting process, the chamber was evacuated to about 5×10^{-4} Pa and backfilled chamber at about 3.4×10^3 Pa with Argon gas by using a two-stage oil sealed pump. This procedure was repeated seven times to reduce the concentration of oxygen in the chamber.

In this process, Lincoln Arc welder at 230 Ampere generated the arc and the arc was produced when tungsten electrode hits the tungsten striker. Manipulating the electrode above the sample melted the sample. It was melted quickly due to higher energy, but the some particles were also observed when melting process was just started. Further, sample was mixed (Ni-Ge) in 15 to 20 seconds. Sample was already in contact with water cooled copper hearth, and due to this water cooling sample was quickly solidified.

Splash out particles were also observed during melting and after opening the chamber (completing of melting), they were observed in hearth. This splash out particles may be because of non-conductive behaviour of Ge in solid state, or Ni can splash out because of higher arc energy on the sample. Therefore, this splash out might result in weight loss of metal. Moreover, this sample was not homogenised as shown in **Figure 3.2a**. Therefore, this process was repeated seven to eight times and sample was turned in each step to achieve the complete melted and homogenised sample as shown in **Figure 3.2b**. All melting were performed in round shape mould cavity, see **Figure 3.3**, (because of easily melting and mixing) except last melting was performed at

longitudinal shape of mould cavity (because of easily sectioning the sample for material characterisation).

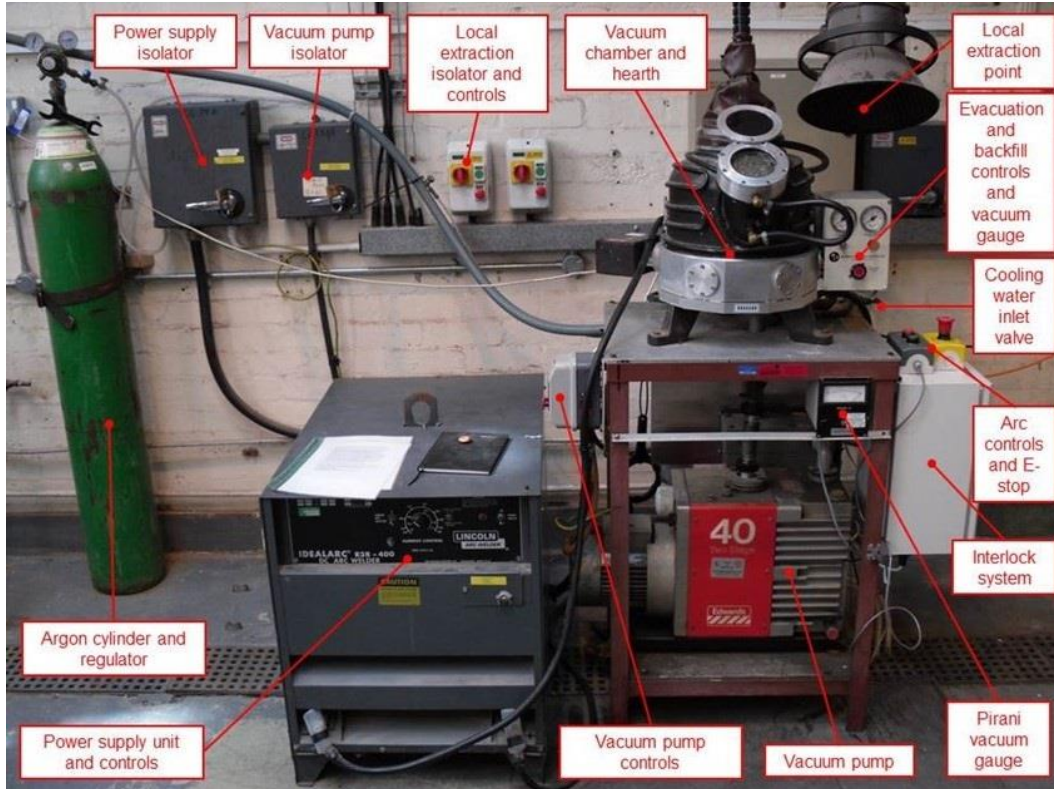


Figure 3.1 Arc-melter furnace setup [University of Leeds].

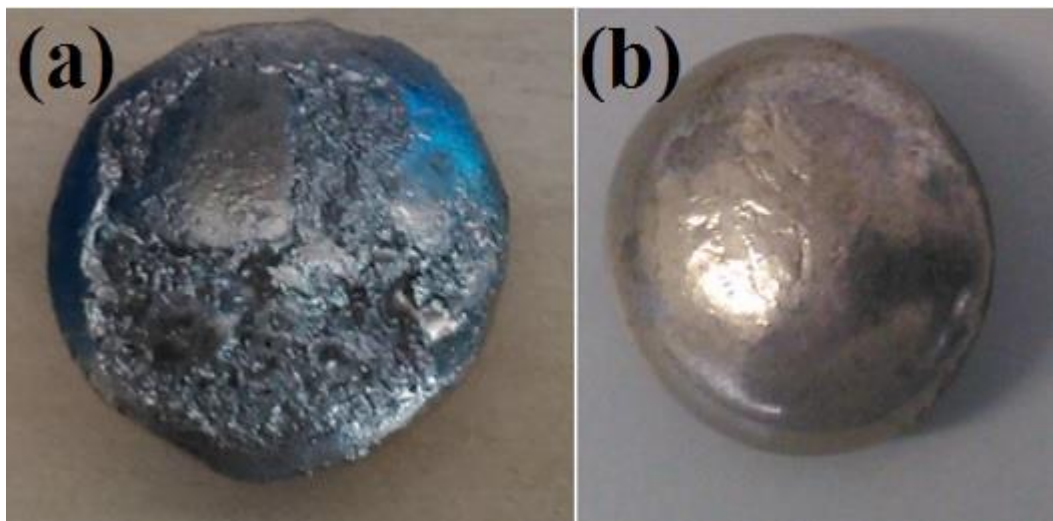


Figure 3.2 Arc melted samples of Ni-Ge (a) inhomogeneous and (b) and homogeneous.



Figure 3.3 Internal shape of chamber (tungsten striker stub, longitudinal and round shapes of moulds).

3.2 Selection of Materials/Compound for Drop-tube Process

Two main criteria guided the choice of material selection for the experiments in rapid solidification. The compound's melting temperature was the first criterion that guided this choice. This was so because the compound's melting temperature needed to be in the confines of the temperature range for processing. Consequently, there was a need to select an alloy system, which would allow processing at a lower temperature in comparison to the drop-tube process, maximum temperature for operating, which is around 1300°C. For the first criterion, we confirmed from Ge-Ni phase diagram [18] that the melting temperature of our both compounds $\beta\text{-Ni}_3\text{Ge} = 1132^\circ\text{C}$ and $\varepsilon\text{-Ni}_5\text{Ge}_3 = 1185^\circ\text{C}$ were within the temperature range of drop-tube system.

The second selection criterion pertained to the necessity of choosing a material/compound, which constitutes a single phase (especially for this project). It follows that, for the drop-tube process, there would also be the necessity to choose a compound that was clearly a distinctly phase such as $\beta\text{-Ni}_3\text{Ge}$ and $\varepsilon\text{-Ni}_5\text{Ge}_3$ which are shown in the Ge-Ni phase diagram [18] to have a clearly specified minimum on a phase

diagram (**Figure 2.2a**). For confirmation of this criterion, we sectioned our prepared arc-melted ingots by using a Struers Accutom diamond precision saw and its phase composition checked using a PANalytical X'pert Pro X-ray diffractometer (XRD). The sectioned ingot was then mounted in Trans Optic™ resin using a Buehler Simplimet 1000 Automatic mounting press before being ground using progressively finer (P220, P400, P800 and finally P1200) Silicon carbide grinding papers. The sample was then prepared for microstructural analysis by polishing with 6 μm, 3μm and 1μm diamond paste, with the sample being washed and dried between each polishing step. The sample was then etched using Nital before being subject to microstructural analysis using an Olympus BX51 optical microscope (OM) and a Carl Zeiss EVO MA15 scanning electron microscope (SEM) equipped with X-Max Oxford instrument Energy-Dispersive X-Ray (EDX) detector. If the alloy ingots were to show local deviations from single phase, due for instance to incomplete mixing of the elemental constituents during arc-melting, this would be apparent from the formation of fine eutectic structures at the boundaries of the Ni₃Ge grains. On the Ni-rich side of the Ni₃Ge/Ni₅Ge₃ compounds this will be a Ni-Ni₃Ge/ Ni-Ni₅Ge₃ eutectic, whereas on the Ge-rich side this will be a eutectic between the Ni₃Ge/Ni₅Ge₃ compounds and either the other compounds as shown in **Figure 2.2a** (Ge - Ni phase diagram). Only if one observes no evidence of intergranular eutectic following Nital etching, nor of any phases other than Ni₃Ge/Ni₅Ge₃ in the XRD analysis, then the alloys/compounds are deemed suitable for rapid solidification processing. However, XRD was not only route to determine the single phase. Microstructure was also examined for looking any evidence of second phase eutectic particular on the grain boundaries, which we observed at our trail/rejected samples.

3.3 Drop-tube Process

A prepared sample (congruent melting compound, single phase – β-Ni₃Ge or ε-Ni₅Ge₃), which obtained through arc-melted process was used as a raw material for the drop-tube process. Rapid solidification was affected by drop-tube processing, using a 6.5 m drop-tube. A schematic illustration of the drop-tube equipment shown in **Figure 3.4** is the one used in this project. Induction furnace was placed at the top of the drop-tube to serve to melt the metal and produce a fine spray of droplets. Rotary pump and turbo-molecular pump were used in drop tube process for achieving desired level of

vacuum in the chamber. In the base of drop tube, one rotary pump was connected, while, in the middle part of drop-tube, the turbo-molecular pump was connected. In the bottom of the drop-tube, where nitrogen gas line is also passing through towards the chamber, pressure gauges was also connected to monitor the pressure in the system. Preceding melting process, the tube was rough pumped to a pressure of 2×10^{-4} Pa before being flushed with N_2 gas. The rough pump – flush cycle was repeated three times before the tube was evacuated to a pressure of 4×10^{-7} Pa using a turbo-molecular pump. For sample processing the tube was filled with dried, oxygen free N_2 gas at a pressure of 50 kPa. The alloy sample, of approximately 9.5 g mass ($\beta-Ni_3Ge$)/9.4 g mass ($\epsilon-Ni_5Ge_3$) was loaded into an alumina crucible, which has three 300 μm laser drilled holes in the base. Induction heating of a graphite subsector was used for heating the sample. This subsector remained innermost of an alumina radiation shield and 3 KW RF generator was applied for induction heating process. The temperature was determined by means of an R-type thermocouple, which sits inside the melt crucible, just above the level of the melt. When the temperature in the crucible attained 1480 K (75 K superheat) for $\beta-Ni_3Ge$ / 1533 K (75 K superheat) for $\epsilon-Ni_5Ge_3$, the melt was ejected by pressuring the crucible with ~ 400 kPa of N_2 gas. This produces a fine spray of droplets, which subsequently solidify in-flight and are collected at the base of the tube.

As the bottom of the drop-tube tightened and was blanked off with a ConFlat flange, all the powder sample was accumulated at the bottom of the drop tube, which means that after completion of process, this part can be removed. Therefore, after completion of this process, a number of steps followed for collecting the rapidly solidified drop-tube samples. First, the whole equipment was gradually and properly cooled in a monitored and controlled fashion. Second, the pot for collection, which is situated towards at the base of the tube was opened. This is done, when the cooling process has resulted in the system as a whole, attaining room temperature as well as when the surrounding atmosphere and tube pressure have been normalised together. Once the pot for collection was opened, the collection of the nearly spherical sample droplets and needles of the sprayed Ni_3Ge/Ni_5Ge_3 happened for the purposes of being sieved, stored, identified and analysed. The sample was weighed following removal from the drop-tube and sieved into the following size fractions: $\geq 850 \mu m$, 850 - 500 μm , 500 -

300 μm , 300 - 212 μm , 212 - 150 μm , 150 - 106 μm , 106 - 75 μm , 75 - 53 μm , 53 - 38 μm and $\leq 38 \mu\text{m}$.

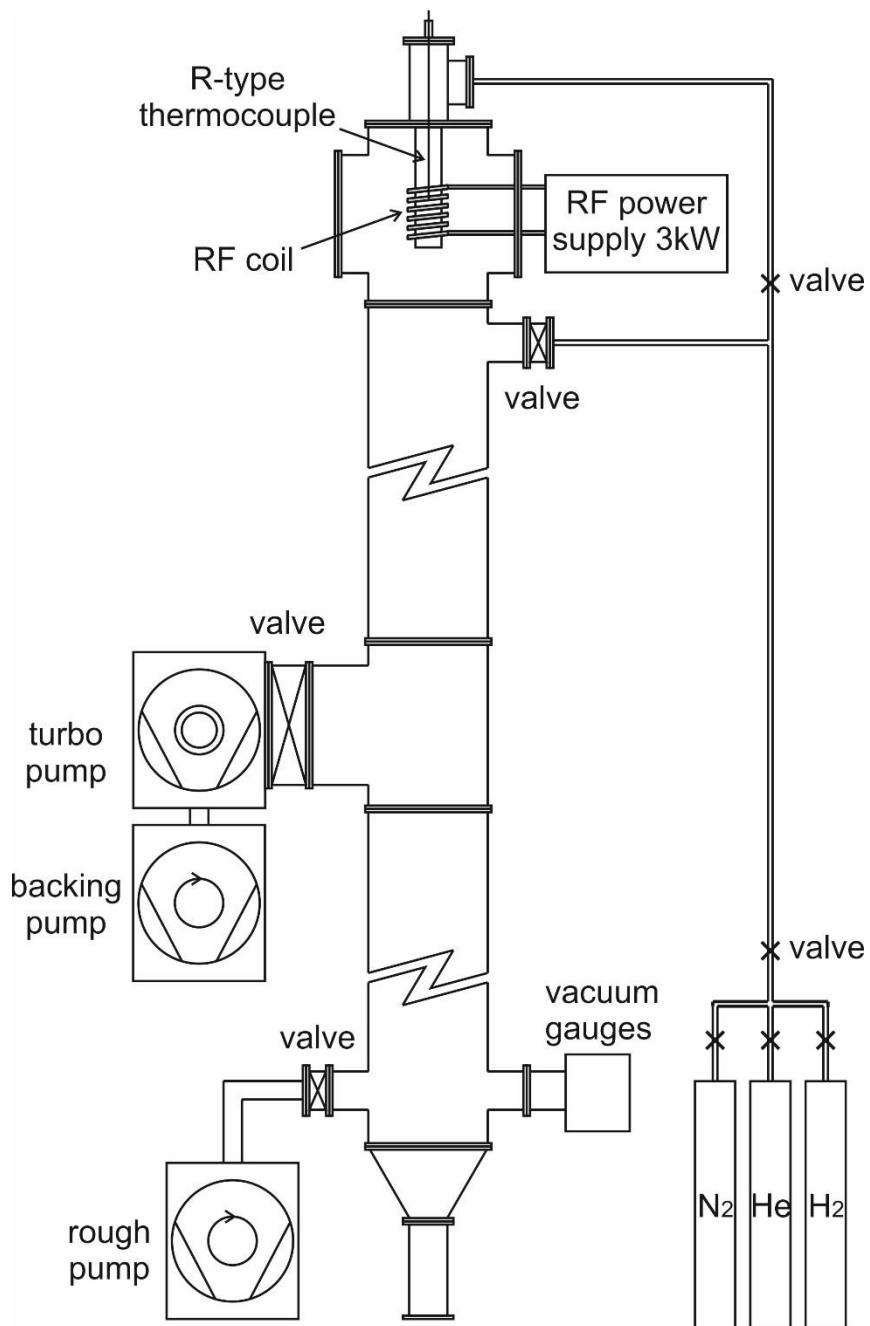


Figure 3.4 Schematic diagram of the drop-tube apparatus used in this research.

3.3.1 Drop-tube Cooling Rate Calculation Method

Neither the cooling rate nor the undercooling can be determined in a direct way because temperature determination for individual droplets is not conceivable during free-fall in the drop-tube. Based on the balance of heat fluxes, the cooling rate can be estimated as a function of droplet size [108],

$$\frac{dT_d}{dt} \left[c_l(1-f) + c_s f - L \frac{df}{dt} \right] = \frac{6h}{\rho d} (T_d - T_g) + \frac{6\varepsilon\sigma_b}{\rho d} (T_d^4 - T_g^4) \quad (3-1)$$

In which, T_d is the instantaneous temperature of the particle; c_l and c_s are the specific heat of the compound in the liquid and solid states respectively; f is the solid fraction; ρ the density of the compound; d the diameter of the droplet; ε the emissivity of the droplet surface; σ_b the Stefan-Boltzman constant and T_g the temperature of the gas. h , the heat transfer coefficient, is normally estimated from:

$$h = \frac{K_g}{d} \left(2 + 0.6\sqrt{\text{Re}}\sqrt[3]{\text{Pr}} \right) \quad (3-2)$$

K_g is the thermal conductivity of the gas. Re and Pr are the Reynolds and Prandtl numbers for the flow, which are given by:

$$\text{Pr} = \frac{c_{pg}\mu}{K_g}, \quad \text{Re} = \frac{\rho_g d}{\mu} |v_d - v_g| \quad (3-3)$$

where, c_{pg} is the specific heat capacity of the gas, μ is its kinematic viscosity. $|v_d - v_g|$ is the differential velocity between the droplet and the gas. $|v_d - v_g|$ can be assumed to be the terminal velocity, v_T , for the particle of diameter, d , under the conditions prevailing in the tube. For a spherical droplet that includes buoyancy effects, it is given as:

$$|v_d - v_g| = v_T = \sqrt{\frac{4gd}{3C_d} \left(\frac{\rho - \rho_g}{\rho_g} \right)} \quad (3-4)$$

where, ρ_g is the density of the gas, g is the acceleration due to gravity and C_d is the drag coefficient, which can be estimated with the following equation:

$$C_d \text{Re}^2 = \frac{4mg\rho_g}{\pi\mu^2} \quad (3-5)$$

where, m is the mass of the drop-tube sample. Hence, employing the thermophysical properties of the N_2 cooling medium in the drop tube as shown in **Table 3.1** and considering the obtained sample's composition [109, 110]. **Figure 3.5** shows the resulting cooling rate, evaluated for parameters appropriate for Ni_3Ge . For each size fraction the cooling rate, calculated using the above equations and methodology are as follows:

$\geq 850 \mu\text{m}$ ($< 700 \text{ K s}^{-1}$), $850 - 500 \mu\text{m}$ ($700 - 1400 \text{ K s}^{-1}$), $500 - 300 \mu\text{m}$ ($1400 - 2800 \text{ K s}^{-1}$), $300 - 212 \mu\text{m}$ ($2800 - 4600 \text{ K s}^{-1}$), $212 - 150 \mu\text{m}$ ($4600 - 7800 \text{ K s}^{-1}$), $150 - 106 \mu\text{m}$ ($7800 - 13000 \text{ K s}^{-1}$), $106 - 75 \mu\text{m}$ ($13000 - 26000 \text{ K s}^{-1}$), $75 - 53 \mu\text{m}$ ($26000 - 42000 \text{ K s}^{-1}$), $53 - 38 \mu\text{m}$ ($42000 - 62000 \text{ K s}^{-1}$) and $\leq 38 \mu\text{m}$ ($> 54500 \text{ K s}^{-1}$).

Finally, above 10 different sieve size fractions were prepared for microscopy examination and other characterizations techniques.

Table 3.1 Thermophysical properties of N_2 and Ni_3Ge compound

Material	Parameter	Value
N_2 gas [109]	c_{pg}	$1039 \text{ J kg}^{-1} \text{ K}^{-1}$
	μ	$1.78 \times 10^{-5} \text{ N s m}^{-2}$
	k_g	$2.6 \times 10^{-2} \text{ W m}^{-1} \text{ K}^{-1}$
	ρ_g	1.16 kg m^{-3} (at 0.1 MPa)
Ni_3Ge [110]	c_l	$416.5 \text{ J kg}^{-1} \text{ K}^{-1}$,
	L	$22.33 \text{ k J mol}^{-1}$
	ρ	8005 kg m^{-3}

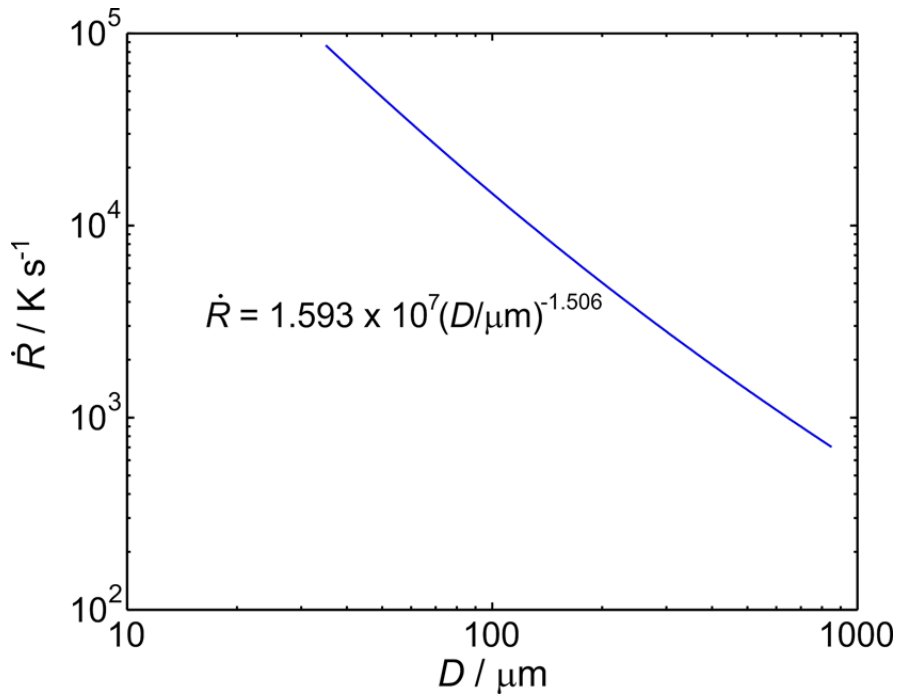


Figure 3.5 Estimated cooling rate of droplets cooled in N₂ as a function of their diameter.

3.4 Sample Analysis and Microstructural Characterisation

Different techniques of characterisation were used to prepare attentively the samples for the purposes of analysis. This was done after the rapidly solidified samples had been taken from the process of the drop-tube. In order to examine quantitatively the microstructure that the solidification process produces directly, several metallographic experimental methods can be used. The determination of possible correlations between the microstructure and rapidly solidified levels that may have developed in the process occurs through the same quantitative examination or analysis. The techniques described in this section were used in the characterisation of the solidified $\beta\text{-Ni}_3\text{Ge}$ and $\varepsilon\text{-Ni}_5\text{Ge}_3$ compounds samples.

3.4.1 Metallography: Specimen Preparation and Etching

The Ni₃Ge and Ni₅Ge₃ drop-tube powders were prepared for analysis by mounting, grinding polishing and etching. First, the sieving into particle size ranges of the powders was performed. This was done by utilising nine wire mesh stacking sieves that have apertures that decrease: 850 μm, 500 μm, 300 μm, 212 μm, 150 μm, 106 μm, 75 μm, 53 μm and 38 μm. For a whole 10 minutes the entire stack was actively agitated, after the powder was put in the top sieve. The mounting of the powder in a Trans Optic™ resin at 140 °C (there is no risk of phase transformation at this low temperature) followed from its removal from all the sieves of varying size ($\geq 850 \mu\text{m}$ to $\leq 38 \mu\text{m}$). Once mounted, the grinding of the powders was conducted through the only use of the finest grinding stage, P1000 and P1200 silicon carbide papers. In this way, an extreme loss of the compound could be prevented. Even though the grinding of the powders went on for a sufficiently long duration so as to assurance the exposure of the particles' interior through a sufficient removal of the sample. During the whole process, optical microscopy was utilised in order to verify the average particle grinding cross-section's diameter as well as looking for scratches, circumvent the risk of over grinding as the latter may cause the effect on the quality of finished polished sample. Diamond compounds of different sizes (6 μm, 3 μm, 1 μm and 0.25 μm) were then used to polish the well ground samples on different cloths placed on the automatic machines. Diluted detergent and methanol were then used to wash the samples. Next, the samples underwent a drying process using an electrical drier. In order to check for any scratches on the surface of the samples and verify the good level of polish of the samples, an optical microscope was also utilised. SEM-EDX analysis that identifies the chemical composition of the sample requires unscratched and generally well-polished samples. These samples, then, underwent an etching process in order to reveal the microstructure. The appropriate etchant was used to acquire SEM images with high resolution. **Table 3.2** lists the etchant appropriate for Ni-Ge compound particles. There was a variation in the time of etching between the two compounds, Ni₃Ge and Ni₅Ge₃. Consequently, there was a requirement to use an optical microscope during the etching procedure. Every section that was etched underwent a good wash in running tap water. After that it was cleaned using ethanol. Before analysis under the optical and scanning electron microscope, the sections/samples were put under in a continuous flow of dry air in order to dry the samples. Finally, mounted/prepared samples were attached to an

aluminium stub with a conductive carbon paste (for SEM analysis). In this project, EBSD, XRD and TEM were also used to further investigate the morphology of grains, phase identity (EBSD analysis), orientation and boundaries, preferred crystal orientation (texture), identify the phases (XRD analysis) and to identify the structure of microstructure (TEM analysis). The techniques for preparing the samples for EBSD, XRD and TEM analysis will be introduced in later sections.

Table 3.2 Etchants used for each compound.

Compound	Etchant	Comments
β -Ni ₃ Ge	5ml Hydrofluoric acid (HF) + 5ml Nitric acid (HNO ₃) + 5ml Hydrochloric acid (HCl)	<ul style="list-style-type: none"> • For the drop-tube sample size ranges ($\geq 850 \mu\text{m}$ to $106 \mu\text{m}$), 20 – 25 Second (immerse). • For the drop-tube sample size ranges ($75 \mu\text{m}$ to $\leq 38 \mu\text{m}$), 30 – 35 Second (immerse).
ϵ -Ni ₅ Ge ₃	5ml Hydrofluoric acid (HF) + 5ml Nitric acid (HNO ₃) + 5ml Hydrochloric acid (HCl)	<ul style="list-style-type: none"> • For the drop-tube sample size ranges ($\geq 850 \mu\text{m}$ to $106 \mu\text{m}$), 35 – 40 Second (immerse). • For the drop-tube sample size ranges ($75 \mu\text{m}$ to $\leq 38 \mu\text{m}$), 55 – 60 Second (immerse).

3.5 Characterisation Techniques Employed

In this project, the following techniques were employed for microstructural characterisation of the arc-melted and rapidly solidified (drop-tube) Ni_3Ge and Ni_5Ge_3 samples. These techniques include: X-ray diffraction (XRD), optical microscope (OM), scanning electron microscope (SEM), energy dispersive x-ray spectrometry (EDX) - Area and Line-scan, electron backscatter diffraction (EBSD), differential scanning calorimetry (DSC), focused ion beam (FIB) and transmission electron microscopy (TEM).

3.5.1 X-ray Diffraction (XRD)

X-ray diffraction (XRD) analysis (arc melted solid ingots and drop-tube powder samples) is commonly used in university research laboratories and industries for characterisation of structural, phase identification, preferred orientation, crystallite size, residual stress and thin film analysis of different materials. The nature of X-rays and light are the same. Both have electromagnetic radiation, but the only difference is in wave length. X-rays have shorter wavelength ($0.5 - 2.5 \text{ \AA}$), while, light has larger wave length ($750 - 400 \text{ nm}$).

The main principle of XRD comprises three basic components: a radiation source (X-ray tube), a sample stage (holder) and an X-ray detector. In this process, electrons are produced through heating a filament. After that these electrons bombard the source and affect the emitting of core electrons. Then the outer shell of electrons fills this hole of electrons, during this process a characteristic wavelength is generated, which is referred to as X-rays. In this analysis, the beam of x-ray is incident on the crystalline material, which is diffracted by crystalline planes. The angle between the particular crystal plane and the incident beam is called Bragg's angle (θ) as shown in **Figure 3.6**, where, the distance $bc = d\sin\theta$ and also $cb' = d\sin\theta$, therefore the total path difference can be calculated by following equation (3-6).

$$bc + cb' = 2d\sin\theta \quad (3-6)$$

These diffracted rays from different crystalline planes (A and B) are overlaid with each other, there is a superposition of waves from crystal planes of varying depth within the sample. This results in interference between the waves. Where the waves are in phase

the interference is constructive, where they are out of phase it is destructive. It is this that gives the resulting diffraction pattern, represented by intense peak. These peaks can only occur when Bragg's law is satisfied and formed due to constructive superposition as shown by following equation (3-7). However, these intense peaks will not form if superposition is destructive.

$$n\lambda = 2d\sin 2\theta \quad (3-7)$$

where, n = an integer, λ = wavelength of x-rays, d = inter planar distance, 2θ = angle between transmitted and diffracted beam. According to Bragg's law, the incident of x-ray beam and diffracted beam to the plane must be co-planar and in phase. The angle between diffracted and transmitted beam should be 2θ . Moreover, to satisfy the Bragg's equation, diffraction must takes place at particular angle [111].

In X-ray diffraction (XRD), arc melted solid ingots and drop-tube powder samples were analysed. The phase composition of the subsequent arc-melted ingots and rapidly solidified drop-tube powder of Ni_3Ge and Ni_5Ge_3 compounds were confirmed by XRD using a PANalytical Xpert Pro (**Figure 3.7a**). The data were collected over a range of $20 - 100^\circ$ in 2θ using $\text{Cu-K}\alpha$ radiation ($\lambda = 0.15418 \text{ nm}$) generated at an anode voltage of 40 kV and with a current of 40 mA. XRD was performed on arc-melted ingot sample that had been mounted with Trans Optic™ resin and polished for microstructural examination as per the procedure described in metallography section. However, drop-tube samples directly used in this analysis (**Figure 3.7b**). Detector recorded the position and strength of reflected beams and the data was plotted by software as position vs intensity to give series of peaks, which are called diffraction pattern. Target material can be identified if position and intensity of diffraction peaks were compared against database of pattern for known crystalline materials. X'pert High score plus software was used for the diffractogram analysis, where background correction and peak position were also measured for instrumental broadening. X'pert High score plus software also provided reference files from the International centre for diffraction data (ICDD) library.

In powder XRD for the drop tube and XRD on the solid ingot, whether the arc melt sample and we acknowledge that in for the solid sample peak height do not corresponds to reference pattern but we only use 2θ for identification, because its single phase. As one set of samples are spherical, one would expect that the XRD scan

is only giving surface information hence other methods such as EDX and EBSD is also used to verify the composition.

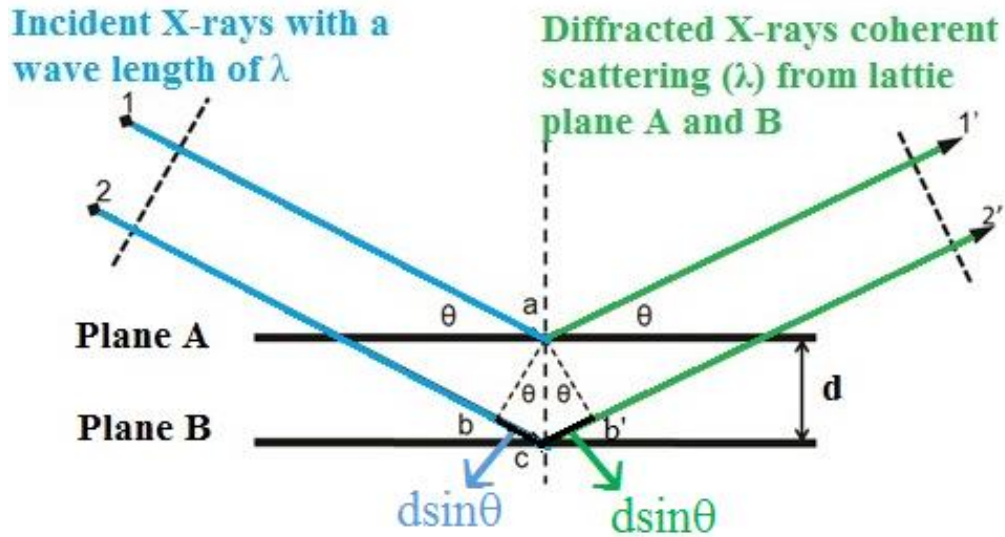


Figure 3.6 Diffraction X-rays on parallel atomic planes satisfying Bragg's law [111].



Figure 3.7 (a) Picture – PANalytical X'pert Pro XRD (University of Leeds) and, (b) drop-tube sample.

3.5.2 Optical Microscopy (OM)

The Olympus BX51 microscope was used to view the microstructure of etched and unetched samples. In this analysis, bright field reflected light method was applied on the surface of the samples. The source of light was directed vertically through the microscope objective (10x, 20x, 50x and 100x) and reflected back through the objective to an eyepiece (10x). Different magnification (100x, 200x, 500x and 1000x) of microstructure for different locations of sample surface were captured by inbuilt Carl Zeiss AxioCam MRc5 Zeiss digital camera. This unit is attached to a computer system for micrograph display, adjustment and storage. The samples were handy enough to go under the microscope /SEM for examination. In order to optimise the image's contrast using the light microscope, a range of modes of illumination can be utilised. A bright field mode is utilised without any polarisers or filters. This mode produces a contrasting effect through the light reflecting on the surface. In a bright field mode, the sample appears as a surface of light with dark features.

3.5.3 Scanning Electron Microscope (SEM)

SEM is a most powerful characterisation tools in many diverse field such as processing of new materials, including metallic materials, intermetallic compounds, ceramics, semiconductors and also it is widely used in medical and biological science. SEM allows for materials of an organic as well as non-organic kind to be examined and characterised on a scale that ranges from the micrometre to nanometre. SEM is a most important in research and technology. It permits the acquisition from a sample of various kinds of information, including information pertaining to the topography, crystallography and information of chemical composition.

In this study a Carl Zeiss EVO® MA 15 SEM with Oxford Instruments Aztec Energy EDX system with 80mm X-Max SDD detector- secondary and backscattered imaging, EDX elemental mapping and line-scans plus CZ STEM detector were utilised. This kind of SEM is capable of producing images that are magnified at the maximum by 1, 000 000. Tungsten (W) filament or LaB₆ can be used as a source of electron in this system. This particular tool's electron source is usually termed a Schottky emitter. The working principle of SEM is that a suitable source such as a tungsten filament or field emission gun is used to produce an electron beam (1-1000 nm). The beam is

accelerated with a high voltage (e.g. 20kV). It is passed through a system of apertures and electromagnetic lenses to make a thin beam of electrons. After this, the scan coils from the beam are used to scan the specimen's surface. A detector then collects the electrons that are emitted from the specimen by the action of the scanning beam.

In order to perform the scanning of the sample's surface, SEM utilises a very sharp focus electron beam that has a diameter of ≥ 20 nm. Images may be produced in two ways. The first consists in capturing secondary electrons from the sample's surface. This is called the SE mode. The second way is by capturing back-scattered electrons, known as the BSE mode. Images produced by the SE mode reveal a sample surface's sharp three-dimensional features. In contrast the BSE mode reveals difference in-between the areas with chemically diverse compositions. Consequently, it is important for the technique of microscopy to be successful that there is a careful preparation to achieve a mirror-like finish for the sample. Additionally, the samples should be conductive electrically. Finally, the grounding of the sample by placing it in the chamber of the microscope. The scanning electron microscopy, such as the EVO that was utilised in this study, necessitates a complete evacuation because electrons are subject to a stronger scattering by gas in comparison to light of an ordinary kind.

The interaction between the specimen and the electrons can have as a consequence that the specimen emits different secondary emissions (**Figure 3.8**). Usually, the detection of secondary and backscattered electrons can be performed by scanning electron microscopes, as all of them have this aptitude. Atoms that have been excited using the incident electron beam with low energies (< 50 eV) produce the secondary electrons. These secondary electrons are emitted right under the surface of the specimen, from a short distance. Certainly, in SEM and for studying specimen surface features, the most commonly used signal is the secondary electron signal. Elastic scattering produces back scattered electrons, which are reflected from the sample. Consequently, SEM utilises secondary electrons (SE) in order to study the features of the surface. For that reason, micrographs of BSE make available information concerning the distribution of divergent phases by making use of the sample's different average atomic numbers. Moreover, BSE imaging has a lower resolution than SE imaging. This is because the higher energy of BS electrons leads to a greater interaction volume.

Using this instrument (**Figure 3.9**), there is no problem to obtain high quality micrographs for any kind of samples, providing one follows the correct method of sample preparation and proper coating the sample (conductive). Nevertheless, if the resin or sample that is utilised lacks sufficient conduction, charging will occur due to the aggregation of electrons and lack of coating. This issue can find a resolution through the application of a thin coating layer of carbon, gold or platinum, through which to achieve better conduction. This will help obtaining a good quality of images/micrographs.

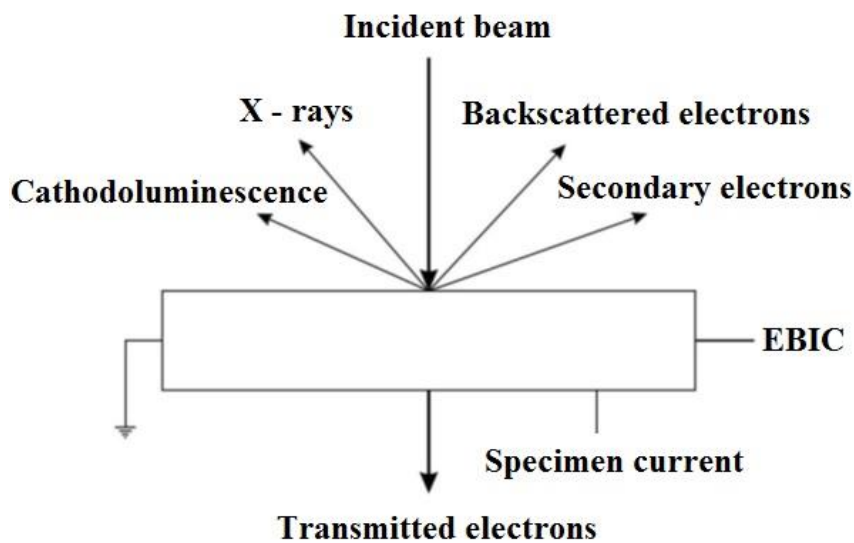


Figure 3.8 Signals from the interaction of an electron beam with a sample [112].



Figure 3.9 Picture (Carl Zeiss EVO® MA 15 SEM – University of Leeds).

3.5.4 Energy Dispersive X-Ray Spectrometry and Line-scan Techniques

Energy Dispersive X-Ray Spectrometry (EDX) is a technique of characterisation, which lends itself to use in the elemental analysis of compounds. With EDX, the irradiation of a sample occurs. The radiation emitted during this technique has the ability of creating vacant spaces in its atom's inner electron shells. The vacant spaces are subsequently charged through electrons that emanate from atomic orbitals of higher energy. This process leads to the characteristic X-rays being emitted, which can be called 'secondary' X-rays. This occurs as the higher energy radiation being absorbed result in radiation of lower energy being re-emitted. The excitation of the sample allows for the determination of the compositional information about the sample can occur by measuring the energy and quantity of X-rays emission. This is so because the X-rays' energy is typical of the irradiated element's atomic structure.

Line-scanning can be used to obtain qualitative information about elemental distributions, by which it is meant that a form of mapping is produced without the concentration profiles being determined exactly. A full mapping can also be achieved in the case of several elements through the use of hardware that is integrated into the EDX analyser. In this technique, the probe of the electron is shown on the sample through a line that cuts across a given region of interest. By this it is meant that, a graph is produced that represents the counting of the number of X-ray quanta being (approximately the quantity in the given element) against how they are spatially located on a given line. In this manner, the plotting of diffusion profile of elements at an interface is possible.

For above two techniques (EDX and line-scan), the Carl Zeiss EVO® MA 15 SEM with Oxford Instruments Aztec Energy EDX system (80mm X-Max SDD detector-secondary and backscattered imaging) and EDX elemental mapping and line-scans plus CZ STEM detector was used in this project. Meanwhile, the composition of the compounds (single phase) was also checked by EBSD to verify the reliability of the EDX results. This system is calibrated by the manufacturer (Carl Zeiss EVO).

3.5.5 Electron Backscatter Diffraction (EBSD)

EBSD provides information about grain size, grain boundary, grain orientation, texture and also different phases can be easily identified through this useful technique. It also enables centimetre-sized samples with millimetre-sized grains, metal thin films with nano-grains to be analysed. The basic components of an EBSD consist of SEM column, SEM stage, EBSD detector, controller, camera, picoammeter, and display system, are also shown in **Figure 3.10**.

The working principle of an EBSD is established by interaction of a stationary electron beam with a tilted crystalline sample about 70° from the horizontal of the SEM stage. When the beam of electrons is focused at a region of interest then the atoms of targeted region inelastically scatter a segment of the electrons with loss of small energy. Moreover, some electrons are incident on every set of atomic planes at certain angles that can satisfy the Bragg equation (3-8):

$$n\lambda = 2d\sin\theta \quad (3-8)$$

where n represent an integer, λ is the wavelength of the electrons, d represent the spacing of the diffraction plane, and θ represent the angle of incident of the electrons on the diffraction plane. Consequently, these diffracted electrons generate a set of cones, which represent each diffracted plane. This pattern is known as Kikuchi pattern and can be captured by using a mounted camera on EBSD system. These Kikuchi pattern/diffraction pattern is matched with the reference pattern generated from compound, on the basis of these data crystal structure and orientation at each point of the sample can be identified. Therefore, the diffraction pattern can be used to obtain very useful information of samples including crystal orientation, phases, and grain boundaries.

In this project, electron backscatter diffraction (EBSD) was performed on unetched samples of both compounds Ni_3Ge and Ni_5Ge_3 drop-tube samples ranges from $\geq 850 \leq 38 \mu\text{m}$, using a FEI Quanta 650 FEGSEM with Oxford/HKL Nordlys EBSD system. The sample preparation technique plays a crucial role for obtaining good EBSD results, because from a few tens of nanometres of the sample the diffracted beam can escape and also presence of any contamination, deformation and oxidize would affect the formation of diffraction pattern. Therefore, a scratch free and optimum polishing surface is compulsory to produce a good electron backscattered diffraction pattern.

The same procedure of SEM sample preparation was performed for preparing EBSD samples. As the sample of EBSD required ultra-fine polishing surface, therefore, after repetition of SEM sample preparing then one additional method of polishing were also performed with EBSD samples. In this final polishing step, Buehler Automet 250 grinder-polisher machine (Force = 25 N, speed = 130 rpm -base and 50 rpm - head, time =10 min) was used and colloidal silica suspension was used for polishing the samples. In EBSD, the result of scanned electron beams within a selective region of sample was produced in the form of map, which reveals the grain morphology, phase identity, orientation and boundaries. Also, preferred crystal orientation (texture) within the same region of sample was established by using this data. Therefore, in this project for both compounds (Ni_3Ge and Ni_5Ge_3), a complete and quantitative description of the microstructure was generated through EBSD.

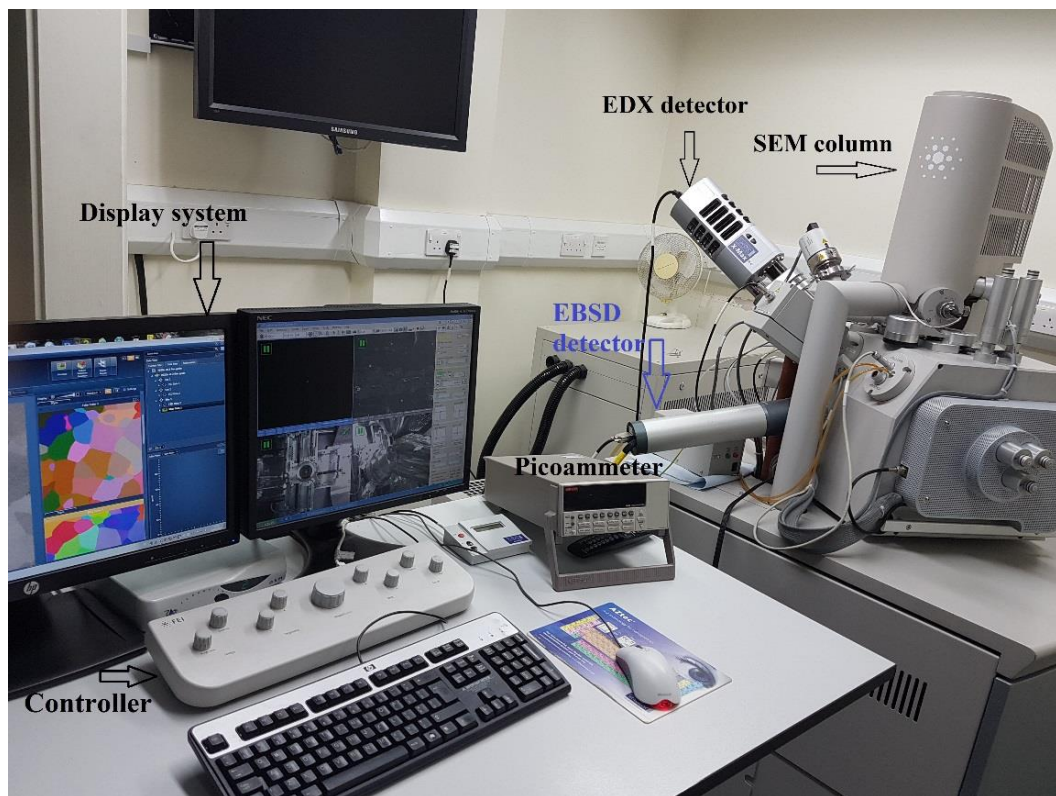


Figure 3.10 The basic components of an EBSD (FEI Quanta 650 FEGSEM with Oxford/HKL Nordlys EBSD - University of Leeds).

3.5.6 TEM

The transmission electron microscope (TEM) is used to examine the structure, phase, composition, and for crystallography. Electron microscopy was invented because of the restrictions relating to the use of light in for magnification purposes. For the maximum given resolution is, in the end, determined by the light's wavelength utilised for the illumination of the sample. From Abbe's equation (3-9), one can deduce that ~200 nm is the limit of resolution (d) for optical microscopy in the case of a perfect system. A perfect system is one in which two adjacent sources are resolved. In the equation below, λ is the illuminating source's wavelength. NA is the objective numerical aperture. NA can be calculated by the following equation: $NA = n\sin\theta$, n being the refractive index of the medium and θ the aperture angle.

$$d = \frac{\lambda}{2NA} \quad (3-9)$$

Consequently, using a beam that has a comparative small wavelength provides one way of attaining a resolution that is greater. Equation (3-10) describes this. Here, Planck's constant is h , the rest of an electron's mass is m_0 , an electron's charge is e , the speed of light is c , and the electron beam's accelerating voltage is V .

$$\lambda = \frac{h}{2m_0eV(1+\frac{eV}{2m_0c^2})} \quad (3-10)$$

In the case of a 200 kV electron beam, this produces a small wavelength (~2.5 pm). This is a good deal lower in comparison to visible light's wavelength (550 nm for green light). Consequently, it is possible that an electron beam attains a theoretical resolution limit that is lesser than atoms. The optical microscope is one technique that can be used for the transmission of light through the sample. This method of optical microscopy relies on the use of a compound microscope. Transmission electron microscopy (TEM) can replicate this technique but with electrons. In 1931, Ernst Ruska and Max Knoll created the first TEM. It was only two years after that the development of a microscope with a resolution that is higher in comparison to an optical microscope occurred.

It is also notable that TEM is amongst the most significant tools for characterising materials microstructurally. Indeed, by using X-ray techniques a greater amount of quantitative diffraction pattern analysis can be obtained in comparison to patterns of

electron diffraction. However, with TEM, it is also easier to focus electrons. Both TEM and SEM use a similar system for beaming electrons (i.e. condenser lenses, an electron gun and a vacuum system).

Despite these commonalities, the manner in which images are formed is completely different. SEM is more fundamentally utilised for the examination of a bulk specimen's surface structure. In contrast, TEM is a technique for transmission. Consequently, it gives information concerning a thin specimen's internal structure [112]. At the time of an electron beam passing through a specimen that is thin, variations that occur in the intensity of the diffraction of the electron produce what is termed a 'diffraction contrast' in the image. This contrast is useful for micro-structural characterisation as well as the characterisation of certain defects, including second phase particles, dislocations and interfaces [113]. Selected-area diffraction (SAD) is also a commonly used and valued technique for examining patterns of diffraction in small regions of the specimen. Additionally, in order to form images of columns of atoms, high-resolution transmission electron microscopy (HRTEM) can also be utilised.

TEM is broadly characterised by two main modes of working. The first is the image mode. The second is the diffraction mode (**Figure 3.11**). Within a TEM, the transmission of electrons varies according to the demands, but always transmitted through an extremely thin sample. The image mode and diffraction mode function in different ways in relation to this transmission. In the case of the diffraction mode, the electrons are transmitted across the specimen and diffracted by the internal structure of the sample. Then, these diffracted electrons are converged through objective aperture in order to construct the diffraction pattern of the specimen in the back focal plane. For the image mode, electrons travel and transmitted across the specimen. Then, the scattered electrons are converged through the objective aperture and arrange in the focal plane. It is in the focal plan that the formation of the intermediate image happens. Finally, the image of the sample appears in a magnified form, through projection, on the microscope screen.

The TEM's imaging mode functions through contrast. That is to say that if a dense sample is used, some of its thicker areas will be, in comparison to the areas that are thin, more dark on account of an increase in inelastic scattering/absorbed electrons.

This contrast is sometime termed ‘mass-thickness contrast’. There are two methods for performing the diffraction contrast in order to produce imaging. The first way is the Bright Field method (BF) (**Figure 3.12a**). In this method, an aperture is fitted so as to allow only the passage of the unscattered beam. The formation of image is based on the result of contrast whereas the crystalline will occur darker if they diffract at the Bragg orientation or are amorphous regions. The orientation of the crystal also determines the degree of contrast for crystals. The crystallised area will be shown to be dark, if the Bragg condition is satisfied in the orientation of crystal. The Dark Field mode (DF) is the other imaging mode in which TEM functions (**Figure 3.12b**). Here, particular diffracted rays are allowed to pass by the aperture. The aperture also stops the incident beam from being a part of the image. The contrast in the image is opposed to the one produced through the Bright Field method. The Dark Field mode is used in case of an interest in particular defects or certain structures of the specimen.

Electron diffraction mode finds its basis in the sample’s crystallographic planes elastic scattering of electrons. The forming of diffraction pattern is formed according to the same rules as the X-ray diffraction shown in section 3.5.1. The sample’s area that makes up the diffraction pattern is definable by the utilisation of a selected area (SA) aperture found in an intermediate image plane (**Figure 3.13**). This produces crystallographic information that is resolved spatially, from areas in the sample that range from 0.2 μm to a few microns.

As a matter of fact, the diffraction angle θ is not so significant (**Figure 3.13**). This figure shows that the Bragg angle for 200 kV electrons is 0.14° in the case of a crystal plane that has d-spacing of 0.5 nm. Consequently, the diffraction of the electron beams that occurs from the crystal planes nearly parallels the electron beam itself. In the alternative case that there is a parallel between a number of planes and the electron beam, a series of diffraction spots will appear. These diffraction spots, which will occur from the diffraction pattern’s centre in the normal direction to the plane, will be characterised by a distance of $1/d_{hkl}$. **Figure 3.14** shows the manner in which the formed lattice of spots has a reciprocal relationship to the real lattice of the crystal, also called the reciprocal lattice. The angle ϕ is the same as the angle between the normal directions to the planes. This is the basis for the identification of the phase through TEM analysis. The related equations of this identification process are shown

in **Table 3.3**. A formula of a cubic crystal structure was used for the phase identification of the compound Ni_3Ge . In which all lattices were considered equally ($a = b = c = 3.26 \text{ \AA}$) and all angles were 90° ($\alpha = \beta = \gamma = 90^\circ$). While, for the phase identification of $\epsilon\text{-Ni}_5\text{Ge}_3$ compound, monoclinic crystal structure formula was used with $a \neq c \neq b$, $\alpha = \gamma \neq \beta$ conditions. However, for the phase identification of $\epsilon\text{-Ni}_5\text{Ge}_3$ a hexagonal crystalline formula was used, where $a = b \neq c$ and $\alpha = \beta \neq \gamma$ condition satisfied.

In this project, FEI Tecnai TF20 (**Figure 3.15**) transmission electron microscopy (TEM), was used to distinguish between the ordered and disordered variants of the Ni_3Ge and Ni_5Ge_3 compounds. For in situ observation of the order-disorder transformation upon heating the TEM was fitted with a Gatan 901 hot stage controller. Despite these strengths, there are some disadvantages to the use of TEM. First, there is a requirement that the sample that is made ready for TEM detection should be thin and small. Additionally, TEM can only analyse a small part of the sample. Consequently, it is better to perform the examination of general structural information using other techniques under low magnification. These techniques include scanning electron microscopy and optical microscopy. The second drawback is that the specimens prepared for the purposes of TEM need to be sufficiently thin for the transmission of electrons to occur in sufficient quantity so that, in turn, sufficient transmitted intensity may be projected on the screen in order to compose an image that is interpretable [114]. The particles of a drop tube are tiny if they have diameters within a range of $850 - \leq 38 \text{ \mu m}$. Additionally, with TEM, the analysis of the examined microstructures are also complicated for nano-crystalline phase grains. Additionally, the samples need to be extremely thin because it should facilitate the transmission of electrons. For this, there is a need to involve special procedures, including high precision milling technique, which requires the use of focused ion beam (FIB). This process of specimen preparation is shown in the next **section (3.5.7)**.

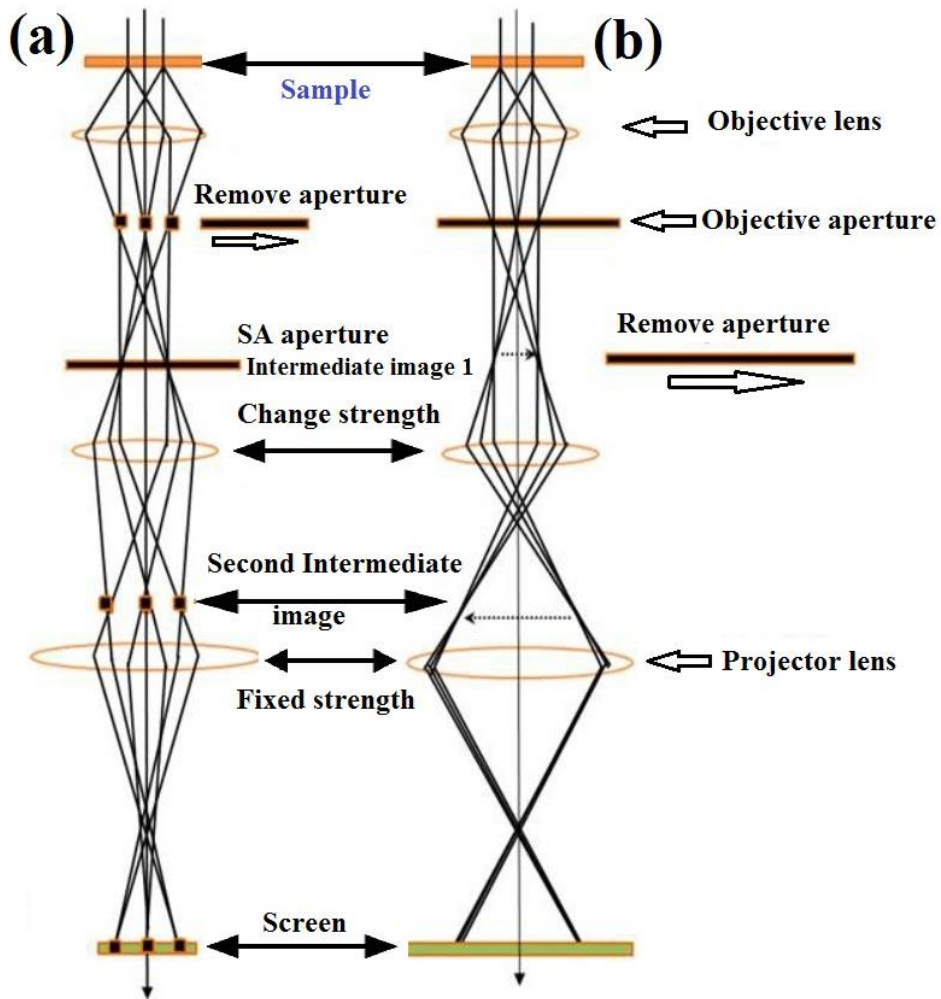


Figure 3.11 TEM operating modes (a) diffraction mode which produce DP and (b) image mode [114].

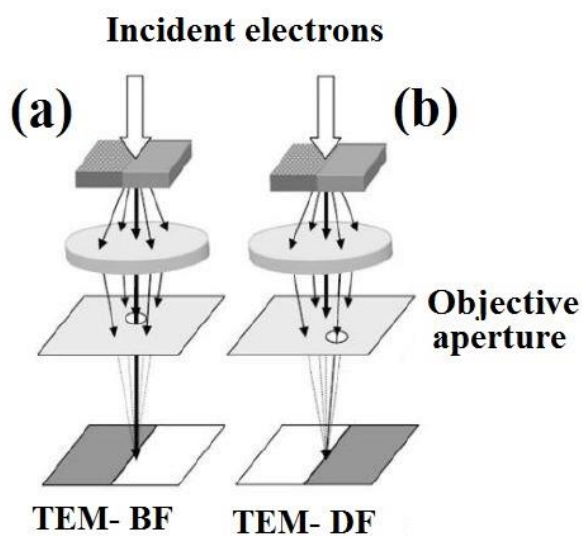


Figure 3.12 Imaging mode of TEM - (a) Bright field image and (b) dark-field image.

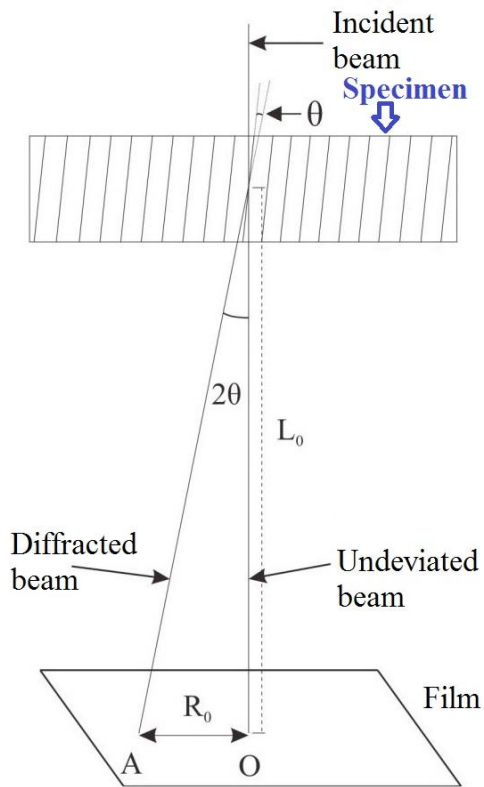


Figure 3.13 Geometry of construction of an electron diffraction pattern. On the film, the diffracted spot A occurs at a distance R_0 from the central spot, O in a direction perpendicular to the planes. L_0 is known as the camera length [115].

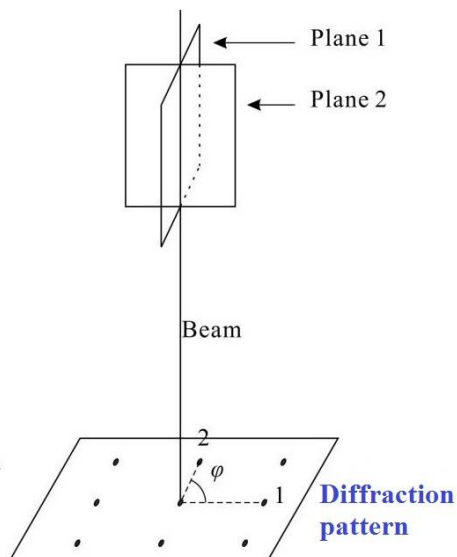


Figure 3.14 Geometry of the construction of an electron diffraction pattern from a single crystal in TEM. The beam is parallel to a zone axis including two planes (1 and 2). The included angle ϕ is equal to the angle between the normal directions of the planes [115].

Table 3.3 Calculation of interplanar angle, θ , between planes $(h_1k_1l_1)$ and $(h_2k_2l_2)$ and interplanar spacing, d_{hkl} in cubical and hexagonal crystals [115].

Crystal structure	$\cos\theta$	d_{hkl}
Cubic	$\cos\theta = \frac{(h_1h_2 + k_1k_2 + l_1l_2)}{\sqrt{[(h_1^2 + k_1^2 + l_1^2)(h_2^2 + k_2^2 + l_2^2)']}}$	$\frac{1}{d_{2hkl}} = \frac{h_2^2 + k_2^2 + l_2^2}{a^2}$
Hexagonal	$\cos\theta = \frac{[h_1h_2 + k_1k_2 + \frac{1}{2}(h_1k_2 + h_2k_1) + (\frac{3a^2}{4c^2})l_1l_2]}{\sqrt{[h_1^2 + k_1^2 + h_1k_1 + (\frac{3a^2}{4c^2})l_1^2] + [h_2^2 + k_2^2 + h_2k_2 + (\frac{3a^2}{4c^2})l_2^2]}}$	$\frac{1}{d_{2hkl}} = \frac{4}{3} \left(h_2^2 + k_2^2 + \frac{l_2^2}{a^2} \right)$
Monoclinic	$\cos\theta = \frac{[\frac{1}{a^2}h_1h_2 + \frac{1}{b^2}k_1k_2\sin 2\beta + \frac{1}{c^2}l_1l_2 - \frac{1}{ac}(l_1h_2 + l_2h_1)\cos\beta]}{\sqrt{[(\frac{1}{a^2}h_1^2 + \frac{1}{b^2}k_1^2\sin 2\beta + \frac{1}{c^2}l_1^2 - \frac{2h_1l_1}{ac}\cos\beta) \times (\frac{1}{a^2}h_2^2 + \frac{1}{b^2}k_2^2\sin 2\beta + \frac{1}{c^2}l_2^2 - \frac{2h_2l_2}{ac}\cos\beta)}}$	$\frac{1}{d_{2hkl}} = \frac{1}{a^2} \left(\frac{h_2}{\sin 2\beta} \right) + \frac{1}{b^2} (k_2) + \frac{1}{c^2} \left(\frac{l_2}{\sin 2\beta} \right) - \frac{2hl\cos\beta}{ac \sin 2\beta}$

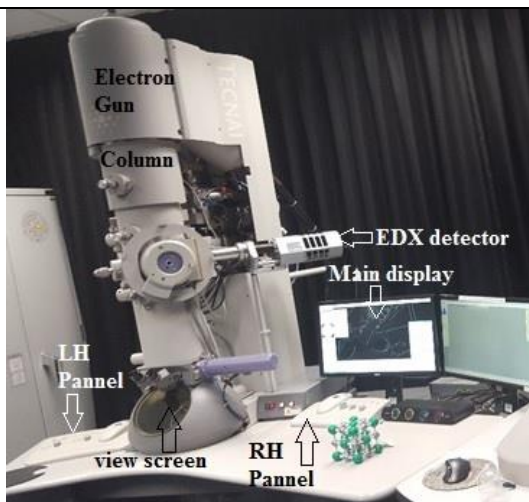


Figure 3.15 Transmission electron microscope - (FEI Tecnai TF20 - TEM with Oxford control instruments - University of Leeds).

3.5.7 FIB

In addition to sample preparation (metallography techniques) for microstructural analysis using optical microscopy and scanning electron microscopy, samples were also prepared for selected area diffraction analysis and images (dark field and bright field) in the transmission electron microscopy (TEM), using an FEI Nova 200 Nanolab FEGSEM focused ion beam (FIB). FIB is mainly used in semiconductor research, chip-design industry, failure analysis, trimming of thin film (magnetic storage disk) and also used to prepare the specimen for TEM analysis.

There are three main components of FIB: (i) the ion column, (ii) the chamber, and (iii) Vacuum and Gas transfer system. The structure of ion column of FIB and SEM are identical, the only difference between these two systems are the use of source beam. The gallium ion (Ga^+) are used in FIB, while electron beam are used in SEM. Ga is an applicable choice to use in FIB, because it can operate near room temperature (30°C) and also it has low melting point (29.76°C). A strong electric field normally 108 volts per cm is used for producing ion beam by a liquid metal ion source. Liquid gallium discharged positive charge ions because of strong electric field. These ions are composed at the sharp needle of tungsten tips. The working stage of FIB for operating samples can be moved on all five-axis inside the chamber. Combination of turbo pump and oil sealed rotary vane pump is used for maintaining the vacuum inside the column and working chamber. Gas system is also used for selective etching and deposition of materials, which is placed outside the vacuum chamber, and gas source is connected with a nozzle inside the chamber through a piping system.

The working principle of FIB is initiated, when the Gallium beam hits the sample, this followed by sputtering of ions and secondary electrons and these ions and electrons can be stored for formation of an image. Platinum organometallic gas is ejected by gun and this gas breaks down when it is struck via an ion or electron beam, depositing platinum (Pt). This platinum may be accumulated in the sample within the area of interest with purpose to avoid damage of delicate region. The micromanipulator is used to move the sample within the chamber and the micromanipulator is also used to take sample to a grid for mounting in the TEM.

Following steps are briefly described to prepare the sample by FIB technique and the sequence of this technique is shown in **Figure 3.16**. Firstly, to find and mark the

identified region (**Figure 3.16a**). Secondly, to protect the identified region in the course of cutting session (milling), by coating of a thin, narrow layer of platinum on the surface of the targeted region (**Figure 3.16b and c**). Subsequently the preferred region of the specimen (lamella) formed, in order to transport a small specimen on to the TEM copper grid, this FIB sample was welded on the tip of a tungsten micro-manipulator by using Pt (**Figure 3.16d and e**). Repeat the welding process when the specimen (lamella) fixed to the grid of copper for mounting in the TEM (**Figure 3.16f**). Finally, ion beam used to ensure the thickness of the central part of the specimen was less than 100nm this followed by sliced the specimen (**Figure 3.16 g and h**). **Figure 3.16i** showed the prepare FIB sample within the grid of Cu and this final specimen was stored into a vacuum container before analysis in the transmission electron microscope (TEM).

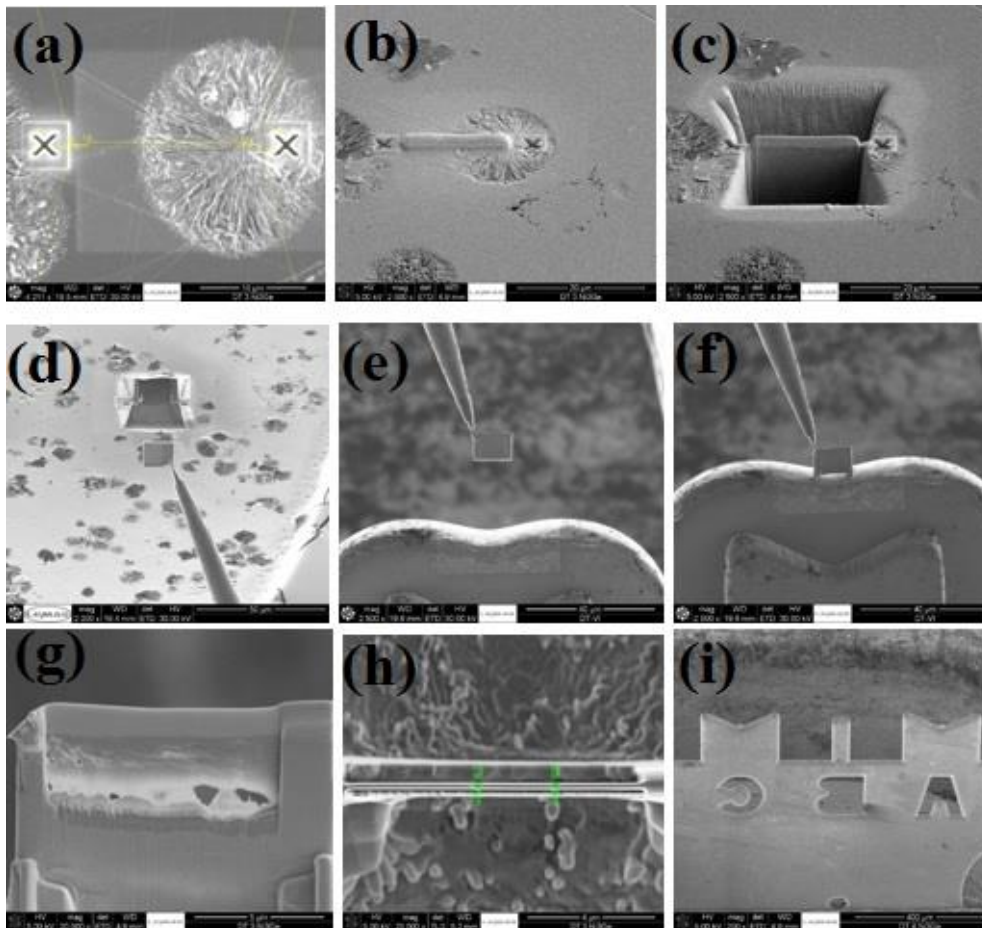


Figure 3.16 FIB process technique for TEM sample preparation.

3.5.8 Differential Scanning Calorimetry (DSC)

Differential Scanning Calorimetry (DSC) is a well-established measuring method which is used on a large scale in relation to a diversity of research areas as well as development, and quality inspection and testing. This technique is utilised for measuring of changes of differences in the rate of the flow of heat to the compound and to a reference compound, while they are conducted to a controlled temperature program either compound is heated or cooled. Through the utilisation of substance quantities in the mg range, a quick identification of thermal effects as well as the determination of the temperature that is pertinent and the typical values of calories can be performed over a considerable range of temperatures. Because of DSC, it is possible to produce values of measurement that can be acquired, which facilitate the determination of the capacity of heat, transition heat, kinetic data as well as purity and glass transition. DSC curves have three roles. The first is to identify substances. The second is to establish phase diagrams. The third is to ascertain the crystallinity degrees [116].

Typically, DSC experiments comprise two heating/cooling cycles so that reversible and irreversible transitions can be distinguished through this technique. In this project (rapidly solidified, drop-tube process), we observed a mixture of ordered and disordered material. Upon slow heating there should be an ordered transformation in which any disordered material irreversibly transforms to the ordered state. The main aim/idea to perform DSC analysis to determine the temperature at which order/disorder occurs. As throughout the progression of the DSC experiment, a curve is secured across the flux of heat (heat flow endo up) and temperature ($^{\circ}\text{C}$). In fact, the ordered state is more stable than disordered state this should be evident as an exothermic peak. Therefore, it can be easily differentiate any discontinuity in the shape of curve, which indicate the presence of transition/disorder at particular temperature. In this experiment, Perkin Elmer STA 8000 (simultaneous thermal analyser) and Lauda Alpha RA 8 Chiller unit are used to determine the order/disorder transition in the Ni_5Ge_3 compound. The temperature range was subsequently adjusted to room temperature to $1085\text{ }^{\circ}\text{C}$, double cycle runs at $10\text{ }^{\circ}\text{C}/\text{mint}$ heating/cooling rate in a constant Nitrogen atmosphere of 0.4 MPa . **Figure 3.17** shows the setup of a thermal analyser.

3.5.9 Micro-hardness Measurements

In order to determine the effect of cooling rate upon mechanical properties, Vickers micro-hardness tests were performed on rapidly solidified drop-tube samples size from the ranges $\geq 850 \mu\text{m}$ to $\leq 38 \mu\text{m}$ of both intermetallic compounds Ni_3Ge and Ni_5Ge_3 . Normally, the capacity of a material to resist to a form of damage or deformation that would be permanent is what defines its hardness. In spite of this, the material's actual value of hardness is variable. This value changes in relation to the properties of the material that make up the indenter, the force and shape of the indenter. The value also changes in relation to the applied load and how long the load was applied on samples. Consequently, except if specific conditions of similarity are observed in a strict fashion during the experiment, the indentation measurement and hardness values cannot be compared.

For measurement of micro-hardness of the drop-tube samples a TUKONTM 1202 Wilson Vickers micro-hardness test was used in this project. Using tester (**Figure 3.18a**), the Trans Optic™ resin mounted and well-prepared sample was brought into focus under the tester microscope. 100 gf was the press load that was chosen. 15 seconds press time was also utilised. At the level of the surface, an indent was created. Placing filar lines all around the ends of the indent, the measurement of the indentation's size was performed using the software. The measurement of every diagonal of the indent and the determination of the average distance was also done with the help of the software. The final measurement of hardness for each sample was based upon an average of at least 10 individual measurements. An example of micro-Vickers hardness indentations are shown in the **Figure 3.18b**.

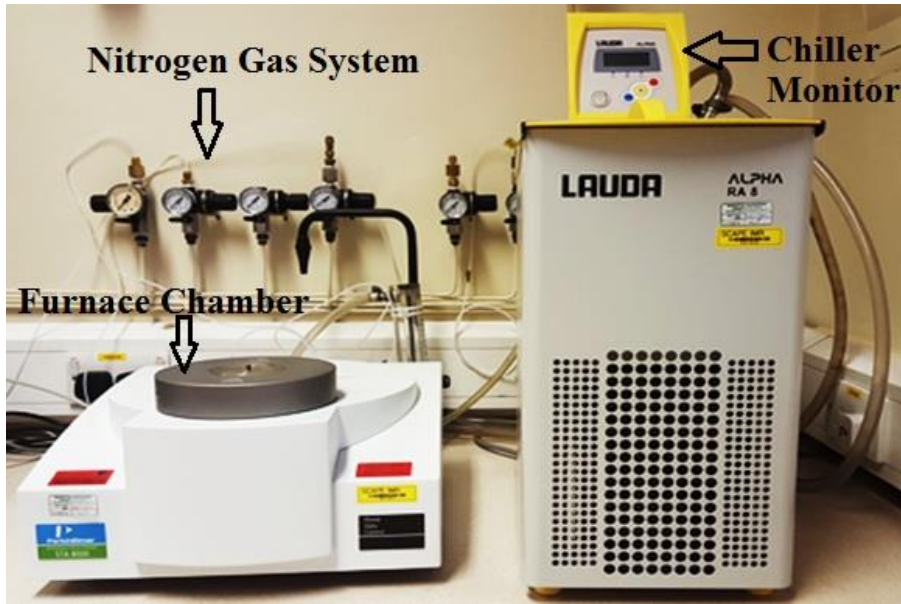


Figure 3.17 Differential Scanning Calorimetry - Perkin Elmer STA 8000 and Lauda Alpha RA 8 Chiller unit (University of Leeds).

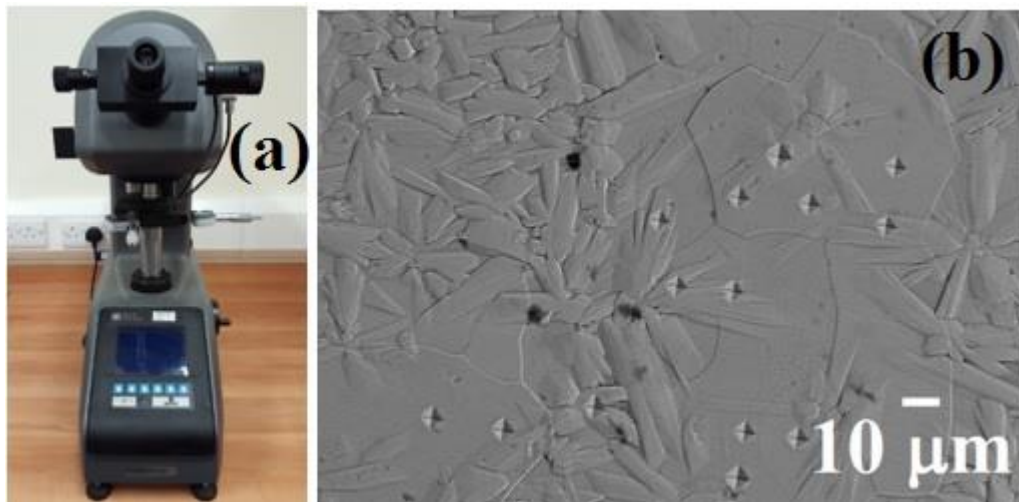


Figure 3.18 (a) TUKONTM 1202 Wilson Vickers micro-hardness analyser with resultant measurement and (b) an example of micro-Vickers hardness indentation in a drop-tube sample (Ni_5Ge_3).

Chapter 4 Experimental Results

This chapter contains all of the experimental results associated with congruent melting intermetallic compounds Ni_3Ge and Ni_5Ge_3 . Firstly, the results of the characterisation of the arc-melted produced compounds (Ni_3Ge and Ni_5Ge_3) will be present, after ensuring the single phases compound then the results of disorder – order morphologies and microstructural evolution of these two compounds (single phases) via drop-tube processed will be presented in this chapter.

4.1 Preparation of Ingot - Ni_3Ge

The congruent melting intermetallic compound Ni_3Ge was produced in the arc-melting furnace, which is considered as a starting material/parent material of this project. Before, presenting the final product of arc-melting process, there is also a selective result of unsuccessful attempt of this process. Initially, Ni and Ge elements were calculated at at.% exactly on an stoichiometry basis as shown in the **Table 4.1a**. The characterisation (XRD and EDX data) of initially stoichiometric alloys suggested the material was Ge-rich, and consequently Ni is being lost during arc-melting. Therefore, some modification (Ni - enhancement) in calculation was performed to compensate this loss, which can be seen in the **Table 4.1b**. The stated Ni-enhancement was not the first tried, but that this was actually the result of several iterations towards the correct composition to obtain a single- phase material.

All of the characterisation results of arc melted process presented here will be useful to understand the production of desired compound, single phase (Ni_3Ge). **Figure 4.1a** and **Figure 4.1b** shows XRD analysis on the polished surface of the arc-melted ingots on the basis of stoichiometry and Ni- enhanced compositions respectively. SEM micrograph of a polished and etched arc-melted samples from stoichiometry and from Ni - enhanced are showed in **Figure 4.2a** and **Figure 4.2b** respectively. It can be seen that on-stoichiometry composition base, sample was not a single phase. The SEM micrograph (**Figure 4.2a**) showing eutectic phase with a single phase. However, Ni-enhanced composition produced successfully a single phase sample ($\beta\text{-Ni}_3\text{Ge}$) as shown in **Figure 4.2b**. The extensive black and white dots (gas porosity) also observed across the microstructure from arc-melting process, which can be seen in the **Figure 4.2b**. For confirmation of no argon gas is dissolve in Ni–Ge alloys, the later of the

suggestion has proposed for future work. The EDX area analysis have been taken from the two different regions (i) and (ii) from each sample of stoichiometry composition and Ni-enhanced sample, the results can be seen from the **Table 4.2 (a and b)**.

EBSA analysis was also performed on freshly prepared Ni-enhanced arc-melted sample, polished using 0.1 μm colloidal silica and without etching. The EBSA phase map (**Figure 4.3**) further confirms the XRD analysis of Ni-enhanced sample is completely single phase $\beta\text{-Ni}_3\text{Ge}$.

4.2 Rapidly Solidified Drop-tube Sample - Ni_3Ge

The arc-melted prepared ingot of single phase Ni_3Ge compound was rapidly solidified and obtained $\geq 850 \mu\text{m}$ to $\leq 38 \mu\text{m}$ sieve size fractions using a drop-tube technique. Firstly, EDX analysis was carried out on freshly polished samples to ensure the chemical composition of the all ranges of drop-tube samples. For this, EDX area scanning was randomly performed at least on 10 particles of all ranges of drop-tube samples ($\geq 850 \mu\text{m}$ to $\leq 38 \mu\text{m}$) and measured chemical compositions were within the homogeneity range Ni – 23.8 at.% Ge as shown in **Figure 4.4**. Consequently, all ranges of drop-tube particles have the average chemical composition within the range of single phase, congruently melting compound, $\beta\text{-Ni}_3\text{Ge}$ [18]. Samples from all sieve fractions ($\geq 850 \mu\text{m}$ to $38 \mu\text{m}$) shown in **Figure 4.5** have also been subject to XRD analysis, which, by comparison with ICDD reference pattern 04 – 004 – 3112 (fcc $a = b = c = 3.566 \text{ \AA}$), confirms that the material remain fully single phase $\beta\text{-Ni}_3\text{Ge}$, irrespective of the imposed cooling rate. Moreover, EBSA analysis was also performed on freshly prepared drop-tube samples with all sieve size fractions ranges from $\geq 850 \mu\text{m}$ to $< 38 \mu\text{m}$, polished using 0.1 μm colloidal silica and without etching. The EBSA phase map for all drop-tube samples further confirms the XRD analysis in that all ranges ($\geq 850 \mu\text{m}$ to $< 38 \mu\text{m}$) samples are completely single phase $\beta\text{-Ni}_3\text{Ge}$. An example of EBSA phase map within 75 – 53 μm sieve is shown in **Figure 4.6**. After that several analysis techniques were used to study the effect of rapid solidification process, evolution of microstructures, phase transformation, to study of crystal structure and mechanical properties through using SEM, TEM, EBSA and micro-Vickers hardness test.

Table 4.1a Shows the calculation of Ni and Ge composition (on-stoichiometry), at atomic percentage.

Element	Composition (at. %)	Molar mass (g/mol)	Mole*Comp. (g)	Comp (mass) = Mol *Comp/Total mass (g)	Comp (g) Used in arc melt process
Ni	0.75	58.693	58.693 * 0.75 = 44.01975	44.01975/62.17975 = 0.70794	0.70794 *20 = 14.16
Ge	0.25	72.64	72.64* 0.25 =18.16	18.16/62.17975 = 0.29205	0.29205*20 = 5.841
			= 62.17975		= 20

Table 4.1b Shows the calculation of Ni and Ge composition (Ni-enhanced), at atomic percentage.

Element	Composition (at. %)	Molar mass (g/mol)	Mole*Comp. (g)	Comp (mass) = Mol *Comp/Total mass (g)	Comp (g) Used in arc melt process
Ni	0.756	58.693	58.693*0.756 = 44.37190	44.37190/62.09606 = 0.71456	0.71456*15= 10.7184
Ge	0.244	72.64	72.64*0.244 =17.72416	17.72416/62.09606 = 0.28543	0.28543*15 = 4.28145
			= 62.09606		= 15

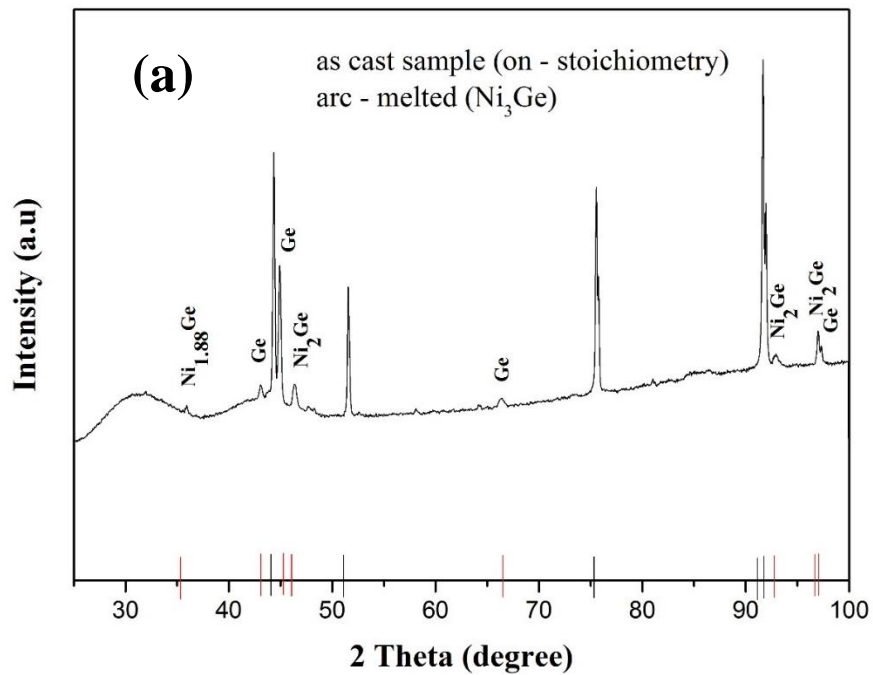


Figure 4.1a X-ray diffraction analysis of as cast (arc-melted, on-stoichiometry) sample prior to drop-tube process. Vertical black lines indicate peak position for the single-phase (β - Ni_3Ge reference pattern, and vertical red lines indicate peak position of $\text{Ni}_{1.88}\text{Ge}$, Ge and Ni_2Ge .

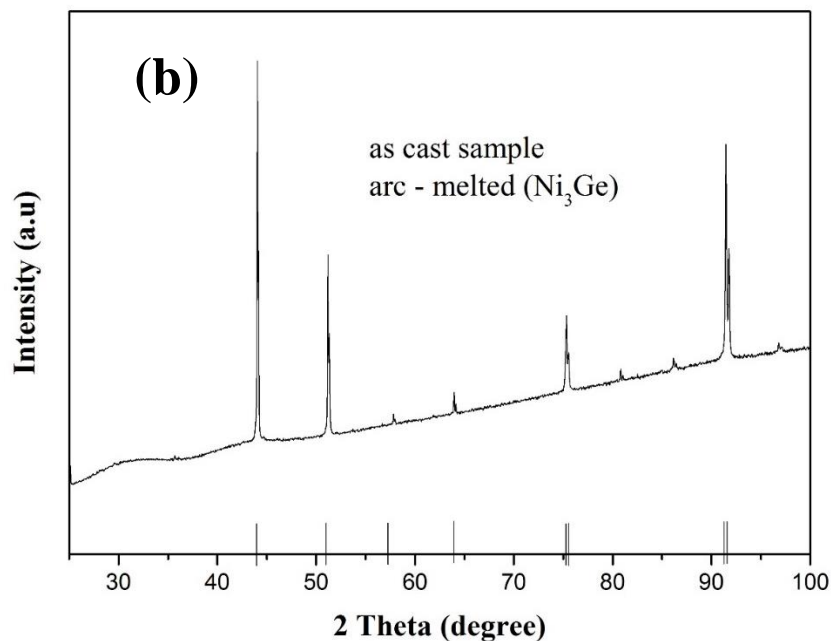


Figure 4.1b X-ray diffraction analysis of as cast (arc-melted, Ni-enhanced) sample prior to drop-tube process. Vertical black lines indicate peak position for the single-phase (β - Ni_3Ge reference pattern).

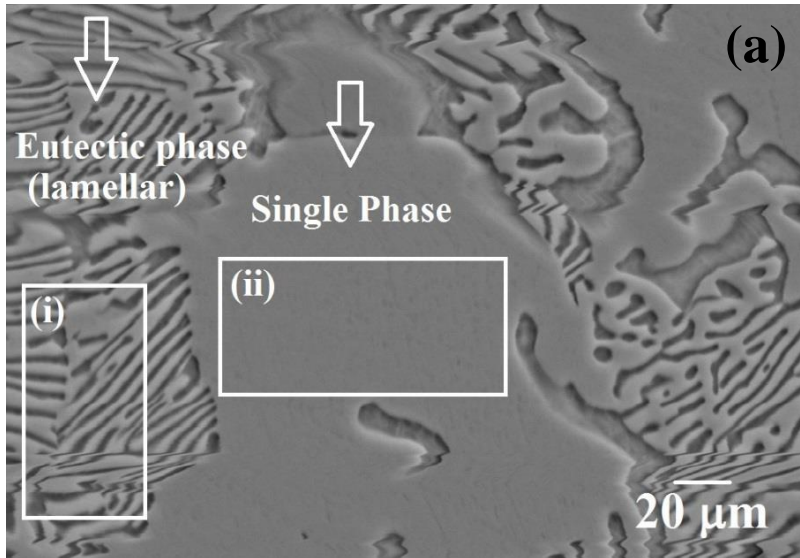


Figure 4.2a SEM (SEI) micrograph of HF etched of as cast (arc-melted, on-stoichiometry) sample prior to drop-tube process, showing eutectic phase with a single phase. The region (i) eutectic phase and region (ii) single phase selected for EDX area analysis.

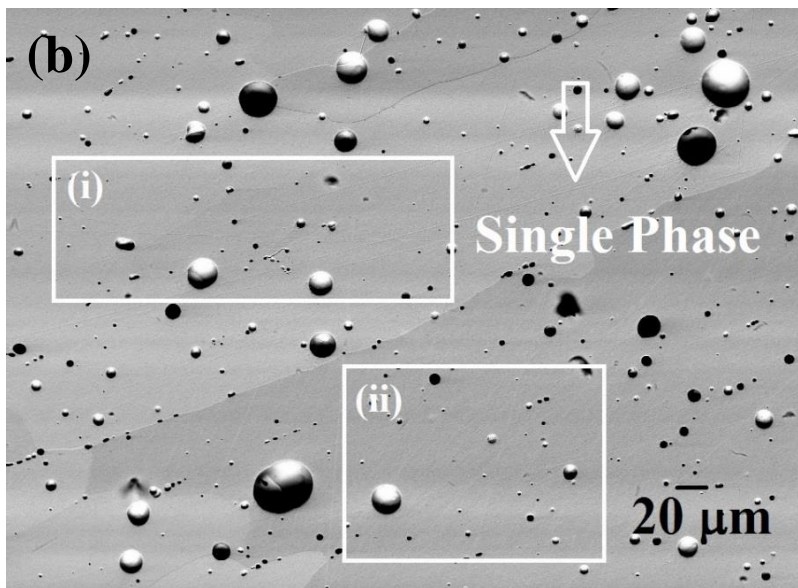


Figure 4.2b SEM (SEI) micrograph of HF etched of as cast (arc-melted, Ni-enhanced) sample prior to drop-tube process, showing sample has completely single phase. The extensive black and white dots (gas porosity) also observed across the microstructure from arc-melting process. The regions (i) and (ii) selected from different regions of sample for EDX area analysis.

Table 4.2a Shows the results of EDX area analysis of Ni and Ge composition (on – stoichiometry) at their atomic percentages. The regions (i) and (ii) have been taken from the **Figure 4.2a**.

(i)	
Element	Atomic %
Ni	70
Ge	30

(ii)	
Element	Atomic %
Ni	75
Ge	25

Table 4.2b Shows the results of EDX area analysis of Ni and Ge composition (Ni-enhanced) at their atomic percentages. The regions (i) and (ii) have been taken from the **Figure 4.2b**.

(i)	
Element	Atomic %
Ni	76
Ge	24

(ii)	
Element	Atomic %
Ni	76
Ge	24

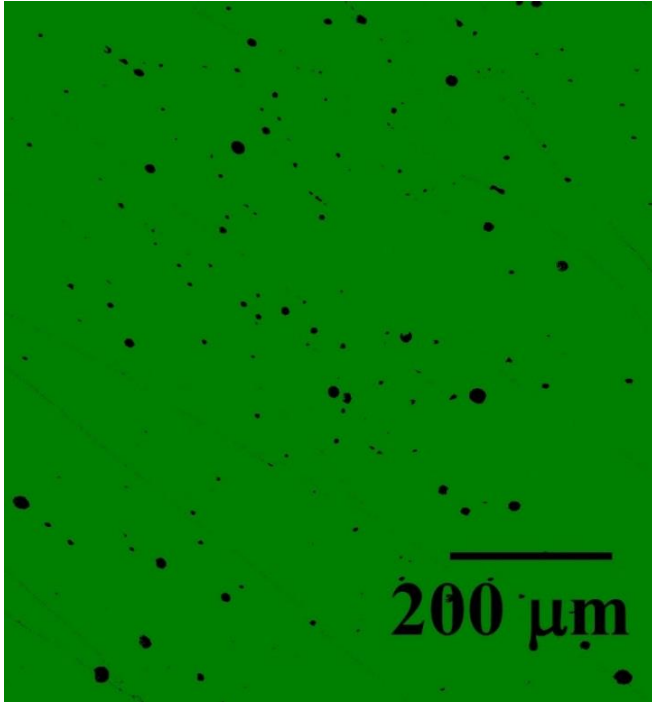


Figure 4.3 Electron backscatter diffraction (EBSD) result of phase map (arc-melted, Ni-enhanced sample).

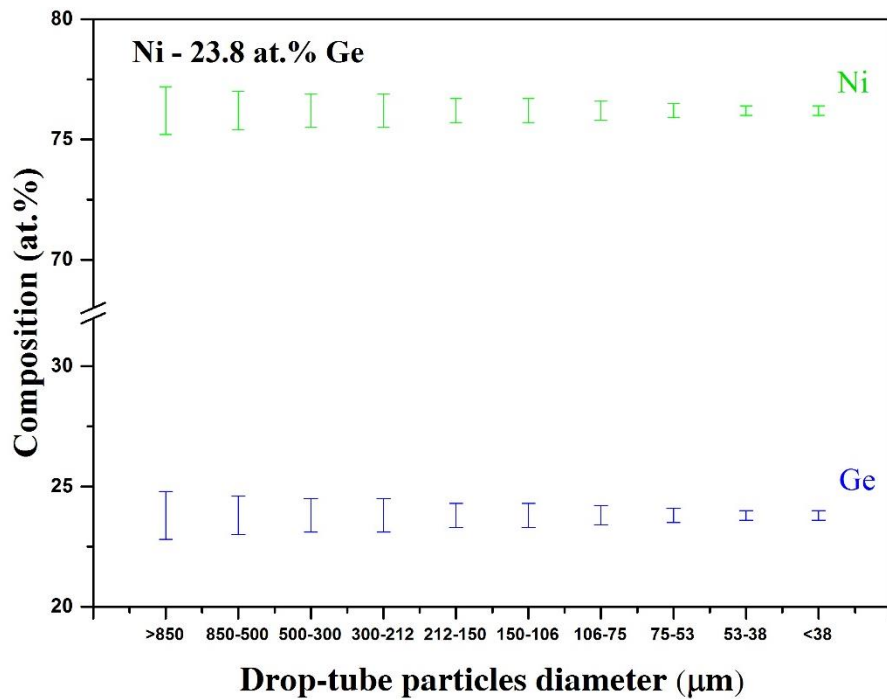


Figure 4.4 Average EDX compositions of Ni and Ge of the Ni-23.8 at.% Ge drop-tube particles. At least 10 particles were analysed in each size range.

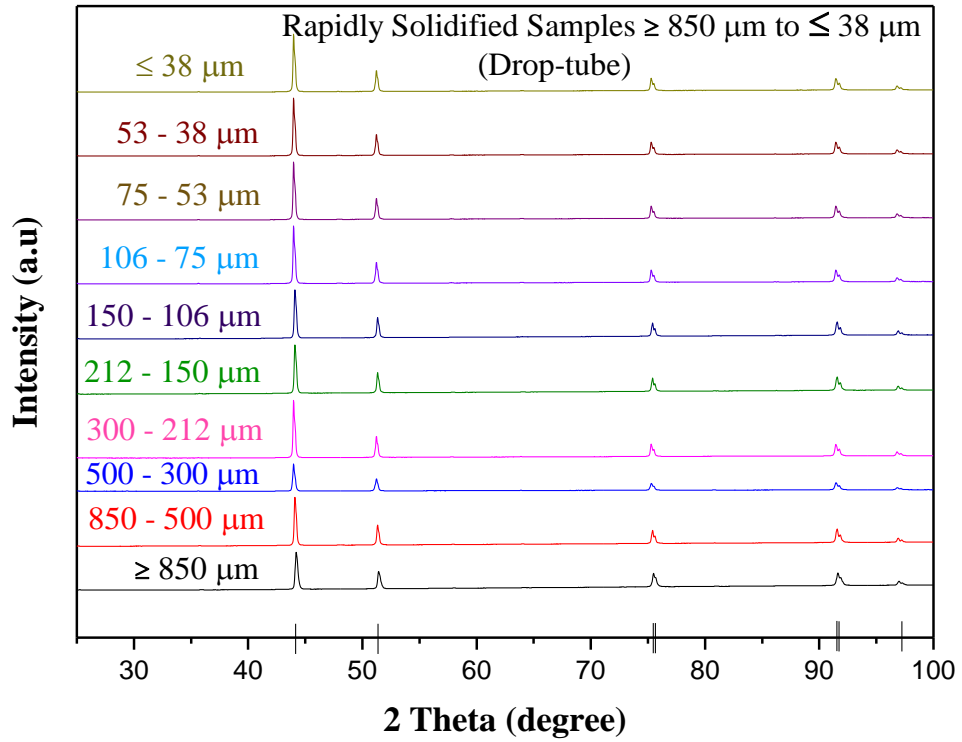


Figure 4.5 X-ray diffraction analysis of rapidly solidified drop-tube processed samples, ranges from ($\geq 850 \mu\text{m}$ to $\leq 38 \mu\text{m}$). Vertical black lines indicate peaks position for the single-phase $\beta\text{-Ni}_3\text{Ge}$ reference pattern and different colours represents XRD patterns of particle sizes from $\geq 850 \mu\text{m}$ to $\leq 38 \mu\text{m}$.

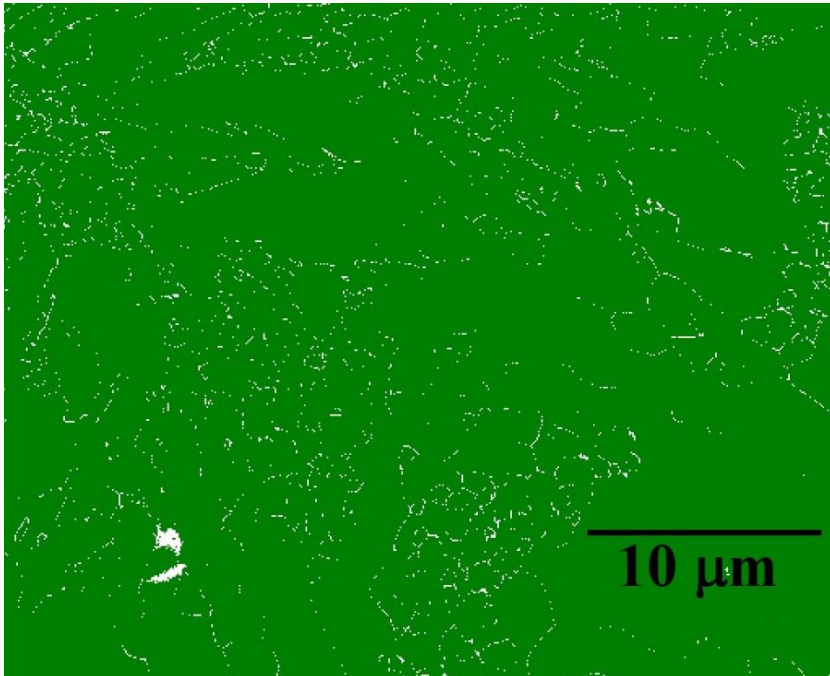


Figure 4.6 Electron backscatter diffraction (EBSD) result of phase map (drop-tube, 75 – 53 μm sample).

4.2.1 Microstructural Characterisation

SEM was used for studying microstructures of the rapidly solidified Ni₃Ge droplets, ranges from $\geq 850 \mu\text{m}$ to $\leq 38 \mu\text{m}$ sieve size fractions. In summary, there were five typical microstructures observed, namely spherulites, dendrites (orthogonal), dendrites (non-orthogonal), crack-like relief (subsequently established as being recrystallised) and dendritic seaweed (dense branched fractal) microstructures. **Figures 4.7 – 4.16** shows SEM micrograph of the polished and HF etched samples from the $\geq 850 \mu\text{m}$, $850 - 500 \mu\text{m}$, $500 - 300 \mu\text{m}$, $300 - 212 \mu\text{m}$, $212 - 150 \mu\text{m}$, $150 - 106 \mu\text{m}$, $106 - 75 \mu\text{m}$, $75 - 53 \mu\text{m}$, $53 - 38 \mu\text{m}$ and $\leq 38 \mu\text{m}$ respectively.

Numerous spherulites microstructures, having a diameter range of $10 - 20 \mu\text{m}$, are evident in the two largest sieve size fractions, $\geq 850 \mu\text{m}$ and $850 - 500 \mu\text{m}$, as shown in **Figure 4.7** and **Figure 4.8** respectively. Although, several spherulite morphologies are also evidently noticeable in the three smaller sieve sizes $500 - 300 \mu\text{m}$, $300 - 212 \mu\text{m}$, and $212 - 150 \mu\text{m}$ but these spherulites are now smaller than largest sieve sizes, typically to $<10 \mu\text{m}$, $< 3 \mu\text{m}$ and less than $1 \mu\text{m}$ respectively. The drop-tube sample sizes $500 - 300 \mu\text{m}$ and $300 - 212 \mu\text{m}$ shows mixed of dendrites and spherulites microstructure (**Figure 4.9** and **Figure 4.10**). The dendrites become more dominant in the drop-tube sample size $212 - 150 \mu\text{m}$ when increasing the cooling rate, but still there is presence of spherulites which can be seen in the **Figure 4.11**, (the row of features along the top of the micrograph as well as the far right-hand end of the longest dendrite trunk).

Finally spherulites was ceased by further reduction (increasing cooling rate) and dendrites becoming the dominant microstructure in the droplets size $150 - 106 \mu\text{m}$. An example of dendrites microstructure is shown in **Figure 4.12**. However, it is not that similar to **Figure 4.11**. Figure 4.11 contains a few isolated dendrites while **Figure 4.12** look like a classic dendrite structure as it observed with multiple mutually intersecting side-branches.

The spherulite is no more noticeable with the further reduction in the particle size to $75 \mu\text{m}$. Moreover, the morphology also shows that the dendrites are more dominant in the drop-tube sieve size fractions to $75 \mu\text{m}$. This is evident that the particle size of sieve fraction $150 - 106 \mu\text{m}$ shows structure with well-developed side branched (as shown in **Figure 4.12**). While, dendrites shows different characteristics/morphology

when observing the particle of size 106 – 75 μm sieve fraction (**Figure 4.13**). **Figures 4.11 – 4.12**, showing that many droplet display a well-developed orthogonal side-branch structures, however within the sieve size fraction of 106 – 75 μm , some of the droplets the side-branches are no longer orthogonal to the main trunk as shown in **Figure 4.13**.

With a yet further reduction in a droplet from the 75 – 53 μm sieve fraction numerous crack-like features are apparent as shown in **Figure 4.14**. Although no such features may be observed prior to etching, so that despite their appearance the features are not therefore cracks, it looks crack-like relief, which will be discuss in detail on next chapter.

Finally, in the two smallest size fractions 53 – 38 μm and $\leq 38 \mu\text{m}$ also investigated as part of this project, yet another structure is observed on both smallest sieve size fractions, which might describe a being of the ‘dense branched fractal’ or ‘dendritic seaweed’ structure, which can be seen in the **Figure 4.15a**. However, crack-like structure (same as **Figure 4.14**) also partially observed with dendritic seaweed, dendrites and along with some featureless matrix in the same drop-tube size fraction 53 – 38 (**Figure 4.15b**). While, further reduction in the smallest size of drop-tube particle $\leq 38 \mu\text{m}$, finally, crack-like relief completely transformed into dendritic seaweed structure. An example of which is shown in **Figure 4.16**.

The EDX line scan technique was used on etched sample for the analysis of contrast between the microstructures (Spherulites, dendrites orthogonal, dendrites non-orthogonal, recrystallised, dendritic seaweed) and the surrounding material (featureless matrix) of rapidly solidified drop-tube samples $\geq 850 \mu\text{m}$ to $\leq 38 \mu\text{m}$. The example of EDX line scan of selective microstructures, Spherulites, dendrites and dendritic seaweed are shown in the **Figures 4.17 (a-c)**. From EDX line scan analysis it is clear that, to within the experimental position error associated with the technique, there is no variation in composition between the structures revealed by etching (as shown in **Figures 4.17 a-c**) and the surrounding featureless matrix. As in above **Figures** the scan across the dendrites /spherulites/ seaweed arms shows in EDX scan lines that there is no compositional difference between the microstructures and featureless matrix. These difference might be due to the solute partitioning during solidification.

- For the EDX line scan of spherulites trunk (**Figure 4.17 a**), time for each step and number of step can be calculated by following equation:

$$\text{Time for each step} = \text{total aquasition time} / \text{number of steps} = 490 \text{ sec} / 500 = \mathbf{0.98 \text{ sec}} \quad (4 - 1)$$

$$\text{Number of step} = \text{Total length of scan/step size from the lateral resolution} = 21 \mu\text{m} / 500 = 0.042 * 1000 = \mathbf{42} \quad (4 - 2)$$

- For the EDX line scan of dendrites trunk (**Figure 4.17 b**):

$$\text{Time for each step} = \text{total aquasition time} / \text{number of steps} = 520 \text{ sec} / 500 = \mathbf{1.04 \text{ sec}} \quad (4 - 3)$$

$$\text{Number of step} = \text{Total length of scan/step size from the lateral resolution} = 13 \mu\text{m} / 500 = 0.026 * 1000 = \mathbf{26} \quad (4 - 4)$$

- For the EDX line scan of seaweed trunk (**Figure 4.17 c**):

$$\text{Time for each step} = \text{total aquasition time} / \text{number of steps} = 460 \text{ sec} / 500 = \mathbf{0.92 \text{ sec}} \quad (4 - 5)$$

$$\text{Number of step} = \text{Total length of scan/step size from the lateral resolution} = 15 \mu\text{m} / 500 = 0.03 * 1000 = \mathbf{30} \quad (4 - 6)$$

It can be conclude that **Figure 4.17 (a-c)** showed some noise signal which is effect of limited time of EDX-line scanning. Also, given the limited number of effective steps in the line scan, the ability to distinguish compositional features is limited.

4.2.2 EBSD Analysis

EBSD Euler map was used to study the grain structures of observed microstructure (Spherulites, dendrites orthogonal, dendrites non-orthogonal, recrystallised and dendritic seaweed). For this, drop-tube sieve size fractions $\geq 850 \mu\text{m}$ to $\leq 38 \mu\text{m}$ ranges have been undertaken on freshly prepared samples, polished using $0.1 \mu\text{m}$ colloidal silica and without etching. The grain structure for the $\geq 850 \mu\text{m}$ to $\leq 38 \mu\text{m}$ sample are very clearly revealed in the EBSD Euler map as shown in the **Figures 4.18a – 4.27a**. **Figure 4.18a** and **Figure 4.19a** contain many equiaxed grains of near equal size within drop-tube sample sizes $\geq 850 \mu\text{m}$ and $850 - 500 \mu\text{m}$ respectively. whereas **Figure**

4.20a within drop-tube sample size 500 – 300 μm contains a mix of large and very small grains, the number of which increase as we move to **Figure 4.21a** (300 – 212 μm). As this progression continues we get to **Figure 4.23a** (150 – 106 μm) which is dominated by small grains. **Figure 4.25a** (75 – 53 μm) is then different again, with large grains, some of which contain a large number of small sub-grains, which indicated that these grains (crack-like structure) as being recrystallised. Finally, when we reached to **Figure 4.26a/4.27a**, then some elongation observed in grains which speculate that these might be related to the occurrence of the seaweed structure. The orientation of each grain relative to its neighbours are shown by the histogram of grain orientations in the **Figures 4.18b – 4.27b**, within the drop-tube sample sizes 150 μm to $\leq 38 \mu\text{m}$. The histogram of all above figures (**Figure 18b – 27b**) match – mismatch with the EBSD pattern, but at least **Figure 4.24b** looks random orientation and **Figure 4.25 b/Figure 4.26b/Figure 4.27b** looks low angle grain boundaries.

The grain orientation spread (GOS) map and data of selective drop-tube sieve size fractions (basis of their microstructure/different morphologies) also obtained for further understanding of orientations of grains, which are shown in the **Figures 4.28 a – 4.31a** and **4.28b – 4.31b** respectively. Spherulites shows deeper grain orientation spread (**Figure 4.28**), while dendritic microstructure shows comparatively low grain orientation spread (**Figure 4.29**). However, recrystallised microstructure shows higher orientation spread and when it transit to seaweed then we obtained highest grain orientation spread , this can be seen from the **Figure 4.30** and **Figure 4.31** respectively.

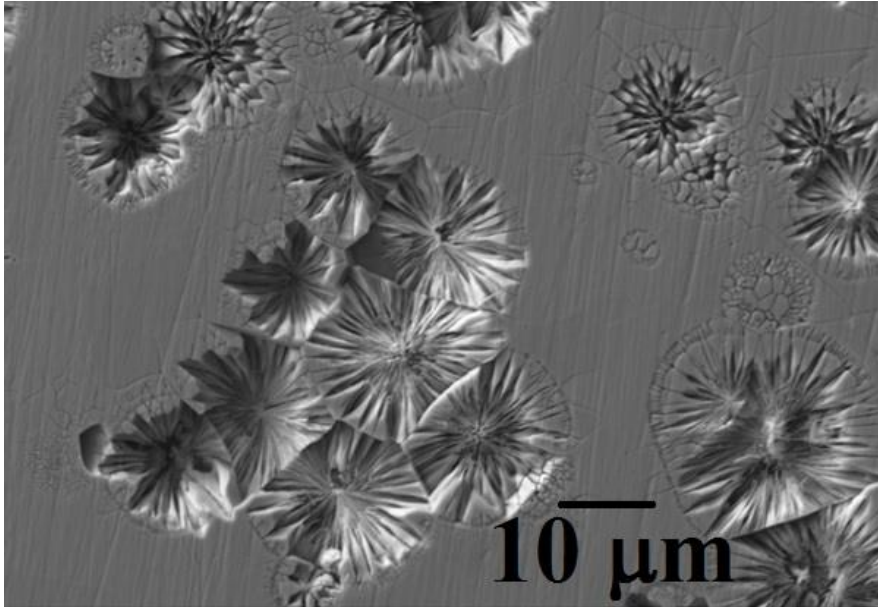


Figure 4.7 SEM (SEI) micrograph of an HF etched β -Ni₃Ge drop-tube particle from the $\geq 850 \mu\text{m}$ size fraction. Numerous spherulite structures are evident in a more-or-less featureless matrix.

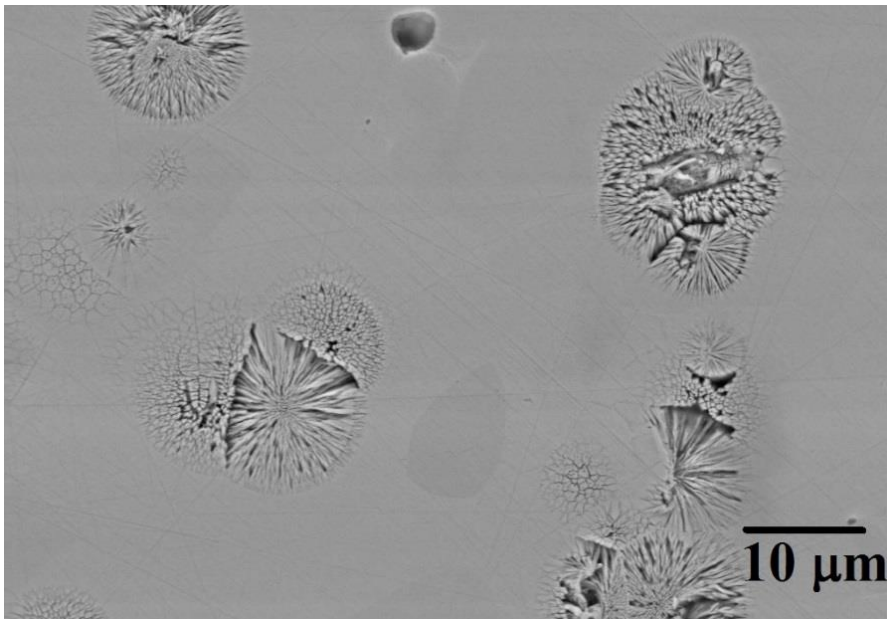


Figure 4.8 SEM (SEI) micrograph of an HF etched β -Ni₃Ge drop-tube particle from the $850 - 500 \mu\text{m}$ size fraction. Numerous spherulite structures are evident in a more-or-less featureless matrix.

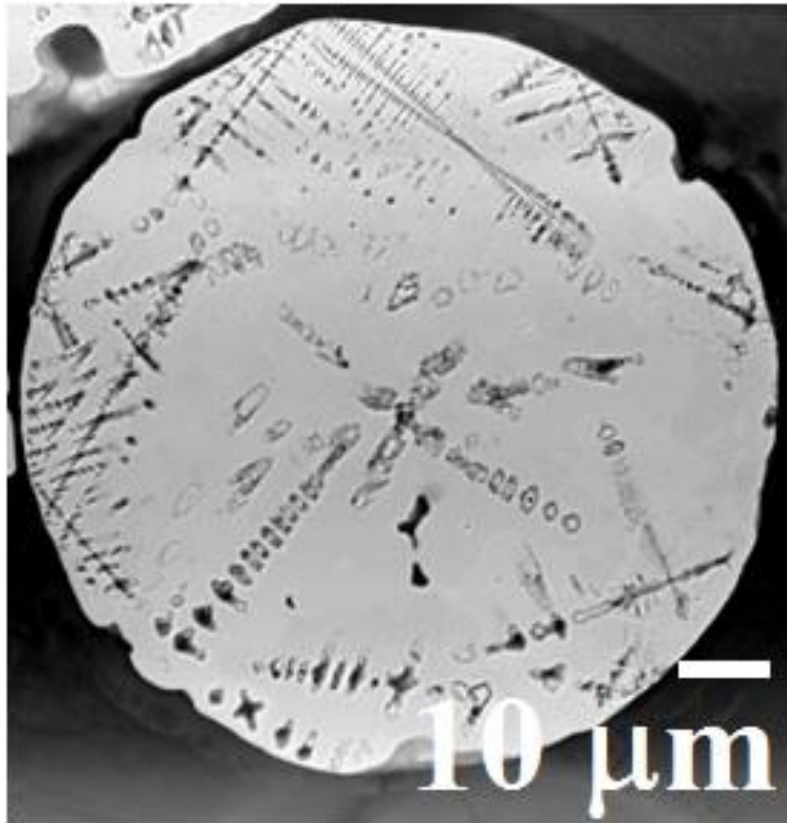


Figure 4.9 SEM (SEI) micrograph of an HF etched β -Ni₃Ge drop-tube particle from the 500 – 300 μm size fraction. Shows co-existence of spherulites with dendritic microstructure.

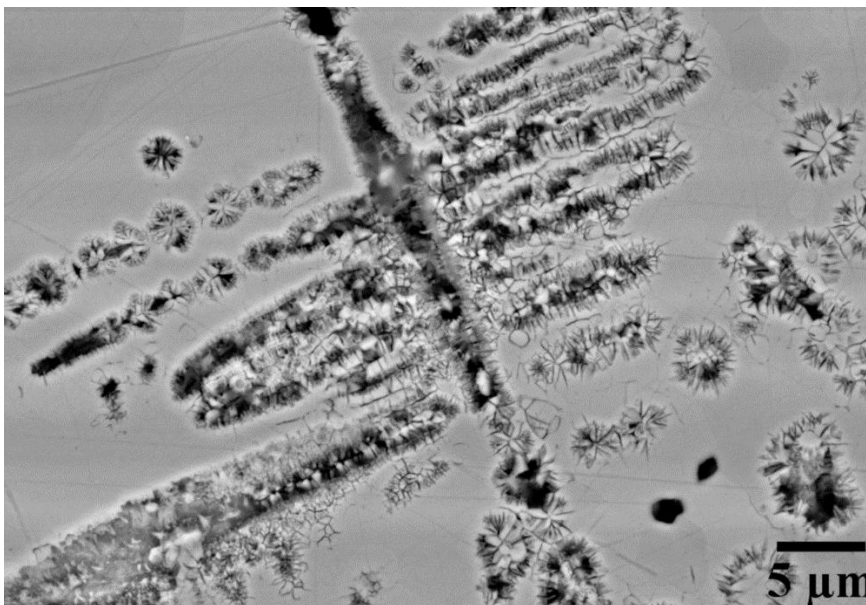


Figure 4.10 SEM (SEI) micrograph of an HF etched β -Ni₃Ge drop-tube particle from the 300 – 212 μm size fraction. Shows co-existence of spherulites with dendritic microstructure.

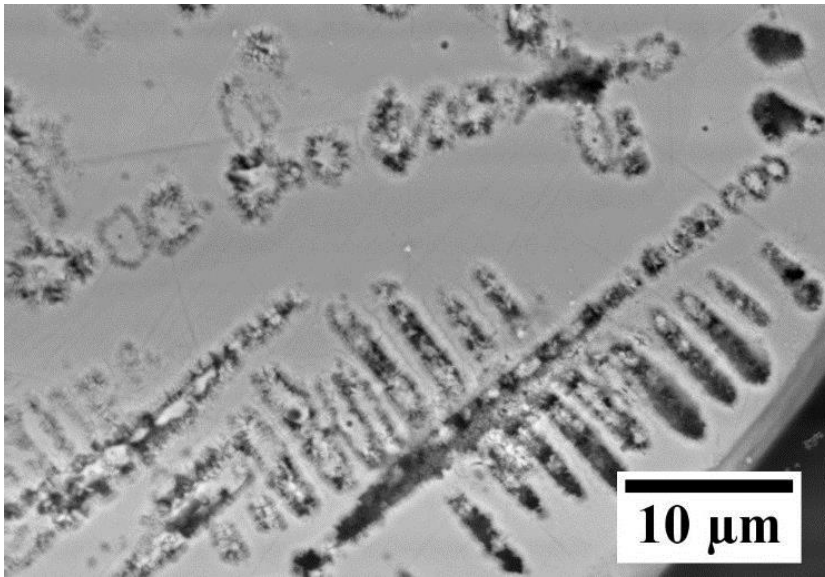


Figure 4.11 SEM (SEI) micrograph of an HF etched β -Ni₃Ge drop-tube particle from the 212 – 150 μm size fraction showing dendritic structures in a featureless matrix.

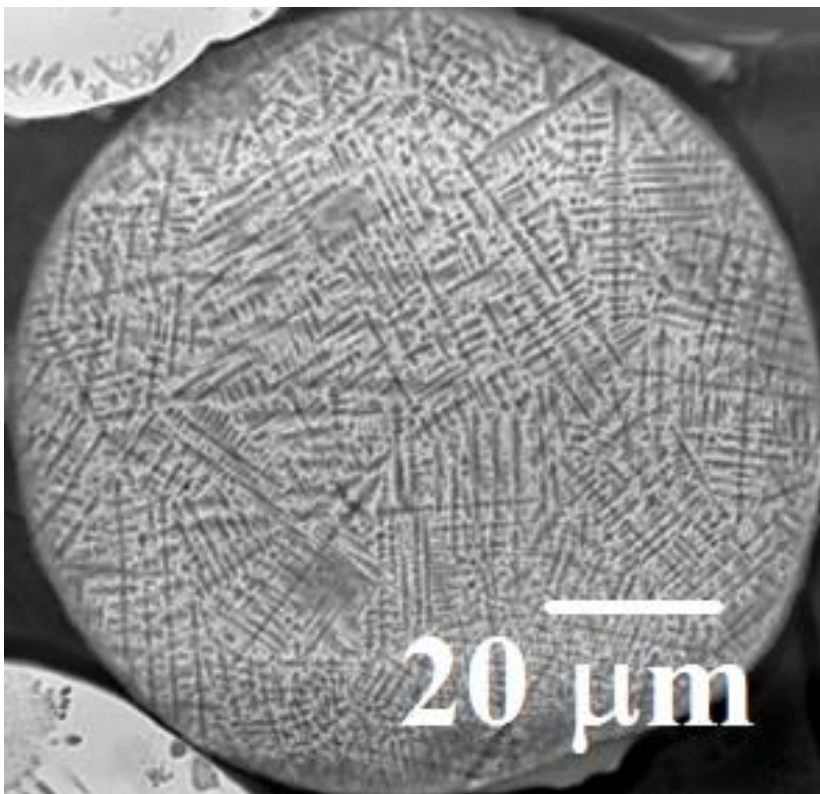


Figure 4.12 SEM (SEI) micrograph of an HF etched β -Ni₃Ge drop-tube particle from the 150 – 106 μm size fraction showing dendritic structures in a featureless matrix.

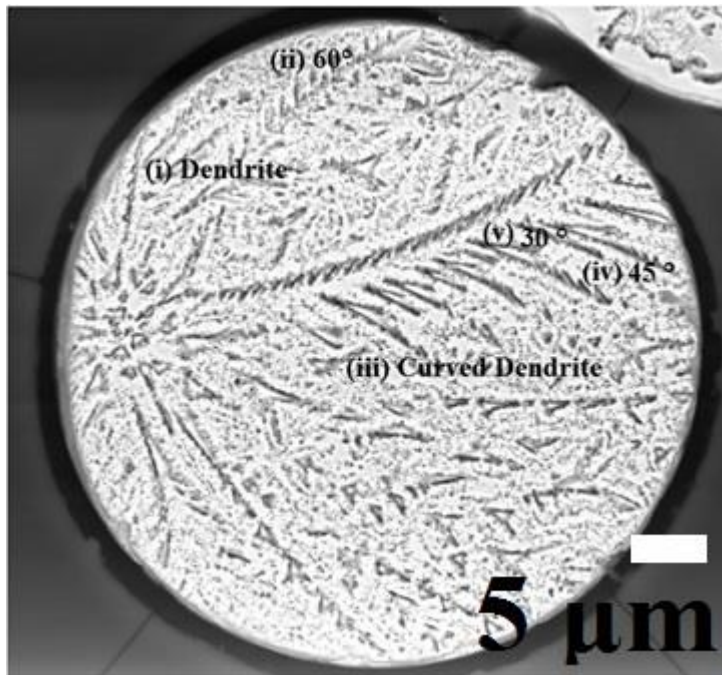


Figure 4.13 SEM (SEI) micrograph of an HF etched β -Ni₃Ge drop-tube particle from the 106 – 75 μm size fraction, showing dendritic structure with non-orthogonal side branching. Two dendrites in particular are indicated with side-branches at angles of (i) 60° and (ii) 45° and 30°.

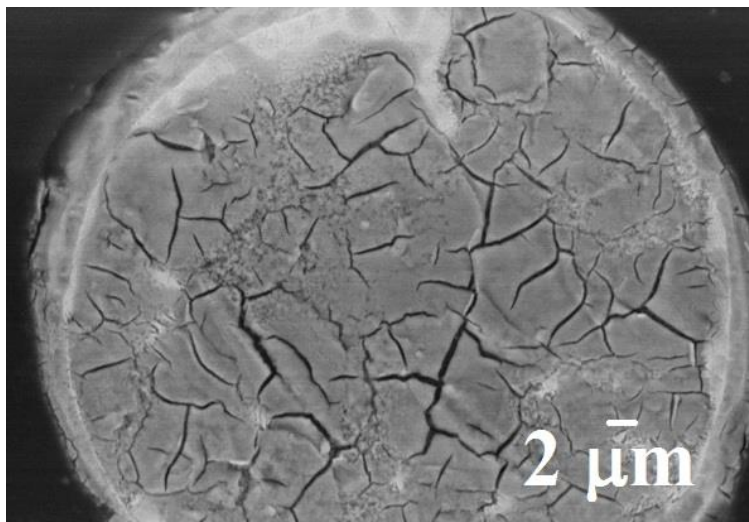


Figure 4.14 SEM (SEI) micrograph of an HF etched β -Ni₃Ge drop-tube particle from the 75-53 μm size fraction showing crack-like relief (recrystallised microstructure).

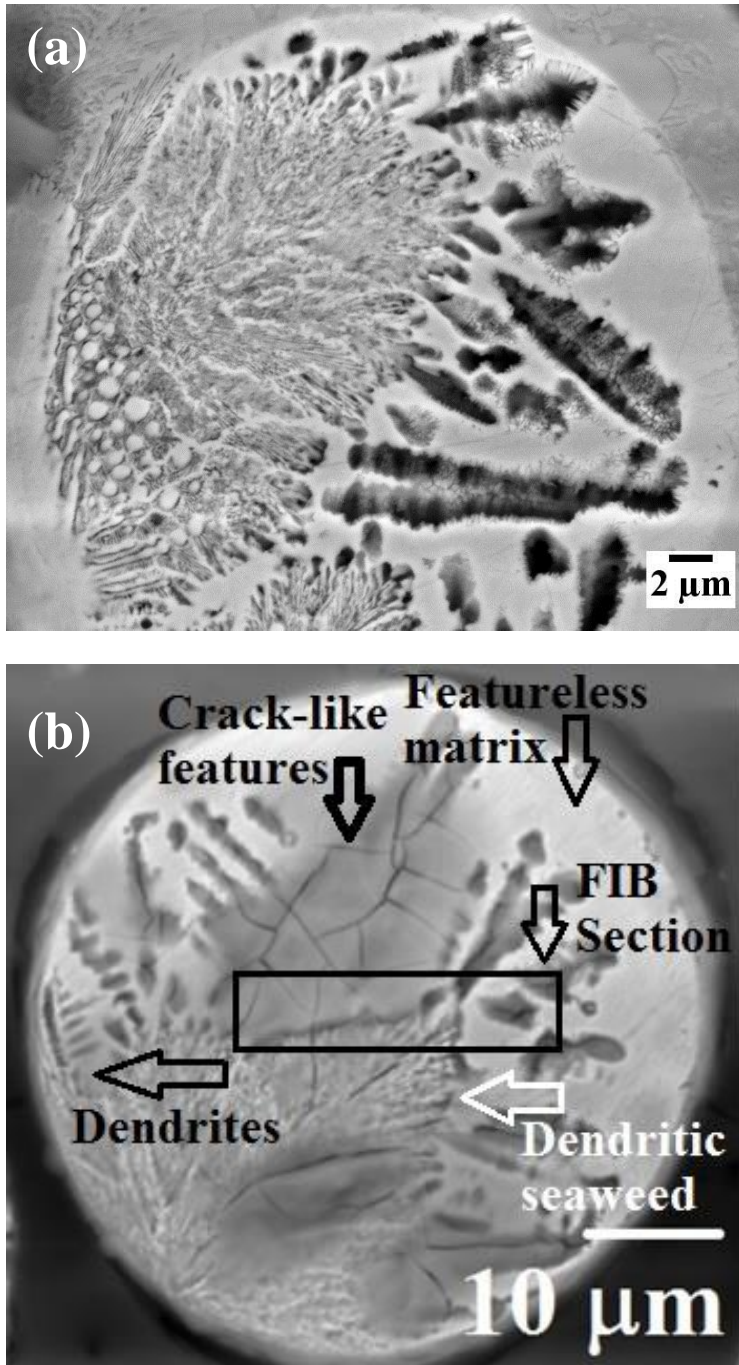


Figure 4.15 (a) SEM (SEI) micrograph of an HF etched β -Ni₃Ge drop-tube particle from the 53 - 38 μm size fraction showing dendritic seaweed structure and (b) dendritic seaweed structure, dendrites, crack-like relief (recrystallised-microstructure) along with featureless matrix; within the same size of drop-tube particle (a).

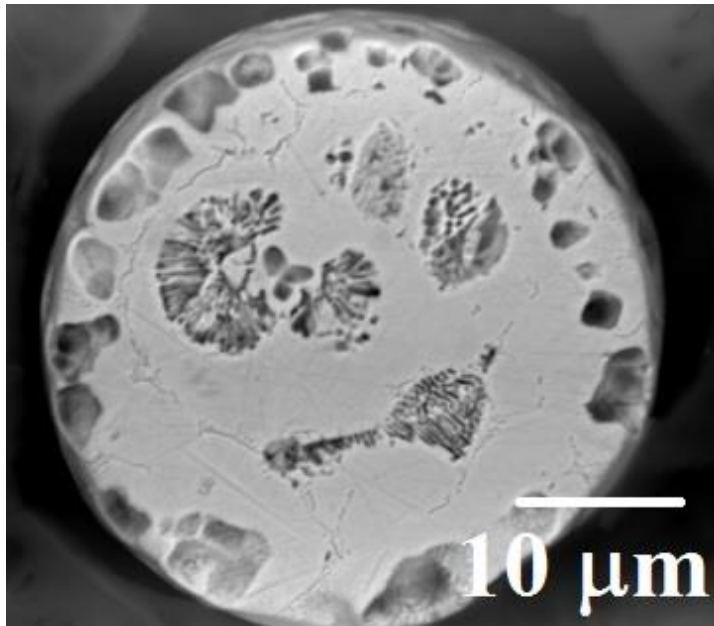
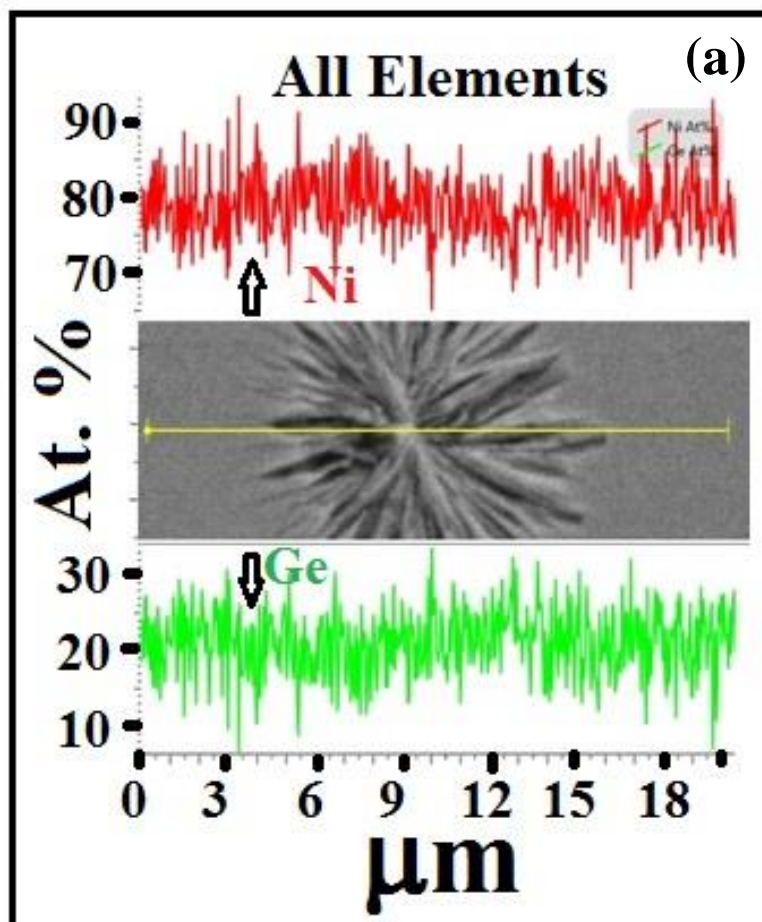


Figure 4.16 SEM (SEI) micrograph of an HF etched β -Ni₃Ge drop-tube particle from the $\leq 38 \mu\text{m}$ size fraction showing dense branched fractal or ‘dendritic seaweed’ structure.



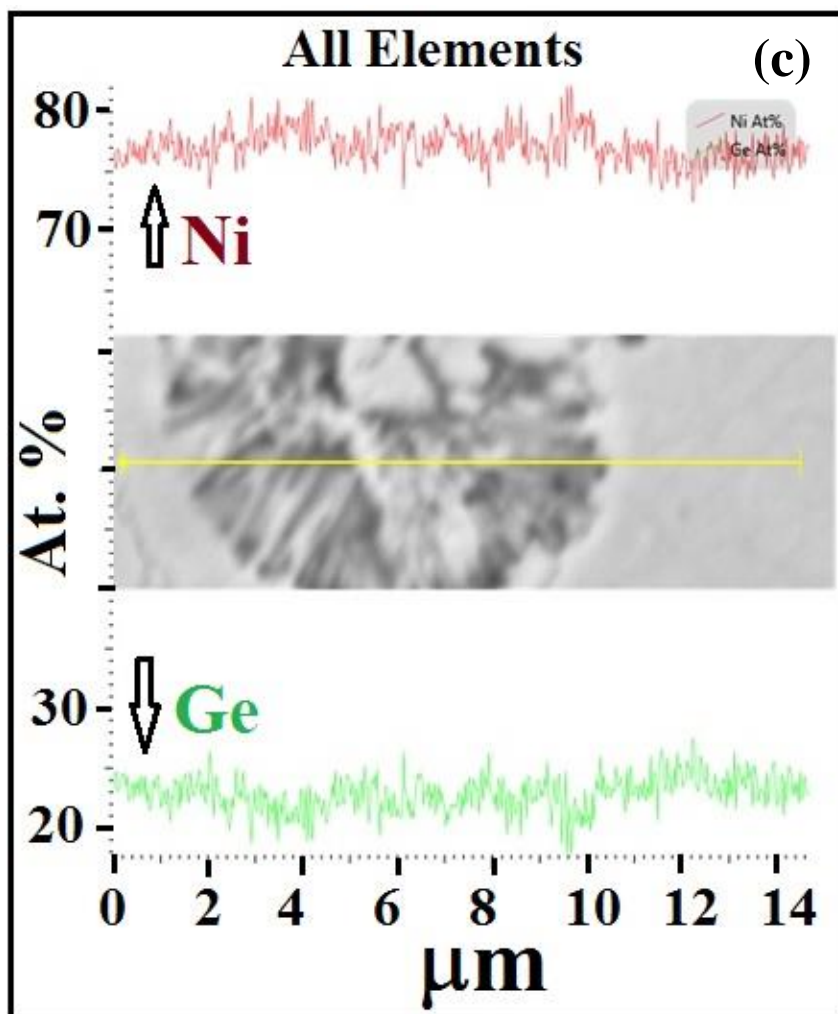
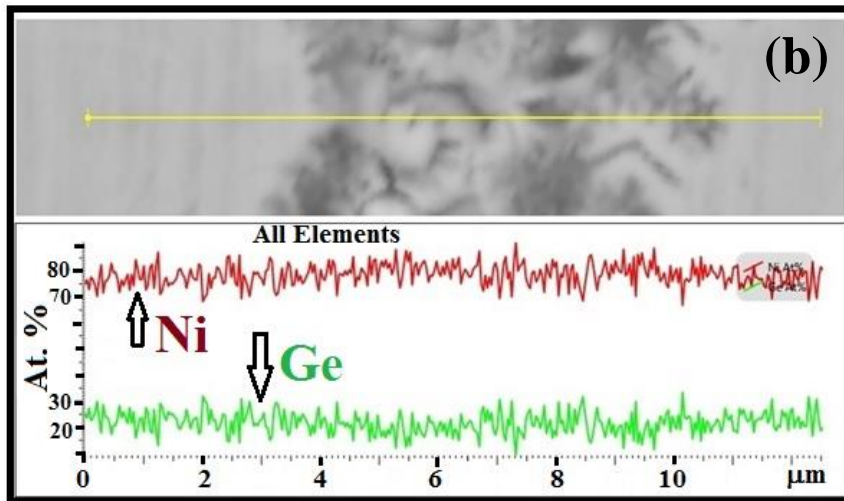


Figure 4.17 (a) EDX line scan across a spherulite trunk (b) dendrite trunk and (c) seaweed trunk, showing that the contrast revealed by etching is not the result of solute partitioning.

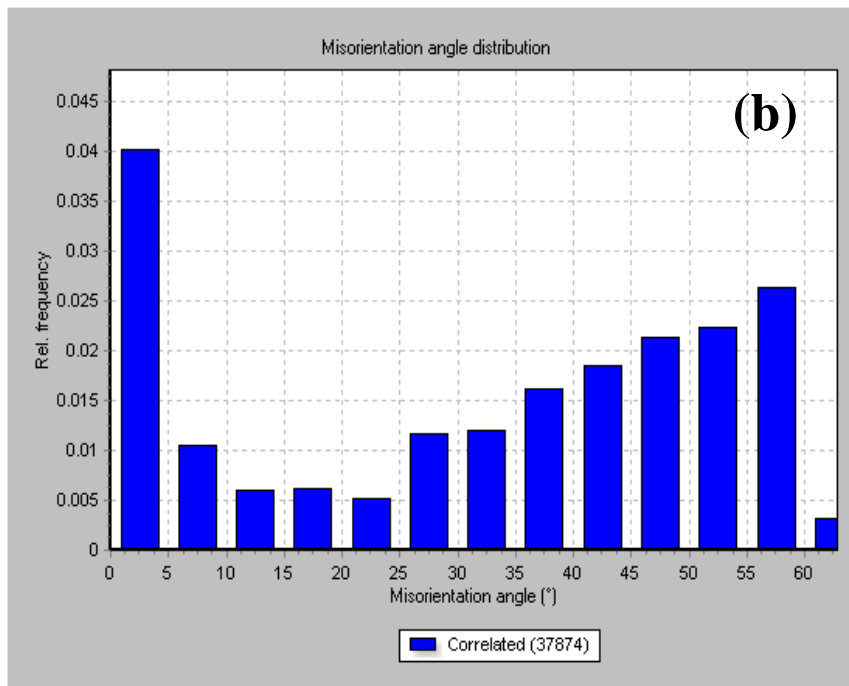
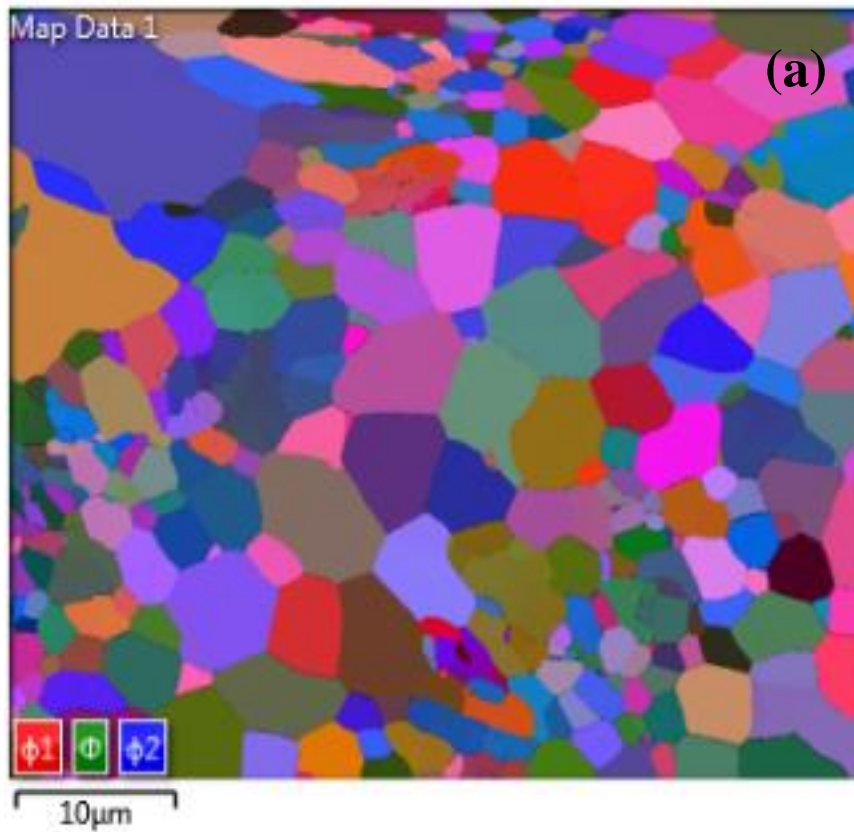


Figure 4.18 (a) Electron backscatter diffraction (EBSD) result of Euler texture map of unetched β -Ni₃Ge drop-tube particle size $\geq 850 \mu\text{m}$; (b) Histogram of the correlated misorientation angle distribution across grain boundaries for the image shown in (a).

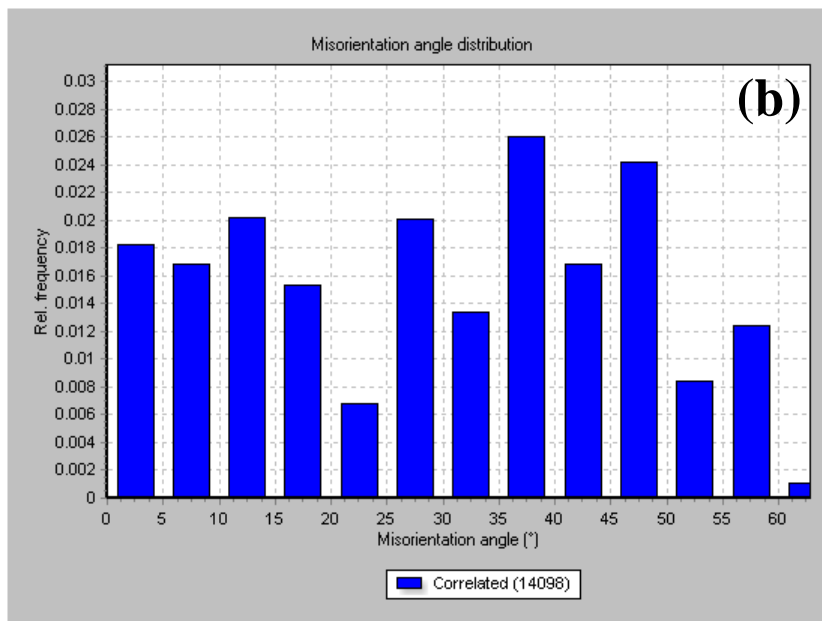
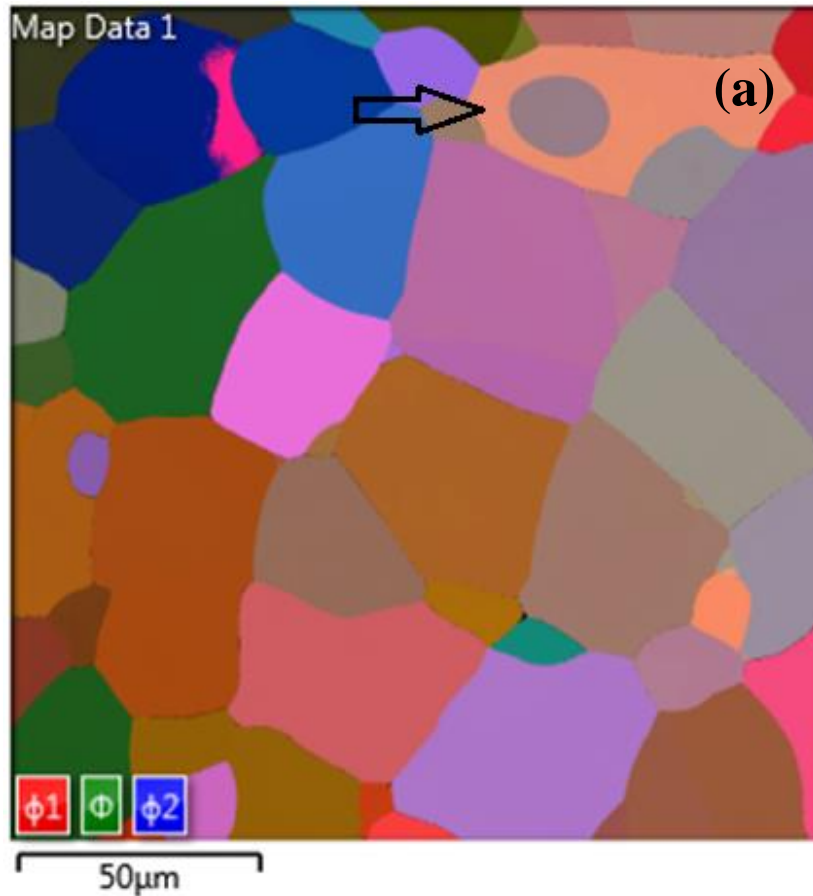


Figure 4.19 (a) Electron backscatter diffraction (EBSD) result of Euler texture map of unetched β -Ni₃Ge drop-tube particle size 850 – 500 μm (arrow indicates presence of spherulite); (b) Histogram of the correlated misorientation angle distribution across grain boundaries for the image shown in (a).

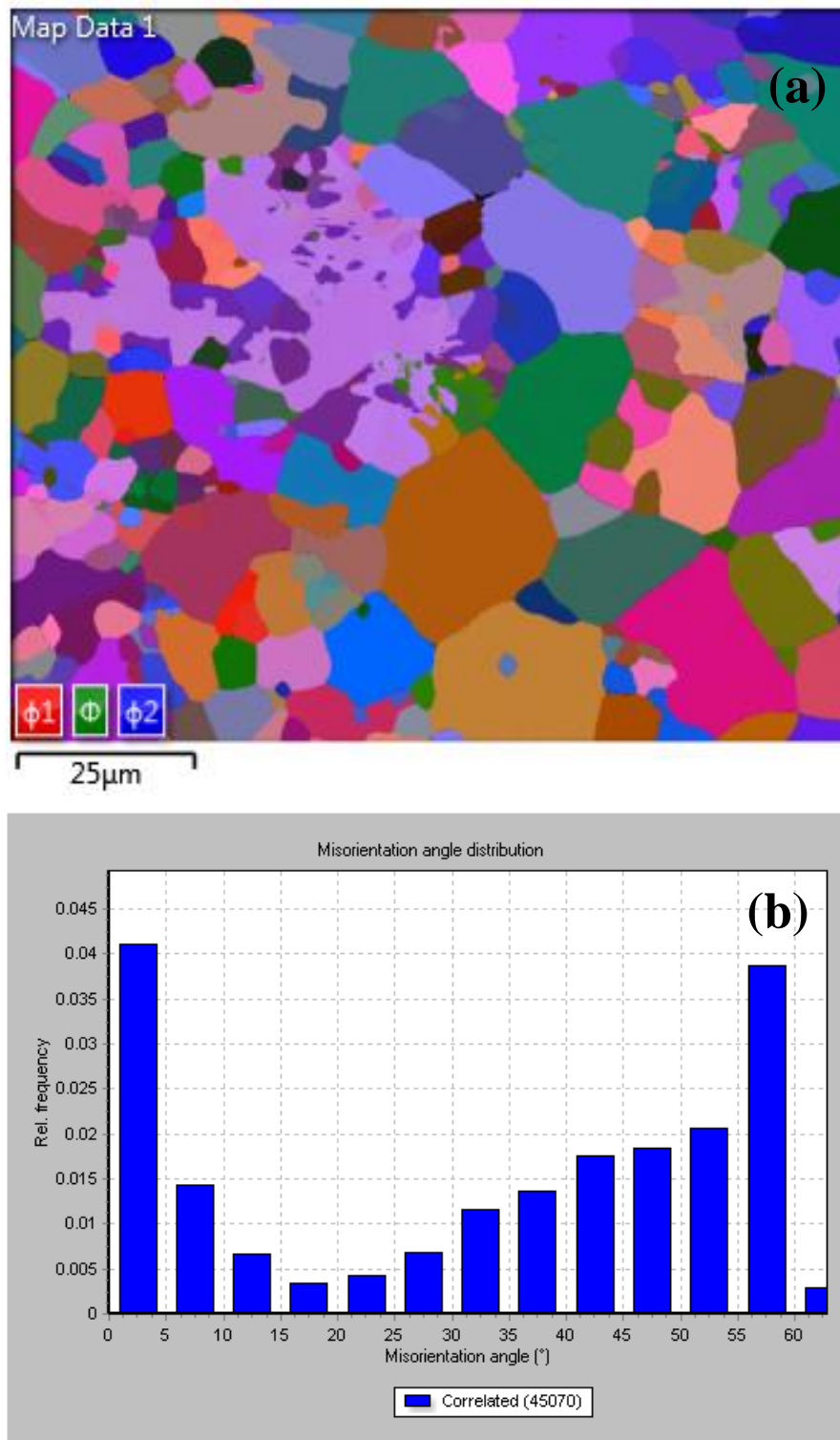


Figure 4.20 (a) Electron backscatter diffraction (EBSD) result of Euler texture map of unetched β -Ni₃Ge drop-tube particle size 500 – 300 μ m; (b) Histogram of the correlated misorientation angle distribution across grain boundaries for the image shown in (a).

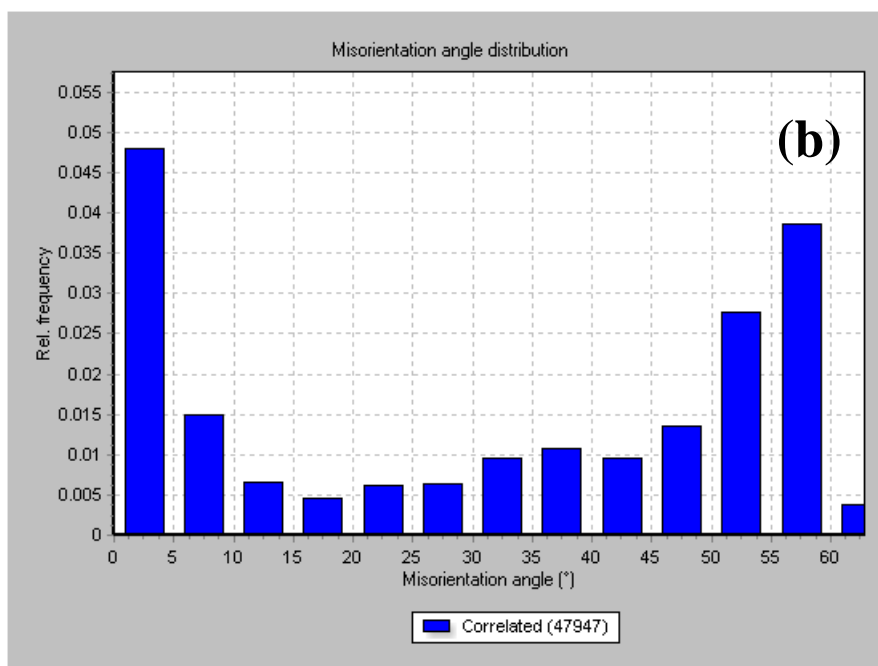
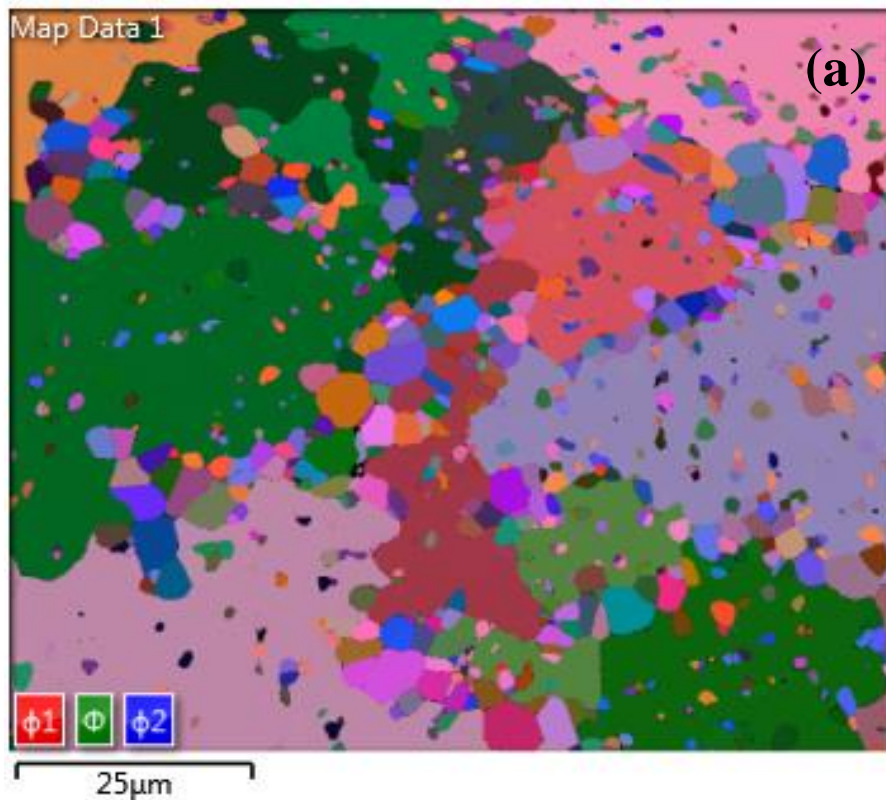


Figure 4.21 (a) Electron backscatter diffraction (EBSD) result of Euler texture map of unetched $\beta\text{-Ni}_3\text{Ge}$ drop-tube particle size 300 – 212 μm ; (b) Histogram of the correlated misorientation angle distribution across grain boundaries for the image shown in (a).

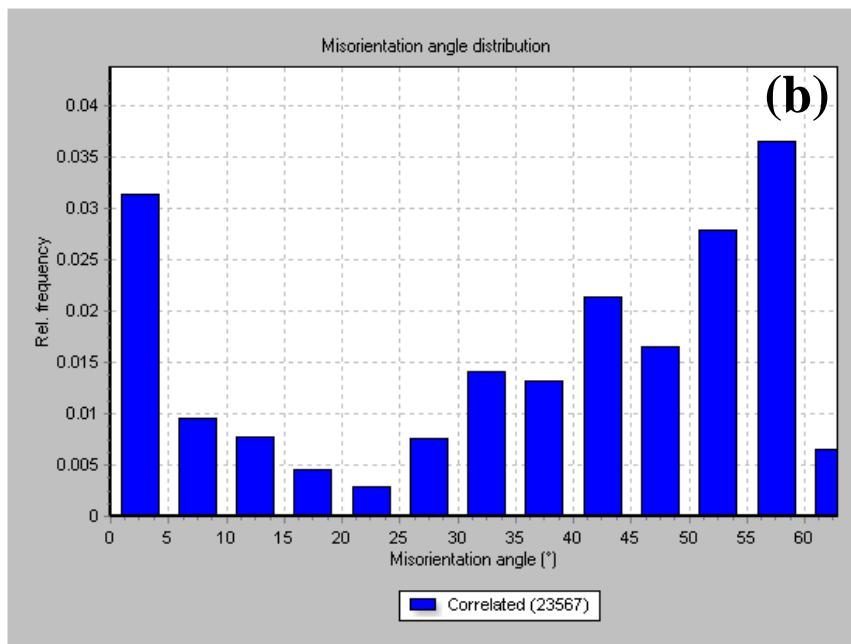
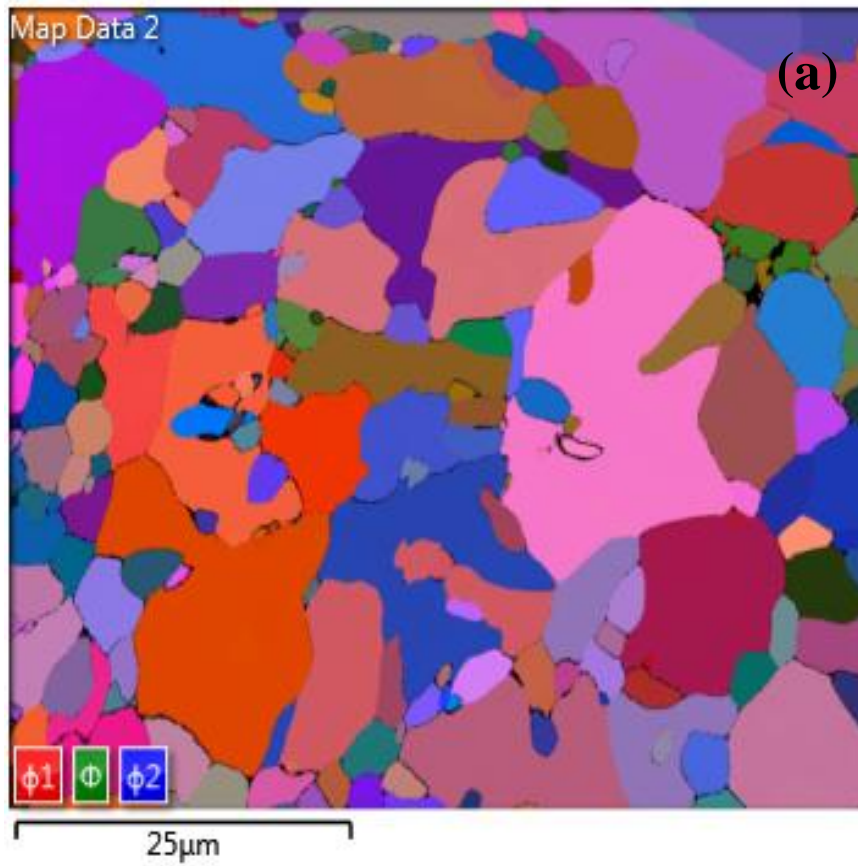


Figure 4.22 (a) Electron backscatter diffraction (EBSD) result of Euler texture map of unetched β -Ni₃Ge drop-tube particle size 212 – 150 μm ; **(b)** Histogram of the correlated misorientation angle distribution across grain boundaries for the image shown in **(a)**.

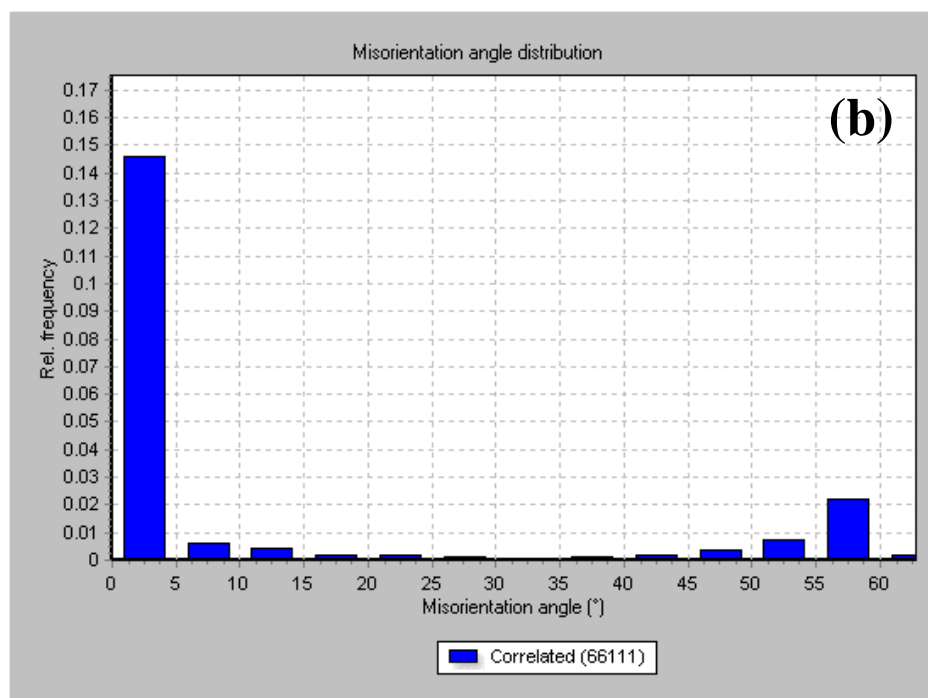
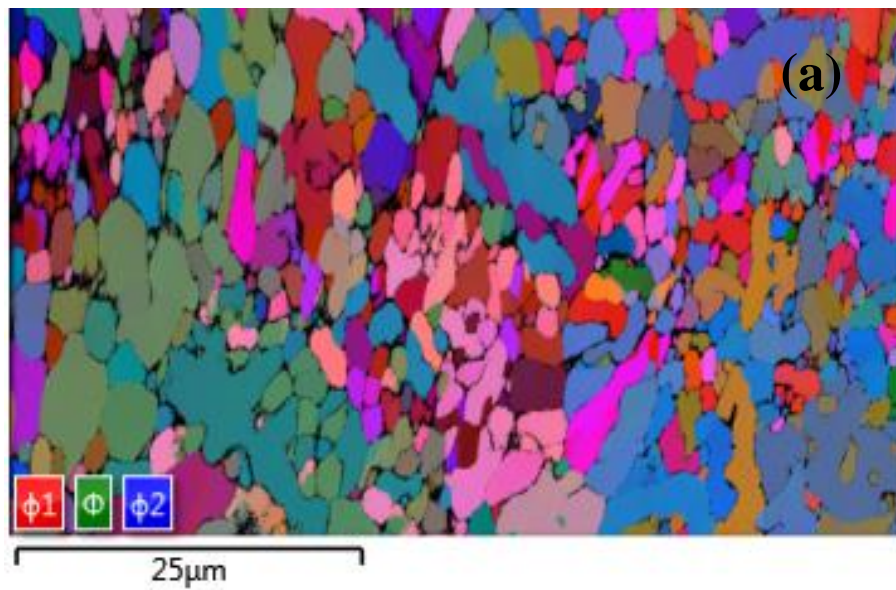


Figure 4.23 (a) Electron backscatter diffraction (EBSD) result of Euler texture map of unetched β -Ni₃Ge drop-tube particle size 150 – 106 μ m; (b) Histogram of the correlated misorientation angle distribution across grain boundaries for the image shown in (a).

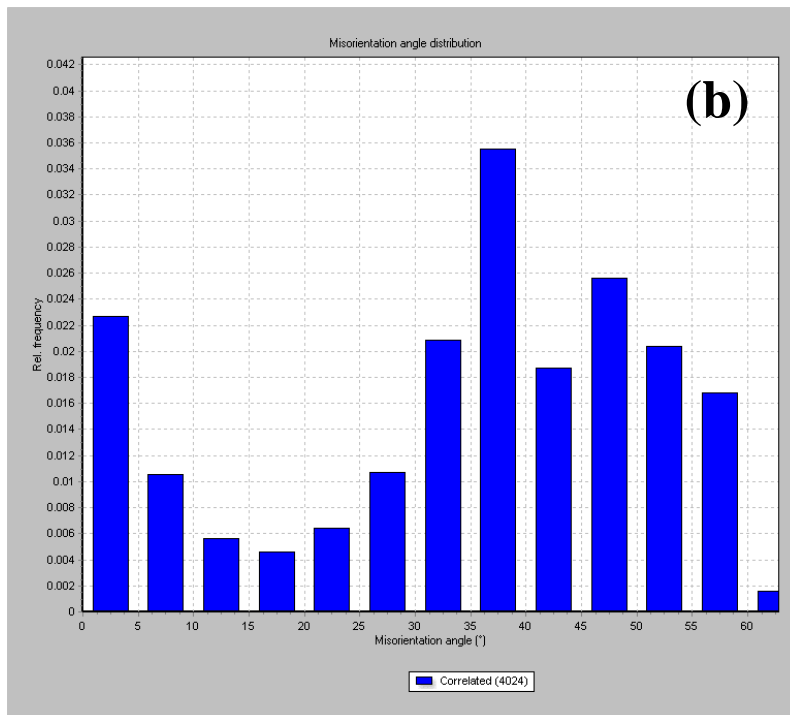
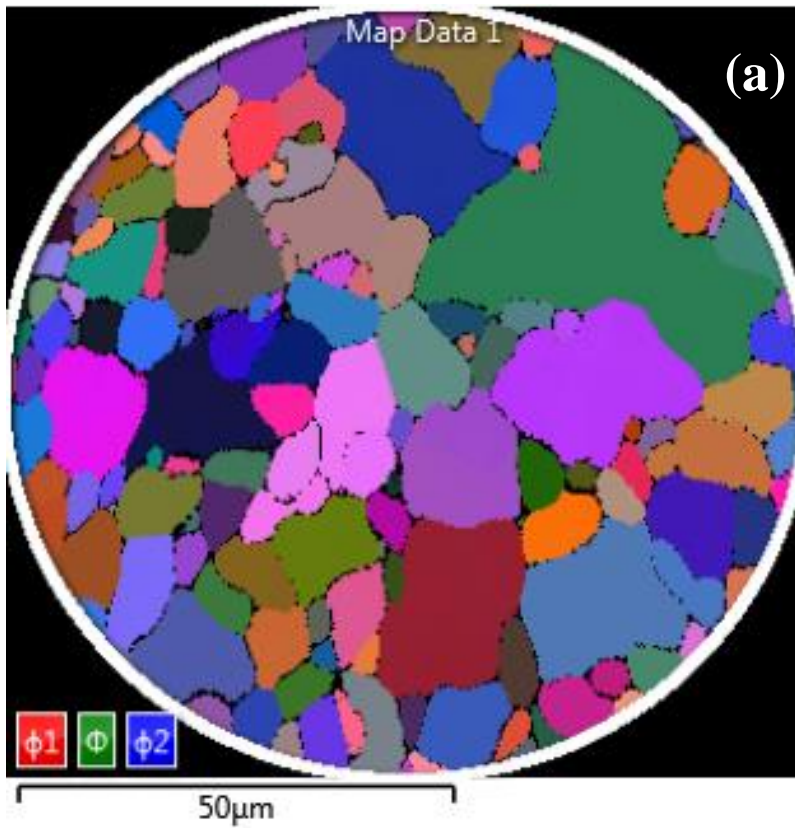


Figure 4.24 (a) Electron backscatter diffraction (EBSD) result of Euler texture map of unetched $\beta\text{-Ni}_3\text{Ge}$ drop-tube particle size 106 – 75 μm ; (b) Histogram of the correlated misorientation angle distribution across grain boundaries for the image shown in (a).

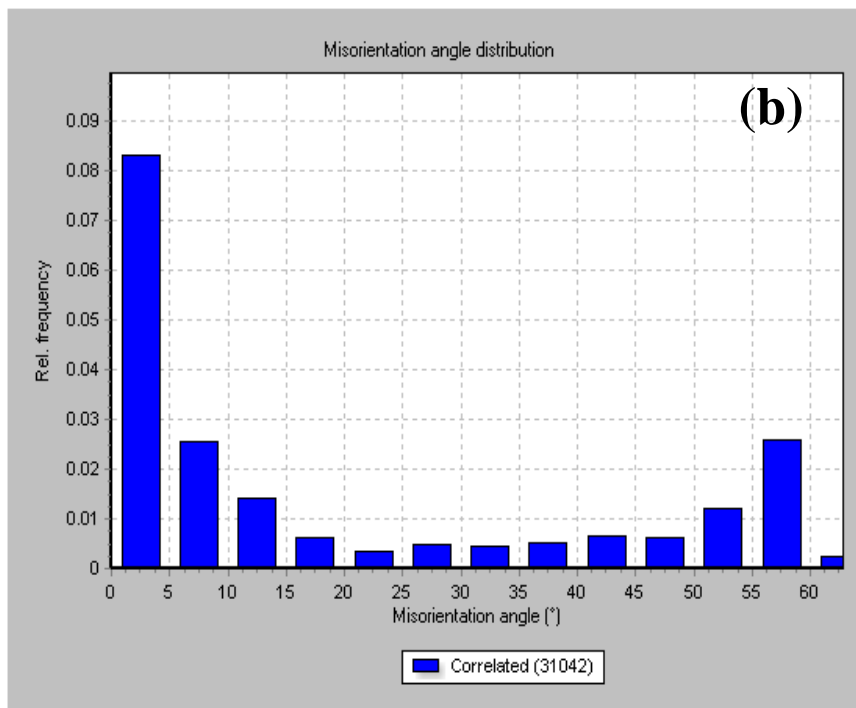
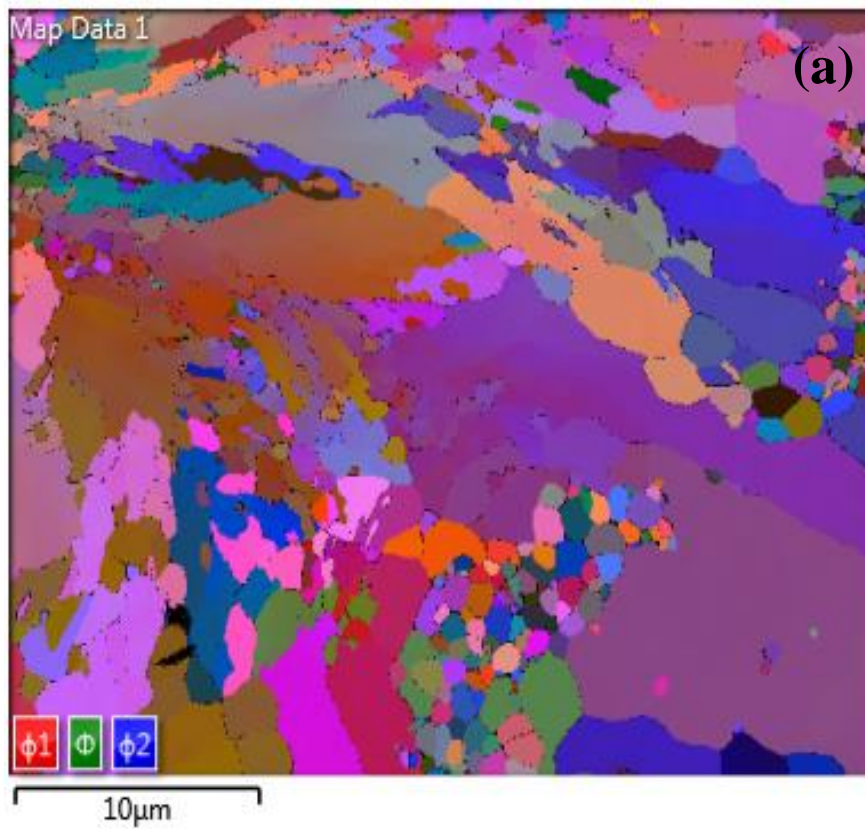


Figure 4.25 (a) Electron backscatter diffraction (EBSD) result of Euler texture map of unetched $\beta\text{-Ni}_3\text{Ge}$ drop-tube particle size 75 – 53 μm ; (b) Histogram of the correlated misorientation angle distribution across grain boundaries for the image shown in (a).

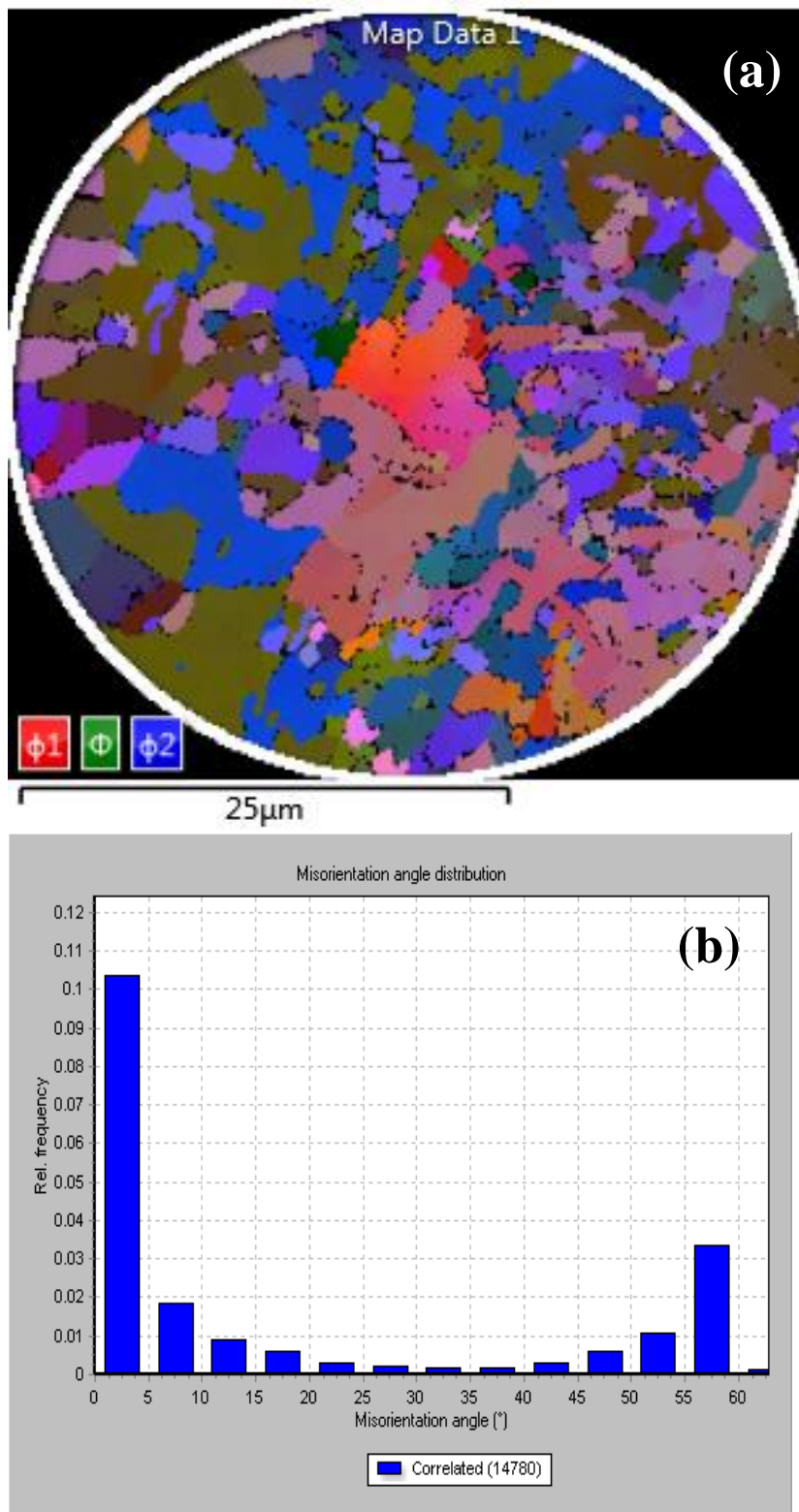


Figure 4.26 (a) Electron backscatter diffraction (EBSD) result of Euler texture map of unetched $\beta\text{-Ni}_3\text{Ge}$ drop-tube particle size 53 – 38 μm ; (b) Histogram of the correlated misorientation angle distribution across grain boundaries for the image shown in (a).

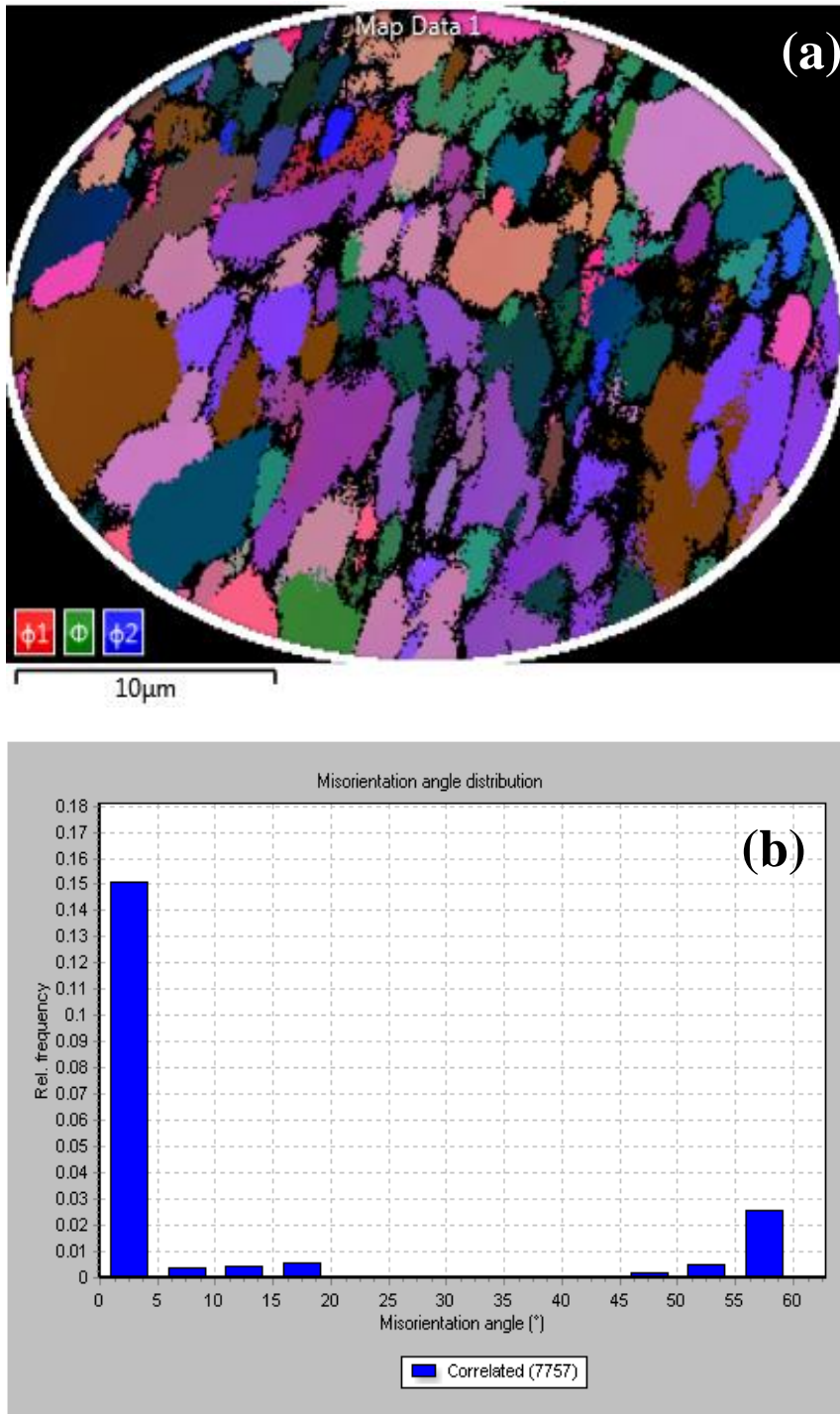


Figure 4.27 (a) Electron backscatter diffraction (EBSD) result of Euler texture map of unetched β -Ni₃Ge drop-tube particle size $\leq 38 \mu\text{m}$; (b) Histogram of the correlated misorientation angle distribution across grain boundaries for the image shown in (a).

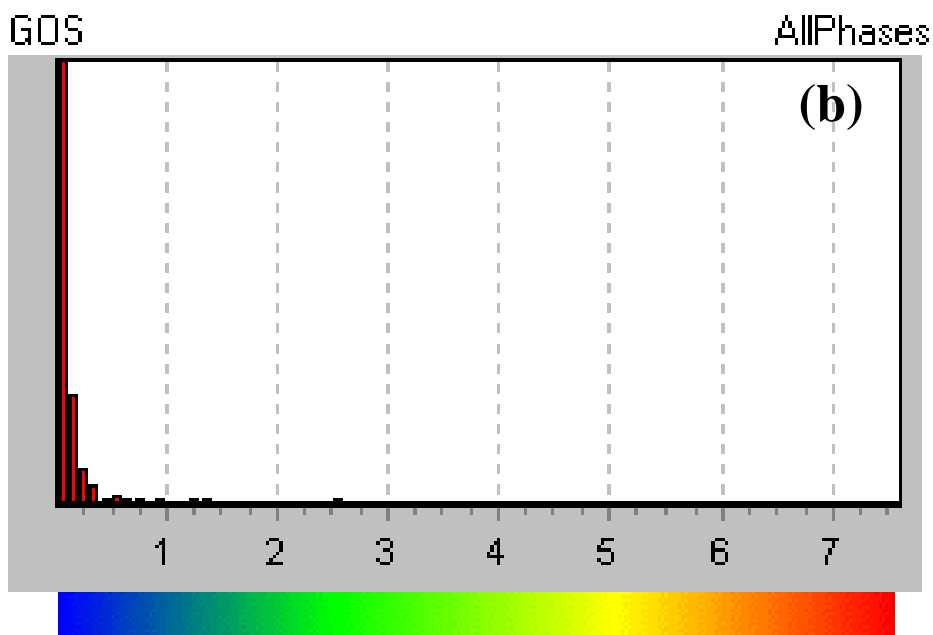
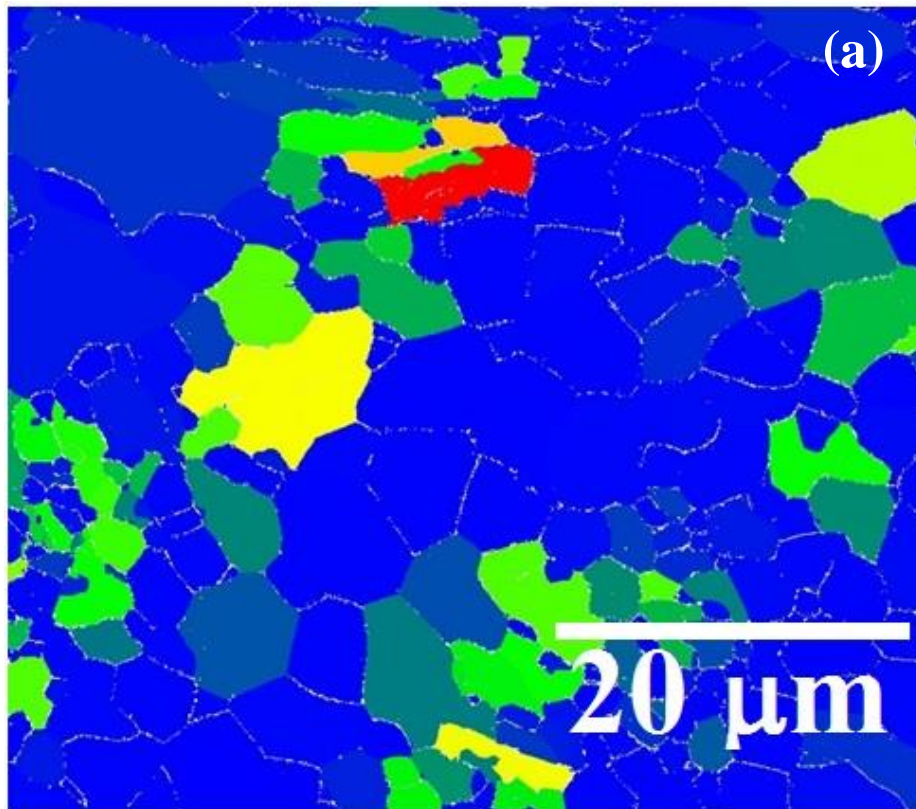


Figure 4.28 (a) shows EBSD results of grain orientation spread (GOS) map of unetched β -Ni₃Ge drop-tube particle size $\geq 850 \mu\text{m}$. Grains are outlined with white boundaries and were constructed presuming a 5 deg tolerance angle (success rate of indexing is 99.5 pct) ; (b) Histograms for the image shown in (a), where colour indicates the range of orientation angle.

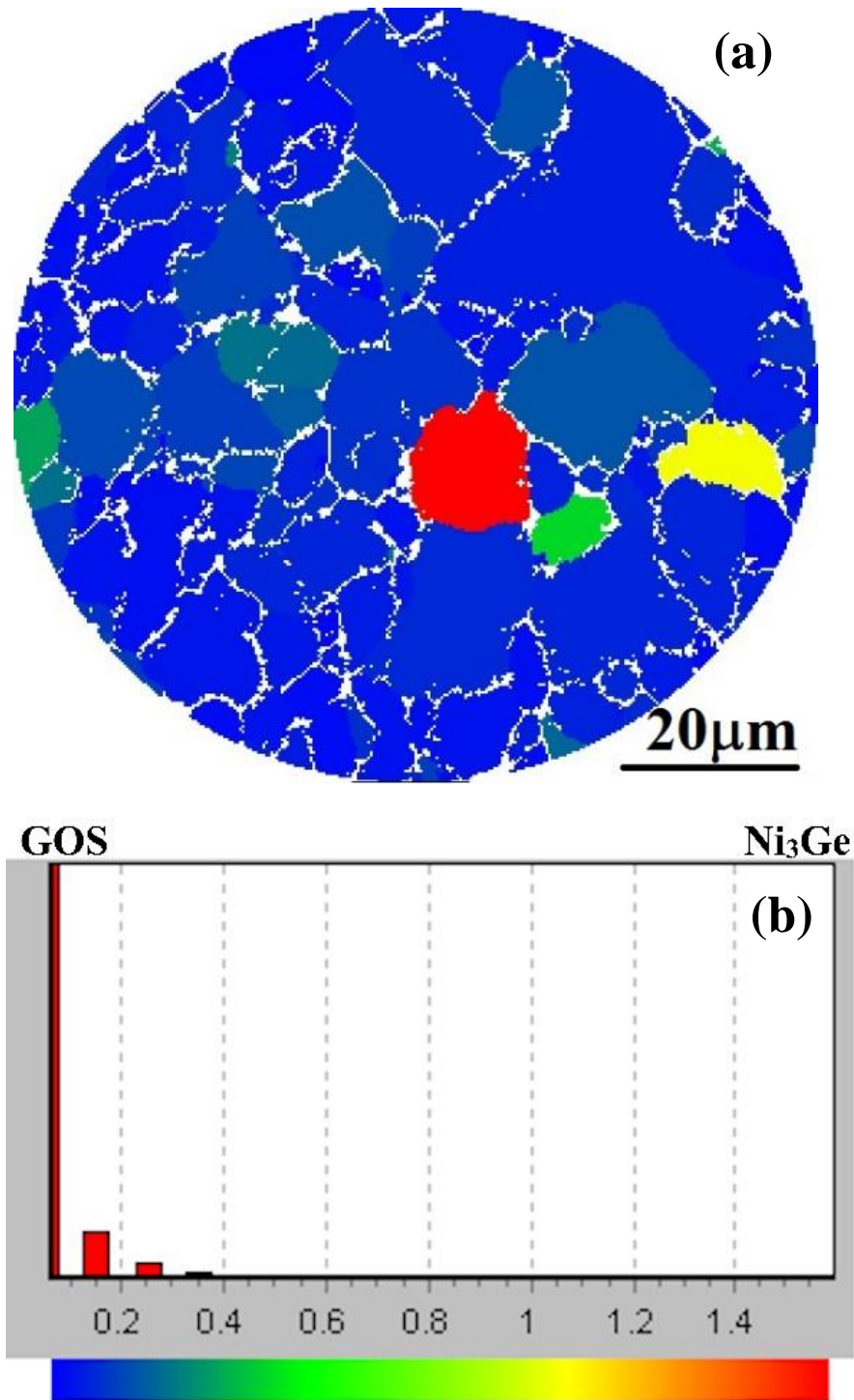


Figure 4.29 (a) shows EBSD results of grain orientation spread (GOS) map of unetched β -Ni₃Ge drop-tube particle size 106 – 75 μm . Grains are outlined with white boundaries and were constructed presuming a 5 deg tolerance angle (success rate of indexing is 99.5 pct) ; (b) Histograms for the image shown in (a), where colour indicates the range of orientation angle.

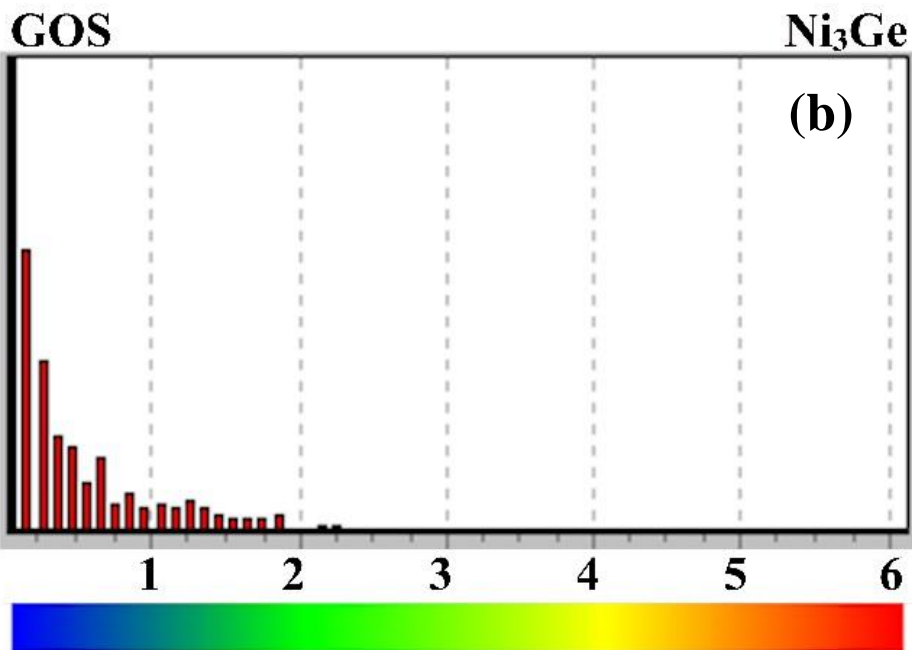
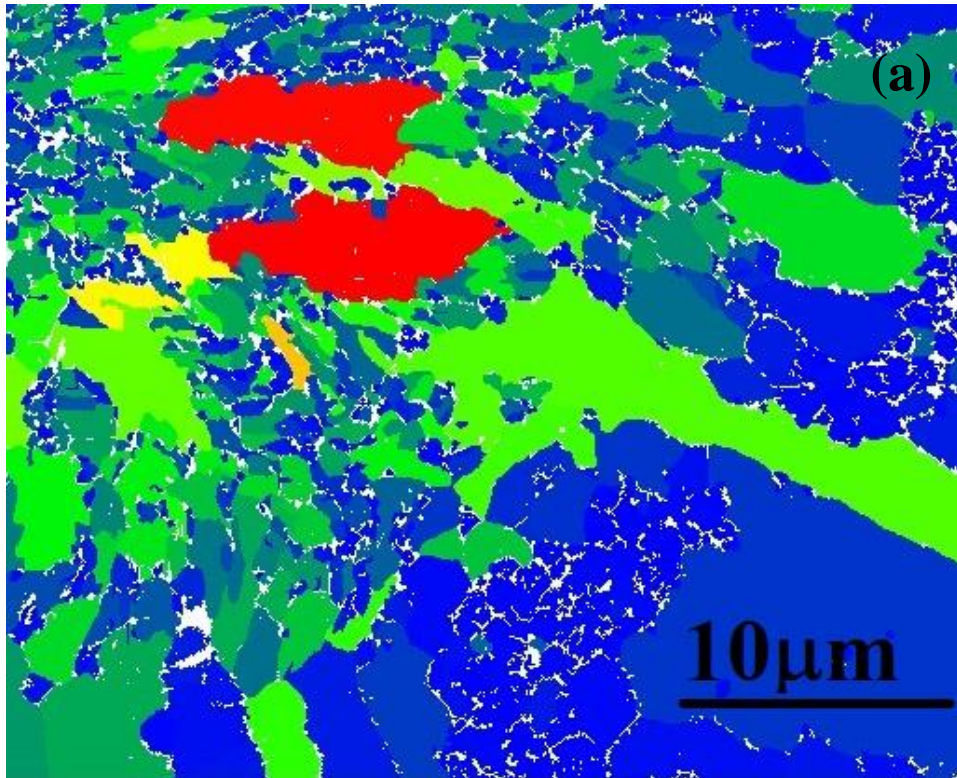


Figure 4.30 (a) shows EBSD results of grain orientation spread (GOS) map of unetched β - Ni_3Ge drop-tube particle size $75 - 53 \mu\text{m}$. Grains are outlined with white boundaries and were constructed presuming a 5 deg tolerance angle (success rate of indexing is 99.5 pct) ; (b) Histograms for the image shown in (a), where colour indicates the range of orientation angle.

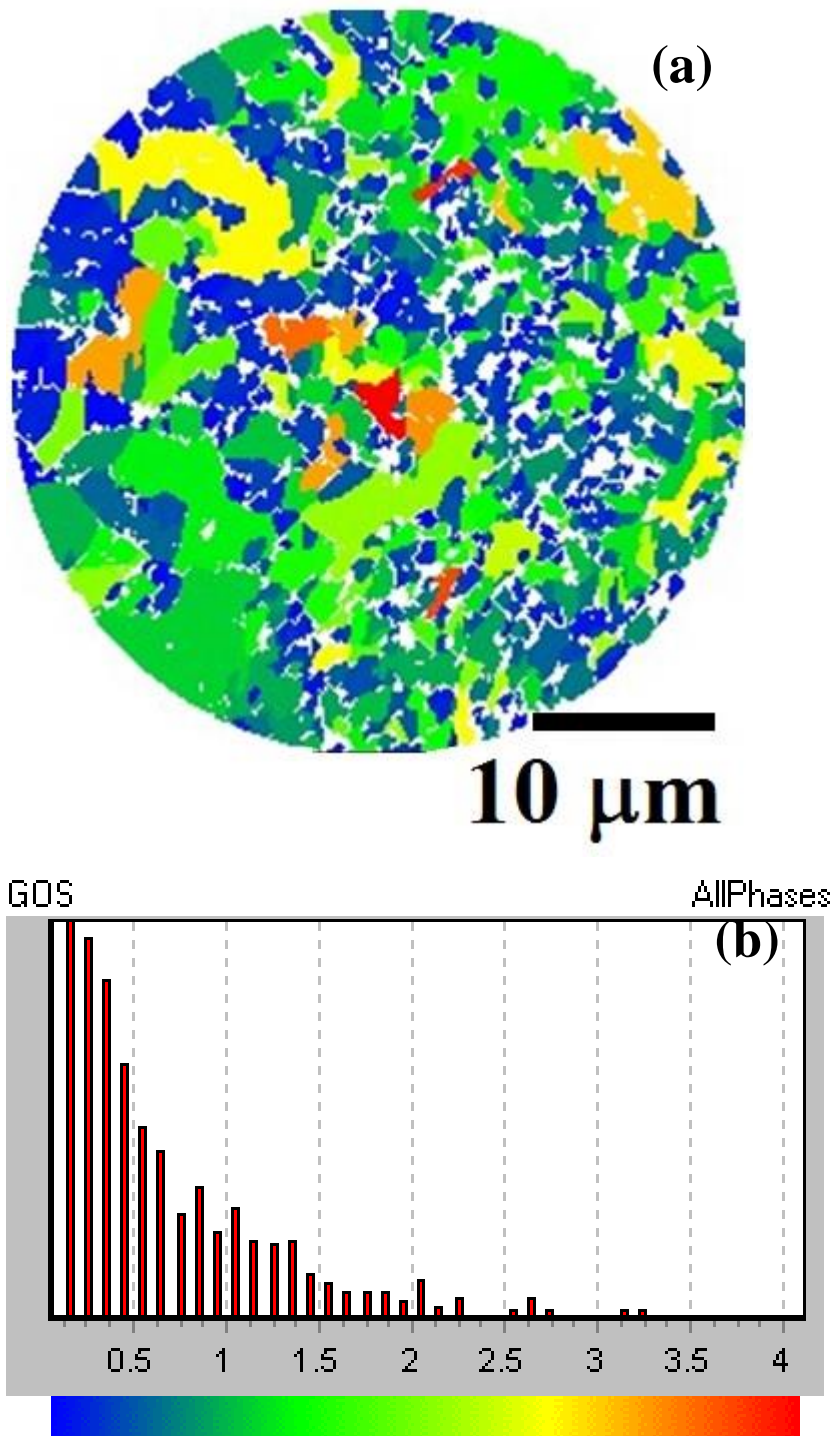


Figure 4.31 (a) shows EBSD results of grain orientation spread (GOS) map of unetched β -Ni₃Ge drop-tube particle size 53 – 38 μ m. Grains are outlined with white boundaries and were constructed presuming a 5 deg tolerance angle (success rate of indexing is 99.5 pct) ; (b) Histograms for the image shown in (a), where colour indicates the range of orientation angle.

4.2.3 TEM Analysis

In order to understand the mechanism giving rise to these five typical structures, spherulites, dendrites (orthogonal), dendrites (non-orthogonal), recrystallised, dendritic seaweed with recrystallised, dendritic seaweed and their matrix phases, transmission electron microscope (TEM) is used to obtain selected area diffraction pattern (SADP) on focus ion beam (FIB) milled sections from the polished - etched and mounted samples. **Figure 4.32** to **Figure 4.35** shows a TEM bright field image of a FIB section through a spherulite and some of the immediately surrounding matrix material.

Many coarse and fine filament like crystallites radiating out from the centre of the spherulite are evident. Selected area diffraction patterns obtained from the **Figure 4.32** to **Figure 4.35**, specifically two regions, labelled (i) taken from the spherulites structure, and (ii) taken from the matrix materials well away from the spherulites. Interestingly, the SADP of all four figures of spherulites microstructures was same within above mentioned two regions (i and ii), where, superlattice spots are clearly evident with the diffraction pattern, which indicates that the material display at least partial chemical ordering within the spherulites (i). The same is also true with featureless matrix material throughout all the same region (ii) at the **Figure 4.32** to **Figure 4.35**. Therefore, here presented only one set of SADP results which obtained from **Figure 4.35**, and an example of this SADP are shown in the **Figure 4.36 (a and b)**, where, the superlattice spots in **Figure 4.36 b** appear better developed than in **Figure 4.36 a**. Which indicates that the spherulite structure **Figure 4.35 (i)** is the partial ordered structure while, featureless matrix **Figure 4.35 (ii)** are completely ordered structure.

In order to understand the morphology of spherulite, further analysis were carried out by TEM to obtain more selected area diffraction pattern (SADP) within the spherulite structure. **Figure 4.37a** shows typical bright-field TEM images of such isolated spherulite structure. **Figures 4.37 (b-d)** show three selected area diffraction patterns obtained from the microstructure shown in **Figure 4.37a**, first SADP obtained from the initial core of the spherulites at the region (i), second SADP obtained from the spherulites structure at the region (ii) and third SADP obtained from the featureless matrix well away from the spherulite at the region (iii). **Figure 4.37b** illustrates that

the spherulite core is disordered (no superlattice spots), **Figure 4.37c** demonstrate that the outer spherulite is partially ordered (presence of few superlattice spots) and **Figure 4.37d** indicate that the material is fully ordered (superlattice spots) in the matrix material. It looks like ordering progressively increases as we move away from the spherulite core. In order to get detail of the spherulite structures, TEM dark-field images obtained from the each of the sieve fractions between $\geq 850 \mu\text{m}$ to $300 - 212 \mu\text{m}$, as shown in **Figure 4.38 (a-d)**. These images were obtained from one of the superlattice spots within the selected area diffraction pattern and as a consequence of this only the chemically ordered material was illuminated. In all cases the spherulites appear to be composed of lamellae of ordered material separated by inter-lamella material of the disordered phase.

Figure 4.39. shows the measured lamellar size ($d/\mu\text{m}$) of spherulites from $\geq 850 \mu\text{m}$ to $300 - 212 \mu\text{m}$ samples as a function of drop-tube cooling rate (K s^{-1}). It can be seen that the average lamellar size are decreasing from $0.45 \mu\text{m}$ to $0.11 \mu\text{m}$ at a cooling rate 700 K s^{-1} and 4600 K s^{-1} respectively. The very large error bar corresponding to the measurement for the $\geq 850 \mu\text{m}$ sieve fraction is indicative of the seemingly non-constant lamellar widths observed in this sample, which can be clearly seen in **Figure 4.38a**. Notwithstanding this, there is a clear trend for the lamellar width to decrease with decreasing particle size (increasing cooling rate) are noticeable in the **Figure 4.39**.

Figure 4.40a shows typical bright-field TEM images of dendritic structure (orthogonal). **Figures 4.40 (b and c)** show two selected area diffraction patterns obtained from the microstructure shown in **Figure 4.40a**, first SADP obtained from the dendritic region (i) and second SADP obtained from the matrix materials well away from the dendrites (ii). The spherulite region appeared partially ordered (superlattice), while SADP of dendrites region shows absence of superlattice (chemically disordered structure) as shown in **Figure 4.40b**. However, the featureless matrix still consistent with the superlattice (chemically ordered structure) as shown in **Figure 4.40c**.

Also, a TEM SADP obtained from the dendritic structure (non-orthogonal dendrites), **Figure 4.41a** shows typical TEM bright-field of dendritic structure (non-orthogonal) and SADP obtained from the dendritic region (circle) as shown in **Figure 4.41b**. The SADP of dendritic region (non-orthogonal) is same as SADP of dendritic region

(orthogonal) with respect to absence of superlattice (chemically disordered structure). However, the arrangement of crystal lattice non-orthogonal dendrites is different than orthogonal dendrites, which is shown in **Figure 4.41b**. The all angles of α , β and γ are same ($a = b = c$) in non-orthogonal dendrites system, while in orthogonal dendrites system only two angles are same ($a = b \neq c$).

Figure 4.42 a shows a TEM bright field image with regards to understand unusual ‘crack-like’ morphology (recrystallisation), which were observed in the drop-tube sieve size fraction 75 – 53 μm , a selected area diffraction pattern (**Figure 4.42b**) is taken from the large blocky area between the ‘cracks’, which are shown by a circle at **Figure 4.42a**. It indicates that the large blocky areas between the ‘cracks’ are indeed of the $L1_2$ ordered structure. This is evident from the super-lattice spots visible in **Figure 4.42b**. For the further analysis with respects to understand morphology of this microstructure, a high resolution TEM image of the structure of one of these blocky regions is obtained, which shown in **Figure 4.43a** bright-field image, with the corresponding dark-field image shown in **Figure 4.43b**. The region that appears bright white in **Figure 4.43a** and black in **Figure 4.43b** actually contains some material. i.e. we are not just looking at a hole where the material is completely etched away. The dark-field image was obtained from the super-lattice spot indicated by the arrow in **Figure 4.42b** and therefore shows ordered material as light.

Further reduction in drop-tube sample sieve size to 53 – 38 μm , another microstructure, ‘dendritic seaweed’ are observed. For understanding morphology of this seaweed structure, a TEM SADP (**Figure 4.44b**) was obtained from the region of dendritic seaweed, which is indicated by a circle at **Figure 4.44a**. The diffraction pattern of dendritic seaweed is entirely different crystal system. As within the same size of drop-tube sample (53 – 38 μm) crack-like (recrystallised structure) also observed with dendritic seaweed, pure dendritic structure and featureless matrix, which can be seen in the **Figure 4.45a**. Therefore, SADP (**Figure 4.45 b-d**) also obtained from these three main regions, (i) crack-like (recrystallized), (ii) featureless matrix and also from the (iii) seaweed microstructure for understating their morphologies. The diffraction pattern of crack-like features (**Figure 4.45b**) are also same as we observed in **Figure 4.42b** (crack-like region). However, the diffraction pattern of dendritic seaweed (**Figure 4.45d**) is look disordered structure (without the superlattice spots).

Finally, **Figure 4.46a** shows typical bright-field TEM image from the smallest droplet in the $< 38 \mu\text{m}$ sieve size fraction (dendritic seaweed). **Figures 4.46 (b and c)** show two selected area diffraction patterns obtained from the microstructure shown in **Figure 4.46a**, first SADP obtained from the dendritic seaweed at the region (i) and second SADP obtained from featureless matrix at the region (ii). The featureless matrix is still in ordered structure however, SADP of seaweed structure observed disordered structure. In addition to that in TEM SAD analysis sample has been tilted while obtaining diffraction pattern at different location. There is also some bend contrast was observed in TEM analysis, which can be seen by **Figure 4.44 (a)**, implying that the sample was not completely flat. Hence, the orientation of diffraction patterns from different regions should not be treated as comparable.

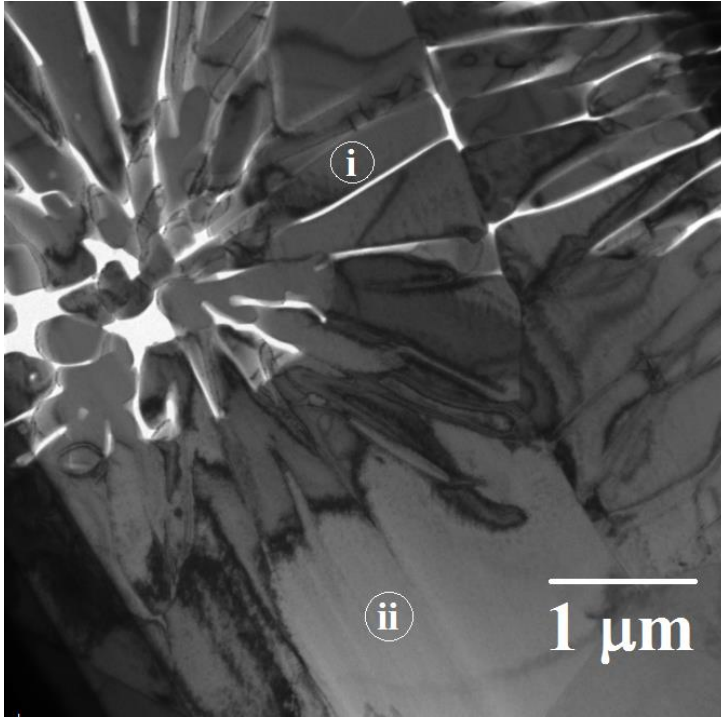


Figure 4.32 TEM bright field image of a spherulite (i) and surrounding matrix material (ii) in a β -Ni₃Ge drop-tube particle $\geq 850 \mu\text{m}$ particle.

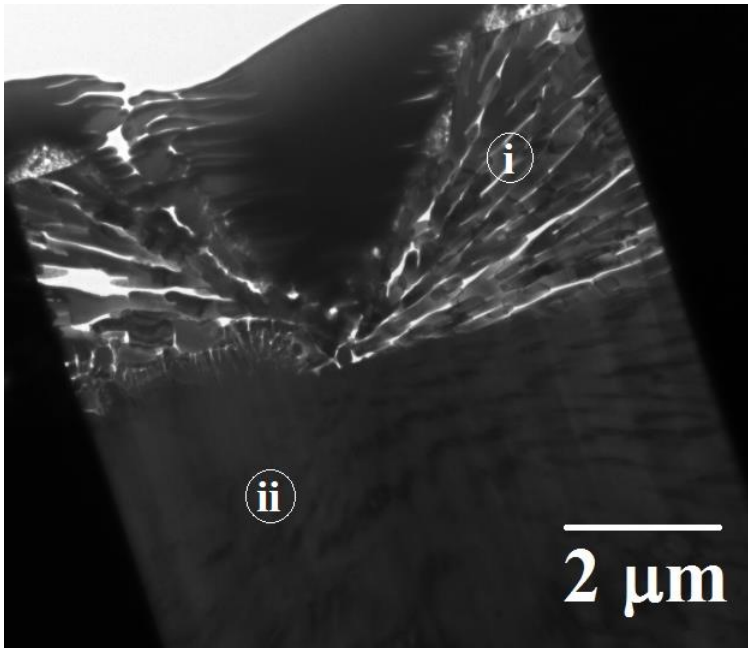


Figure 4.33 TEM bright field image of a spherulite (i) and surrounding matrix material (ii) in a β -Ni₃Ge drop-tube particle $850 - 500 \mu\text{m}$ particle.

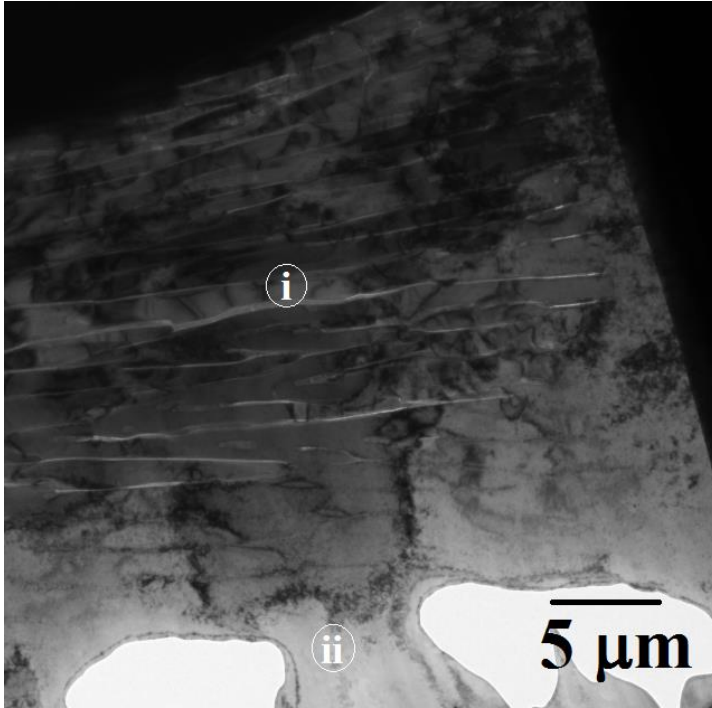


Figure 4.34 TEM bright field image of a spherulite (i) and surrounding matrix material (ii) in a β -Ni₃Ge drop-tube particle 500 – 300 μm particle.

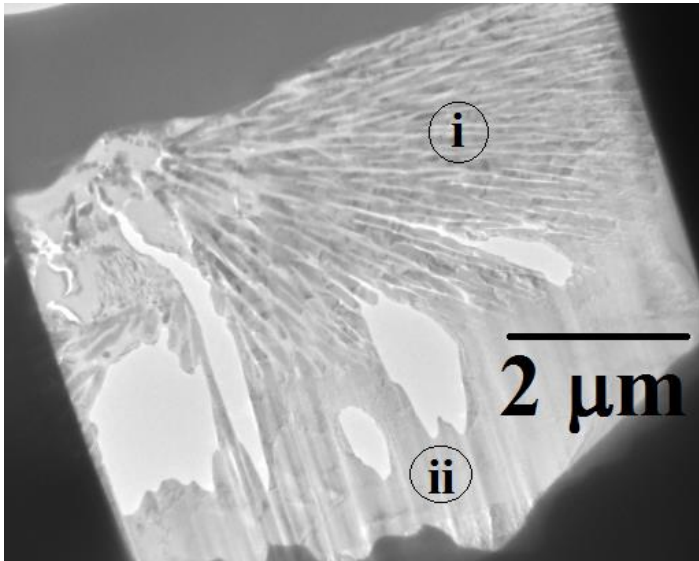


Figure 4.35 TEM bright field image of a spherulite and surrounding matrix material in a β -Ni₃Ge drop-tube particle 300 – 212 μm particle.

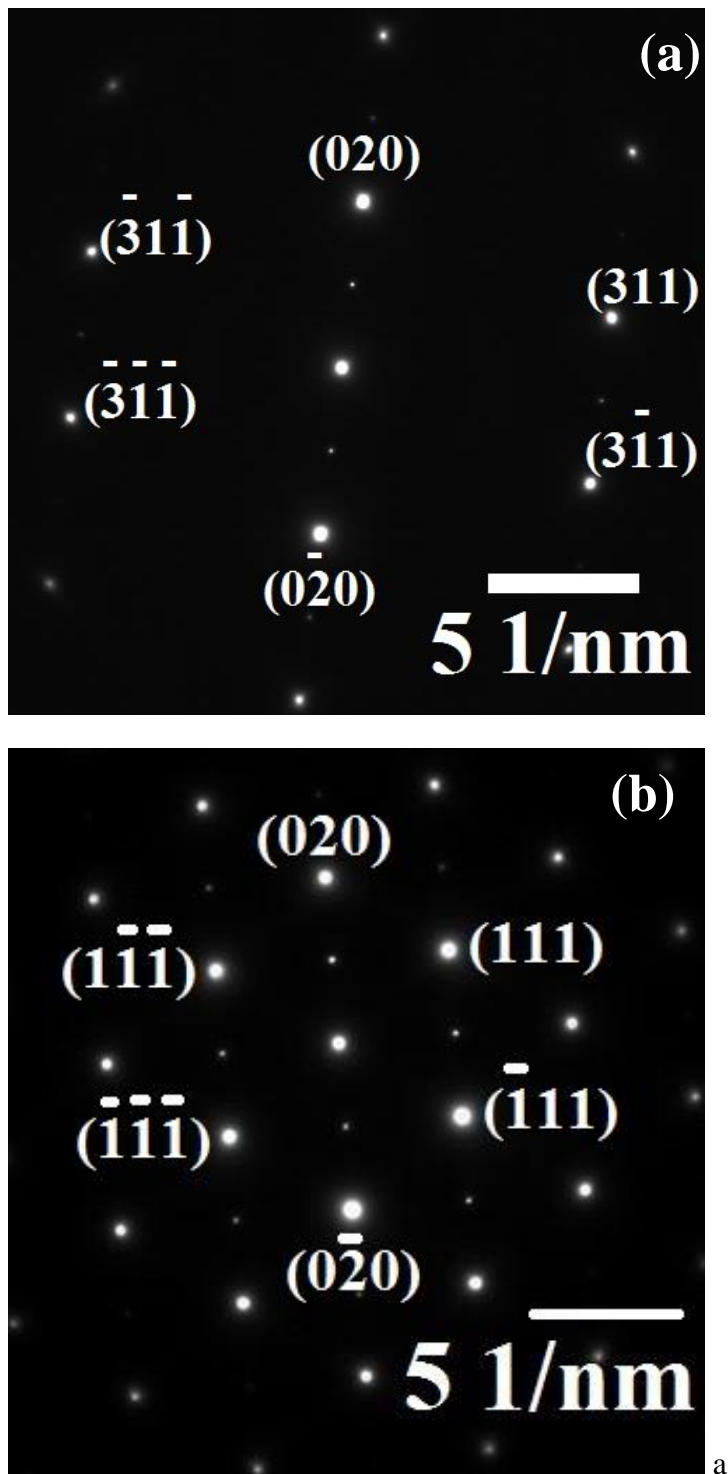


Figure 4.36 (a) Selected area diffraction patterns from **Figure 4.35** at region (i) spherulite, and (b) from the featureless matrix well away from the spherulite at region (ii).

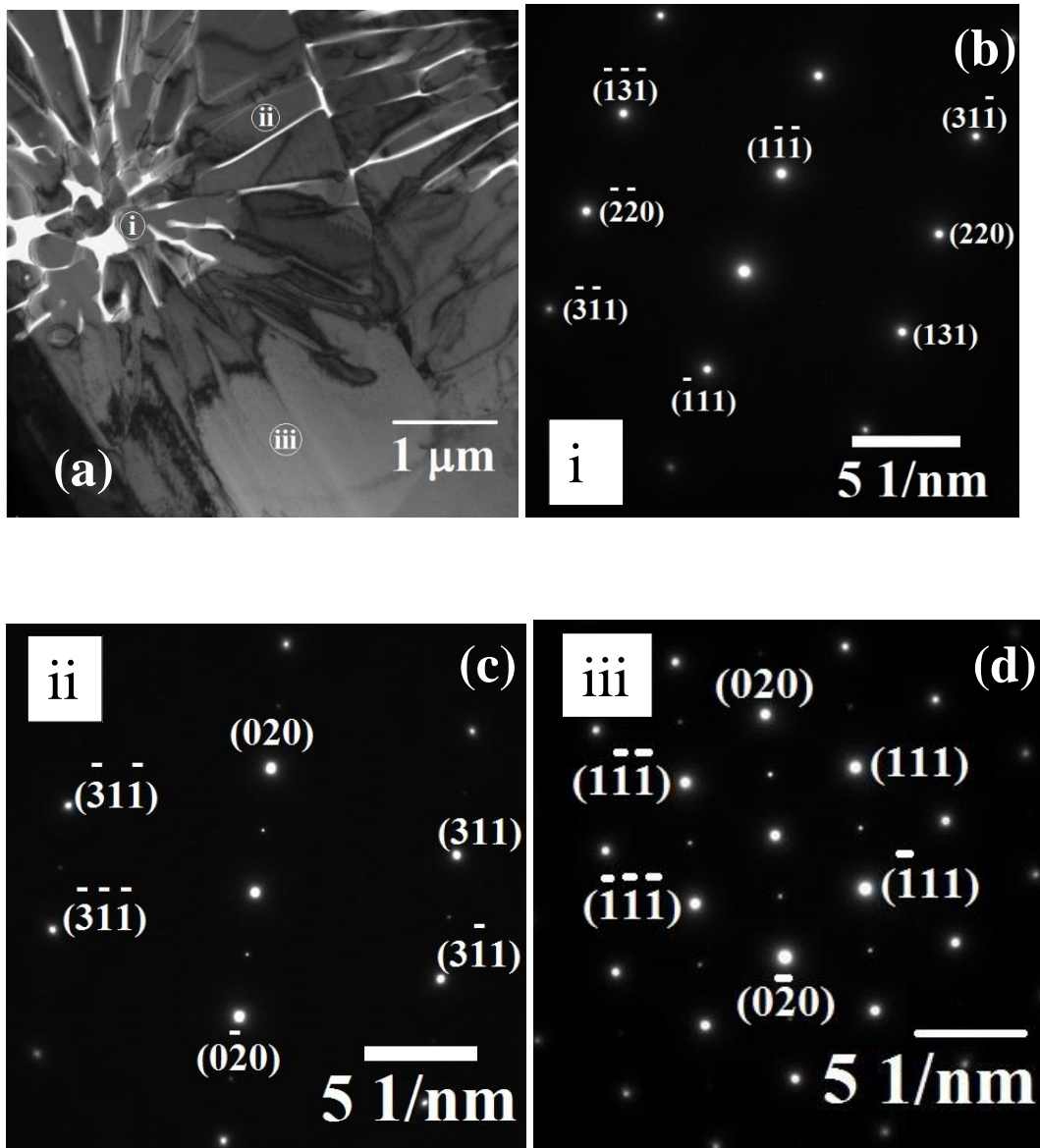


Figure 4.37 (a) TEM bright field image of a spherulite, (b) selected area diffraction patterns obtained from the initial core of the spherulite at region (i), c from the region (ii) - spherulites and (d) from the featureless matrix well away from the spherulite at the region (iii).

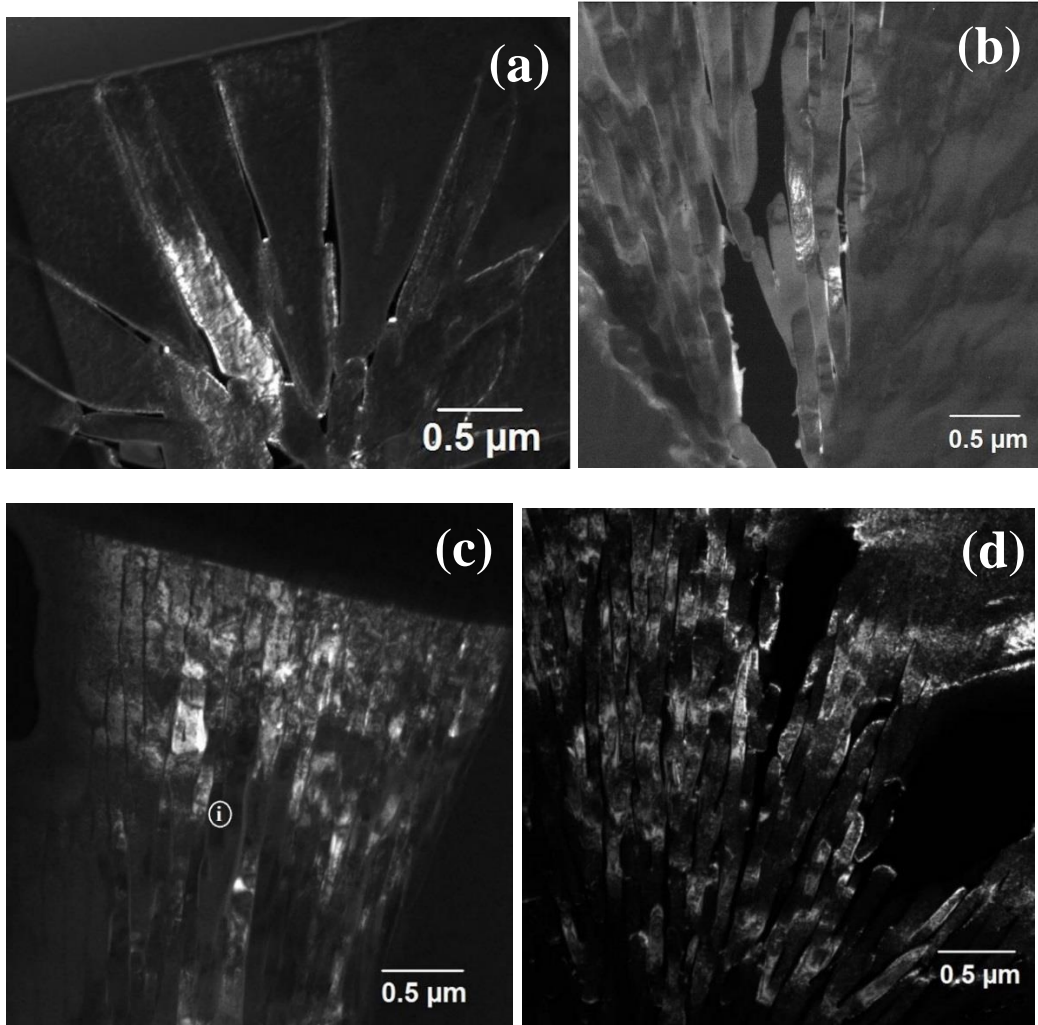


Figure 4.38 TEM dark-field image of HF etched drop-tube processed β -Ni₃Ge droplets obtained from one of the superlattice spots within the diffraction pattern of drop-tube particles (**a**) $\geq 850 \mu\text{m}$ (**b**) $850 - 500 \mu\text{m}$, (**c**) $500 - 300 \mu\text{m}$, and (**d**) $300 - 212 \mu\text{m}$ respectively.

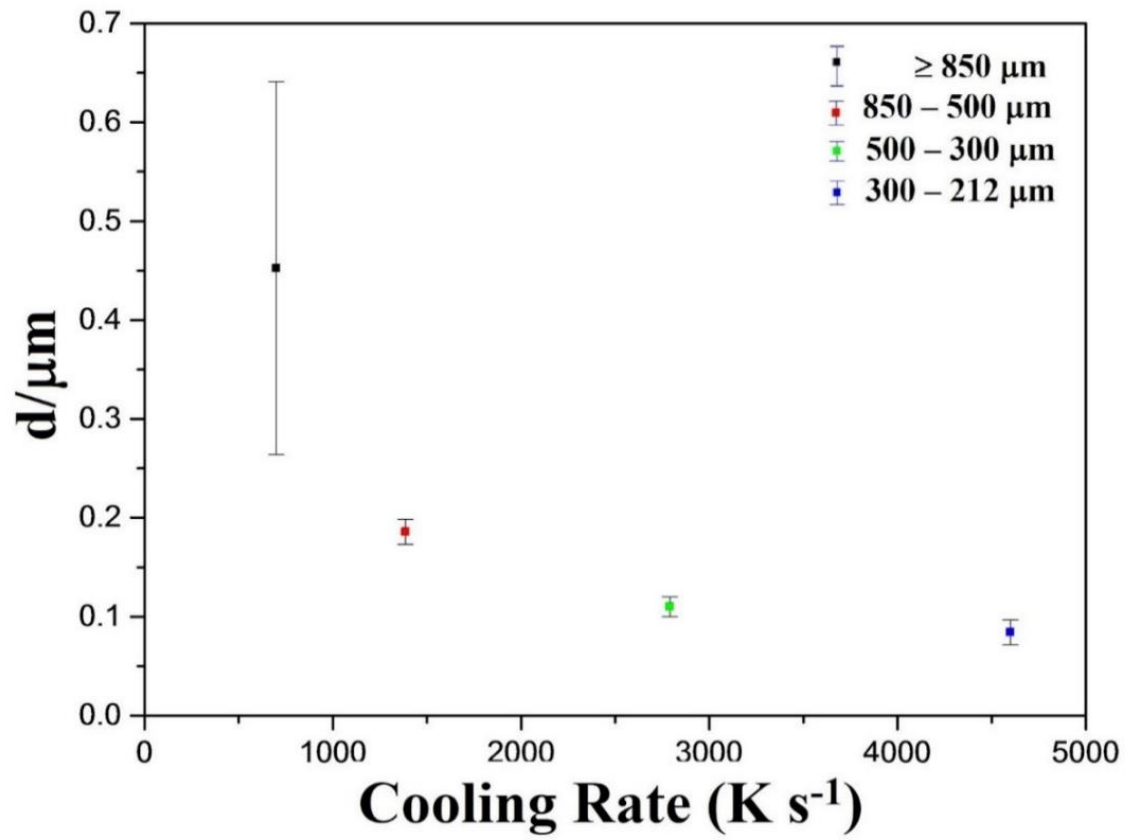


Figure 4.39 Average spherulite lamellar width as a function of cooling rate.

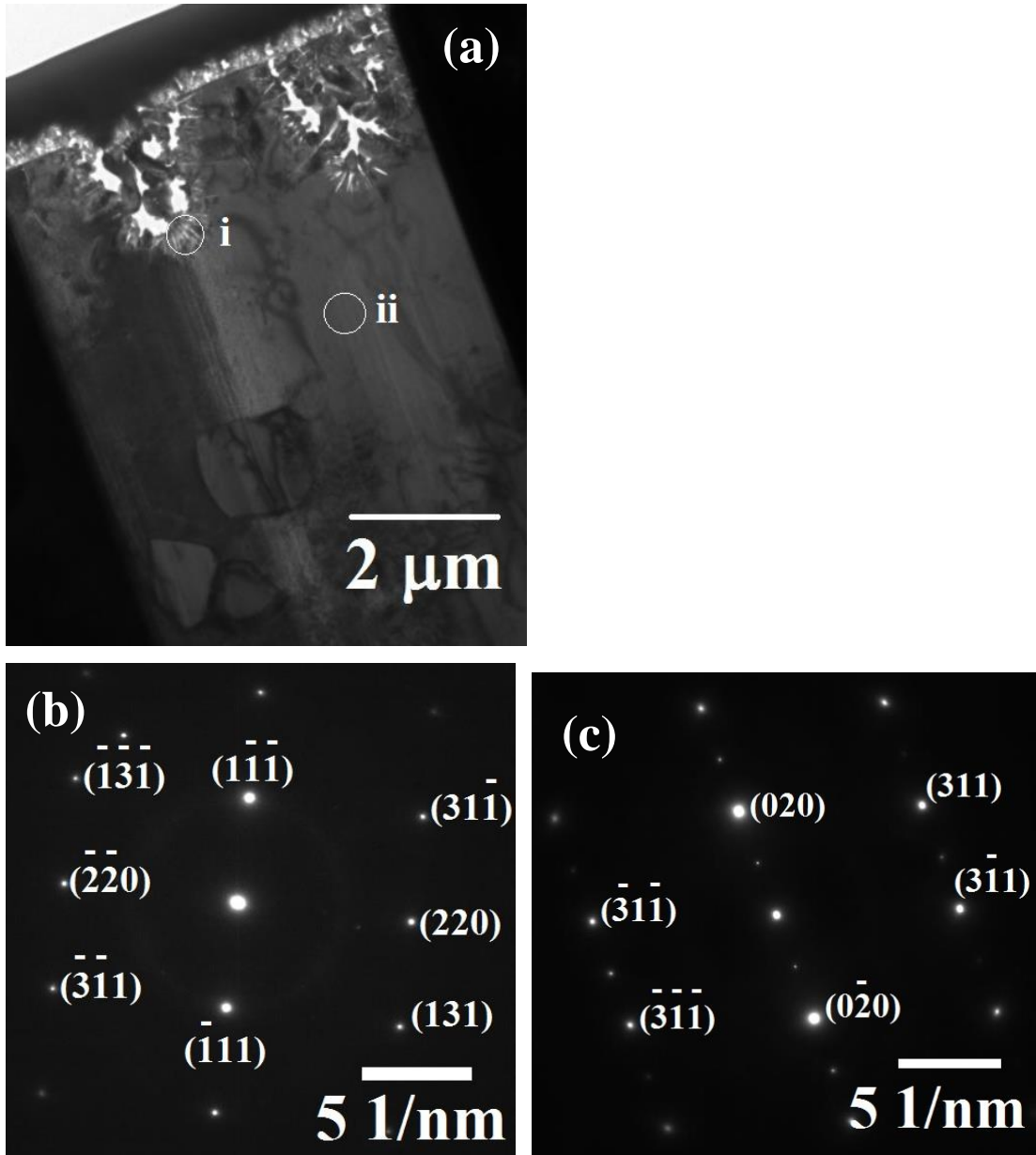


Figure 4.40 (a) TEM bright field image of a dendrite (orthogonal) and surrounding matrix material in a 212 – 150 μm drop-tube sample, (b) selected area diffraction patterns obtained from the region (i) dendrite and (c) from the region (ii) matrix material.

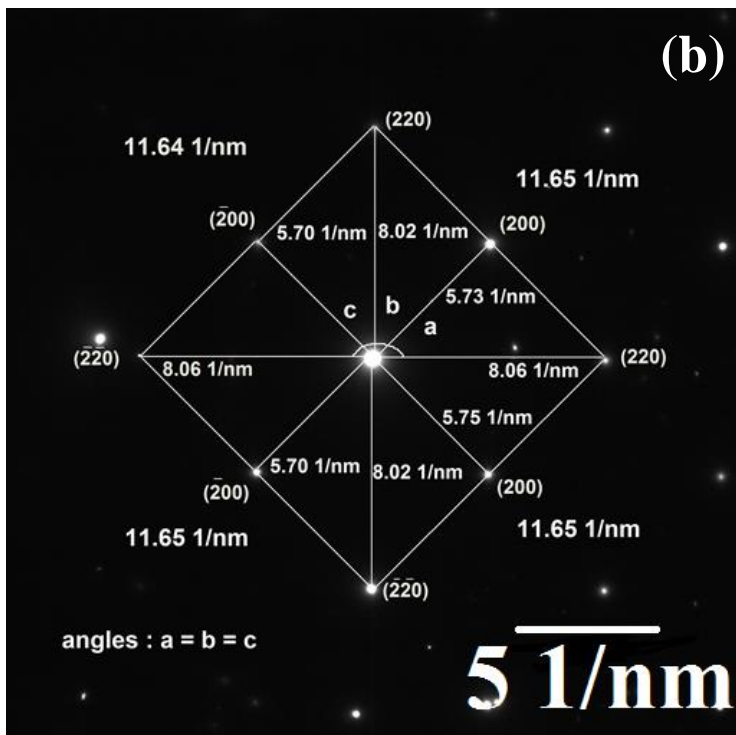
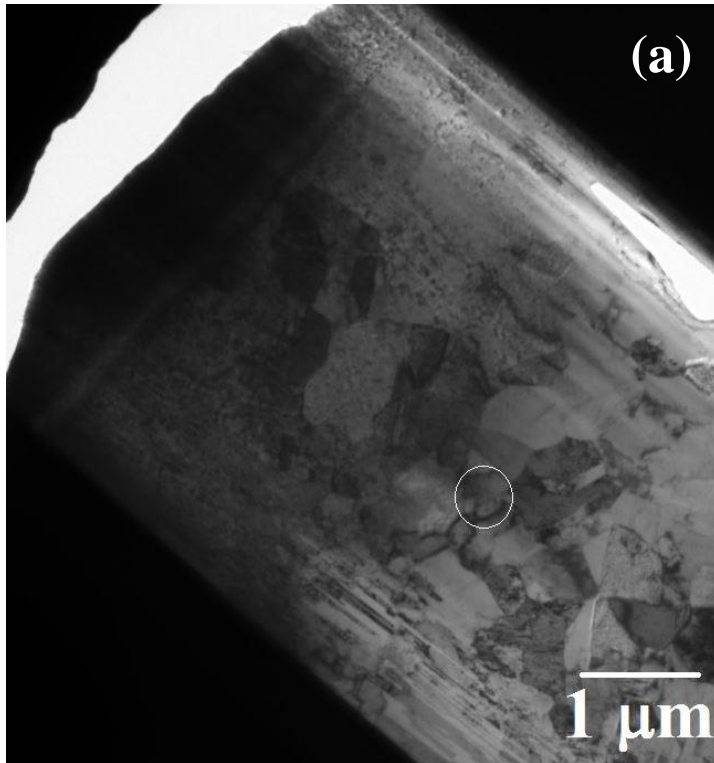


Figure 4.41 (a) TEM bright field image of a dendrite (non-orthogonal) in a 106 – 75 μm drop-tube sample, (b) selected area diffraction patterns obtained from the dendrites (as shown by a circle on **Figure a**).

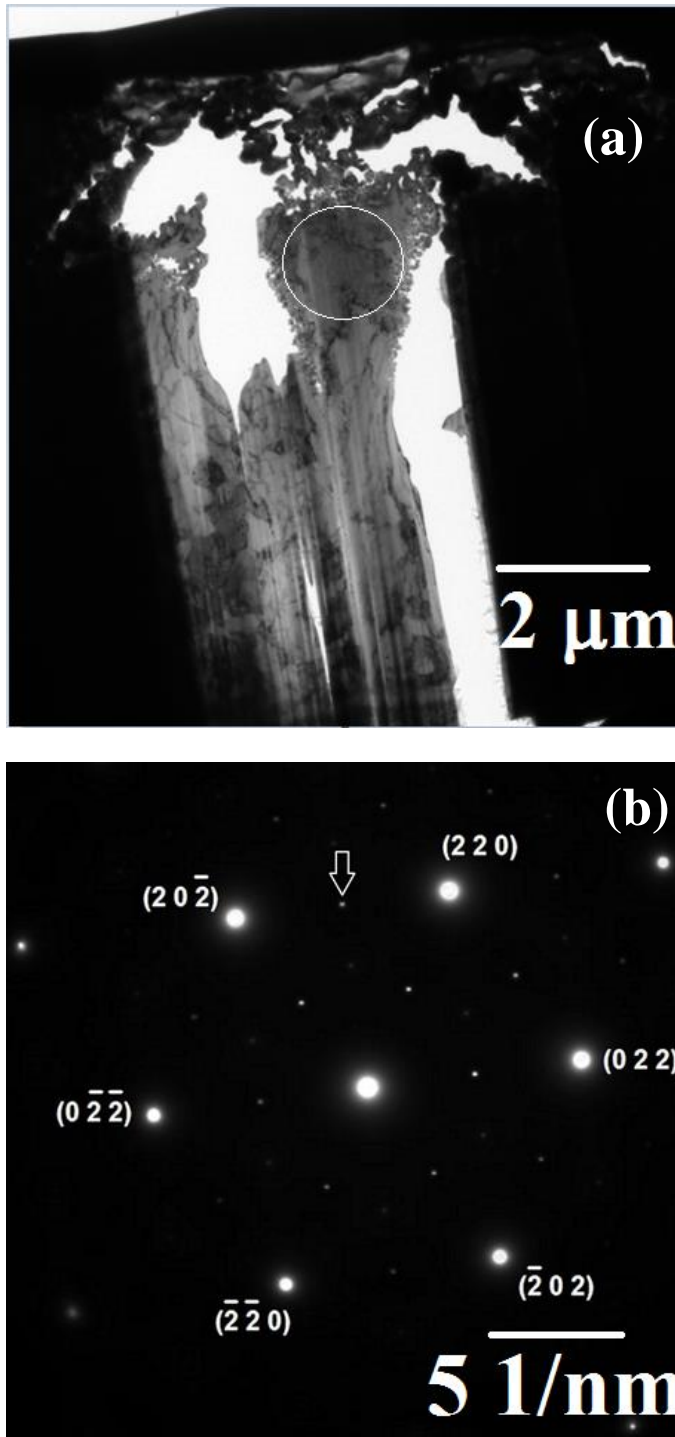


Figure 4.42 (a) TEM bright field image of a recrystallised structure in a 75 – 53 μm drop-tube sample, (b) selected area diffraction patterns obtained from the large blocky areas between the cracks-like features as shown in **Figure (a)**. Arrow shows the specification of the spot from which the dark-field image shown in **Figure 4.43 (b)**.

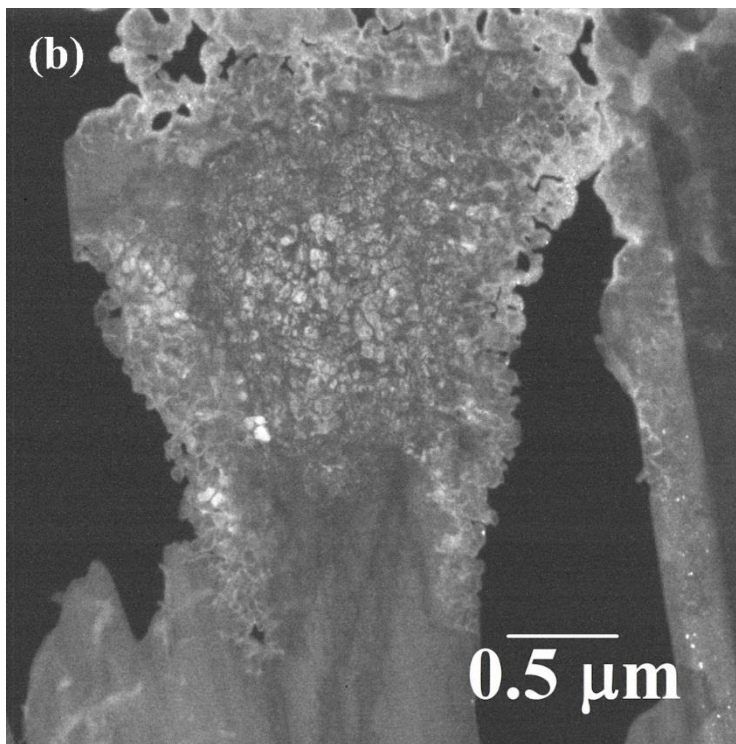
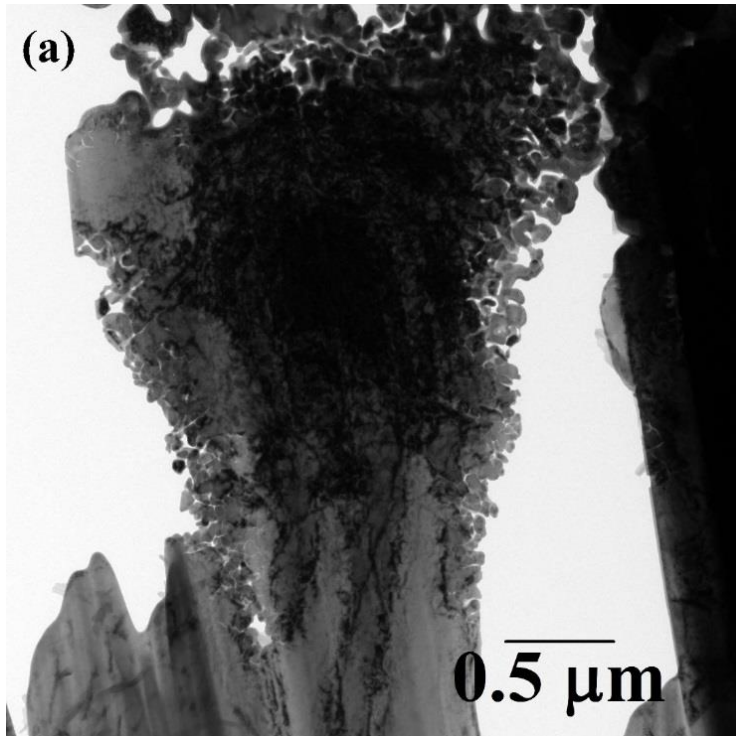


Figure 4.43 (a) : Transmission electron microscope (TEM) bright-field image of the blocky region occurring between the ‘cracks’ in the 75 - 53 μm size fraction and **(b)** TEM dark-field image of same region obtained from one of the super-lattice spots within the diffraction pattern (**Figure 4.42b**).

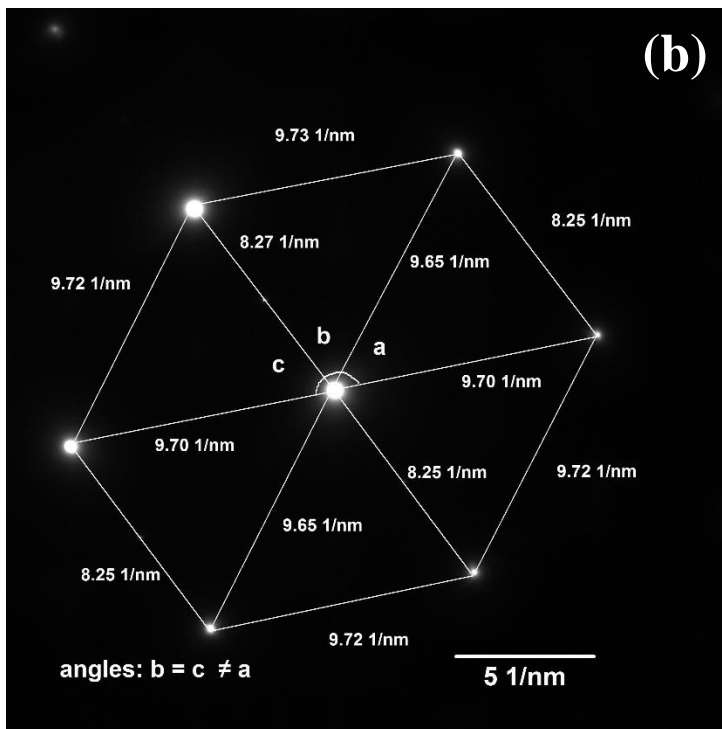
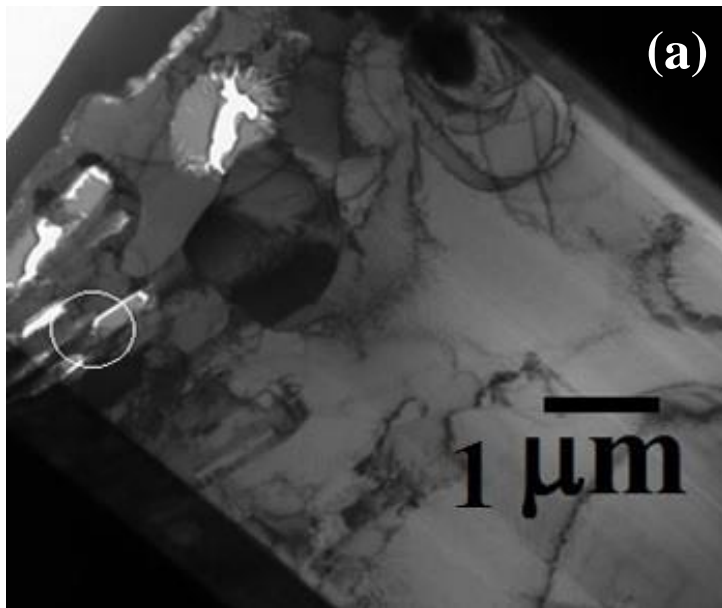


Figure 4.44 (a) TEM bright field image of a dendritic seaweed in a 53 – 38 μm drop-tube sample, (b) selected area diffraction patterns obtained from the region (circle) at dendritic seaweed.

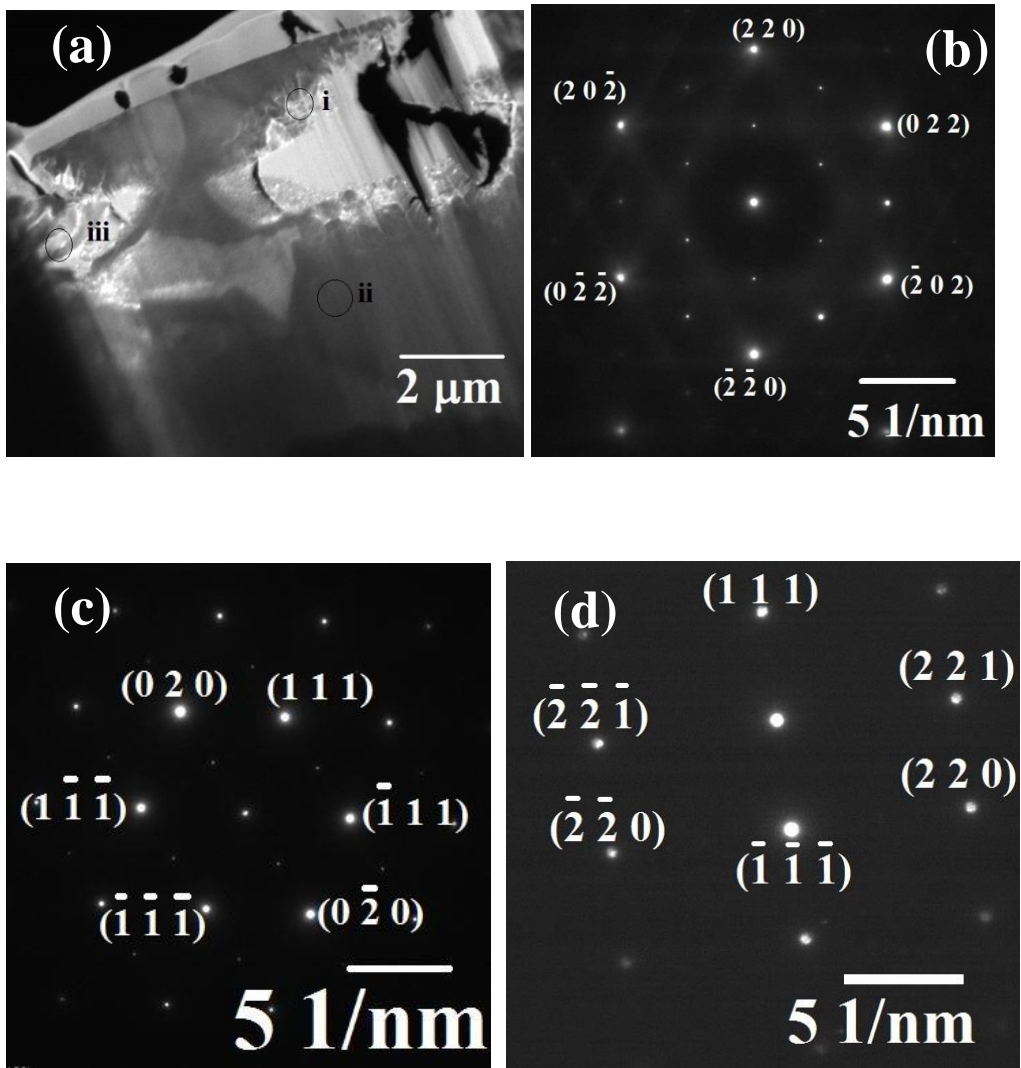


Figure 4.45(a) TEM bright field image of a dendritic seaweed and surrounding crack-like features in a 53 – 38 μm drop-tube sample, (b) selected area diffraction patterns obtained from the region (i) crack-like features, (c) from the region (ii) featureless matrix and (d) from the region (iii) dendritic seaweed.

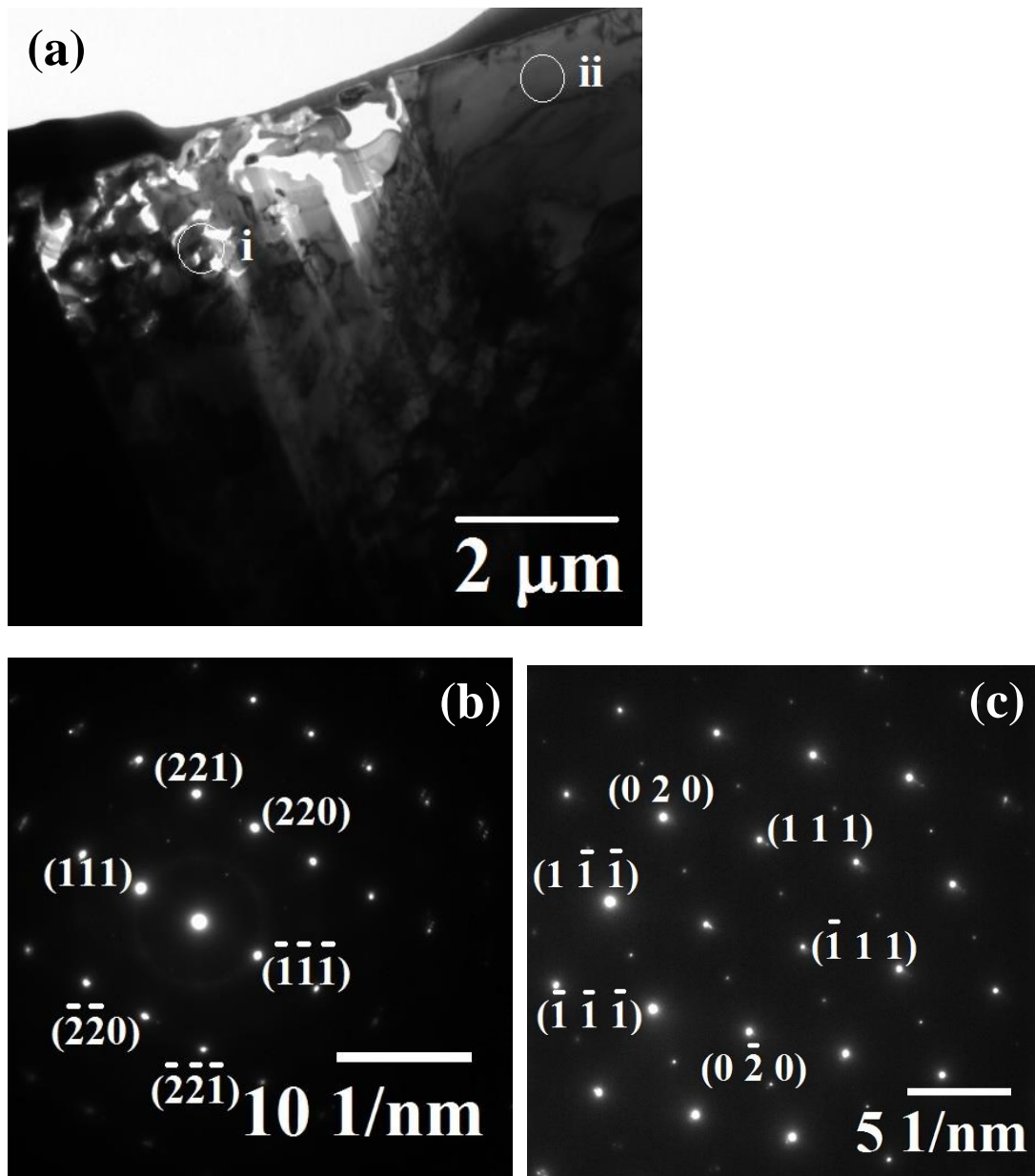


Figure 4.46 (a) TEM bright field image of a dendritic seaweed and surrounding matrix material in a $\leq 38 \mu\text{m}$ drop-tube sample, (b) selected area diffraction patterns obtained from the region (i) dendritic seaweed and (c) from the region (ii) matrix material.

4.3 Preparation of Ingot – Ni₅Ge₃

The congruent melting intermetallic compound Ni₅Ge₃ was produced in the arc-melting furnace, which is considered as a starting material/parent material of this project. For this, Ni and Ge elements were calculated at at. % (Ni-enhancement), as we experienced the loss of Ni during preparation of Ni₃Ge ingot. Therefore, we also used additional amount of Ni to compensate the loss during preparation of Ni₅Ge₃ ingot. Which is shown in the **Table 4.3**, through which the single phase, Ni₅Ge₃-ingot was produced. X-ray diffraction analysis was performed on the polished surface of the arc-melted ingot for confirmation of single phase compound. **Figure 4.47** show XRD analysis result and black vertical line indicate peak position for the single-phase, ε-Ni₅Ge₃ reference pattern (ICCD 04 – 004 – 7364). A strange signal/‘hump’ also appeared between 35 - 40 deg in 2 theta (**Figure 4.48**). Normally, such a ‘hump’ would be associated with the presence on amorphous phase. However, as there is no other evidence of such a phase here the likelihood is that this is due to surface contamination.

Figure 4.48 shows SEM micrograph (featureless) of a polished and etched arc-melted sample, which may be compatible with a single phase material. For confirmation, the EDX area analysis have been taken from the three different regions (square boxes), the large one area of region (i) shows the average chemical composition, (ii) and (iii) shows two small regions from the **Figure 4.48**, these are shown in the **Table 4.4**. All three regions of EDX analysis indicates that composition is within the homogeneity range of single phase [18]. EBSD analysis was also performed on freshly prepared arc-melted sample, polished using 0.1 μm colloidal silica and without etching. The EBSD phase map (**Figure 4.49**) further confirms the XRD analysis of arc melted sample is completely single phase (Ni₅Ge₃).

4.4 Rapidly Solidified Drop-tube Sample – Ni₅Ge₃

The arc-melted prepared ingot of single phase (Ni-enhanced) Ni₅Ge₃ compound was rapidly solidified and obtained $\geq 850 \mu\text{m}$ to $\leq 38 \mu\text{m}$ sieve size fractions using a drop-tube technique. Firstly, EDX analysis was carried out on freshly polished samples to ensure the chemical composition of the all ranges of drop-tube samples. For this, EDX area scanning was randomly performed at least 10 particles of all ranges of drop-tube samples ($\geq 850 \mu\text{m}$ to $\leq 38 \mu\text{m}$) and measured chemical compositions were within the homogeneity range Ni – 37.2 at.% Ge as shown in **Figure 4.50**. Consequently, all ranges of drop-tube particles have the average chemical composition within the range of single phase, congruently melting compound, ϵ -Ni₅Ge₃. Samples from all sieve fractions ($\geq 850 \mu\text{m}$ to $38 \mu\text{m}$) shown in **Figure 4.51** have also been subject to XRD analysis, which, by comparison with the ICDD reference patterns for ϵ -Ni₅Ge₃ (04 – 004 – 7364) and ϵ' -Ni₅Ge₃ (01-075-6729), confirms that the material remain fully single phase Ni₅Ge₃, irrespective of the imposed cooling rate. In this way, the largest sieve fraction ($\geq 850 \mu\text{m}$) of this material was ϵ' , while the smaller than $850 \mu\text{m}$ ($850 – 38 \mu\text{m}$) size fractions were ϵ . Where, ϵ' is the equilibrium low temperature phase and ϵ a retained high temperature phase. Moreover, EBSD analysis was also performed on freshly prepared drop-tube samples with all sieve size fractions ranges from $\geq 850 \mu\text{m}$ to $< 38 \mu\text{m}$, polished using $0.1 \mu\text{m}$ colloidal silica and without etching.

The EBSD phase map for all drop-tube samples further confirms the XRD analysis in that all ranges ($\geq 850 \mu\text{m}$ to $< 38 \mu\text{m}$) samples are completely single phase ϵ -Ni₅Ge₃/ ϵ' -Ni₅Ge₃. An example of EBSD phase map within $850 – 500 \mu\text{m}$ sieve is shown in **Figure 4.52**. After that several analysis techniques were used to study the effect of rapid solidification process, evolution of microstructures, phase transformation, to study of crystal structure, thermal analysis and mechanical properties through using SEM, TEM, EBSD, DSC and Vickers micro-hardness test.

Table 4.3 Shows the calculation of Ni and Ge composition (Ni-enhanced) at their atomic percentage.

Element	Composition (at. %)	Molar mass (g/mol)	Mole*Comp. (g)	Comp (mass) = Mol *Comp/Total mass (g)	Comp (g) Used in arc melt process
Ni	0.631	58.693	58.693*0.631 = 37.03528	37.03528/63.83944 = 0.58013	0.58013*15 = 8.70195
Ge	0.369	72.64	72.64*0.369= 26.80416	26.80416/63.83944 = 0.419868	0.419868*15 = 6.2980
			= 63.83944		= 15.00

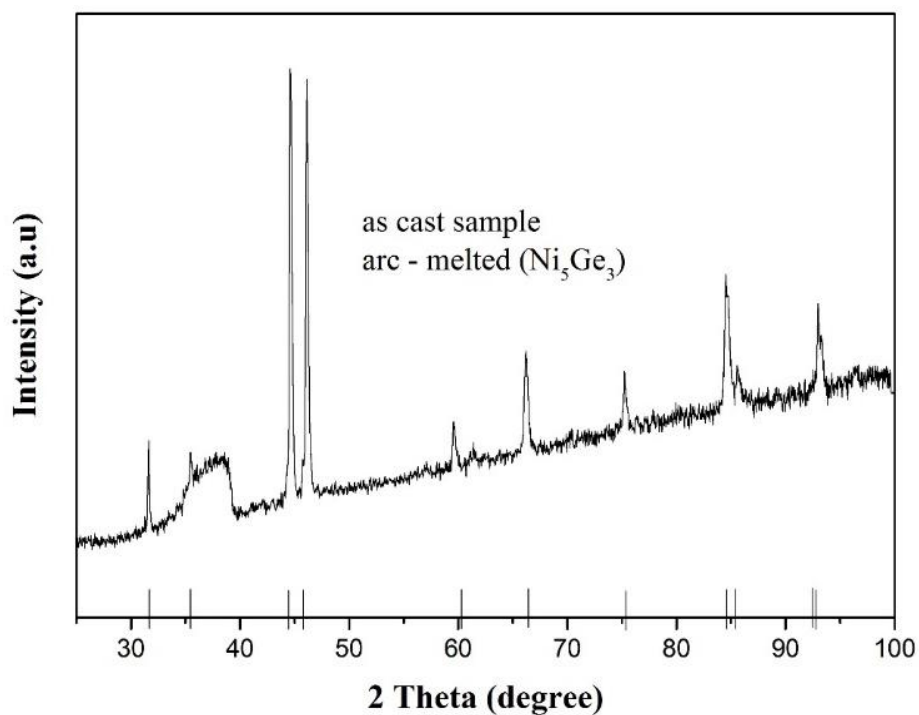


Figure 4.47 X-ray diffraction analysis of as cast (arc-melted, Ni-enhanced) sample prior to drop-tube process. Vertical black lines indicate peak position for the single-phase ($\epsilon\text{-Ni}_5\text{Ge}_3$ reference pattern).

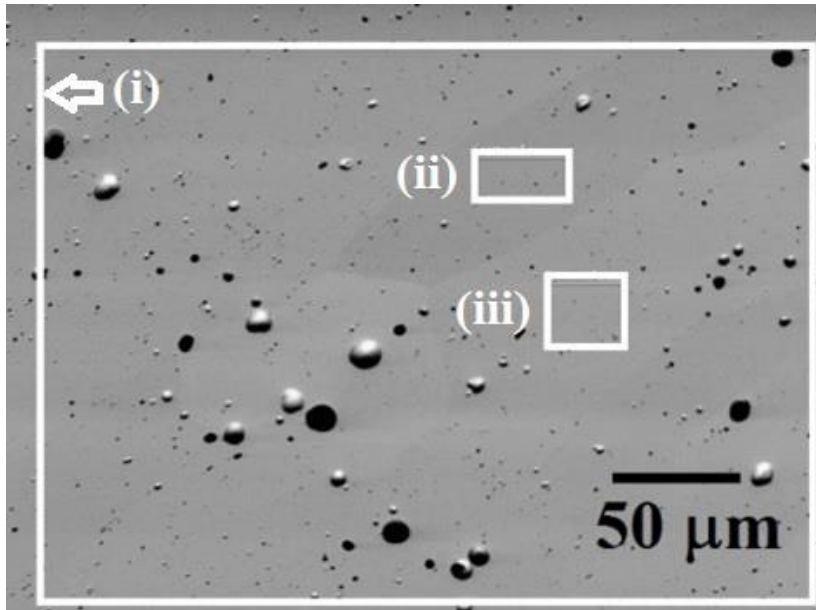


Figure 4.48 SEM micrograph of HF etched of as cast (arc-melted, Ni-enhanced) sample prior to drop-tube process, showing sample has completely single phase (featureless matrix). The regions (square blocks) selected from different regions of sample for EDX area analysis.

Table 4.4 (i) shows the average result of EDX area analysis of Ni and Ge composition at. % from the larger area, (ii) and (iii) shows results of EDX area analysis of Ni and Ge composition at. % from the two smaller regions of **Figure 4.2b**.

(i)		(ii)		(iii)	
Element	Atomic (%)	Element	Atomic (%)	Element	Atomic (%)
Ni	62.8	Ni	62.6	Ni	62.5
Ge	37.2	Ge	37.4	Ge	37.5

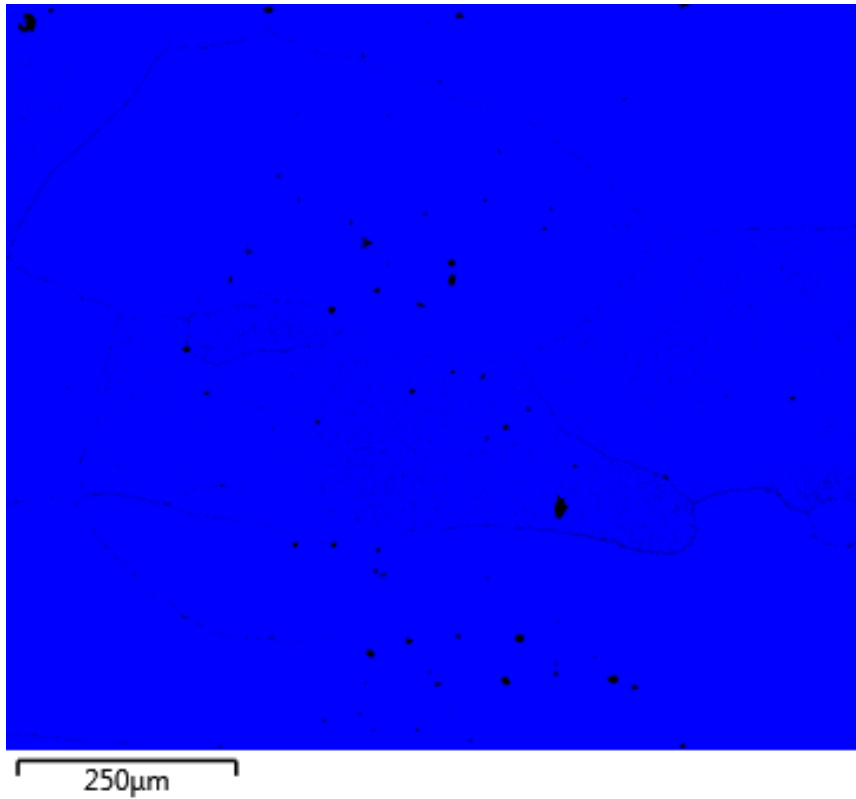


Figure 4.49 Electron backscatter diffraction (EBSD) result of phase map (arc-melted, Ni-enhanced sample).

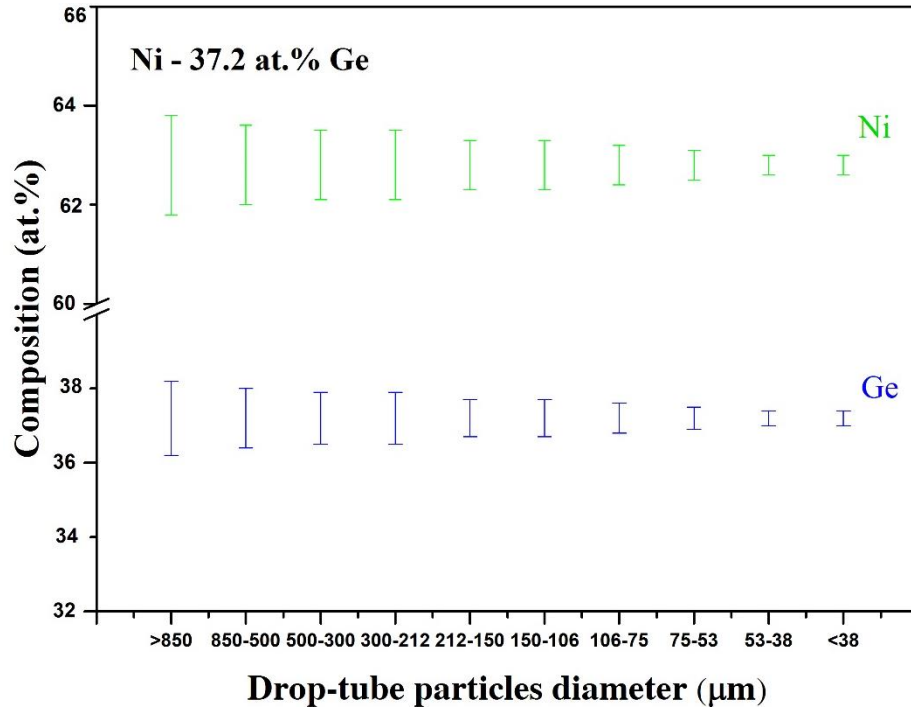


Figure 4.50 Average EDX compositions of Ni and Ge of the Ni – 37.2 at. % Ge drop-tube particles. At least 10 particles were analysed in each size range.

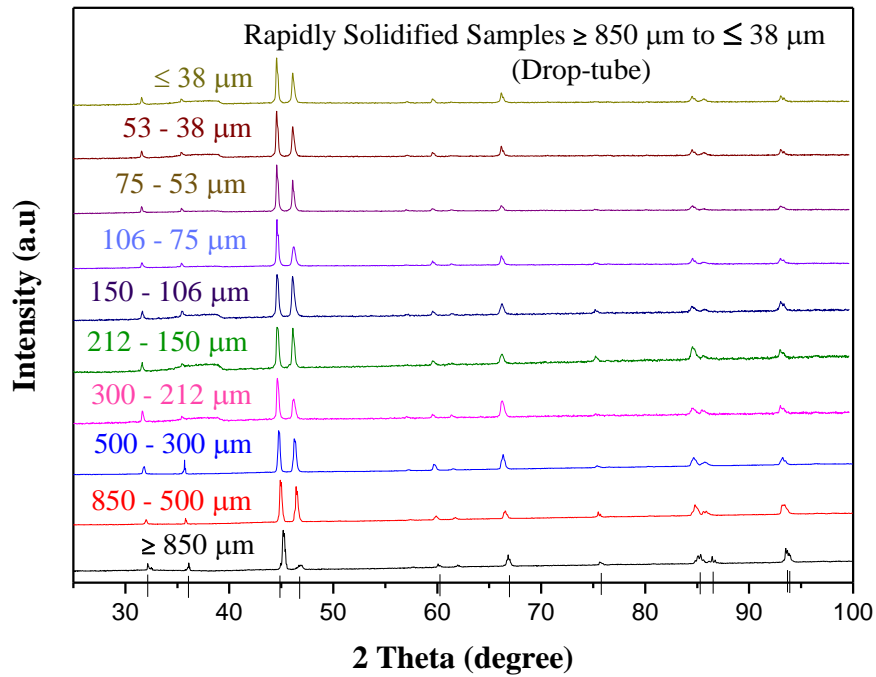


Figure 4.51 X-ray diffraction analysis of rapidly solidified drop-tube processed samples, ranges from ($\geq 850 \mu\text{m}$ to $\leq 38 \mu\text{m}$). Vertical black lines indicate peak positions for the single-phase $\epsilon\text{-Ni}_5\text{Ge}_3$ / $\acute{\epsilon}\text{-Ni}_5\text{Ge}_3$ reference pattern and different colours represents XRD patterns of particle sizes from $\geq 850 \mu\text{m}$ to $\leq 38 \mu\text{m}$.

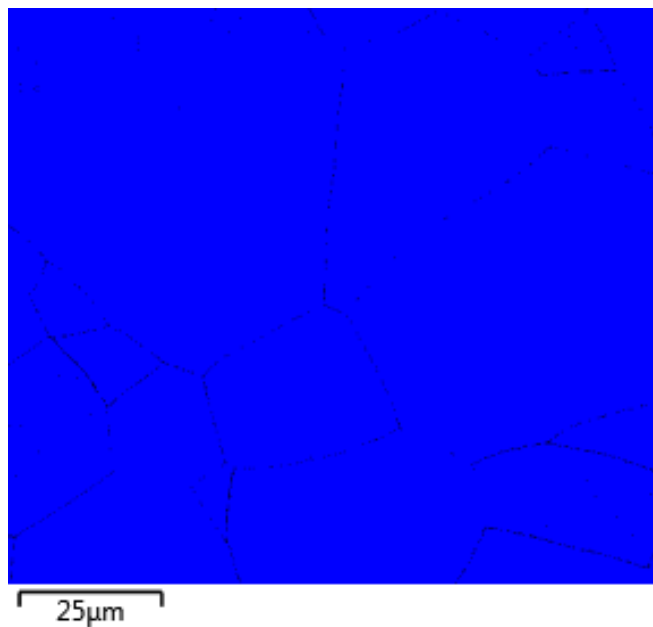


Figure 4.52 Electron backscatter diffraction (EBSD) result of phase map (drop-tube, 850 – 500 μm sample).

4.4.1 Microstructural Characterisation

SEM was used for studying microstructures of the rapidly solidified Ni_5Ge_3 droplets, ranges from $\geq 850 \mu\text{m}$ to $\leq 38 \mu\text{m}$ sieve size fractions. Numerous plate and lath like structures are evident in the drop-tube samples, in sieve size fractions ranges from $\geq 850 \mu\text{m}$ to $212 - 150 \mu\text{m}$. SEM micrograph of a polished and HF etched samples of sieve fractions $\geq 850 \mu\text{m}$ to $212 - 150 \mu\text{m}$ in powder form shown in the **Figures 4.53 – 4.57**, where grain boundaries are also evident and that many of the plate and lath morphologies appear to cross the grain boundaries unaltered. Such structures remain the dominant morphology between the sieve size fractions $\geq 850 - 150 \mu\text{m}$. However for particle size smaller than $150 \mu\text{m}$, these lath and plate structures are replaced by numerous isolated faceted hexagonal crystallites in a more-or-less uniform featureless matrix. These isolated faceted hexagonal microstructures are evidently in the three small sieve size fractions, $150 - 106 \mu\text{m}$, $106 - 75 \mu\text{m}$, and $75 - 53 \mu\text{m}$, which can be seen in the **Figures 4.58 – 4.60** respectively. In **Figure 4.60**, it also appears that a grain boundary cuts straight through one of the isolated hexagonal crystallites. Finally, in the two smallest sieve size fractions $53 - 38 \mu\text{m}$ and $\leq 38 \mu\text{m}$, the isolated faceted hexagonal microstructures are ceased and samples transform into a single crystal structure on both smallest drop-tube samples. These single crystal structure can be observed in the **Figures 4.61 – 4.62**.

The EDX line scan technique was used for the analysis of contrast between the microstructures (plate and lath and isolated faceted hexagonal crystallites) and the surrounding material (featureless matrix) of rapidly solidified drop-tube samples $\geq 850 \mu\text{m}$ to $53 \mu\text{m}$. The example of EDX line scan of selective sieve size fractions of microstructures, $500 - 300 \mu\text{m}$ (plate and lath structure) and from $150 - 106 \mu\text{m}$ (isolated faceted hexagonal crystallites) are shown in the **Figures 4.63a and b** respectively. From EDX line scan analysis it is clear that, to within the experimental error associated with the technique, there is no variation in composition between the structures revealed by etching (as shown in **Figures 4.63 a-b**) and the surrounding featureless matrix. This contrast is not the result of compositional difference between the plate and lath/isolated faceted hexagonal crystallites and the surrounding matrix due to the solute partitioning during solidification.

- For the EDX line scan of plate and lath trunk (**Figure 4.63 a**), time for each step and number of step can be calculated by following equation:

$$\text{Time for each step} = \text{total acquisition time} / \text{number of steps} = 437 \text{ sec} / 500 = \mathbf{0.9 \text{ sec}} \quad (4 - 7)$$

$$\text{Number of step} = \text{Total length of scan/step size from the lateral resolution} = 154 \mu\text{m} / 500 = 0.308 * 1000 = \mathbf{308} \quad (4 - 8)$$

- For the EDX line scan of hexagonal crystallites trunk (**Figure 4.63 b**):

$$\text{Time for each step} = \text{total acquisition time} / \text{number of steps} = 450 \text{ sec} / 500 = \mathbf{0.9 \text{ sec}} \quad (4 - 9)$$

$$\text{Number of step} = \text{Total length of scan/step size from the lateral resolution} = 17 \mu\text{m} / 500 = 0.34 * 1000 = \mathbf{34} \quad (4 - 10)$$

It can be conclude that **Figure 4.63 (a-b)** showed some noise signal which is effect of limited time of EDX-line scanning. Also, given the limited number of effective steps in the line scan, the ability to distinguish compositional features is limited.

4.4.2 EBSD Analysis

EBSD Euler map was used to study the grain structures of observed microstructure (plate and lath, isolated faceted hexagonal crystallites and single crystal structure). For this, drop-tube sieve size fractions $\geq 850 \mu\text{m}$ to $\leq 38 \mu\text{m}$ ranges have been undertaken on freshly prepared samples, polished using $0.1 \mu\text{m}$ colloidal silica and without etching. The grain structure for the $\geq 850 \mu\text{m}$ to $53 \mu\text{m}$ sample are very clearly revealed in the EBSD Euler map, as an example of three selective size fractions $500 - 300 \mu\text{m}$, $300 - 212 \mu\text{m}$ and $212 - 150 \mu\text{m}$ of plate and lath microstructure samples are shown in the **Figures 4.64a – 4.66a**. The EBSD images show no evidence of either the plate and lath nor hexagonal morphologies visible in the SEM images. Also, it suggest that the plate and laths have the same crystallographic orientation as the background. For the plate and lath microstructure sample size fractions $500 - 300 \mu\text{m}$, the orientation of each grain relative to its neighbours are looks random with some additional components of high angle as shown by the histogram of grain orientations in the **Figures 4.64b**. While, for the plate and lath microstructure sample size fractions $300 - 212 \mu\text{m}$ and $212 - 150 \mu\text{m}$, the orientation of each grain relative to its neighbours are looks predominantly low angle grain boundaries (LAGB) as shown by the histogram of grain orientations in the **Figures 4.65b – 4.66b**. **Figure 4.67a** and **b** shows the EBSD Euler map and histogram of isolated faceted hexagonal crystallites, from the sample size $150 - 106 \mu\text{m}$, the orientation of each grain relative to its neighbours are looks predominantly random. However, the EBSD Euler map does not show the presence of any grains in the two smallest sieve size fractions $53 - 38 \mu\text{m}$ and $\leq 38 \mu\text{m}$. An example of Euler map and histogram of grain orientations amongst these two smallest sieve size fractions are shown in the **Figure 4.68a** and **b**. which indicates that these two smallest samples might be single crystal.

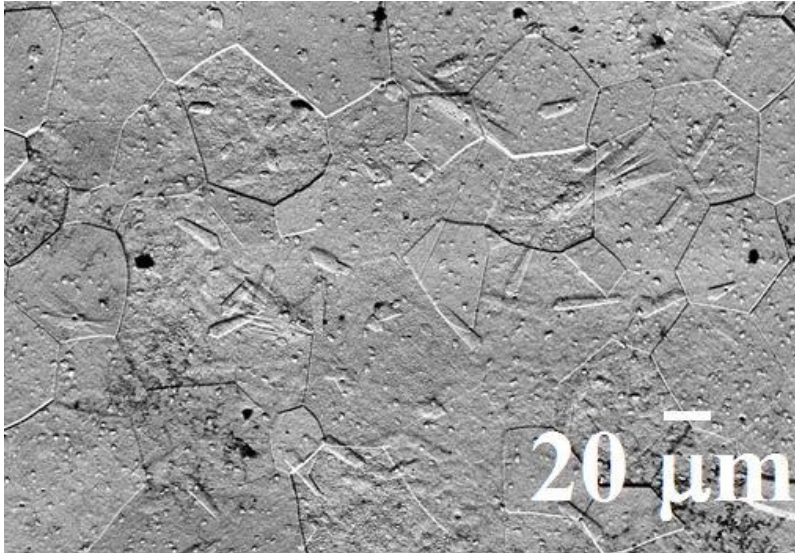


Figure 4.53 SEM (SEI) micrograph of HF etched Ni_5Ge_3 drop-tube particle from the $\geq 850 \mu\text{m}$ size fraction showing numerous plate and lath structures in a more-or-less featureless matrix.

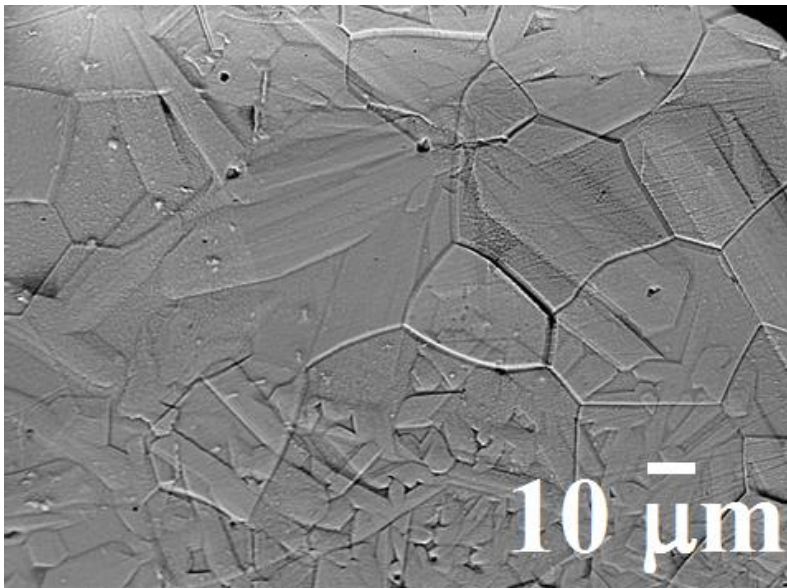


Figure 4.54 SEM (SEI) micrograph of HF etched Ni_5Ge_3 drop-tube particle from the $850 - 500 \mu\text{m}$ size fraction showing numerous plate and lath structures in a more-or-less featureless matrix.

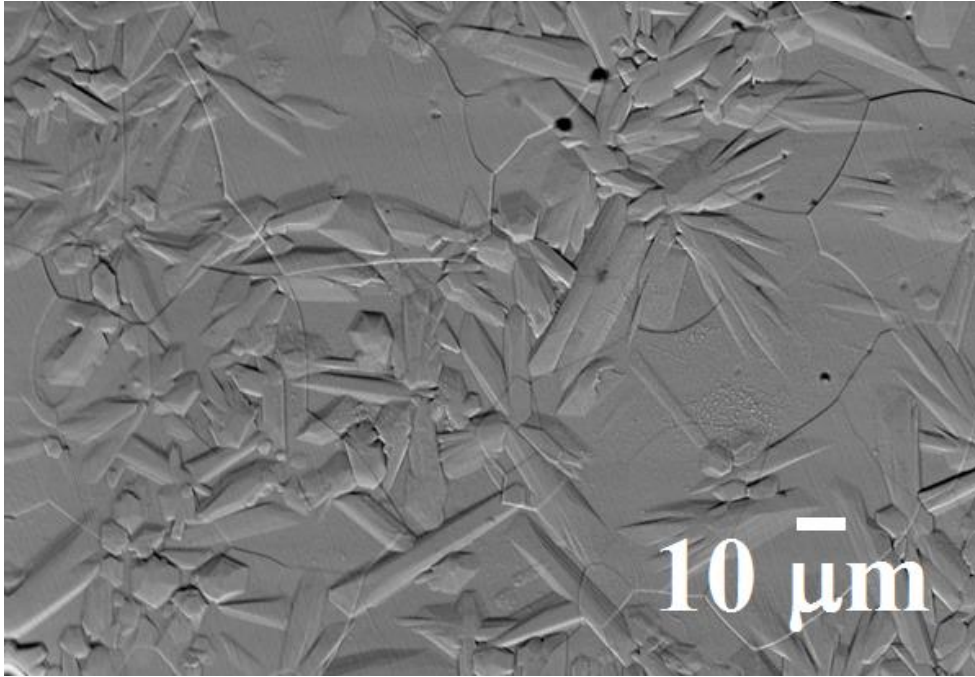


Figure 4.55 SEM (SEI) micrograph of HF etched Ni_5Ge_3 drop-tube particle from the 500 – 300 μm size fraction showing numerous plate and lath structures in a more-or-less featureless matrix.

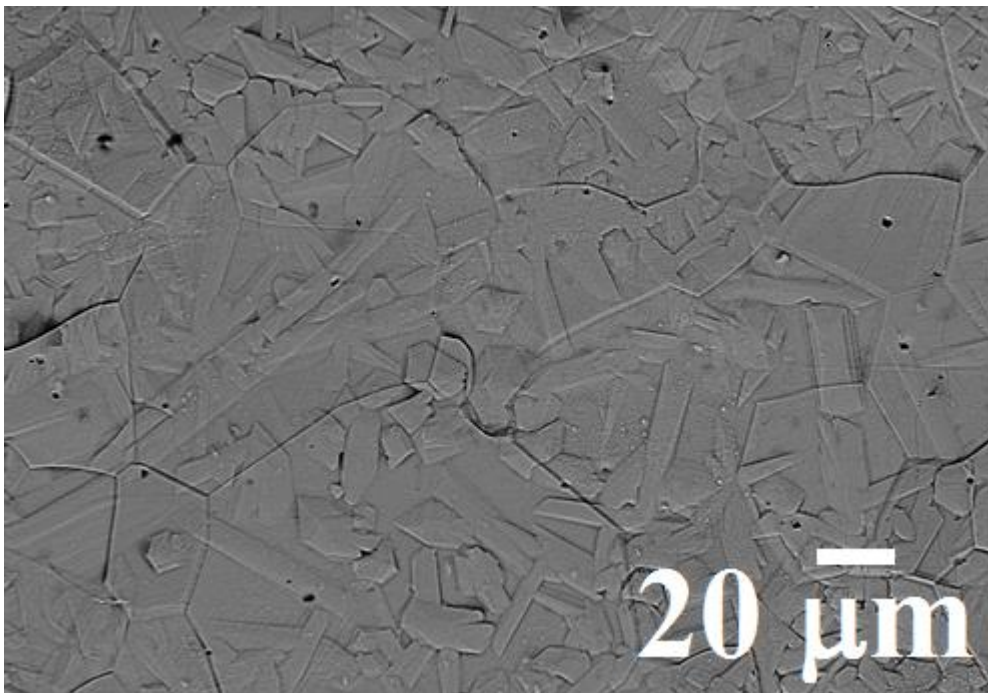


Figure 4.56 SEM (SEI) micrograph of HF etched Ni_5Ge_3 drop-tube particle from the 300 – 212 μm size fraction showing numerous plate and lath structures in a more-or-less featureless matrix.

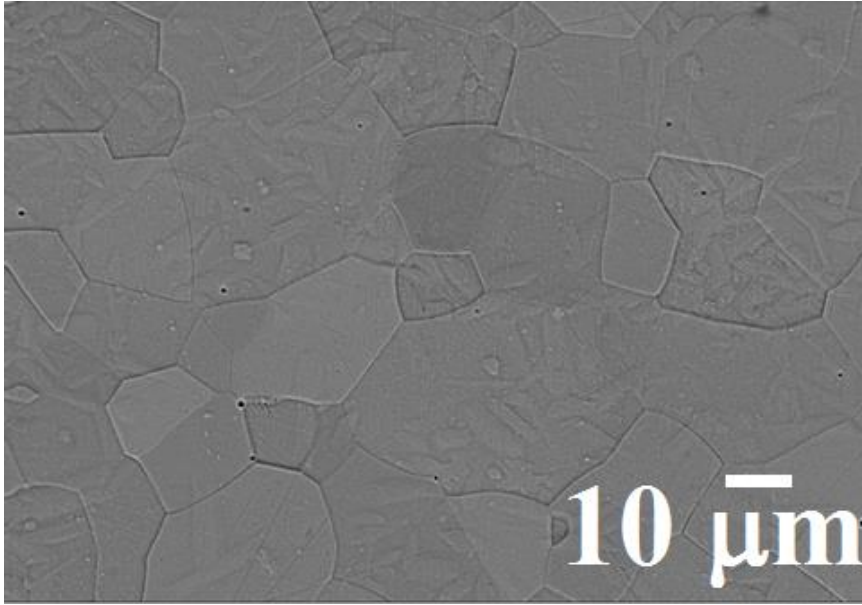


Figure 4.57 SEM (SEI) micrograph of HF etched Ni_5Ge_3 drop-tube particle from the 212 – 150 μm size fraction showing numerous plate and lath structures in a more-or-less featureless matrix.

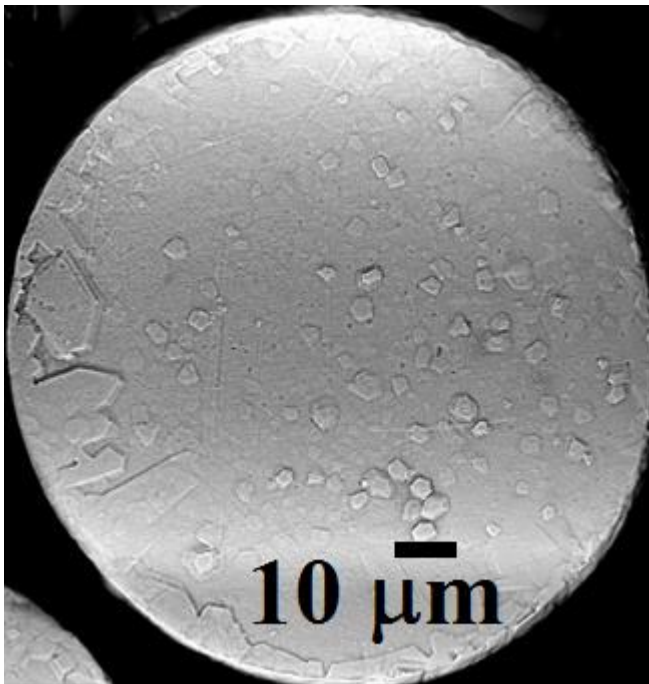


Figure 4.58 SEM (SEI) micrograph of HF etched Ni_5Ge_3 drop-tube particle from the 150 – 106 μm size fraction showing isolated faceted crystallites.

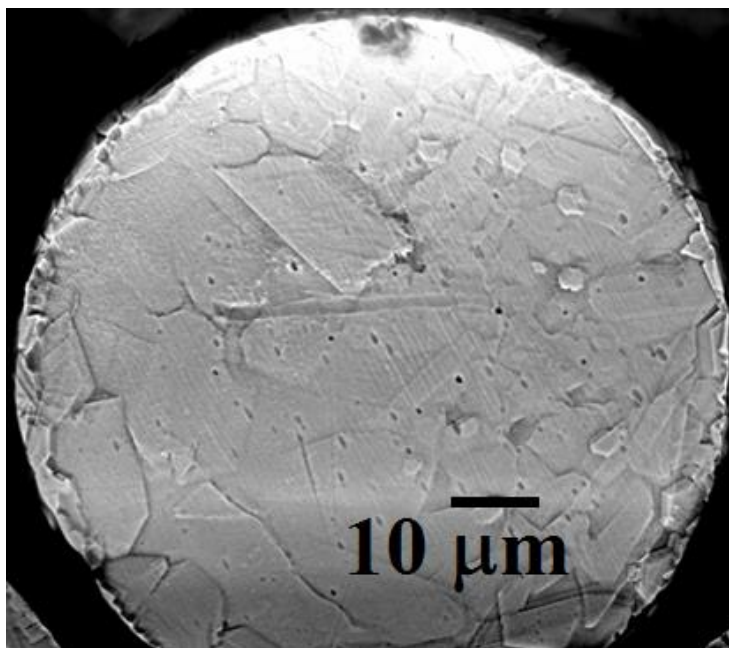


Figure 4.59 SEM (SEI) micrograph of HF etched Ni_5Ge_3 drop-tube particle from the 106 – 75 μm size fraction showing isolated faceted crystallites.

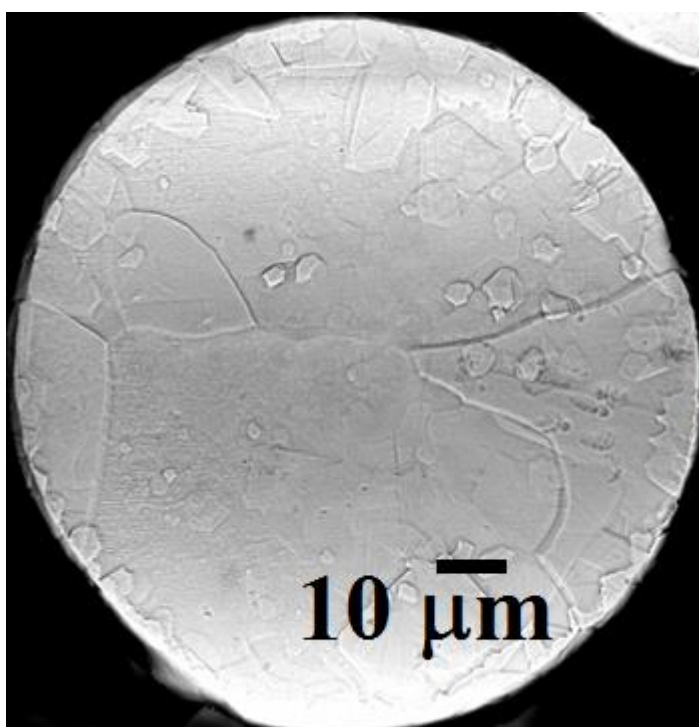


Figure 4.60 SEM (SEI) micrograph of HF etched Ni_5Ge_3 drop-tube particle from the 75 – 53 μm size fraction showing isolated faceted crystallites.

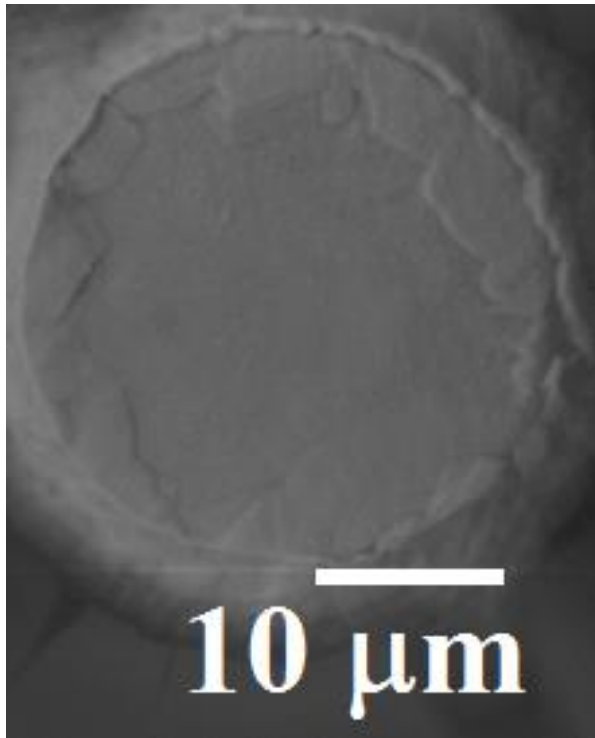


Figure 4.61 SEM (SEI) micrograph of HF etched Ni₅Ge₃ drop-tube particle from the , 53 – 38 μm size fraction showing featureless matrix (single crystal).

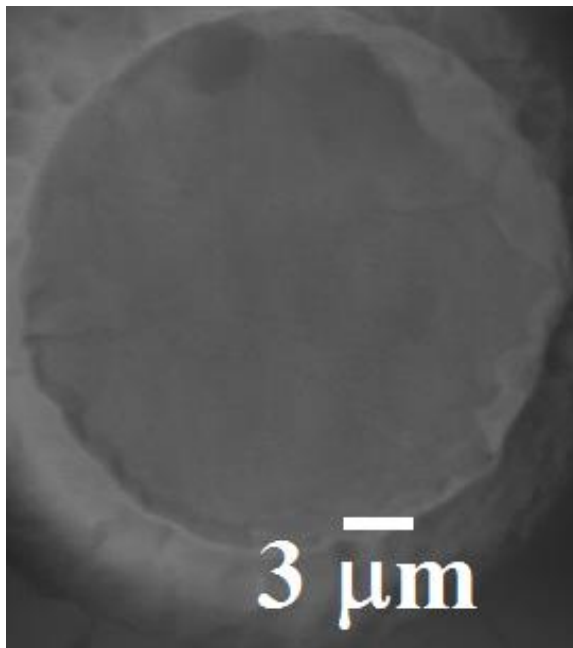


Figure 4.62 SEM (SEI) micrograph of HF etched Ni₅Ge₃ drop-tube particle from the , ≤ 38 μm size fraction showing featureless matrix (single crystal).

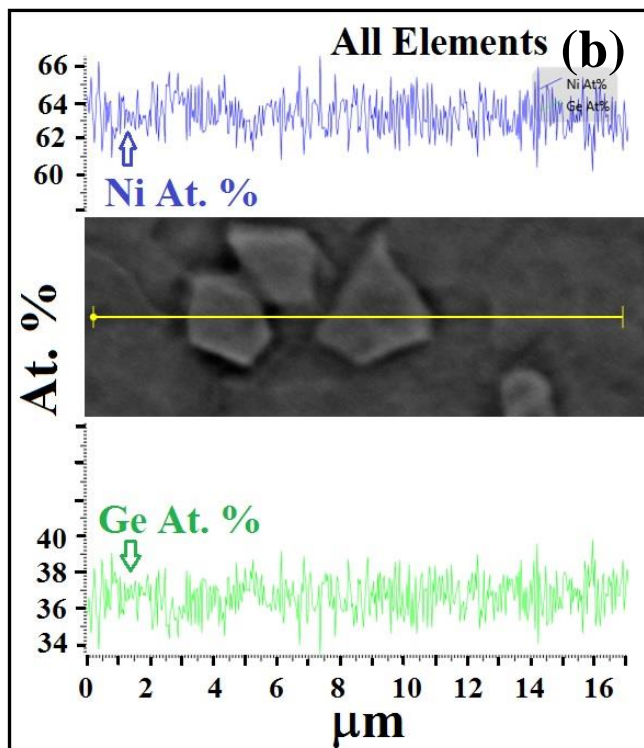
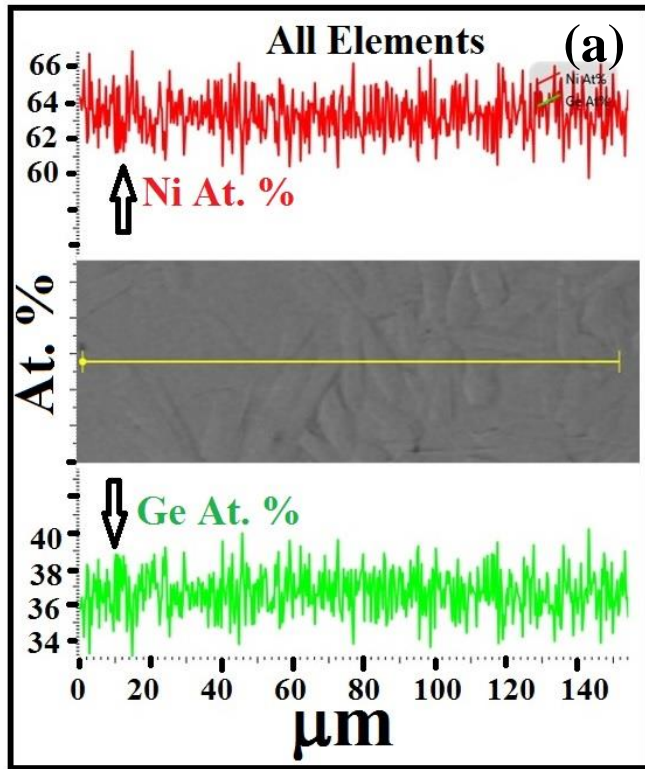


Figure 4.63 (a) EDX line scan across a lath and plate trunk and (b) isolated faceted crystallites trunk, showing that the contrast revealed by etching is not the result of solute partitioning.

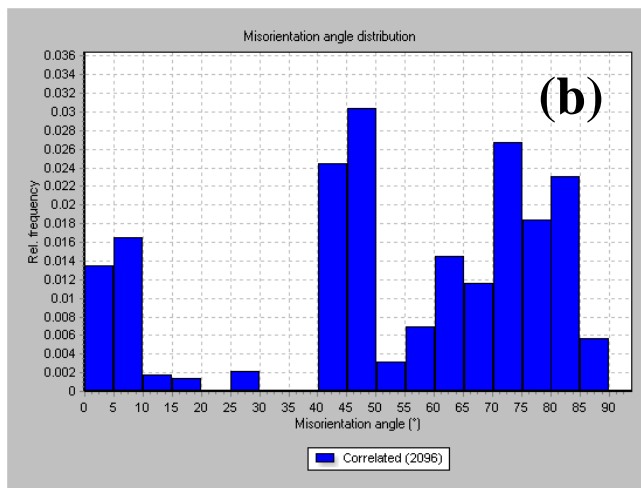


Figure 4.64 (a) Electron backscatter diffraction (EBSD) result of Euler texture map of unetched Ni_5Ge_3 drop-tube particle size 500 – 300 μm ; (b) Histogram of the correlated misorientation angle distribution across grain boundaries for the image shown in (a).

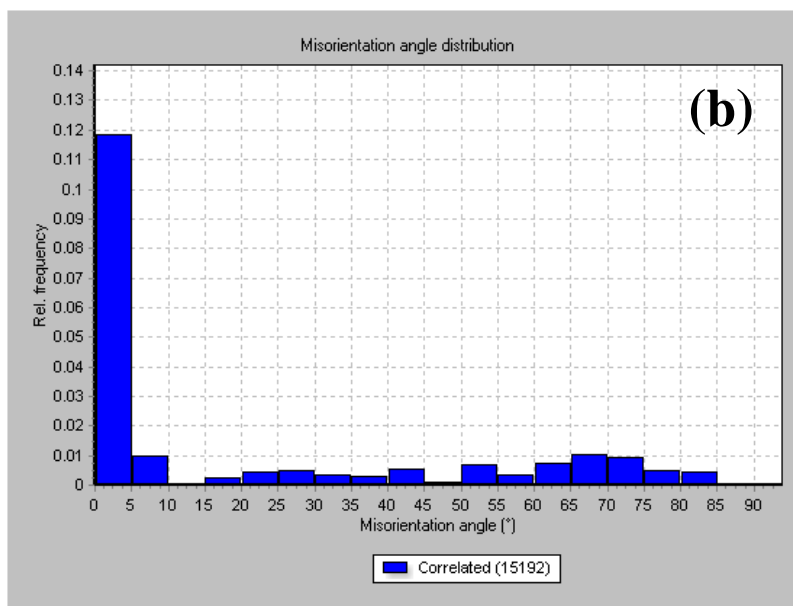
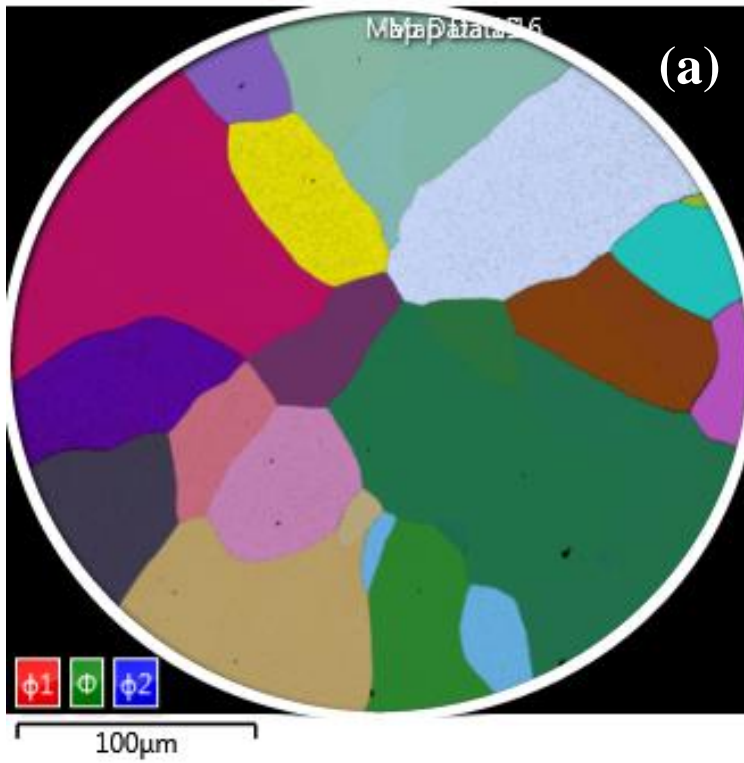


Figure 4.65 (a) Electron backscatter diffraction (EBSD) result of Euler texture map of unetched Ni_5Ge_3 drop-tube particle size 300 – 212 μm ; (b) Histogram of the correlated misorientation angle distribution across grain boundaries for the image shown in (a).

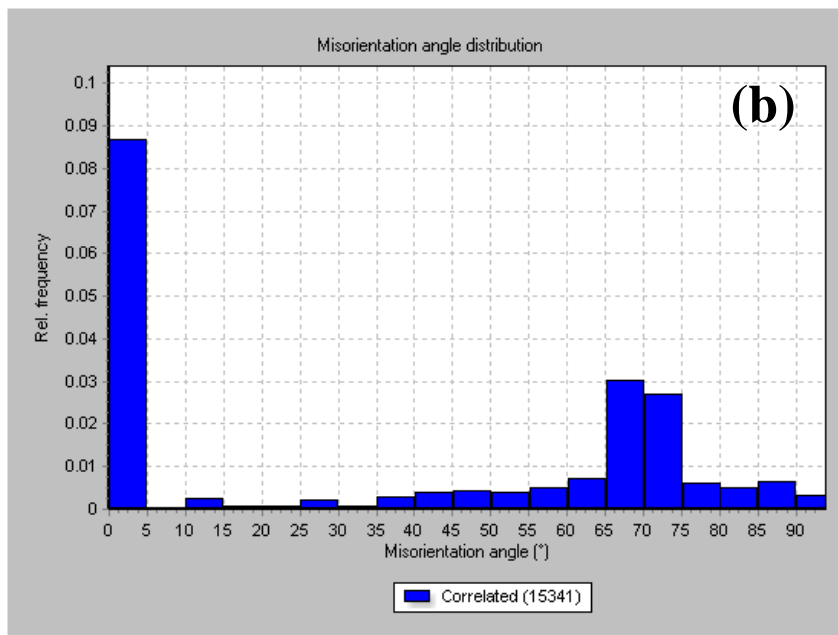
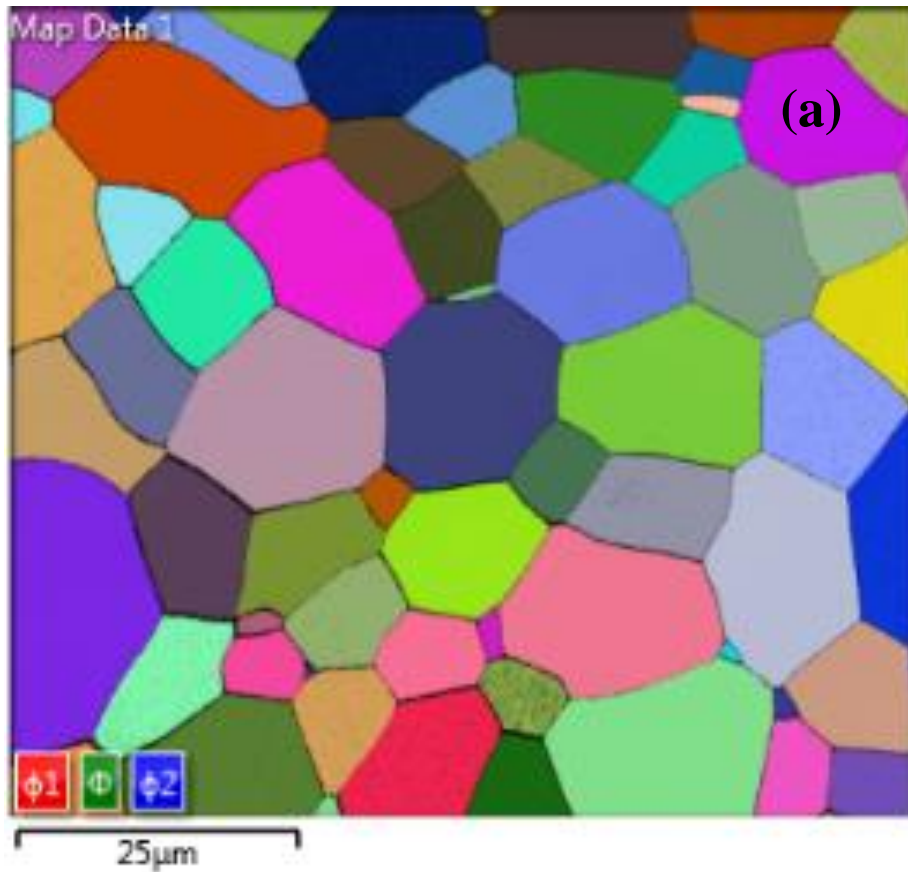


Figure 4.66 (a) Electron backscatter diffraction (EBSD) result of Euler texture map of unetched Ni_5Ge_3 drop-tube particle size 212 – 150 μm ; (b) Histogram of the correlated misorientation angle distribution across grain boundaries for the image shown in (a).

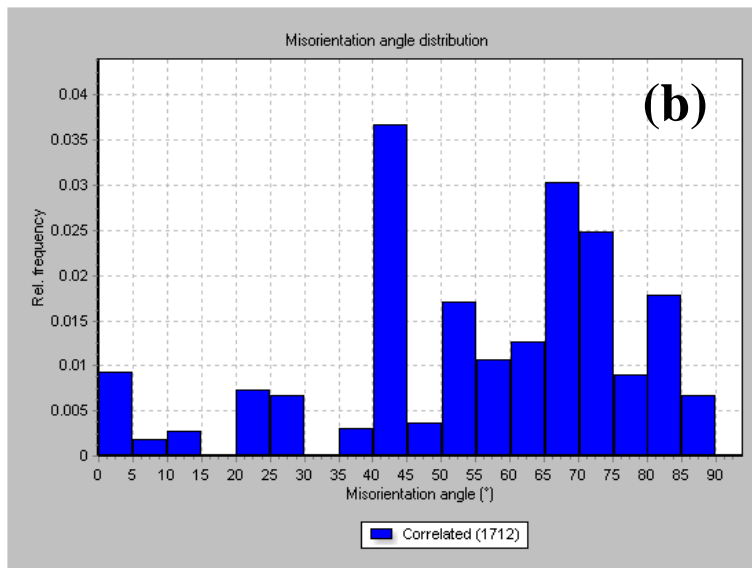
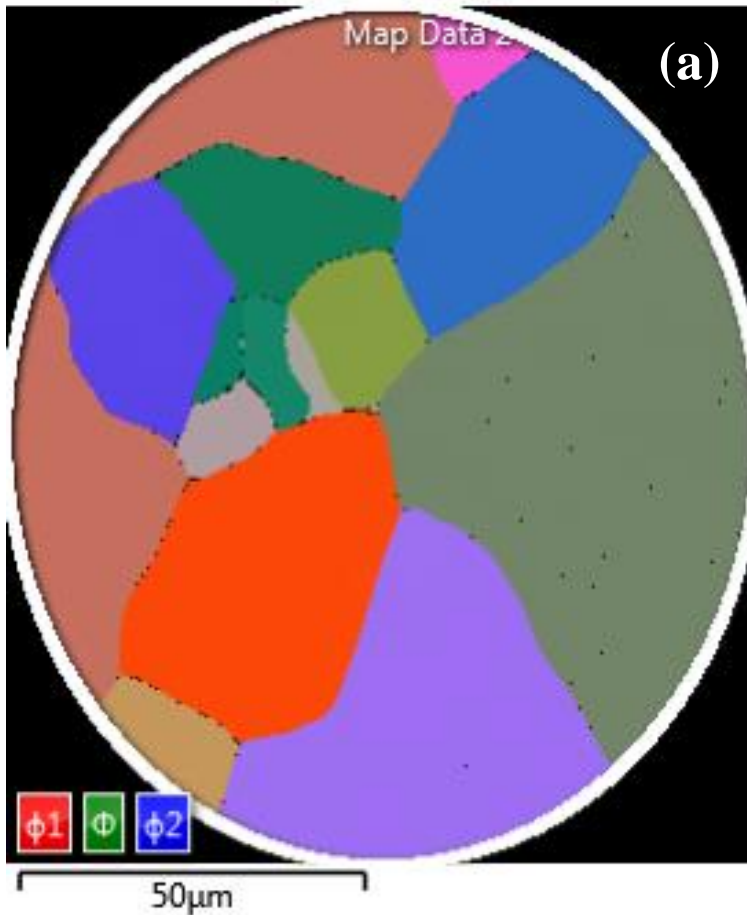


Figure 4.67 (a) Electron backscatter diffraction (EBSD) result of Euler texture map of unetched Ni_5Ge_3 drop-tube particle size 150 – 106 μm ; (b) Histogram of the correlated misorientation angle distribution across grain boundaries for the image shown in (a).

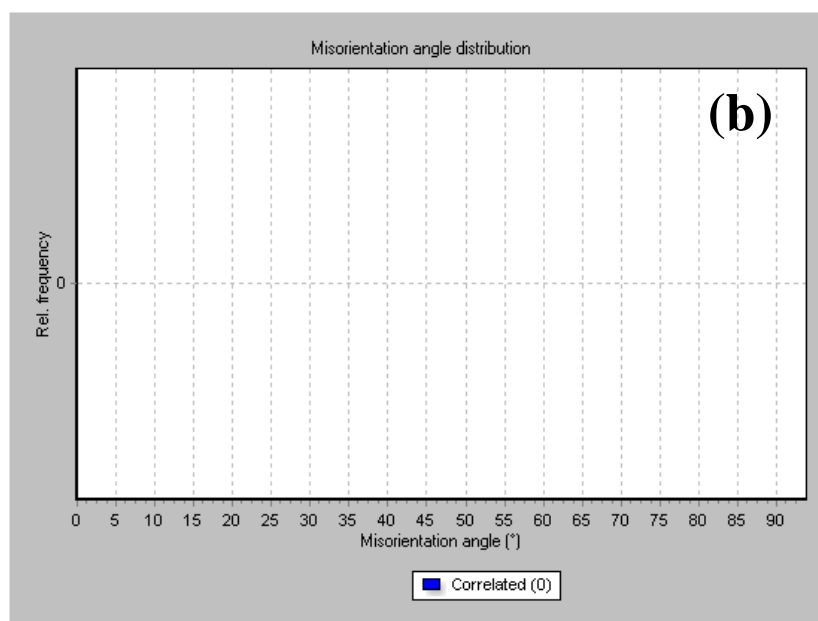
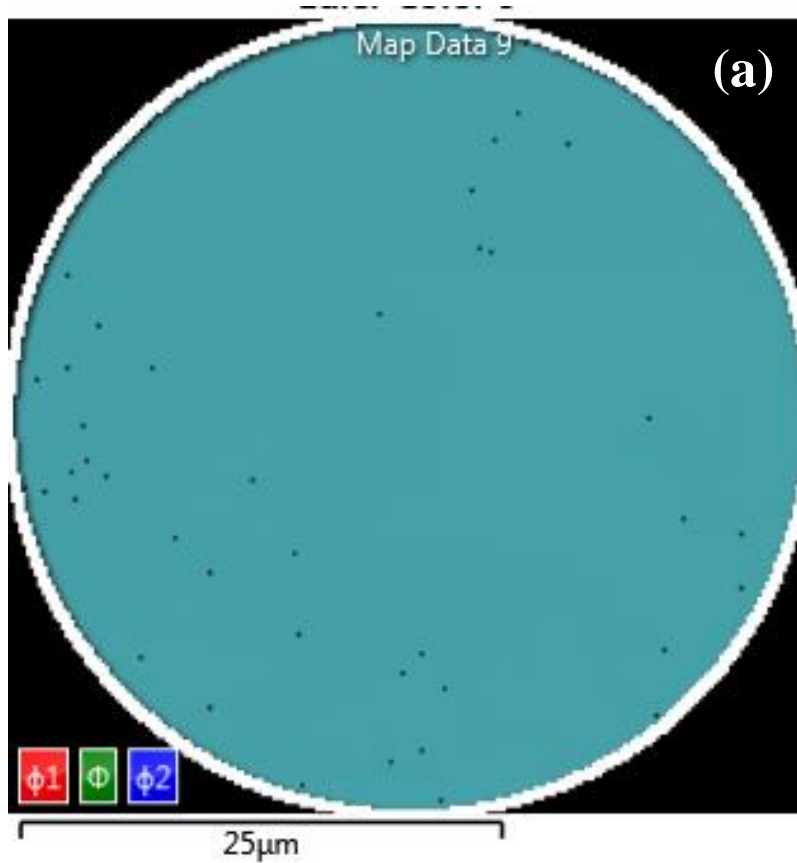


Figure 4.68 (a) Electron backscatter diffraction (EBSD) result of Euler texture map of unetched Ni_5Ge_3 drop-tube particle size 53 – 38 μm ; (b) Histogram of the correlated misorientation angle distribution across grain boundaries for the image shown in (a).

4.4.3 TEM and Thermal Analysis

In order to understand the mechanism giving rise to these three typical structures, plate and lath, isolated faceted hexagonal crystallites, single crystal structure and their matrix phases, transmission electron microscope (TEM) is used to obtain selected area diffraction pattern (SADP) on focus ion beam (FIB) milled sections from the polished - etched and mounted samples.

Figure 4.69a to **4.71a** shows TEM bright field images of a FIB section through a (ϵ) partially plate and lath ($\geq 850 \mu\text{m}$), (ϵ) fully plate and lath ($500 - 300 \mu\text{m}$) and isolated faceted hexagonal crystallites ($150 - 106 \mu\text{m}$) and some of the immediately surrounding matrix material. Selective area diffraction pattern (SADP) identifies two regions as shown in **Figure 4.69a**; (i) Matrix material that is away from the partially plate and lath structure, (ii) Inside the plate and lath structure. The SAD results of region (i) and (ii) are shown in **Figure 4.69 (b-c)**. Here, we observed double superlattice spots (ϵ), which is entirely different kind of crystal structure as compared to other observed drop-tube samples. The example of this double super lattice spots are clearly evident in **Figure 4.69b**, indicating the matrix material anticipated chemically ordered structure. While the absence of super lattice spot in **Figure 4.69c**, indicating the material imply the partially plate and lath morphology anticipated chemically disordered.

Also, selective area diffraction pattern (SADP) obtained as identifies two regions in **Figure 4.70a**; (i) matrix material that is away from the plate and lath structure, (ii) inside the plate and lath structure. The SAD results of region (i) and (ii) are shown in **Figure 4.70 (b-c)** respectively, the crystal structure looks different (cubic in **Figure 4.70 b** and hexagonal in **Figure 4.70c**). In this sample, we observed single lattice spots (**Figure 4.70b**), also indicating the matrix material anticipated chemically ordered structure. While the absence of super lattice spot in **Figure 4.70c**, indicating the material imply the plate and lath morphology anticipated chemically disordered.

Similarly, selective area diffraction pattern (SADP) obtained as identifies two regions in **Figure 4.71a**; (i) matrix material that is away from the isolated faceted hexagonal crystallites, (ii) inside the isolated faceted hexagonal crystallites. The SAD results of region (i) and (ii) are shown in **Figure 4.71 (b-c)** respectively. Super lattice spots are also clearly evident in **Figure 4.71b**, indicating the matrix material anticipated

chemically ordered structure. While the absence of super lattice spot in **Figure 4.71c**, indicating the material imply the isolated faceted hexagonal crystallites morphology anticipated chemically disordered.

Finally, **Figure 4.72a** shows a TEM bright field image of a FIB section through a single crystal structure (53 – 38 μm). As the single crystal structure show complete matrix material, no formation of any microstructure. Therefore, SADP randomly obtained from the matrix material at the regions (i and ii), the results of SADP are shown in the **Figure 4.72 (b-c)**. In contrast to both matrix materials of plate and lath and also isolated faceted hexagonal crystallites microstructure, the matrix material of single crystal structure shows absence of super lattice spot. This indicates that in the smallest drop-tube sieve size sample completely transformed into chemically disordered material.

4.4.4 DSC and In-situ TEM analysis

Differential scanning calorimetry (DSC) was performed on the particle of sieve fraction (150 – 106 μm) with heating rate 10 K min^{-1} , in order to understand the phenomenon whether the reordering was developed in solid state or during solidification at the liquidus temperature. The results of this experiment are given in the **Figure 4.73a**. Two low temperature transformations are apparent. One of these appeared at the temperature range 300 – 320 $^{\circ}\text{C}$, and from the phase diagram is likely to be the $\varepsilon \rightarrow \varepsilon' + \text{Ni}_2\text{Ge}$, as would be expected for material at 37.2 at% Ge. In this respect it is interesting to note that the largest drop-tube sieve fraction, powders > 850 μm , was single phase ε' . This suggests that cooling was sufficiently rapid to suppress the $\varepsilon \rightarrow \varepsilon' + \text{Ni}_2\text{Ge}$, forcing the system to undergo the congruent $\varepsilon \rightarrow \varepsilon'$ transition instead. The second low temperature region noticeable at 460 – 540 $^{\circ}\text{C}$ in DSC, which suggest that it might be associated with higher temperature ε -phase ordered-disordered transformation.

In order to understand order-disorder transformation, an in-situ heating experiment was conducted in the TEM. For this, first we identified featureless matrix in the TEM and then obtained SADP of this region which was ordered structure (presence of superlattice spots). Then, another SADP was obtained by rapidly increasing the

temperature from room temperature to 465 °C, within the same region (ordered/supperlattice region). **Figure 4.73b** explains the initial ordering region with its surrounding featureless matrix using SAD pattern, to confirm that the material remained ordered at temperature 465 °C. Furthermore the material was heated until the point is reached where the super lattice spots disappeared (**Figure 4.73c**), explaining the material has transformed from ordered to fully disordered phase with a corresponding temperature of 485 °C evidently shown by the peak in DSC curve.

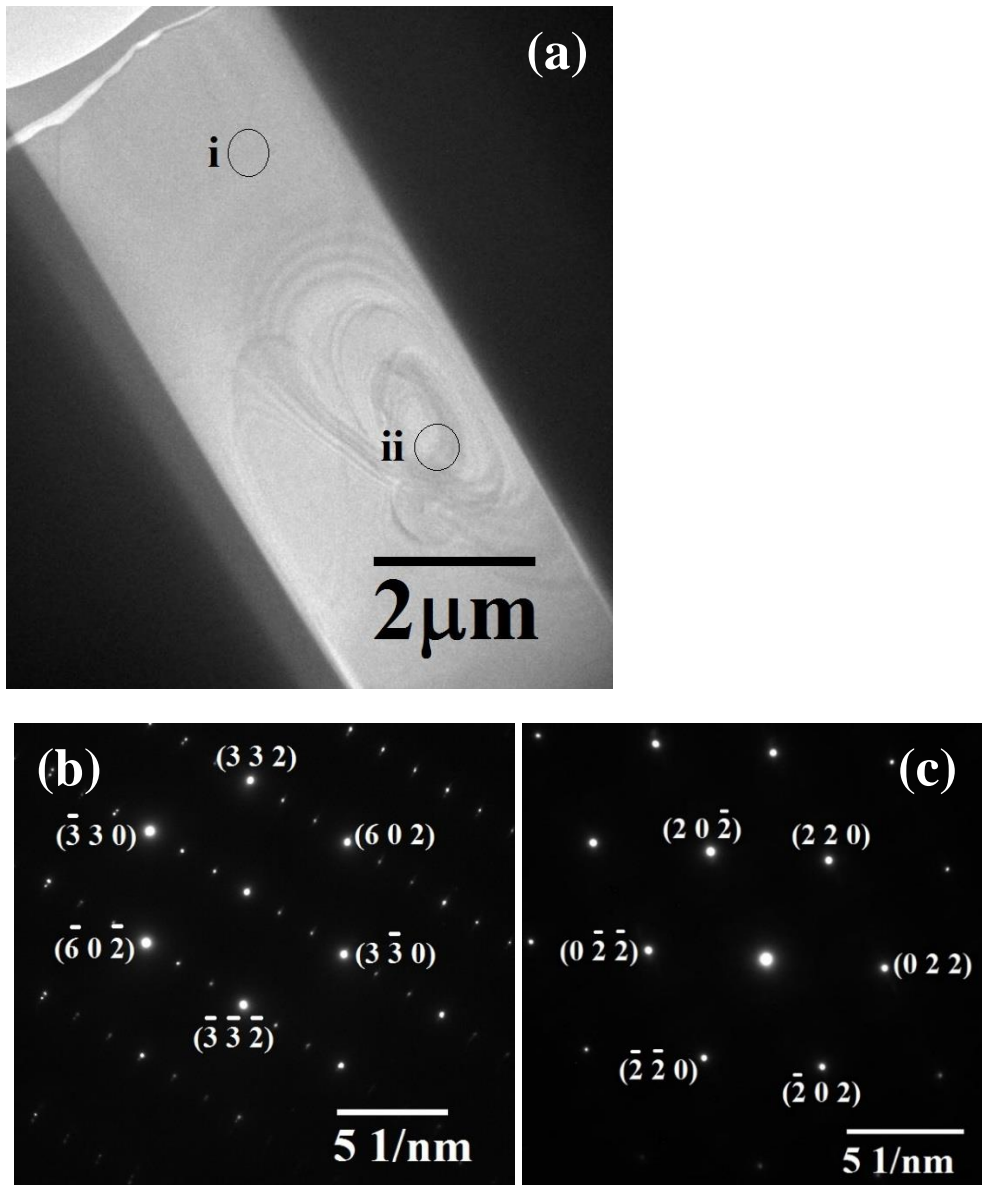


Figure 4.69 (a) TEM bright field image of a partially plate and lath structure (ϵ) and surrounding matrix material in a $\geq 850 \mu\text{m}$ size fraction, (b and c) selected area diffraction patterns from regions (i) and (ii) identified in the bright field image (i) matrix materials well away from the plate and lath structure, (ii) inside the structure.

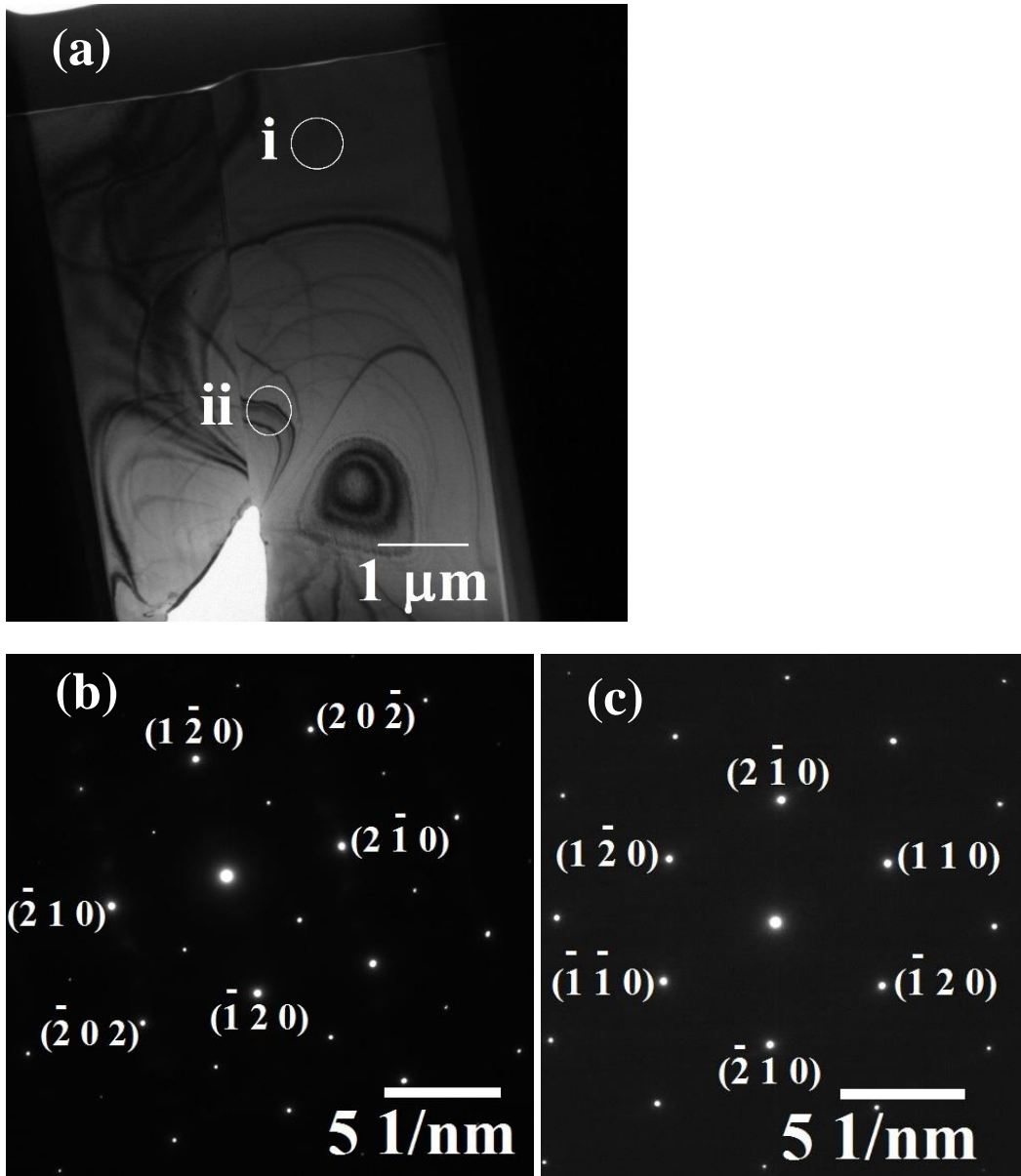


Figure 4.70 (a) TEM bright field image of a plate and lath structure and surrounding matrix material in a 500 – 300 μm size fraction, (b and c) selected area diffraction patterns from regions (i) and (ii) identified in the bright field image (i) matrix materials well away from the plate and lath structure, (ii) inside the structure.

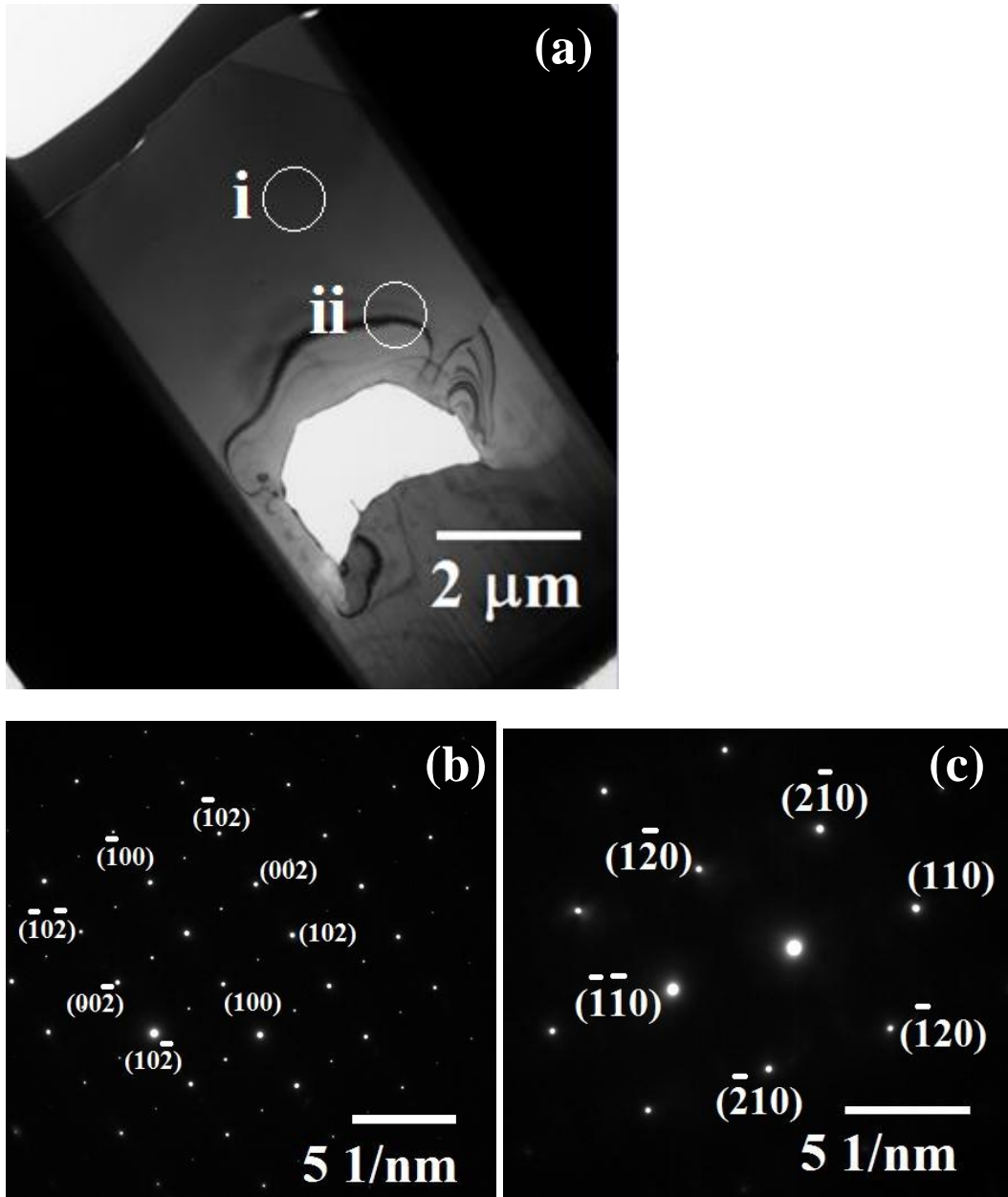


Figure 4.71 (a) TEM bright field image of a plate and lath structure and surrounding matrix material in a 150 – 106 μm size fraction, (b and c) selected area diffraction patterns from regions (i) and (ii) identified in the bright field image (i) matrix materials well away from the isolated faceted hexagonal crystallites microstructure, (ii) inside the isolated faceted hexagonal crystallites microstructure.

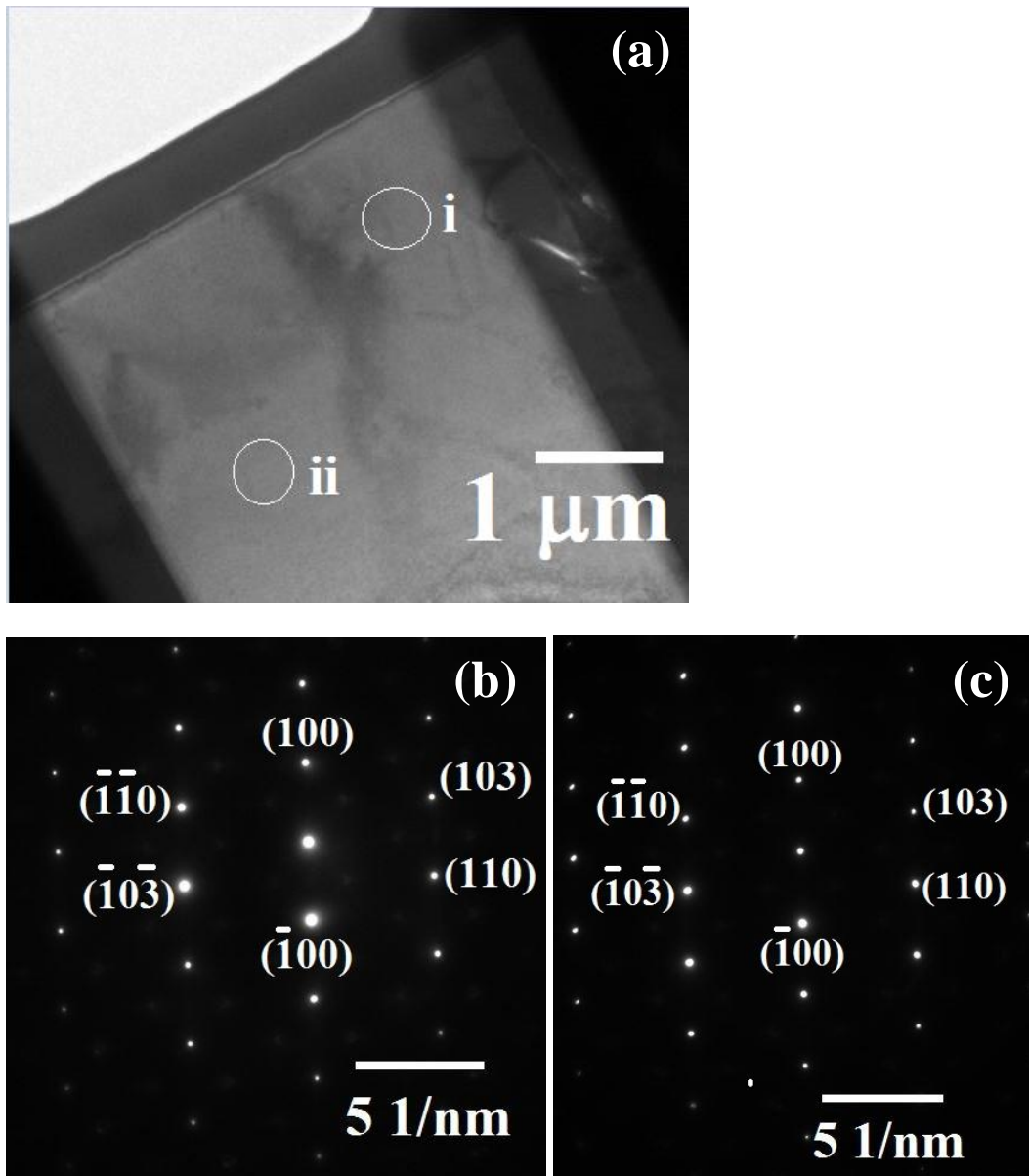


Figure 4.72 (a) TEM bright field image of a plate and lath structure and surrounding matrix material in a 53 – 38 μm size fraction, (b and c) selected area diffraction patterns from regions (i) and (ii) identified in the bright field image, two different regions of matrix materials.

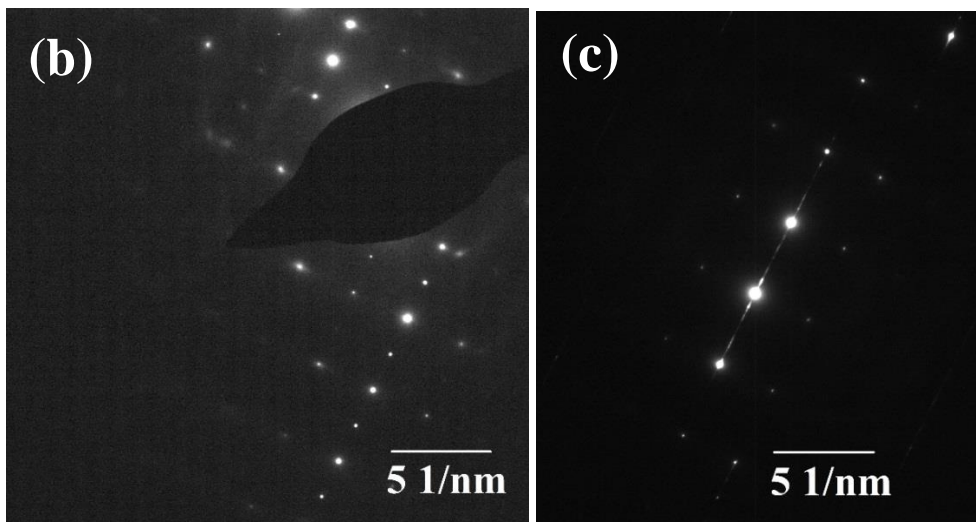
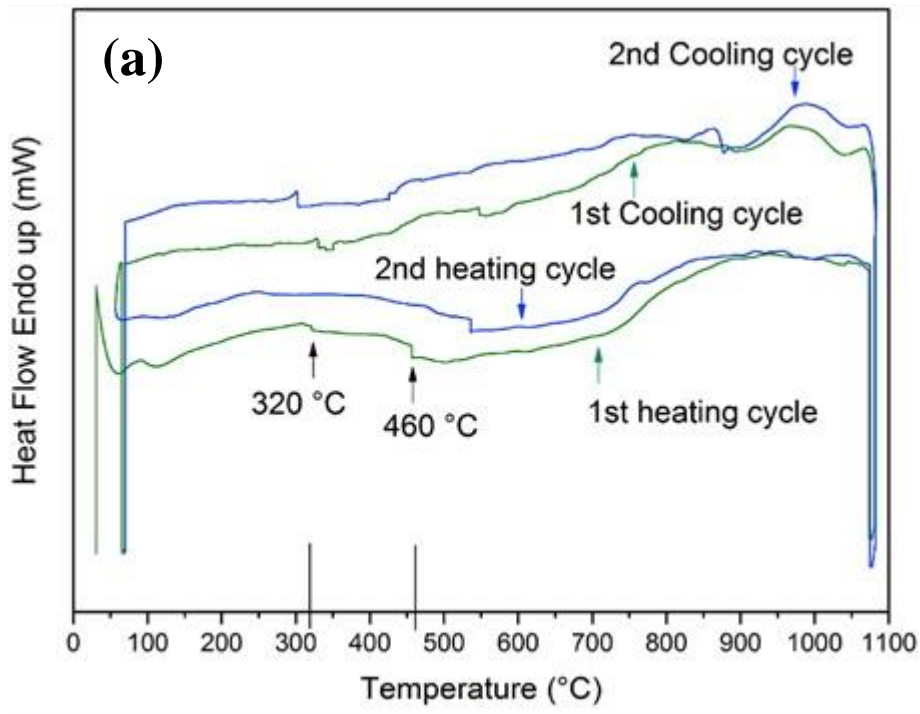


Figure 4.73 (a) DSC trace from a Ni_5Ge_3 drop-tube particle from the 150 – 106 μm size fraction, 1st and 2nd cycle indicated by green and blue respectively, two vertical black line shows the transition temperature at 320 to 460 $^\circ\text{C}$ and (b) TEM (In-situ) SAD pattern taken from **Figure 4.58** at room temperature (ordered) and (c) SAD of the same area but at 485 $^\circ\text{C}$ (disordered).

4.5 Microhardness

In order to determine the effect of cooling rate upon mechanical properties, Vickers micro-hardness tests have performed on the spherulites, mixed spherulites and dendrites, dendrites (orthogonal), dendrites (non-orthogonal), recrystallised, mix recrystallised and seaweed and dendritic seaweed microstructures of intermetallic compound β -Ni₃Ge, rapidly solidified drop-tube sample size from the ranges $\geq 850 \mu\text{m}$ to $\leq 38 \mu\text{m}$. The results of this are shown in the **Figure 4.74**. The maximum hardness, 526 Hv0.01, was observed in smallest size drop-tube sample $\leq 38 \mu\text{m}$ diameter particles (dendritic seaweed) . Conversely, the minimum hardness, 148 Hv0.01, was observed in the large drop-tube sample 106 – 75 μm diameter particles (dendrites – non-orthogonal).

Similarly, Vickers micro-hardness tests were also performed on the plate and lath microstructure, isolated faceted hexagonal crystallites and single crystal structure samples, with our second intermetallic compound Ni₅Ge₃, rapidly solidified drop-tube sample size from the ranges $\geq 850 \mu\text{m}$ to $\leq 38 \mu\text{m}$, to determine the effect of cooling rate upon mechanical properties. The results of this are shown in the **Figure 4.75**. The maximum hardness, 1021 Hv0.01, was observed in smallest size drop-tube sample $\leq 38 \mu\text{m}$ diameter particles (single crystal) . Conversely, the minimum hardness, 671 Hv0.01, was observed in the larger drop-tube sample 75 – 53 μm diameter particles (faceted hexagonal crystallites).

It can be concluded that the mechanical properties can be altered (hardness increased) by increasing the cooling rate (except sample size 106 – 75 μm of Ni₃Ge and sample size 75 – 53 μm of Ni₅Ge₃), in the cases studied here for both intermetallic compounds Ni₃Ge and Ni₅Ge₃ from ≥ 700 to $\leq 54500 \text{Ks}^{-1}$. Further, we will explain this behaviour in the next chapter.

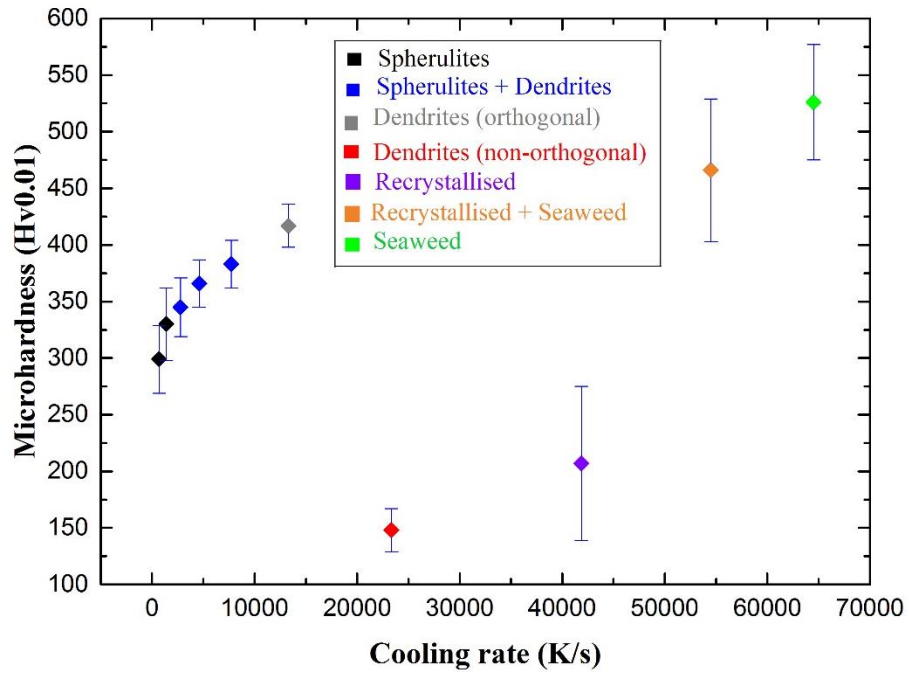


Figure 4.74 Micro-hardness value of Ni_3Ge compound as a function of droplet diameter ranges from $\geq 850 \mu\text{m}$ to $\leq 38 \mu\text{m}$.

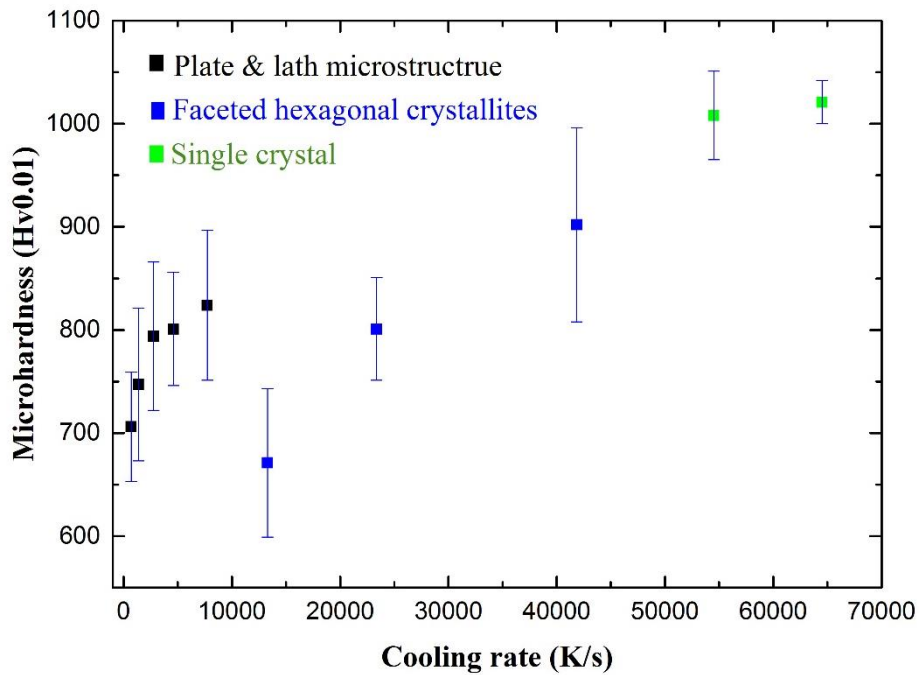


Figure 4.75 Micro-hardness value of Ni_5Ge_3 compound as a function of droplet diameter ranges from $\geq 850 \mu\text{m}$ to $\leq 38 \mu\text{m}$.

Chapter 5 Discussion

In this chapter, we will discuss all the results of our two congruently melting compounds (Ni_3Ge and Ni_5Ge_3), presented in the previous chapters. In this discussion, the primary focus will be the morphology of the observed microstructures that is the consequence of the rapid solidification process (drop-tube). We will also discuss the effect of the cooling rate on the microhardness and microstructures of these two compounds. Finally, we will compare the microhardness results of Ni_3Ge and Ni_5Ge_3 compounds.

5.1 Ni_3Ge Compound

$\beta\text{-Ni}_3\text{Ge}$ is a congruently melting compound, which makes it an ideal system for studying the solidification morphologies associated with high growth rate disorder trapping. $\beta\text{-Ni}_3\text{Ge}$ is also an ideal system because the disorder trapping should occur without the complication of solute trapping.

$\beta\text{-Ni}_3\text{Ge}$ system has been examined before by Ahmed *et al* [15], who performed the undercooling experiments on the same compound. In this experiment, a maximum undercooling of 362 K was observed using a melt-fluxing technique. Although, Ahmed *et al* examined evidence of order and disorder characteristics in this compound, on the velocity-undercooling curve. They observed a discontinuous break in the curve at the onset of fully disordered development. For $\beta\text{-Ni}_3\text{Ge}$, this condition was met with an undercooling of 168 K and with a critical growth velocity of 0.22 m s^{-1} . However, Ahmed *et al* could not get ordered-disordered material as solidified samples. As in the melt flux technique, the cooling rate was slow, therefore the whole sample became ordered only. For this reason, they did not observe an absence of superlattice spots in the solidified sample. In contrast, for this project, we use drop-tube processing technique to explore the rapid solidification behaviour of $\beta\text{-Ni}_3\text{Ge}$. Drop-tube processing is unlike melt flux undercooling techniques. It enables access to high post-recalescence cooling rates in which inherently unstable structures can be retained. Moreover, in the case of smaller droplets sizes, there is a much higher probability that the original solidification morphology will be retained. However, a somewhat surprising outcome of this work on the $\beta\text{-Ni}_3\text{Ge}$ compound, discussed in detail below,

is the ubiquitous occurrence of spherulites, dendrites (orthogonal and non-orthogonal), dendritic seaweed and recrystallised microstructure.

Nonetheless, in flux undercooling experiments ($\sim 10 \text{ K s}^{-1}$), the post-recalescence cooling rate is extremely slow. This means that any evidence of a microstructural kind that relates to disorder trapping will have been extensively modified in the as-solidified sample. In this situation, there is no chance of examining APD's or even disordered material that have been retained. Therefore, Ahmed *et al* did not observe the above mentioned anomalous microstructures even during etching that used the same chemical composition of etchant ($\text{HF}+\text{HCl}+\text{HNO}_3$). We can infer that in the case of Ahmed *et al* using melt flux undercooling produced a $\beta\text{-Ni}_3\text{Ge}$ sample in which everything was ordered. While, in our case (drop-tube technique), our sample had residue disordering. That is why we observed spherulites, dendrites (orthogonal-non-orthogonal), dendritic seaweed and recrystallised microstructures that were disordered with their respective ordered background matrixes. For this reason, in our case, the same chemical etchant was preferentially dissolving the dis-ordered materials only. Consequently, it only revealed disordered materials and produced a range of different microstructures. These different microstructures were produced within different sizes of drop-tube particles under the different cooling rates.

5.5.1 Spherulites Morphology

A surprising outcome of the $\beta\text{-Ni}_3\text{Ge}$ was the ubiquitous occurrence of spherulites. This morphology (spherulites) is rare in intermetallic compound. Spherulites are commonly found in a range of materials, including small molecule organic crystals and polymers. They are also found in other materials, including inorganic crystals, volcanic rocks and a few pure elements (e.g. graphite, sulphur and selenium). However, spherulite development is much rarer in metals that are fully crystalline, sometimes in cast iron (graphite), albeit they are noticed in partially crystalline glass forming alloys, both as residual crystals subsequent solidification and as devitrification products [56].

As mentioned above, spherulites are most common in polymers and small molecule organic crystals. They are especially common in high molecular weight polymers, which have been grown directly from the melt. In these, the long chain molecule

reorientation is restricted by topological constraints. The structure of these kinds of spherulites is characterised by multiply branched crystalline arms, which are separated by amorphous regions between the arms [56]. Spherulites are most common in systems that are unoriented. The suppression of spherulite growth appears where there exists a strong tendency for uniform molecular orientation: for example, in the case of growth that occurs in a gradient of strong, externally imposed temperature [57]. Polymers and metallic glasses are characterised by low diffusivity. Consequently, it is probable that kinetics dominates the development of spherulites. Additionally, the anisotropy of polymers tends to be relatively low.

Similarly, spherulites are also common in amorphous metallic systems. After the glass transition temperature has been reached through a heating process, several amorphous metallic systems (metallic glasses) undergo crystallisation, transforming to the morphology of spherulites. In some respects crystallization from the melt and crystallisation from a metallic glass precursor are comparable, while in other ways it can be different. The principal difference is that in a metallic glass the viscosity of a glass is much higher as compare to that of a melt. In an analogous way, in comparison to a melt of an equivalent composition, the atomic diffusivity is much lower in a glass. As a result, crystallisation from a glass can, but is not always, restricted to short range diffusion that is to say that the atom rearrangement occurs without bulk solute redistribution. In turn this means that it is crystallisation that is dominated by growth kinetics, not diffusion.

In our system (β -Ni₃Ge), a similar situation may be said to exist in the growth of β -Ni₃Ge from its parent melt. There is no need for long range solute transport by diffusion since the compound is congruently melting. This agrees with EDX measurements. These measurements indicate that, within experimental uncertainty, the spherulitic chemical composition is the same as that of the surrounding featureless matrix material. This is also the case for dendrite (orthogonal and non-orthogonal), dendritic seaweed and recrystallised microstructures. In relation to the growth of the spherulite it is possible to postulate that thermal transport within these large particles is fast enough for the droplet to approximate isothermal solidification conditions. The domination of kinetics occurs under these conditions, resulting in a spherulite morphology with kinetically favoured fine needle. Moreover, since spherulites are

only partially disordered, slow growth is likely to occur (ordered phases grow much more slowly than disordered phases) which will favour an isotropic morphology.

In our system, in a β -Ni₃Ge compound, we found numerous spherulite like structures. SEM micrographs show the polished and etched sections from the four sieve size sections $\geq 850 \mu\text{m}$, $850 - 500 \mu\text{m}$, $500 - 300 \mu\text{m}$ and $300 - 212 \mu\text{m}$ (**Figure 4.7 – 4.10**). Numerous spherulite morphologies are visible in the two largest sieve sizes (**Figure 4.7 and 4.8**). Their range of diameter is typically $10\text{-}20 \mu\text{m}$. In a background that is without features, the only solidification morphology observed in these sizes of droplet is of the spherulites. Spherulite morphologies still appear in the smaller sieve sizes, $500 - 300 \mu\text{m}$ and $300 - 212 \mu\text{m}$ (**Figure 4.9 and 4.10**). However, these spherulite now smaller in size and coexist with dendrites. There are also isolated spherulites that coexist with a very prominent pseudo-dendritic structure that comprises orthogonal linear arrays of spherulites. This was obtained from the $300 - 212 \mu\text{m}$ sieve fraction (**Figure 4.10**), and is particularly notable. The top left of the figure shows this particularly well. Linear groups of spherulites are seen to compose the secondary arms of the dendritic structure. From the image, it cannot be known if the dendrite grew with the morphology or if, due to some process of decomposition, for instance, the spherulites formed after the initial dendritic growth. Below, this question is explored further, while noting that we found that classical dendrites become the dominant solidification morphology when further increase in cooling occurs.

By subjecting samples (all spherulites microstructures) from all 4 sieve fractions (**Figure 4.7 – 4.10**) to XRD analysis (**Figure 4.5**), it was confirmed that, irrespective of the imposed cooling rate, the material/compound fully remains single phase β -Ni₃Ge. As such, no variation in chemical composition would be expected within the sample and this has been confirmed by taking a number of EDX line and area scans (**Figure 4.17a**). These EDX scans results showed that the material is chemically homogenous with a composition consistent with β -Ni₃Ge. The contrast that exists between the spherulite and the featureless material from the matrix surrounding it does not appear to result from compositional differences that would result from solute partitioning during solidification. The contrast does not seem to relate to phase differences either. Rather, we believe (it is also confirmed via TEM) that the unambiguous difference is due to a difference between disordered (or partially

disordered) material within the spherulites and a featureless matrix that is ordered. In etching comparison to the disordered material, the ordered material would be more resistant to the chemical attack of the acids used. This conjecture is based on the observation of the behaviour of other intermetallic compounds, in the ordered and disordered state. However, it is not a certain conclusion as we did not measure the chemical resistance of ordered vs disordered in our compound β -Ni₃Ge (we proposed this work for future work/analysis). This is significantly different from instances of spherulitic growth, which occur from the melt in metals in a direct way. In those instances, the spherulites are typically two distinct phases with different crystallography.

In the TEM bright field image of a typical spherulite structure (**Figure 4.37a**), many fine filament like crystallites radiating out from the centre of the spherulite are clearly visible. The SADP results of origin of spherulites does not show the presence of superlattice spots (**Figure 4.37b -i**). This indicates that disordered material is the origin of spherulites. However, the superlattice spots are clearly evident within the diffraction pattern, which indicates that the material displays at least partial chemical ordering within the spherulites (**Figure 4.37c - ii**). The same is also true of the featureless background material (**Figure 4.37d - iii**).

Detail of the spherulite structures in each of the sieve fractions between $\geq 850 \mu\text{m}$ to $212 \mu\text{m}$ are shown in the TEM dark-field images **Figure 4.38 (a-d)**. In these images, only the chemically ordered material is illuminated because the images came from one of the superlattice spots in the diffraction pattern of the SAD. Ordered material lamella separated by inter-lamella material of the disordered phase is seen to compose the spherulites in all of the cases. From this, we can make an inference about the origin of the contrast that occurs during the etching and the solidification pathway giving rise to the spherulite structures. It is difficult to think what else might give rise to the contrast, since the material within the droplets is chemically homogeneous, single phase β -Ni₃Ge. In the dark-field images, one notes in the spherulites the presence of disordered material which is clearly evident within the dark-field images presented in **Figure 4.38 (a-d)** that relate to the second point above. Since β -Ni₃Ge orders at all temperatures below the melting point during equilibrium solidification, the material that comprises the spherulites must have, during growth, been subject to a degree of

disorder trapping. This suggests that the spherulites grew from the undercooled melt during the recalescence phase of solidification. Consequently, the solid fraction formed during recalescence will be reflected in the spherulitic material volume fraction in the sample f_s , given by $f_s = \Delta T \cdot c_p/L$, where c_p and L are the specific heat and latent heat upon fusion respectively. The solidification of the residual liquid (volume fraction $1 - f_s$) will occur following recalescence. This will occur close to equilibrium and therefore to the ordered form of β -Ni₃Ge, giving rise to the matrix material in which the spherulites are embedded. The matrix is resistant to chemical etching, due to the chemical ordering. This is why it appears featureless after etching.

Spherulites are not all align with the crystallographic directions of an fcc structure. Non-crystallographic branching are seen to maintain space-filling, which can be seen most easily with respect to **Figure 4.38b**. In this regard, the observed spherulites have entirely similar with Category 1 polymer spherulites. Here, we seem to be observing a contrast in the same crystal structure between an ordered and disordered variant, instead of between crystalline lamellae in an amorphous matrix (the case for polymer spherulites or those observed in a metallic glass's devitrification). Additionally, in certain cases (**Figure 4.38 b-d**), the widths of the lamellae appear to be nearly constant. The measured lamellar size as a function of drop-tube cooling rate is shown in the **Figure 4.39**. The average lamellar size decreases from 0.45 μm at a cooling rate of 700 K s^{-1} to 0.11 μm at a cooling rate of 4600 K s^{-1} . The non-constant lamellar widths seen in the $\geq 850 \mu\text{m}$ sample are shown in **Figure 4.38a**. These are indicated by the very large error bar corresponding to the measurement for the $\geq 850 \mu\text{m}$ sieve size fraction. There is a clear enough trend, despite this, for the lamellar width to decrease with the decrease of the particle size (the increase of the cooling rate). With decreasing particle size, the melt undercooling would be expected to increase in these droplets. This is because high cooling rate leads to high undercooling, but also due to the effect of melt sub-division by which, in the smaller melt volume, the potential heterogeneous nuclei are potentially smaller in number. There is further correspondence with theoretical models of spherulite formation based on polymeric materials [117], where such a trend has also been observed. Moreover, Jackson and Hunt presented a theory for the growth of lamellar and rod eutectics in which the lamellar width is related to the undercooling and growth. They described the relationship between lamella spacing growth and undercooling rate in terms of $\lambda \propto 1/\Delta T$ [118]. They proposed an inverse

relationship between lamella spacing and undercooling rate, such as if undercooling goes up then lamella spacing goes down. These kinds of relations with spherulites lamella spacing are also observed in our system. However, Jackson and Hunt studied this phenomenon in relation to lamellar spacing and undercooling, not cooling rate. However, for small droplets it would be expected that undercooling will increase in the smaller size fractions, both due to increased cooling rate and the melt sub-division effect. Consequently, a reduction in lamellar spacing with decreasing droplet size is expected, although we cannot determine the actual undercooling of the droplets. However, we also observed the same inverse relationship between spherulites lamella width and drop-tube cooling rates ($\lambda \propto 1/\Delta T$). As we increased drop-tube cooling rate from 700 K s^{-1} to 4600 K s^{-1} , then the width of lamella also decreased from $0.45 \text{ }\mu\text{m}$ to $0.11 \text{ }\mu\text{m}$.

There are two plausible scenarios for trying to understand the origin of the spherulite structures that have occurred in this experimental work:

The spherulites consisting of ordered lamellae, grew directly from the melt in the observed form. In this case it would seem likely that each lamellae grew along a preferred crystallographic direction and that this direction differs from one lamellae to the next.

The spherulites grew as the disorder variant of the $\beta\text{-Ni}_3\text{Ge}$ phase and ordered subsequently in the solid-state. If this is the case, then the crystallographic direction of all lamellae growth would likely have been the same but the chemical ordering would have been distinct.

To understand the origin of the morphology of the spherulitic structures, EBSD analysis was also performed on freshly prepared samples that were polished using $0.1 \text{ }\mu\text{m}$ colloidal silica and without etching in order to distinguish the two alternatives. The XRD analysis shows that all samples are completely single-phase $\beta\text{-Ni}_3\text{Ge}$ is further confirmed by the EBSD phase map for all samples (one of example shown in the **Figure 4.6**). The EBSD Euler map (**Figure 4.19a**) shows very clearly the $850\text{--}500 \text{ }\mu\text{m}$ sample grain structure. There appears a large number of grains, typically of a $30\text{--}50 \text{ }\mu\text{m}$ diameter. The grain orientation histogram (**Figure 4.19b**) shows that the each grain's orientation in relation to the next is look-like random. With one possible exception the spherulites are not visible in EBSD, a notable point that is discussed

below. This contrasts with the SEM secondary electron images in which a minimum of one spherulite is contained in each grain. What we can infer from the invisibility of the spherulites, the size of which could be resolved by EBSD, is that the spherulites' crystallography must be contiguous with the grains in which the spherulites are embedded.

This too is consistent with TEM diffraction analysis, in which sharp diffraction spots are apparent. The appearance of these spots is consistent with the beam being focused on an area that has a single crystallographic orientation. As such the available is consistent with spherulites growing as a disordered phase, with subsequent solid-state ordering. There may be an instance of a spherulite appearing in the EBSD map as a dark circular region. This dark circular region is embedded in a grain of a lighter shade (see top right hand arrow of **Figure 4.19a**). Yet, even in this case, the spherulite is characterised by a crystallographic orientation that is throughout uniform and not consistent with non-crystallographic branching.

A comparatively consistent view of spherulite formation in ordered intermetallics at high cooling rate may be established on the basis of the given evidence, and is shown schematically in the **Figure 5.1**. Melt undercooling is favoured by rapid cooling and the melt dividing into numerous small droplets. In this case, undercooling is favoured by an amount ΔT . As the droplet size decreases, ΔT increases. At some temperature T_N nucleation occurs, which starts the recalescence phase of solidification. In this time, growth of the spherulite precursors occurs. At this stage, due to rapid solidification causing disorder trapping, this process most probably occurs as a fully disordered solid. Partial reordering occurs a short time after the disordered phase growth. This may occur during the plateau phase of solidification during which the residual liquid and the solid formed during recalescence coexist. In the partial reordering, ordered filaments grow radially outward from the centre. This leaves, in the spaces between the filaments, residual disordered material. Since the temperature of the droplet is, at this stage, close to the melting temperature, reordering of the disordered material is feasible. Moreover, it is common during the solidification of undercooled melts. Near isothermal solidification occurs in the residual liquid, on account of the extraction of heat from the droplet during the plateau phase. The featureless ordered matrix that embeds the spherulites since the process occurs close to equilibrium.

The growth of spherulites in polymers shows similarities to this process. These similarities include the constant width of the filaments within a spherulite. Being a function of undercooling during growth, the filament width decreasing as cooling rate increases. Additionally, the filaments branch at non-crystallographic angles in order for the space-filling to be maintained. In intermetallics case, it appears that a contiguous underlies the crystallography and that the branch is only at the level of the chemical ordering.

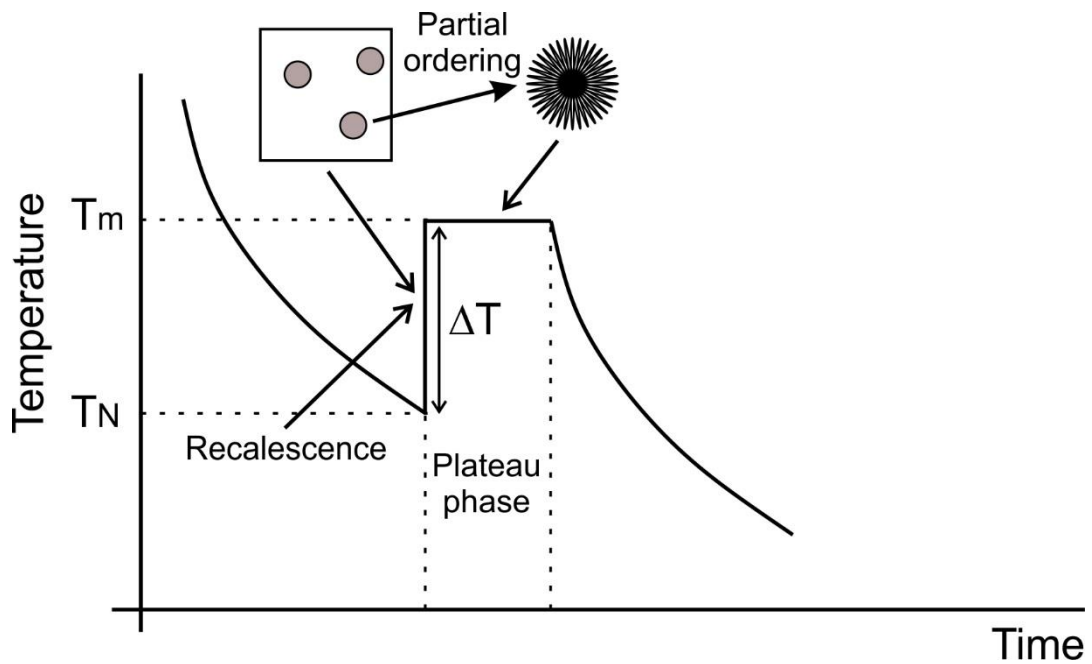


Figure 5.1 Schematic diagram showing proposed model for spherulite formation in β - Ni_3Ge with initial growth to the disordered phase during the recalescence phase of solidification followed by partial reordering during the plateau phase.

5.1.2 Dendrites Morphologies (orthogonal and non-orthogonal and seaweed

Dendritic morphologies are first observed in our compound β -Ni₃Ge, within the drop-tube sieve fraction that ranges from 500 – 300 μm (cooling rate $> 1400 \text{ K s}^{-1}$). For particles with a diameter of 150 – 106 μm (cooling rate $> 7800 \text{ K s}^{-1}$), the dendritic morphology is the predominant one. It is well evidenced in [109] that droplet solidification techniques, including drop-tube processing or gas atomization results in a rapid increase of undercooling in the droplet as the size of the droplet decreases, due to increased cooling rates and the sub-division of the melt. There are two possible explanations of this mechanism. The first explanation is that with increasing undercooling the growth rate will increase. Additionally, the need for efficient diffusion of heat from the growing solid leads to the formation of thermal dendrites. By this it is meant that the dendrites form as a result of growth into a negative temperature gradient, which destabilises the solid-liquid interface. The second explanation derives from Ahmad's [15] work suggests that there is a critical undercooling temperature above which a rapid increase in growth velocity occurs because of a transition to fully disordered growth. In this case, the faster growth would then require the need for dendritic morphologies to diffuse the latent heat away efficiently. In line with most materials we may assume that it is normal capillary anisotropy that gives rise to the directionality observed in the dendritic structures. The second explanation is more plausible because at low cooling rate we observed spherulites (partially ordered), while at high cooling rate the dendrites (completely disordered) were observed.

The spherulites grew as the disorder variant of the β -Ni₃Ge phase and ordered subsequently in the solid-state. If this is the case, then the crystallographic direction of all lamellae growth would likely have been the same but the chemical ordering would have been distinct. It remains unclear whether any other transition in the growth mechanism coexists with the transition that occurs to dendritic growth. Nevertheless, it seems natural to assume that there would be a connection between the transitions from the spherulitic to dendritic growth morphology with the transition to fully disordered growth observed by Ahmad *et al.* at an undercooling of 168K. Another proposition follows from this: the spherulitic structures observed in this case are only partially disordered, and the spherulite structure is a composite of ordered-disordered. This might be considered as an analogue of the crystalline-amorphous type of

spherulites observed in polymers, rather than the eutectic type more common in metals grown from their parent melt. Furthermore, the low velocity of growth observed at low undercooling [119] would be explained by the residual ordering that occurs in these structures.

The SEM micrograph of a polished and etched sample from the drop-tube sieve fraction 212 – 150 μm / 150 – 106 μm (**Figure 4.11/4.12**), shows that well dendrites with orthogonal side-branching constitutes the dominant morphology. This dominant morphology imbedded within a featureless matrix. With regards to the visible contrast between the surrounding matrix material and the dendrites region, TEM SAD (**Figure 4.40**) confirmed that these differences are due to a difference in a chemical ordering. The dendrites regions show a disordered structure (without superlattice spots), while featureless matrix material show an ordered structure (with superlattice structure).

It should also be noted that the TEM analysis shows the material is completely crystalline. With a particle size reduction to 106 - 75 μm (**Figure 5.2a**), the dendrites demonstrate rapid solidification traits that are typical, despite the morphology of the solidification remaining dendritic. Side-branches appear no longer orthogonal in relation to the central trunk. Irregular splitting of arms also occurs as if the branches were taking a character of a doublon type. Predominantly, for the dendrite towards the top of the droplet as pictured (sketched in red in **Figure 5.2b**), there is a variance in the angle in-between the primary trunk and the secondary arms. The angle varies between 45° at the left of the droplet (as viewed) to 63° at its right-hand end. Giving a mean variation of 51.2° . There is an 18° change in the direction of the trunk calculated over its growth length. Conversely, for the dendrite close to the centre of the droplet (sketched in blue in **Figure 5.2b**), the angle between the primary trunk and the longer part of the secondary arms (also shown in blue) is close to 45° along the whole length of the dendrite. Although, for the smaller branches that come out near the root of each secondary arm (shown in green), the angle is closer to 30° .

Transitioning from orthogonal to non-orthogonal side-branching with an increase of the undercooling in a cubic system is indicative of a direction change of the primary growth. It is a move away from the kind of direction growth that is likely at equilibrium [100], which has been noticed before in a number of systems [81].

A similar change has been observed before, as precursor to an evolution from a dendritic to dendritic seaweed transition [79]. This dendrite's curvature is particularly distinctive, with the direction of the growth changing by approximately 30°. Such curved dendrites have been noted before to have been caused by flow during rapid solidification [120]. However, this is not plausible in this case as the droplet size is most probably too small. Instead, it may be better understood as being indicative of a general decrease in directionality within the microstructure.

From the microstructure previously shown (**Figure 4.11**), two selected area diffraction patterns have been obtained (**Figures 4.40b and c**). One of them has been taken from the featureless matrix material, far from the dendrite (**Figures 4.40c**). This is consistent with the ordered L12 crystal structure that would be expected to be associated with β -Ni₃Ge. In contrast, an area diffraction pattern from the center of the dendrite (**Figures 4.40b**) shows a cubic structure that has the same lattice spacing as the matrix material. Nevertheless, there is an absence of superlattice spots that would indicate an ordered structure. This is suggestive of the disordered form of the material being the dendrite, the dendrite being a simple A1 fcc random solid solution. In order to interpret these phenomena, we may postulate that the dendrites, being the rapid solidification morphology, developed as the form of β -Ni₃Ge that was disordered. This form of growth would be due to extensive disorder trapping. We may also postulate that the material of the matrix would have developed post-recalescence. Then, due to the much lower rate of growth, it would have developed as the ordered form of β -Ni₃Ge.

Now we turn to the selected area diffraction pattern (**Figure 4.41b**) obtained from the dendritic region (**Figure 4.41a**). The underlying crystal structure is the same as the one found in the larger droplets. This is despite the somewhat inconsistent character of the morphology of the dendrite, which shows evidence of splitting of tips and shows side-branches developing at varying angles in relation to their primary trunks. The data from the TEM show clearly that the transition in morphology of the dendrite does not arise from a change in phase present, but rather arises within the same crystal structure from a preferred growth direction change.

A dense branched fractal/ dendritic seaweed morphology (**Figure 4.15a**) and also a mix of recrystallised microstructure along with dendritic seaweed structure (**Figure 4.15b**) observed in the same droplets (53 – 38 μm) with a cooling rate that may

approach $40,000 \text{ K s}^{-1}$. Here, we will discuss only seaweed dendritic structure and recrystallised structure will be discuss separately. Dendritic seaweed structures are not unusual at very large departures from equilibrium [81, 86]. Furthermore, these kinds of structures indicate a loss of directionality that occurs during growth. This may be due to a competition occurring between differently directed capillary and kinetic anisotropies [121], or it may be due to the crystalline anisotropy's strength becoming weaker at high growth velocity. It is also likely that, somewhat irregular or distorted dendritic morphology (**Figure 5.2a**) has been caused by the loss of directionality. Similar morphologies have been observed before at undercoolings just lower than those which produce 'dendritic seaweed' morphologies [79, 81].

The morphology at a dendritic seaweed is clearly shown in the SEM micrograph and the corresponding TEM selected area diffraction pattern from a droplet in the $53 - 38 \mu\text{m}$ sieve fraction (**Figure 4.15a**). It shows multiple splitting of tips. It is also evident that it shows a lack of directionality. While the indexing of TEM selected area diffraction pattern is not unambiguous (**Figure 4.44b**), it seems to not be conforming to the $L1_2$ cubic model.

Finally a dense branched fractal/dendritic seaweed morphology also observed in the smallest droplets $\leq 38 \mu\text{m}$ with a cooling rate that may approach $\leq 54,000 \text{ K s}^{-1}$. However, in these ranges of drop-tube samples only dendritic seaweed was observed (**Figure 4.16**). TEM SAD pattern also showed different diffraction pattern in comparison to $53 - 38 \mu\text{m}$ droplets dendritic seaweed. In the smallest droplet sample, SADP shows similar results of orthogonal and non-orthogonal dendrites in reference to disordered materials within the dendrites region and ordered material within the featureless matrix (**Figure 4.46**). Therefore, on the basis of TEM selected area diffraction pattern, except one sample (**Figure 4.44b**), the $\beta\text{-Ni}_3\text{Ge}$ sample still confirms the $L1_2$ cubic model (**Figure 4.46c**). This goes in favour of seaweed formation model that is commonly accepted. With regards to the results of one of the dendritic seaweed structures (**Figure 4.44b**), the crystallography does not confirm the $L1_2$ cubic model. This one observation is unexplained. However, we think that this occurrence may be characteristic of intermetallics or maybe specific to this compound. For there is no evidence of any solid-solution alloy displaying a similar kind of modification, by which there would be a coincidence between a change from the

dendritic to the seaweed and the underlying crystallography (there is also no report of any crystallographic determination from the seaweed morphology in NiAl [89]). One possible explanation may be that high levels of disorder in the orientational ordering that [89] postulate to be required for seaweed growth results in a severe distortion of the crystal lattice.

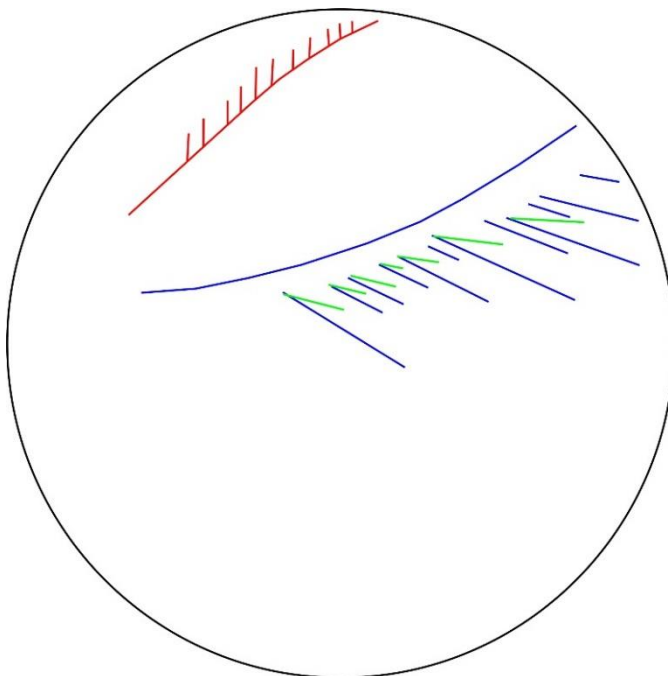
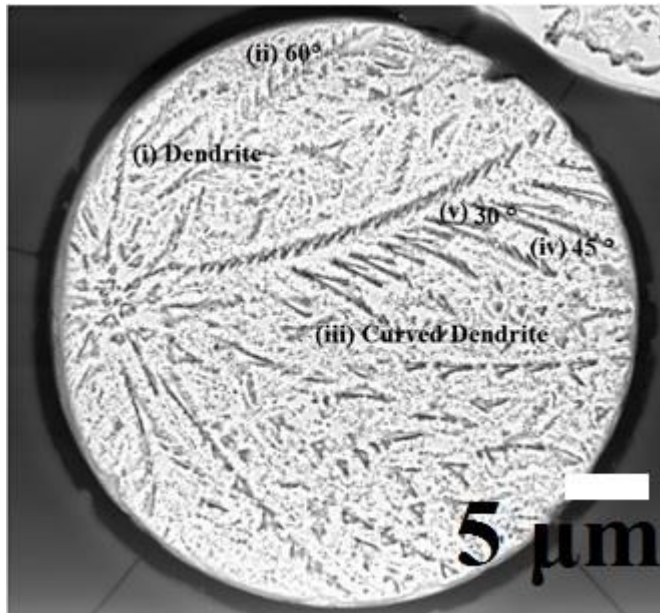


Figure 5.2 (a) SEM micrographs of HF etched β -Ni₃Ge drop-tube particles from the 106 – 75 μm size fraction showing dendritic structure with non-orthogonal side-branching and (b) sketch of same highlighting two bent dendrites with non-orthogonal side-branching.

5.1.3 Recrystallised Morphology

Finally, we are going to discuss another novel investigation (recrystallised microstructure) into spontaneous grain refinement in the same congruently melting intermetallic β -Ni₃Ge compound. As far as we are aware, this is the first report of SGR in a congruently melting compound which is free from solute partitioning and diffusion effects. This means that instead of acting like an alloy it conducts itself in a fashion more typical for a pure metal on account of being free from effects of diffusion and solute partitioning. During rapid solidification of β -Ni₃Ge and as the cooling rate increased, we observed and discussed above that a diverse set of solidification morphologies that included (in order of increasing cooling rate) spherulites, dendrites (orthogonal and non-orthogonal) and dendritic seaweed. We found that all the observed structures, whether spherulites, dendrites orthogonal and non-orthogonal and dendritic seaweed were made of partially (in the case of spherulites) or fully (in the case of dendrites and seaweed) disordered material. For spherulites material was partially disordered. For the dendrites and seaweed, it is fully disordered. This disordered material is embedded in a matrix of material that is fully ordered. The proportion of disordered material has also a tendency to increase as the cooling rate also increases.

A typical microstructure in a droplet from the 75 – 53 μm sieve fraction following etching is apparent, in which 23,000 – 42,000 K s^{-1} is the approximate cooling rate. Despite no specific features are observed before the etching, many crack-like features are apparent after the etching. Therefore, these features are not cracks despite their crack-like appearance (**Figure 4.14**). The image of EBSD band contrast (**Figure 5.3**) also shows that there is no clear relation between the underlying grain structure and the features that resemble cracks/‘crack-like’. In the image, there appears a structure that is very refined. This structure comprises lots of grains that are small ($< 1 \mu\text{m}$). Larger (2-10 μm) grains of a much smaller quantity are also intermixed with the small grains.

The manner in which this grain refined microstructure fits into the overall solidification sequence as a function of cooling rate is revealed in **Figure 5.4**, in which primary solidification morphologies (spherulites, dendrites and seaweed) are discussed above and also reported in [122]. Growth of a dendritic type can be seen in the two

immediately larger size fractions (a: 150 – 106 μm , 8,000 – 13,000 K s^{-1} ; b: 106 – 75 μm , 13,000 – 23,000 K s^{-1}). In the case of a metallic melt, this is predictable. In the fractions that are smaller, the dendrites show non-orthogonal side-branching. This indicates a shift in the direction of the growth. In contrast, within the size fraction that is immediately smaller (c: 53 – 38 μm , 42,000 – 62,000 K s^{-1}), we can clearly observe the formation of dendritic seaweed, which is a morphology that is found solely at very large departures from equilibrium [79, 86].

It is clear from the grain orientation's histogram of the material in the 75 – 53 μm sieve fraction (**Figure 4.25b**) that misorientations of grain boundary of either $< 10^\circ$ or close to 60° are in the majority. This distribution is unexpected in the case of randomly nucleated grains [123]. The microstructure appearance is suggestive recrystallization and recovery that produces grain refinement. This is apparent in the grain sizes that have distributed in an extremely inhomogeneous way. It is also apparent in the very high number of low angle grain boundaries. Due to grains that have been randomly nucleated [123], this is not the kind of distribution that one would expect. The microstructure appearance is suggestive recrystallisation and recovery that produces grain refinement. This is apparent in the grain sizes that have distributed in an extremely non-homogeneous way. It is also apparent in the very high number of low angle grain boundaries.

In comparison, the grain orientation distribution of the immediately large sieve fraction (106 – 75 μm , 13,000 – 23,000 K s^{-1}) sample that corresponds to the deformed dendritic structures (**Figure 4.29b**) appears much closer to what we may expect for a random population of grains [123] (**Figure 4.24b**). From the corresponding grain orientation spread (GOS) data for the two samples (**Figure 4.30ab – 4.29ab**), one can see that in comparison to the 106 – 75 μm sample, the 75 – 53 μm sample (**Figure 4.30ab**) appears to have a considerably higher GOS. This indicates that in the faster cooling powders there are much higher density of dislocations. This suggests a potential driving force for recrystallisation and recovery. Through a comparison (**Figures 4.28 and 4.30a**), it is possible to see that within the 75 – 53 μm sample the low GOS regions correspond to small grain size regions. This is particularly the case with regions, which appear in the micrograph to be towards the centre of the lower edge and near the top right-hand edge. In these areas, this is indicative of

recrystallisation. By contrast, grains of large size can be correlated with high GOS regions in which it can be surmised that recrystallisation and recovery has not occurred because in these grains the local driving force has not yet reached the required level. It is equally clear that in the 106 – 75 μm the small GOS is indicative of insufficiency in the driving force for recrystallisation and recovery.

Next, the process that has produced the unusual ‘crack-like’ morphology apparent after etching needs to be addressed. We already established [124] and also discussed above that distinguishing between the ordered and disordered material is done by etching. A selected area diffraction pattern (**Figure 4.42b**) gives confirmation that the large blocky regions in-between the ‘cracks’ are indeed of the $L1_2$ ordered structure. This is apparent from the super-lattice spots visible in **Figure 4.42b**.

A high resolution TEM image (bright-field) of the structure of one of these block-like areas was made (**Figure 4.43a**). It also has a dark-field image (**Figure 4.43b**) that corresponds to it. The latter was derived from the super-lattice spot shown by the arrow (**Figure 4.42b**). Consequently, it shows ordered material as light. I should also be noted that the region susceptible to etching appears, in the dendritic and the seaweed morphologies, greater than for the crack-like structures.

From this we may speculate that the crack-like structures are regions of residual disordered material, which would appear between the areas that have been subject to reorder during the recrystallisation.

The microstructural and EBSD results discussed above provide a compelling evidence of spontaneous grain refinement by recrystallisation and recovery. This spontaneous grain refinement by recrystallisation and recovery occurs in a narrow size range of drop-tube processed, single phase $\beta\text{-Ni}_3\text{Ge}$ powders spanning the range of cooling rates 23,000 – 42,000 K s^{-1} . As a consequence of these results, new light is thrown on spontaneous grain refinement as a phenomenon, which is also consequent upon how these results fit into the material’s larger solidification sequence. Firstly, it has previously been assumed [101] that very high cooling rates could suppress SGR by recrystallisation, although here we see exactly that mechanism operating at estimated cooling rates up to 42,000 K s^{-1} . This suggests that cooling rate required for recrystallisation suppression varies depending on the material. Consequently, unless there is sufficient independent evidence these results show that it is not safe to assume

that the imposition of high cooling rates leads to the suppression of recrystallisation. For β -Ni₃Ge it appears to be the case that recrystallisation suppression occurs only when the rate of cooling is above 42,000 K s⁻¹ and in which the primary solidification morphology observed is of a dendritic seaweed type.

Secondly, it is noted that recrystallisation grain refinement at low undercooling has been observed by [79]. Contrastingly recrystallisation was observed by [86] at high undercooling. However, this recrystallisation process only occurred at undercooling that were higher than what is required for the change to seaweed morphologies. In contrast, in this study recrystallisation grain refinement can be observed, which occurred at lower undercooling temperatures than the temperatures requires for a change to dendritic seaweed. Similarly, in relation to the past work on SGR by recrystallisation and recovery in ordered intermetallics, [38] in the same manner found that recrystallisation happened at an undercooling rate only slightly above that required for the solid to develop in the disordered form.

In contrast, the likely undercooling temperature for 75 – 53 μ m sample exceeds in a considerable way the temperature required for the disordered solid work, taking into account the fact that direct determination of the droplet undercooling prior to nucleation is impossible in drop-tube processed samples. The onset of the disordered solid work seems to occur in the 300 – 212 μ m size fraction. As a consequence, it seems that recrystallisation grain refinement could be imposed on the solidification morphology at almost any undercooling temperature, independently of the underlying morphology. Additionally, it appears hard to stop the process of recrystallisation, even when the cooling rates are very high.

In intermetallics, recrystallising seems only to proceed when growth is fast enough so that ordering is lost. Having said that whether recrystallising processes occur near the order-disorder transition temperature or only at temperatures that are markedly higher appears to be also system dependent.

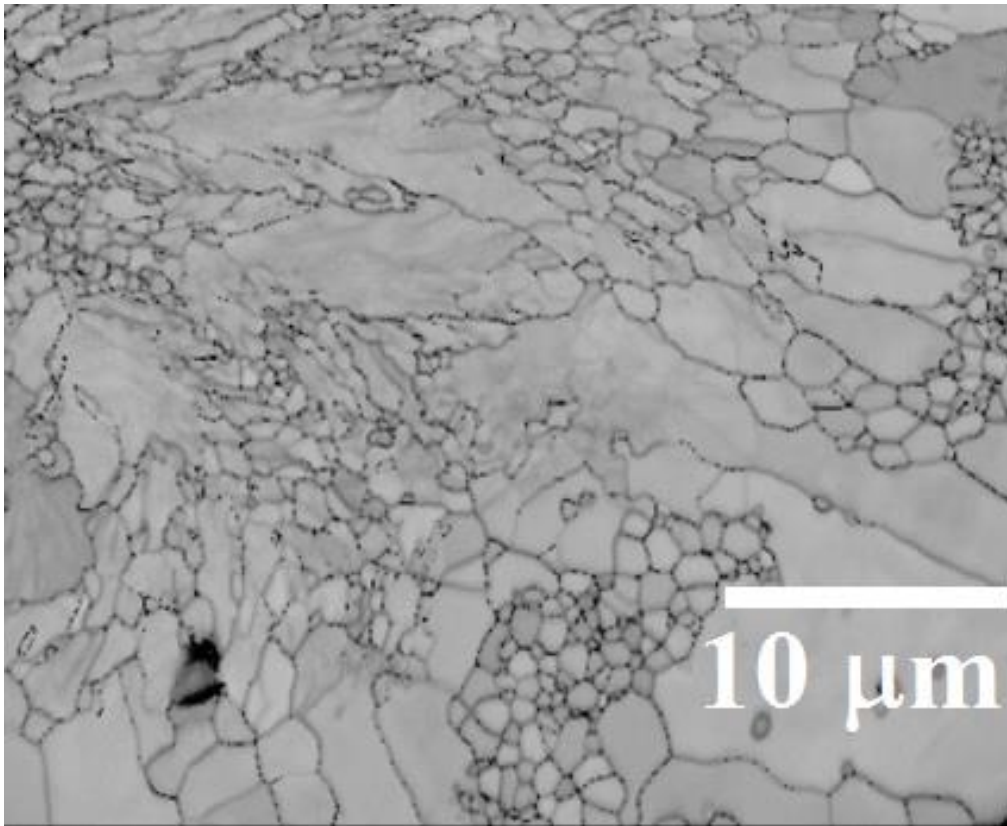


Figure 5.3 EBSD band contrast image of unetched β -Ni₃Ge drop-tube particles from the 75 – 53 μm size fraction showing highly grain refined structure.

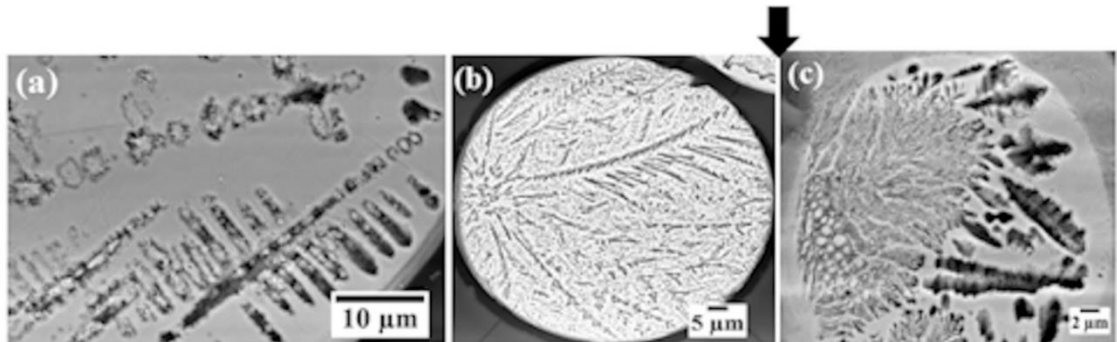


Figure 5.4 Solidification sequence as a function of increasing cooling rate with arrow showing placement of **(Figure 3.5)** in the sequence. **(a)** 150 – 106 μm , 8,000 – 13,000 K s^{-1} and **(b)** 106 – 75 μm , 13,000 – 23,000 K s^{-1} showing dendritic growth with orthogonal and non-orthogonal side-branching respectively, **(c)** 53 – 38 μm , 42,000 – 62,000 K s^{-1} showing development of dendritic seaweed.

5.2 Ni₅Ge₃ Compound

Ni₅Ge₃ is a congruently melting compound. Its homogeneity range of 34.6 – 44.5 at. Ge is for the single-phase compound, only. The Ge-deficient end of this range at 37.2 at. % Ge and 1458 K is where the congruent point is located. Ni₅Ge₃ has two equilibrium crystalline forms, ϵ and ϵ' [18] [20]. ϵ' is the low temperature phase with a C2 crystal structure (Monoclinic, space group 5). In contrast, ϵ is the phase of high temperature. It has a P6₃/mmc crystal structure (Hexagonal, space group 194) [20]. The transition between the two occurs either congruently ($\epsilon \rightarrow \epsilon'$) at 670 K for Ge-rich compositions or via the eutectoid reaction $\epsilon \rightarrow \epsilon' + \text{Ni}_2\text{Ge}$ at 560 K for Ge-deficient compositions. The phase diagram does not show order-disorder transitions. Furthermore, there is no evidence, as far as we know, that the high temperature ϵ phase may order directly from the liquid after solidification or whether it orders below the liquidus temperature in the solid-state.

In previous chapter we presented all the results of rapidly solidified Ni-37.2 at%. Ge (second compound of this project), which is close to the notional stoichiometry of the Ni₅Ge₃ compound. The main objective of the study is to determine whether ordering occurs upon solidification, or whether it occurs in the solid-state at some temperature below the liquidus. The second aim is to elucidate the effect of cooling rate on the suppression of the ordering reaction.

From the XRD patterns it is confirmed that all samples are Ni₅Ge₃. As XRD data for all the sieve fractions ($\geq 850 \mu\text{m}$ to $\leq 38 \mu\text{m}$) is shown in **Figure 4.51**, together with the ICCD reference patterns for ϵ -Ni₅Ge₃ (04-004-7264) and ϵ' -Ni₅Ge₃ (01-075-6729). Many of the peaks for the ϵ - and ϵ' -phases occupy similar positions, although the strong double peaks that occur in the spectrum of the ϵ -phase at 44.72° and 46.28° are shifted to slightly higher angles (45.48° and 46.65°) for the ϵ' -phase, allowing an unambiguous identification.

The $\geq 850 \mu\text{m}$ sieve fraction we identify as the equilibrium (low temperature) ϵ' -phase and the $850 < \text{to} < 38 \mu\text{m}$ sieve fraction, being the high temperature ϵ -phase. Therefore, it seems plausible that cooling rates that are higher than 700 K s⁻¹ are adequate for the suppression of the $\epsilon \rightarrow \epsilon'$ transition. This would result in the retention of the metastable ϵ -phase down to room temperature.

Four different microstructures were observed. First, partial plate and lath type structures (**Figure 4.53**) were observed at low cooling rates ($\geq 700 \text{ K s}^{-1}$, $\geq 850 \text{ }\mu\text{m}$ diameter particles). Then, complete plate and lath type structure (**Figures 4.54 – 4.57**) at medium cooling rates ($700 – 7800 \text{ K s}^{-1}$, $850 – 150 \text{ }\mu\text{m}$ diameter particles). Third, at higher cooling rates ($7800 – 42000 \text{ K s}^{-1}$, $150 – 53 \text{ }\mu\text{m}$ diameter particles) isolated faceted hexagonal crystallites (**Figures 4.58 – 4.60**) in an otherwise featureless matrix were observed. Moreover, EBSD Euler map and histogram data (**Figure 4.68**) confirmed the presence of a single crystal structure (**Figures 4.61 – 4.62**) at the highest cooling rates ($\leq 42000 \text{ K s}^{-1}$, $\leq 53 \text{ }\mu\text{m}$ diameter particles) within the same compound of Ni_5Ge_3 . As there is no existence of grain boundary at this sample.

In intermetallic compounds [104-106], structures of a plate and lath kind are quite common. They are also fairly common in some iron alloys [107]. Hyman *et al.* observed plate and lath structures in γ -TiAl [104]. It is reported that this resulted from α dendrites transforming during solid-state cooling. This transformation led to a mixture of $\alpha_2 + \gamma$ laths surrounded by γ segregates. McCullough *et al.* also stated that plate and lath morphology was found in α_2 -Ti₃Al. Like ε -Ni₅Ge₃, α_2 -Ti₃Al shares the P6₃/mmc space group [105]. Yet, in other materials that exhibit the plate and lath structure, like Ti₃Al, this morphology clearly appeared by a contrast between different phases.

The material being discussed here is single phase, so it is clearly a different case. In the case of a congruently melting compound the contrast would not be expected to arise from solid composition differences. The absence of solute partitioning is established in **Figure 4.63**. This figure displays an EDX line scan that goes across a part of the isolated plate and lath morphology (**a**). From this we can deduce, within the technique's experimental error that only small compositional variations exist between the surrounding matrix that is without features and the structures revealed by etching. This is also the case for the isolated hexagonal crystallites morphology (**b**), EDX also demonstrates that the isolated hexagonal crystallites morphology (**b**) is chemically homogeneous. Consequently, the contrast that is shown by the etching process does not look to be related to differences in the XRD phase. It does not appear to be related to the EDX chemical composition either.

In order to understand the origin of morphologies (plate and lath and isolated crystallites morphologies) revealed by etching in the rapidly solidified Ni_5Ge_3 drop-tube samples TEM imaging and selected area diffraction (SAD) analysis has been performed and results are shown in the previous chapter (**Figures 4.69 – 4.71**). The SADP results confirm that it is only in the featureless matrix materials that the super-lattice spots are apparent. These spots appear far away from the plate and lath as well as from the hexagonal crystallites structures. This indicates that the featureless matrix material is chemically ordered. In contrast, if the super-lattice spots are not apparent in either SADP of plate and lath or the hexagonal crystallites regions, then it indicates that the material is chemically disordered. Therefore, it is possible to conclude that the contrast revealed by the etching is due to a chemical ordering that is incomplete. In this case, the etchant affects the disordered material and leaves intact the ordered material. Similar behaviour has been observed in our first compound Ni_3Ge and we reported in [122, 125]. However, TEM SADP of 53 – 38 μm size fraction of Ni_5Ge_3 compound shows disordered material (**Figure 4.72**). We can postulate that at highest cooling rate ($\leq 42000 \text{ K s}^{-1}$) all material transformed into disordered material.

So as to determine if the ordering process happens in the solid-state or upon solidification at the liquidus temperature differential scanning calorimetry (DSC) was used (**Figure 4.73a**). The results show that two low temperature transformations are evident. As anticipated for materials at 37.2 at % Ge, we can see from the phase diagram that the first transformation is likely to be the $\varepsilon \rightarrow \varepsilon' + \text{Ni}_2\text{Ge}$ eutectoid as it appears to be 300 – 320 °C. Interestingly, a single phase ε' is what characterised the largest drop-tube sieve fraction, powders $> 850 \mu\text{m}$. This indicates that the system was forced to go through the congruent $\varepsilon \rightarrow \varepsilon'$ transition by a cooling process that was rapid enough to suppress the $\varepsilon \rightarrow \varepsilon' + \text{Ni}_2\text{Ge}$ eutectoid. The second low temperature transition that is apparent in the DSC is different. It is shown to be 460 – 540 °C, which could be associated to an order-disorder transformation that would have occurred at high temperature in ε -phase.

In order to acquire a confirmation of this, an in situ heating experiment was conducted in the TEM. A region that was initially ordered was chosen. This corresponded to the featureless matrix material. It also corresponded to the already identified SAD pattern so as to ensure that the material was ordered (**Figure 4.73b**). A heating process was

used in a progressive manner until the point when the super-lattice spots had vanished entirely. This indicated that the material had changed entirely to the disordered phase (**Figure 4.73c**). By then, the temperature had reached 485 °C and in agreement with the peak that was shown in the curve of the DSC.

As a consequence, it is apparent that in the Ni-37.5 at. % Ge melt solidification period, the disordered variant of the high temperature ϵ -Ni₅Ge₃ phase constitutes the primary solidification phase. In the cooling process, there would be an expectation that this primary solidification phase would go through a solid-state change from disorder to order at approximately 485 °C. However, it also shows that ordering could be suppressed partially through cooling rates in excess of 700 K s⁻¹. This would result in structures that are only partially ordered (**Figure 4.54 – 4.60**). The suppression of a change to ϵ' would also occur at these cooling rates, in turn, this would result in ϵ that is retained and metastable at room temperature. Additionally, it is apparent that the suppression of low temperature ϵ' -phase transformation does not occur for cooling rates below 700 K s⁻¹. This suppression could be brought about forcefully through the $\epsilon \rightarrow \epsilon'$ transition that is congruent instead of the $\epsilon \rightarrow \epsilon' + \text{Ni}_2\text{Ge}$ eutectoid reaction.

These results raise an additional question that relates to why Ni₅Ge₃ compound is showing partial ordering. The explanation of this partial ordering is as follows: ordering-disordering is unambiguously understandable from the liquid, such as in the case of our first compound Ni₃Ge. In the case of ordering from liquid, the rapidly solidified material formed during the recalescence phase of solidification is disordered. In contrast, the material that formed during the plateau stage of solidification and which is more slowly solidified is ordered. Therefore, we observed an order-disorder morphology in this compound.

Nevertheless, recalescence does not occur during solid-state ordering. Consequently, disordered material should not form. In contrast, SAD analysis in TEM clearly indicates the presence residue of ordered – disordered transition in Ni₅Ge₃ compound. This anomalous observation could be explained by solidification of first order (nucleation) or second order (spontaneous) transition. If we think that ordering has occurred through a spontaneous process, then the sample should order spontaneously. Otherwise, if the sample is cooled rapidly the ordering process would not take place and the sample would be transformed into a disordered form. The moment that the

sample passes through temperature of transition the sample would order, going from a fully disordered state to a fully ordered one. There, would be no chance of a presence of both ordered and disordered regions, at the same time.

In fact, we observed ordered region and disordered region in the compound Ni_5Ge_3 . From this fact, it is possible to infer that for Ni_5Ge_3 the reaction of solid-state ordering is of the first order (nucleation). Because in the case of a first order transition, the only way possible for going from disorder to order is for something to nucleate the ordering reaction. This ordering reaction would necessitate nucleation that would be suppressible by rapid cooling. This nucleation process would be random because there is a liquid, which starts to nucleate at random points and temperatures. Consequently, nucleation does not occur at the same time. There is order where the nucleation has occurred, and disorder where there is no nucleation. The mixing of order and disorder confirms that the transition is a first order transition.

From this it is possible to infer that for Ni_5Ge_3 the reaction of solid-state ordering is first order. This ordering process necessitates nucleation that would be suppressible by rapid cooling. However, the suppression of a spontaneous, second order reaction could not occur in this way. Therefore, we can only observed an order-disorder morphology in this compound by nucleation.

5.3 Vickers micro-hardness

The results of Vickers micro-hardness tests of our both compounds Ni_3Ge and Ni_5Ge_3 were presented (**Figure 4.74 – 4.75**) in previous chapter so as to establish the cooling rate effect on mechanical properties. It is clear that Ni_5Ge_3 (1021 $\text{Hv}_{0.01}$) is significantly harder than Ni_3Ge (526 $\text{Hv}_{0.01}$) compound. In this section, the Ni_3Ge and Ni_5Ge_3 microhardness results will be compared and contrasted. From this data, it can be concluded for both compounds that the mechanical properties can be altered (hardness increased and decreased) by increasing the cooling rates. However, on account of a microstructural transition, we also observed particular abrupt changes in microhardness which are coincident with changes in morphologies. These kinds of changes are observed in our both compounds (Ni_3Ge and Ni_5Ge_3) and can be seen in the **Figure 5.5**. In the Ni_3Ge compound, these changes occur during the change in morphology from dendrites (orthogonal) to dendrites (non-orthogonal) microstructure

transition (417 to 148 Hv_{0.01}). Similarly, abrupt decreasing in hardness is also observed in our second compound Ni₅Ge₃ during the plate and lath to isolated hexagonal crystallites microstructure transitions (824 to 671 Hv_{0.01}). Overall, in the cases studied in this project, the cooling rates ranged from ≥ 700 to ≤ 54500 K s⁻¹.

Gupta et. al reported microhardness values of Ni₃Ge and Ni₅Ge₃ compounds at equilibrium condition [126]. These microhardness values are different than our compounds. However, they used slow cooling process (water-quench) as compared to our cooling process (rapidly solidified). In fact, there is also a big drop in the results of microhardness between equilibrium [126] and our first observed rapidly solidified sample (≥ 850 μm , 700 K s⁻¹) within both compounds (Ni₃Ge and Ni₅Ge₃).

Gupta reported approx.490 Hv_{0.05} microhardness for the Ni₃Ge compound at 0 K s⁻¹. Conversely, the result of our first drop-tube sample ≥ 850 μm shows 299 Hv_{0.01} at 700 K s⁻¹. Also, we observed the gradual increment in the results of microhardness with respect to the increasing cooling rate (the decreasing size of drop-tube samples). These increment goes up to 417 Hv_{0.01} at 13000 K s⁻¹, where our observed microstructure was transformed into orthogonal dendrites. However, after this cooling rate we also observed a decrease in the microhardness (417 to 148 Hv_{0.01}), which may be caused by the transition of the microstructure to a non-orthogonal dendritic structure at 24000 K s⁻¹. Interestingly, the trend of increasing hardness with increasing cooling rate was re-observed also after the cooling rates increased from 24000 to ≤ 54500 K s⁻¹. The increase in microhardness observed here was from 148 to 526 Hv_{0.01}. This hardness was the highest observed microhardness in our Ni₃Ge compound. It was higher than Gupta Ni₃Ge microhardness (approx.490 Hv_{0.05}).

Similarly, the same kind of trend is also observed in our second congruently melting compound Ni₅Ge₃. Gupta also reported approx.850 Hv_{0.05} microhardness for the Ni₅Ge₃ compound at 0 K s⁻¹. Conversely, the result of our first drop-tube sample ≥ 850 μm shows 706 Hv_{0.01} at 700 K s⁻¹. Moreover, we observed the gradual increment in the results of microhardness with respect to the increasing cooling rate (the decreasing size of drop-tube samples). Where our observed microstructure was plate and lath microstructure, this increment went up to 824 Hv_{0.01} at 7735 K s⁻¹. However, after this cooling rate we also observed a decreasing in the results of microhardness (824 to 671 Hv_{0.01}). This may be caused by the transition of the microstructure as this sample was

an isolated hexagonal crystallites microstructure at 13000 K s^{-1} . Remarkably, the trend of increasing hardness with increasing cooling rate was also re-observed after the cooling rate increased from 13000 to $\leq 54500 \text{ K s}^{-1}$. Then, we observed an increasing in microhardness from 671 to $1021 \text{ Hv}_{0.01}$. This hardness was the highest observed microhardness in our Ni_3Ge compound, which is also higher than the Ni_5Ge_3 microhardness observed by Gupta (approx. $850 \text{ Hv}_{0.05}$). All of these trend can be seen from the **Figure 5.5**.

There are similarities in both techniques. The first similarity is that as the content of Ge increases (Ni_3Ge to Ni_5Ge_3), the hardness is also increased. Secondly, both results show similarity as Ni_3Ge is less hard than Ni_5Ge_3 . In contrast, there is also a difference in the microhardness results of both compounds, which may be caused by using different techniques (slow cooling and rapid cooling). These contrasting results indicate that mechanical properties can be improved by using different techniques regardless of the similarity between compounds or chemical compositions.

The behaviour observed in this instance is anomalous. It is contrary to what is predictable. We would assume that either in the case of spherulites microstructure (Ni_3Ge) or in the case of plate and lath structures (Ni_5Ge_3) the materials would be partially ordered. We would also presume that the matrix material would be nearly fully ordered. This would consistent with the TEM results of both compounds. Nevertheless, we must assume that with an increase in the cooling rate the suppression of the chemical ordering will occur. As a consequence, there will be a decrease of the degree of ordering in the partially ordered material. By this, we mean that on account of the increasing rate of cooling there will be increase in the disordering of the spherulites / plate and lath structures (decreasing the particle sizes of spherulites/plate and lath structure). Conversely, with an increase in the cooling rate, the microhardness would also be expected to decrease instead of increasing, as the disordered material. This is because it is more metallic like with increasing degree of disorder.

Another possible explanation for this is that due to high cooling rate increased growth velocity, in the lattice, defect concentration increases, which could result in dislocation density increase. In turn, this would give an effect that is comparable to work-hardening. Our comprehension of the manner in which rapid solidification can be used

in intermetallic materials processing may be impacted in a significant way by these results.

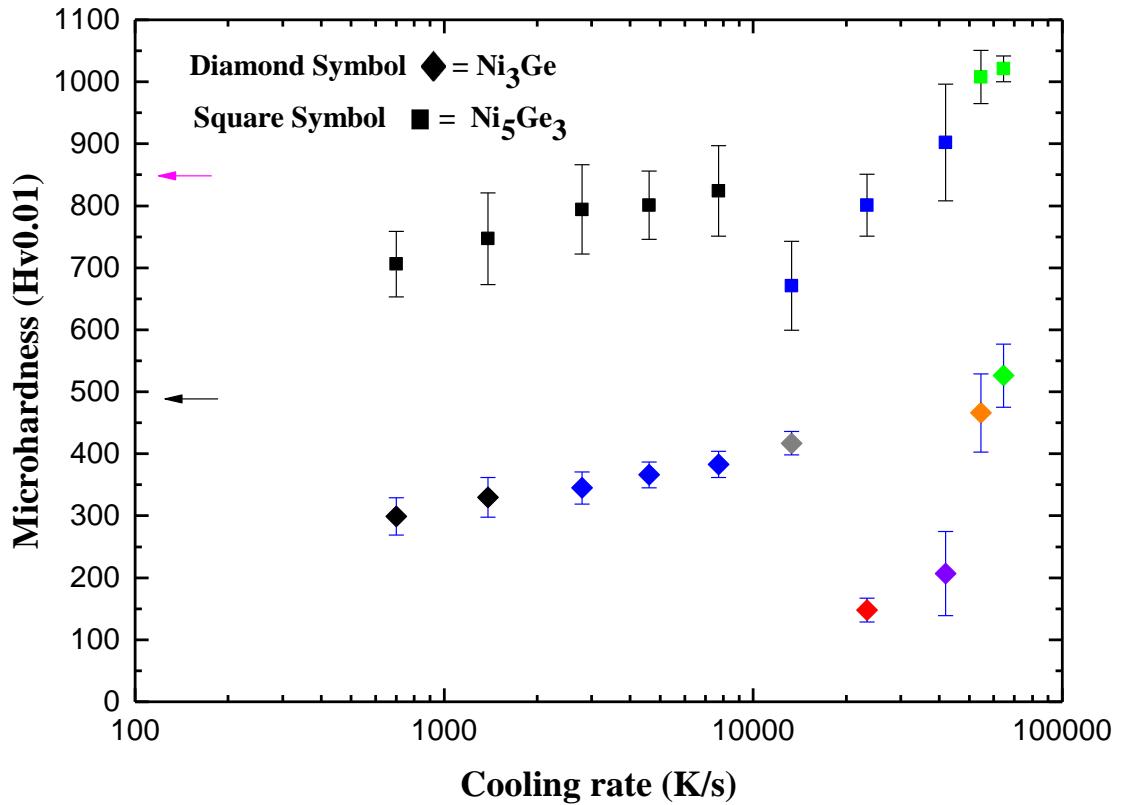


Figure 5.5 Micro-hardness value of Ni₃Ge (diamond symbol) and Ni₅Ge₃ (square symbol) compounds as a function of droplet diameter ranges from $\geq 850 \mu\text{m}$ to $\leq 38 \mu\text{m}$.

Chapter 6 Conclusion

1. The congruently melting, single phase, intermetallic compound β -Ni₃Ge ($T_m = 1132\text{ }^\circ\text{C}$), of composition Ni-23.8. % Ge was successfully produced by arc melting, then the compound was subjected to rapid solidification via drop-tube processing. After this drop-tube process, the compound remained fully single phase β -Ni₃Ge, irrespective of the imposed cooling rate.
2. Rapid solidification of the congruently melting intermetallic compound β -Ni₃Ge has revealed a range of solidification microstructures, imbedded within a featureless matrix. The solidification microstructure, which evolve with increasing departure from equilibrium are as follows:
 - (i) Spherulites microstructure ($\geq 850 - 500\text{ }\mu\text{m}$, $< 700 - 1400\text{ K s}^{-1}$),
 - (ii) mix spherulites and dendrites microstructure ($500 - 150\text{ }\mu\text{m}$, $1400 - 7800\text{ K s}^{-1}$),
 - (iii) well-defined dendrites with orthogonal side-branching ($150 - 106\text{ }\mu\text{m}$, $7800 - 13000\text{ K s}^{-1}$)
 - (iv) dendrites with non-orthogonal side-branching ($106 - 75\text{ }\mu\text{m}$, $13000 - 24000\text{ K s}^{-1}$)
 - (v) recrystallised microstructure ($75 - 53\text{ }\mu\text{m}$, $24000 - 42000\text{ K s}^{-1}$)
 - (vi) dendritic seaweed microstructure ($53\text{ to } \leq 38\text{ }\mu\text{m}$, $42000\text{ to } > 54500\text{ K s}^{-1}$)
3. In the two largest sieve sizes ($\geq 850\text{ }\mu\text{m}$ and $850-500\text{ }\mu\text{m}$) numerous isolated spherulite morphologies are observed with diameters in the range $10-20\text{ }\mu\text{m}$. In these droplets sizes the spherulites are the only solidification morphology observed in what is otherwise a featureless background.
4. In the smaller three sieve sizes ($500 - 300\text{ }\mu\text{m}$, $300 - 212\text{ }\mu\text{m}$ and $212 - 150\text{ }\mu\text{m}$) spherulites coexist with classical dendrites, and structures are observed which consist of linear arrays of spherulites tracing out a dendritic outline.
5. SADP in the TEM analysis confirmed that it is only the spherulite microstructure that is partially ordered amongst the above listed microstructures, which are disordered. However, SAD analysis also indicated that the featureless background material of all above microstructures including that of the spherulites is chemically ordered.

6. It is postulated that the structures composed of a linear array of spherulites develop to start with as a dendrite of the disordered material during the recalescence phase of solidification. During the 'plateau phase' following recalescence, at the time when the solid should have co-existed with the liquid, partial re-ordering then occurred. During this time the dendrite arms were fragmented into the observed linear array of spherulites.
7. Detailed investigation using TEM diffraction analysis and dark-field imaging, combined with EBSD leads to the conclusion that these spherulites are characterised by many similarities, but also some key differences in comparison to spherulites commonly observed in polymers.
8. The intermetallic spherulites are composed of outward radiating lamellae of near constant width that maintain space filling by branching along non-crystallographic directions. Furthermore, the lamellar width is a function of cooling rate, with higher cooling rates giving finer lamellae. In this respect, the spherulites examined in this study closely resemble Category 1 polymer spherulites. However, both lamellae and matrix are here crystalline, instead of the lamellae being crystalline in an amorphous matrix as in the case of the polymer. Undoubtedly, the TEM and EBSD evidence suggests that both share a contiguous underlying crystallography. However, these are characterised by the distinction between the lamellae that are the chemically ordered L12 variant of this structure and the inter-lamella material that is the disordered fcc variant.
9. With regards to dendritic morphology, we can draw conclusion from Ahmad et.al work [15] that a rapid increase in growth velocity occurs above a critical undercooling temperature because of a transition to fully disordered growth. In this case, the faster growth would necessitate dendritic morphologies to diffuse the latent heat away in an efficient way. As in other materials, it can be assumed that it is normal capillary anisotropy that produces the directionality characteristic of the dendritic structures.
10. With increasing cooling rate from $7800 - 13000 \text{ K s}^{-1}$ to $13000 - 24000 \text{ K s}^{-1}$ the dendrites show non-orthogonal side-branching together with some tip-splitting. However, the underlying crystallography, as shown in the selected area diffraction analysis in the TEM, remains the same as at lower cooling rate $< 13000 \text{ K s}^{-1}$.

11. At the highest cooling rates (42000 to $> 54500 \text{ K s}^{-1}$) studied dendritic growth (non-orthogonal) is replaced by growth of dendritic seaweed. Despite the transition of microstructures, the drop-tube sample had still the same underlying crystallography of a cubic ($L1_2$).
12. This is in favour of seaweed formation model that is commonly accepted. However, with respects to the result of one of the dendritic seaweed structures, the crystallography does not confirm the $L1_2$ cubic model. This one observation is unexplained.
13. Spontaneous grain refinement (SGR) is also observed below the cooling rate 42000 K s^{-1} in the same congruently melting intermetallic compound $\beta\text{-Ni}_3\text{Ge}$. As far as we know, this is the first report of SGR in the congruently melting compound.
14. Microstructural and EBSD data is believed to provide compelling evidence of spontaneous grain refinement by recrystallisation and recovery within a narrow size range of drop-tube processed, single phase $\beta\text{-Ni}_3\text{Ge}$ powders spanning the range of cooling rates $24000 - 42000 \text{ K s}^{-1}$, $75 - 53 \mu\text{m}$.
15. This recrystallisation grain refinement is observed at lower undercooling than the transformation to dendritic seaweed structure. However, very high cooling rates ($> 42000 \text{ K s}^{-1}$) recrystallisation suppressed and freeze in seaweed structures.
16. Despite each of these morphologies being observed in various metallic systems at different undercooling, it is very rare to find the entire range of morphologies in a single material $\beta\text{-Ni}_3\text{Ge}$.
17. The second congruently melting, single phase, intermetallic compound $\varepsilon\text{-Ni}_5\text{Ge}_3$ ($T_m = 1185 \text{ }^\circ\text{C}$), of composition Ni-37.2 % Ge, was also successfully produced and then the compound was subjected to rapid solidification via drop-tube processing. From this process, the compound remains fully single phase $\varepsilon\text{-Ni}_5\text{Ge}_3$, irrespective of the imposed cooling rate.
18. Rapid solidification of the congruently melting intermetallic compound $\varepsilon\text{-Ni}_5\text{Ge}_3$ has revealed a range of solidification microstructures, imbedded within a featureless matrix. The solidification microstructure, which evolve with increasing departure from equilibrium are as follows:
 - (i) Partial plate and lath microstructure ($> 850 \mu\text{m}$, $< 700 \text{ K s}^{-1}$),

- (ii) Plate and lath microstructure (850 – 150 μm diameter particles, 700 – 7800 K s^{-1})
 - (iii) Faceted hexagonal crystallites microstructure (150 – 53 μm diameter particles, 7800 – 42000 K s^{-1})
 - (iv) Single Crystal microstructure (53 to $\leq 38 \mu\text{m}$, 42000 to $> 54500 \text{K s}^{-1}$)
19. Only in the lowest cooling rate $< 700 \text{K s}^{-1}$, $> 850 \mu\text{m}$ the low temperature ϵ' -phase was observed to be retained upon cooling to room temperature. The dominant solidification morphology, revealed after etching, is that of isolated partial plate and laths within a featureless matrix.
 20. In all powder sizes except the largest sieve fraction ($> 850 \mu\text{m}$) the high temperature ϵ -phase was found to be retained upon cooling to room temperature.
 21. Selected area diffraction analysis in the TEM reveals that the partial plate and laths and plate and laths are partial ordered variant of ϵ' - Ni_5Ge_3 and ϵ - Ni_5Ge_3 respectively, whilst the featureless matrix of both microstructures are the ordered variant of the same compound. However, SAD analysis in the TEM also reveals that the isolated hexagonal crystallites are the disordered variant of ϵ - Ni_5Ge_3 , whilst the featureless matrix is the same as the partial plate and laths and plate and laths.
 22. SAD analysis in the TEM reveals the single crystal structure including their featureless background sample are the completely disordered variant of ϵ - Ni_5Ge_3 because at the highest cooling rate the material does not have sufficient time to reorder even its featureless matrix.
 23. Differential scanning calorimetry (DSC) indicates two low temperatures transformations. The first of these appears between 300 – 320 $^\circ\text{C}$ and is likely to be the $\epsilon \rightarrow \epsilon' + \text{Ni}_2\text{Ge}$ eutectoid decomposition. The second appears to be in the range 460 – 540 $^\circ\text{C}$ and we postulate may be associated with the order-disorder transformation in the high temperature ϵ -phase.
 24. An in situ heating in the TEM also indicated a solid-state order-disorder transformation between 470 - 485 $^\circ\text{C}$, with the material transforming to the fully disordered phase above 485 $^\circ\text{C}$.
 25. When DSC data and an in situ heating in the TEM analysis is combined with microstructural analysis, it is possible to conclude that for Ni_5Ge_3 the reaction

of solid-state ordering is first order, where the nucleation has occurred, there is ordered and where there is no nucleation there is disordered region. Therefore, ordered-disordered transformation observed in Ni_5Ge_3 compound even in the solid-state condition.

26. The Vickers micro-hardness results confirmed that the $\epsilon\text{-Ni}_5\text{Ge}_3$ (1021 $\text{Hv}_{0.01}$) is significantly harder than the $\beta\text{-Ni}_3\text{Ge}$ (526 $\text{Hv}_{0.01}$) compound.
27. There was a similar trend in the results of hardness of both compounds. In both, the hardness increased and decreased by increasing the cooling rates.
28. On account of a microstructural transition, we also observed abrupt changes in microhardness (decreases), which are coincident with changes in morphologies. Otherwise, the hardness is gradually improved in both compounds by increasing cooling rates.
29. In the Ni_3Ge compound, these changes occur during the change in morphology from dendrites (orthogonal) to dendrites (non-orthogonal) microstructure transition (417 to 148 $\text{Hv}_{0.01}$).
30. Similarly, abrupt decreasing in hardness is also observed in our second compound Ni_5Ge_3 during the plate and lath to isolated hexagonal crystallites microstructure transitions (824 to 671 $\text{Hv}_{0.01}$).
31. Overall, in the cases studied in this project, the cooling rates ranged from ≥ 700 to $< 54500 \text{ K s}^{-1}$.

Future Work

This research has yielded several interesting results. However, a number of points still remain unclear and would benefit from further study:

1. Our both congruently melting compounds (Ni_3Ge and Ni_5Ge_3) produced a range of microstructures that were the consequence of the rapid solidification process (drop-tube). Moreover, these microstructures were revealed through an etching process that produced a contrast in the form of the microstructures and the featureless background materials. However, we have confirmed by SAD analysis in the TEM that these differences were caused by disordered (microstructures) and ordered (featureless matrix) materials. In comparison to the disordered material, we found that the ordered material would be more resistant to the chemical attack of the acids used in etching. This conjecture is based on the observation of the behaviour of other intermetallic compounds in the ordered and disordered state. However, it is not a certain conclusion as we did not measure the chemical resistance of ordered vs disordered in our compounds (Ni_3Ge and Ni_5Ge_3). Consequently, this would be one of the important aspects for the further investigation.
2. The extensive black and white dots (gas porosity) also observed across the microstructure from arc-melting process, there is also need to confirm that there is no argon gas is dissolved in Ni–Ge alloys.
3. In this project, we used Vickers micro-hardness tester for understanding the mechanical properties of these two compounds. However, nano-indentation can also use for measuring hardness. This technique would give spatially resolved mechanically properties of the compound.
4. In this project, we mainly focused on the congruently melting, single phase compound (Ni_3Ge and Ni_5Ge_3). However, with a combination of other alloying elements (boron, molybdenum, cobalt, chromium, aluminium, titanium) in these compounds, their mechanical properties could be further improved. For example, it has been proved that researchers also used one of above mentioned alloying element for improving mechanical properties in compounds that are similar to the compounds studied here (Ni_3Al and Ti_3Al).

5. The wear resistance of these two compounds (Ni_3Ge and Ni_5Ge_3) might be improved by conducting cryogenic treatment on rapidly solidified samples.

References

- [1] S. Murarka, Metallization: Theory and practice for VLSI application, (1993).
- [2] K. Moris, Review: Reaction Synthesis Processing of Ni-Al Intermetallics, Mater. Sci. Eng. A, 299 (2001) 1-15.
- [3] F. Scheppe, P. Sahm, W. Hermann, U. Paul, J. Preuhs, Nickel aluminides: a step toward industrial application, Materials Science and Engineering: A, 329 (2002) 596-601.
- [4] A. Jena, M. Chaturvedi, On the stability of Ni₃Ge, Journal of Materials Research, 4 (1989) 1417-1420.
- [5] Y.-W. Kim, Intermetallic alloys based on gamma titanium aluminide, Jom, 41 (1989) 24-30.
- [6] H.A. Lipsitt, D. Shechtman, R.E. Schafrik, The deformation and fracture of TiAl at elevated temperatures, Metallurgical Transactions A, 6 (1975) 1991-1996.
- [7] T. Kawabata, M. Tadano, O. Izumi, Effect of purity and second phase on ductility of TiAl, Scripta metallurgica, 22 (1988) 1725-1730.
- [8] S.-C. Huang, E.L. Hall, Plastic deformation and fracture of binary TiAl-base alloys, Metallurgical Transactions A, 22 (1991) 427-439.
- [9] V. Vasudevan, M. Stucke, Court SA and Fraser HL, Phil. mag. lett, 59 (1989) 299.
- [10] L. Zhao, K. Tangri, TEM investigation on the interfacial boundaries in as-cast Ti₃Al+ TiAl alloy, Acta metallurgica et materialia, 39 (1991) 2209-2224.
- [11] L. Zhao, K. Tangri, Transmission electron microscopy characterization of interfacial boundaries in heat-treated Ti₃Al+ TiAl two-phase alloy, Philosophical Magazine A, 64 (1991) 361-386.
- [12] H. Inui, A. Nakamura, M. Oh, M. Yamaguchi, High-resolution electron microscope study of lamellar boundaries in Ti-rich TiAl polysynthetically twinned crystals, Ultramicroscopy, 39 (1991) 268-278.
- [13] H. Inui, A. Nakamura, M. Oh, M. Yamaguchi, Deformation structures in Ti-rich TiAl polysynthetically twinned crystals, Philosophical Magazine A, 66 (1992) 557-573.

- [14] P. Shang, T. Cheng, M. Aindow, A high-resolution electron microscopy study of steps on lamellar γ - α_2 interfaces in a low-misfit TiAl-based alloy, *Philosophical Magazine A*, 79 (1999) 2553-2575.
- [15] R. Ahmad, R. Cochrane, A. Mullis, Disorder trapping during the solidification of β Ni₃Ge from its deeply undercooled melt, *Journal of Materials Science*, 47 (2012) 2411-2420.
- [16] D.R. Askeland, P.P. Phulé, *The science and engineering of materials*, Publisher Thomson Brooks/ Cole,.
- [17] M. Ellner, T. Gödecke, K. Schubert, Zur struktur der mischung Nickel-Germanium, *Journal of the Less Common Metals*, 24 (1971) 23-40.
- [18] A. Nash, P. Nash, The Ge–Ni (Germanium-Nickel) system, *Journal of Phase Equilibria*, 8 (1987) 255-264.
- [19] Y. Liu, D. Ma, Y. Du, Thermodynamic modeling of the germanium–nickel system, *Journal of Alloys and Compounds*, 491 (2010) 63-71.
- [20] S. Jin, C. Leinenbach, J. Wang, L.I. Duarte, S. Delsante, G. Borzone, A. Scott, A. Watson, Thermodynamic study and re-assessment of the Ge-Ni system, *Calphad*, 38 (2012) 23-34.
- [21] S. Reutzel, H. Hartmann, P. Galenko, S. Schneider, D. Herlach, Change of the kinetics of solidification and microstructure formation induced by convection in the Ni–Al system, *Applied Physics Letters*, 91 (2007) 041913.
- [22] D.M. Herlach, Metastable materials solidified from undercooled melts, *Journal of Physics: Condensed Matter*, 13 (2001) 7737.
- [23] T. Massalski, *Structure of Solid Solutions*, Elsevier Sci. Publ., Amsterdam, (1983).
- [24] D.A. Porter, K.E. Easterling, M. Sherif, *Phase Transformations in Metals and Alloys*, (Revised Reprint), CRC press, 2009.
- [25] R. Cahn, P. Siemers, J. Geiger, P. Bardhan, The order-disorder transformation in Ni₃Al and Ni₃Al-Fe alloys—I. Determination of the transition temperatures and their relation to ductility, *Acta metallurgica*, 35 (1987) 2737-2751.

- [26] A. Inoue, H. Tomioka, T. Masumoto, Microstructure and mechanical properties of rapidly quenched L11 alloys in Ni-Al-X systems, *Metallurgical Transactions A*, 14 (1983) 1367-1377.
- [27] H. Assadi, M. Barth, A. Greer, D.M. Herlach, Microstructural development in undercooled and quenched Ni₃Al droplets, in: *Materials Science Forum*, Trans Tech Publ, 1996, pp. 37-44.
- [28] W. Boettinger, M. Aziz, Theory for the trapping of disorder and solute in intermetallic phases by rapid solidification, *Acta Metallurgica*, 37 (1989) 3379-3391.
- [29] M. Aziz, Model for solute redistribution during rapid solidification, *Journal of Applied Physics*, 53 (1982) 1158-1168.
- [30] J. Baker, J. Gahn, Solute trapping by rapid solidification, *Acta Metallurgica*, 17 (1969) 575-578.
- [31] M. Barth, B. Wei, D. Herlach, Crystal growth in undercooled melts of the intermetallic compounds FeSi and CoSi, *Physical Review B*, 51 (1995) 3422.
- [32] J.A. West, M.J. Aziz, Kinetic Disordering of Intermetallic Compounds Through First- and Second-Order Transitions by Rapid Solidification, in: *Ordering and Disorder in Alloys*, Springer, 1992, pp. 23-30.
- [33] H. Assadi, A. Greer, Modelling of kinetics of solidification of intermetallic compounds, *Materials Science and Engineering: A*, 226 (1997) 70-74.
- [34] P. Haasen, *Physical Metallurgy*, Cambridge University Press, Cambridge, 1978.
- [35] A. Greer, H. Assadi, Rapid solidification of intermetallic compounds, *Materials Science and Engineering: A*, 226 (1997) 133-141.
- [36] S. Vitta, A. Greer, R. Somekh, Rapid solidification of cobalt-titanium alloys induced by nanosecond laser pulses, *Materials Science and Engineering: A*, 179 (1994) 243-248.
- [37] A. Nash, P. Nash, *Binary Alloy Phase Diagrams*, in: *US National Bureau of Standards Monograph Series 25*, Elsevier, ASM, Ohio, 1976, pp. 35.
- [38] K. Biswas, G. Phanikumar, D. Holland-Moritz, D.M. Herlach, K. Chattopadhyay, Disorder trapping and grain refinement during solidification of undercooled Fe-18 at% Ge melts, *Philosophical Magazine*, 87 (2007) 3817-3837.

- [39] M. Durand-Charre, The microstructure of superalloys: Gord. and Breach Sc, in, Pub, 1997.
- [40] C. Brandt, O. Inal, Mechanical properties of Cr, Mn, Fe, Co, and Ni modified titanium trialuminides, *Journal of materials science*, 37 (2002) 4399-4403.
- [41] Y. Harada, D. Dunand, Creep properties of Al_3Sc and $\text{Al}_3(\text{Sc}, \text{X})$ intermetallics, *Acta materialia*, 48 (2000) 3477-3487.
- [42] P. Hill, N. Adams, T. Biggs, P. Ellis, J. Hohls, S. Taylor, I. Wolff, Platinum alloys based on Pt–Pt₃Al for ultra-high temperature use, *Materials Science and Engineering: A*, 329 (2002) 295-304.
- [43] J. Fang, E. Schulson, Microstructures of rapidly solidified powder and extruded rod of Ni_3Ge , *Materials characterization*, 37 (1996) 23-30.
- [44] A.I. Taub, C. Briant, S. Huang, K.-M. Chang, M. Jackson, Ductility in boron-doped, nickel-base L12 alloys processed by rapid solidification, *Scripta metallurgica*, 20 (1986) 129-134.
- [45] T. Massalski, H. Okamoto, P. Subramanian, L. Kacprzak, 1990, *Binary Alloy Phase Diagrams*, 2nd ed., ASM International, Materials Park, OH, 1089-1091.
- [46] R. Ahmad, R. Cochrane, A. Mullis, The formation of regular $\alpha\text{Ni}-\gamma$ ($\text{Ni}_{31}\text{Si}_{12}$) eutectic structures from undercooled Ni–25 at.% Si melts, *Intermetallics*, 22 (2012) 55-61.
- [47] L. Cao, R.F. Cochrane, A.M. Mullis, Microstructural Evolution and Phase Formation in Rapidly Solidified Ni-25.3 At. Pct Si Alloy, *Metallurgical and Materials Transactions A*, 46 (2015) 4705-4715.
- [48] R. Ahmad, R. Cochrane, A. Mullis, The formation of regular $\alpha\text{Ni}-\gamma$ ($\text{Ni}_{31}\text{Si}_{12}$) eutectic structures from undercooled Ni–25 at.% Si melts, *Intermetallics*, 22 (2012) 55-61.
- [49] G. Phanikumar, K. Biswas, O. Funke, D. Holland-Moritz, D.M. Herlach, K. Chattopadhyay, Solidification of undercooled peritectic Fe–Ge alloy, *Acta Materialia*, 53 (2005) 3591-3600.
- [50] H. Kerr, W. Kurz, Solidification of peritectic alloys, *International Materials Reviews*, 41 (1996) 129-164.

- [51] T. Massalski, Binary Alloy Phase Diagrams 2nd edn (Metals Park, OH: American Society for Metals), (1990).
- [52] W.H.F. Talbot, Phil. Trans. R. Soc. London, London, 1837.
- [53] F. Padden Jr, H. Keith, Crystalline morphology of synthetic polypeptides, Journal of Applied Physics, 36 (1965) 2987-2995.
- [54] D. Norton, A. Keller, The spherulitic and lamellar morphology of melt-crystallized isotactic polypropylene, Polymer, 26 (1985) 704-716.
- [55] B. D., Trans. R. Soc. Edinburgh, Edinburgh, 1853.
- [56] J. Magill, Review spherulites: A personal perspective, Journal of materials science, 36 (2001) 3143-3164.
- [57] A. Keller, The spherulitic structure of crystalline polymers. Part I. Investigations with the polarizing microscope, Journal of Polymer Science, 17 (1955) 291-308.
- [58] C. Bunn, R. Hill, Fibres from Synthetic Polymers, Elsevier, Amsterdam, (1953) 253.
- [59] Z. Lu, T. Goh, Y. Li, S. Ng, Glass formation in La-based La–Al–Ni–Cu–(Co) alloys by Bridgman solidification and their glass forming ability, Acta materialia, 47 (1999) 2215-2224.
- [60] J. Cheng, G. Chen, P. Gao, C. Liu, Y. Li, The critical cooling rate and microstructure evolution of $Zr_{41.2}Ti_{13.8}Cu_{12.5}Ni_{10}Be_{22.5}$ composites by Bridgman solidification, Intermetallics, 18 (2010) 115-118.
- [61] T. Aboki, F. Brisset, J. Souron, A. Dezellus, P. Plaindoux, Microstructure studies of $Zr_{65}Cu_{17.5}Al_{7.5}Ni_{10}$ and $Zr_{65}Cu_{15}Al_{10}Ni_{10}$ glass forming alloys: Phase morphologies and undercooled melt solidification, Intermetallics, 16 (2008) 615-624.
- [62] K. Chrissafis, M. Maragakis, K. Efthimiadis, E. Polychroniadis, Detailed study of the crystallization behaviour of the metallic glass Fe 75 Si 9 B 16, Journal of alloys and compounds, 386 (2005) 165-173.
- [63] T. Yano, Y. Yorikado, Y. Akeno, F. Hori, Y. Yokoyama, A. Iwase, A. Inoue, T.J. Konno, Relaxation and crystallization behavior of the $Zr_{50}Cu_{40}Al_{10}$ metallic glass, Materials transactions, 46 (2005) 2886-2892.

- [64] K. Ziewiec, Kinetics of phase transformations in Ni₈₇P₁₃ alloy upon heating, *Journal of alloys and compounds*, 397 (2005) 207-210.
- [65] C. Xia, L. Xing, W.-Y. Long, Z.-Y. Li, Y. Li, Calculation of crystallization start line for Zr₄₈Cu₄₅Al₇ bulk metallic glass at a high heating and cooling rate, *Journal of Alloys and Compounds*, 484 (2009) 698-701.
- [66] J. Liu, H. Zhang, H. Fu, Z.-Q. Hu, X. Yuan, In situ spherical B2 CuZr phase reinforced ZrCuNiAlNb bulk metallic glass matrix composite, *Journal of Materials Research*, 25 (2010) 1159-1163.
- [67] H. Sun, K. Flores, Microstructural analysis of a laser-processed Zr-based bulk metallic glass, *Metallurgical and Materials Transactions A*, 41 (2010) 1752-1757.
- [68] H. Sun, K.M. Flores, Spherulitic crystallization behavior of a metallic glass at high heating rates, *Intermetallics*, 19 (2011) 1538-1545.
- [69] H. Sun, K.M. Flores, Spherulitic crystallization mechanism of a Zr-based bulk metallic glass during laser processing, *Intermetallics*, 43 (2013) 53-59.
- [70] H. Keith, F. Padden Jr, A phenomenological theory of spherulitic crystallization, *Journal of Applied Physics*, 34 (1963) 2409-2421.
- [71] H.W. Morse, C.H. Warren, J.D.H. Donnay, Artificial spherulites and related aggregates, *American Journal of Science*, (1932) 421-439.
- [72] H. Morse, J. Donnay, Optics and structure of three-dimensional spherulites, *American Mineralogist*, 21 (1936) 391-427.
- [73] L. Gránásy, T. Pusztai, G. Tegze, J.A. Warren, J.F. Douglas, Growth and form of spherulites, *Physical Review E*, 72 (2005) 011605.
- [74] S.F. Swallen, P.A. Bonvallet, R.J. McMahon, M. Ediger, Self-diffusion of tris-naphthylbenzene near the glass transition temperature, *Physical review letters*, 90 (2003) 015901.
- [75] A. Masuhr, T. Waniuk, R. Busch, W. Johnson, Time scales for viscous flow, atomic transport, and crystallization in the liquid and supercooled liquid states of Zr_{41.2}Ti_{13.8}Cu_{12.5}Ni_{10.0}Be_{22.5}, *Physical Review Letters*, 82 (1999) 2290.
- [76] J. Bisault, G. Ryschenkow, G. Faivre, Spherulitic branching in the crystallization of liquid selenium, *Journal of crystal growth*, 110 (1991) 889-909.

- [77] J.A. Dantzig, M. Rappaz, *Solidification*, EPFL press, 2009.
- [78] H. Assadi, M. Oghabi, D. Herlach, Influence of ordering kinetics on dendritic growth morphology, *Acta Materialia*, 57 (2009) 1639-1647.
- [79] E.G. Castle, A.M. Mullis, R.F. Cochrane, Evidence for an extensive, undercooling-mediated transition in growth orientation, and novel dendritic seaweed microstructures in Cu–8.9 wt.% Ni, *Acta Materialia*, 66 (2014) 378-387.
- [80] Y. Sawada, Transition of growth form from dendrite to aggregate, *Physica A*, 140 (1986) 134-141.
- [81] E.G. Castle, A.M. Mullis, R.F. Cochrane, Mechanism selection for spontaneous grain refinement in undercooled metallic melts, *Acta Materialia*, 77 (2014) 76-84.
- [82] K. Dragnevski, R. Cochrane, A. Mullis, The solidification of undercooled melts via twinned dendritic growth, *Metallurgical and Materials Transactions A*, 35 (2004) 3211-3220.
- [83] A. Mullis, A study of kinetically limited dendritic growth at high undercooling using phase-field techniques, *Acta materialia*, 51 (2003) 1959-1969.
- [84] S. Akamatsu, G. Faivre, T. Ihle, Symmetry-broken double fingers and seaweed patterns in thin-film directional solidification of a nonfaceted cubic-crystal, *Physical Review E*, 51 (1995) 4751-4773.
- [85] K. Taguchi, H. Miyaji, K. Izumi, A. Hoshino, Y. Miyamoto, R. Kokawa, Growth shape of isotactic polystyrene crystals in thin films, *Polymer*, 42 (2001) 7443-7447.
- [86] K. Dragnevski, R. Cochrane, A. Mullis, Experimental evidence for dendrite tip splitting in deeply undercooled, ultrahigh purity Cu, *Physical review letters*, 89 (2002) 215502.
- [87] A. Mullis, K. Dragnevski, R. Cochrane, The transition from the dendritic to the seaweed growth morphology during the solidification of deeply undercooled metallic melts, *Materials Science and Engineering: A*, 375 (2004) 157-162.
- [88] T. Haxhimali, A. Karma, F. Gonzales, M. Rappaz, Orientation selection in dendritic evolution, *Nature Materials*, 5 (2006) 660-664.
- [89] H. Assadi, M. Oghabi, D. Herlach, Influence of ordering kinetics on dendritic growth morphology, *Acta Materialia*, 57 (2009) 1639-1647.

- [90] S. Battersby, R. Cochrane, A. Mullis, Growth velocity-undercooling relationships and microstructural evolution in undercooled Ge and dilute Ge-Fe alloys, *Journal of materials science*, 34 (1999) 2049-2056.
- [91] K.I. Dragnevski, R.F. Cochrane, A.M. Mullis, The mechanism for spontaneous grain refinement in undercooled pure Cu melts, *Materials Science and Engineering: A*, 375 (2004) 479-484.
- [92] D. Li, K. Eckler, D. Herlach, Development of grain structures in highly undercooled germanium and copper, *Journal of crystal growth*, 160 (1996) 59-65.
- [93] D. Li, K. Eckler, D. Herlach, Undercooling, crystal growth and grain structure of levitation melted pure Ge and Ge-Sn alloys, *Acta materialia*, 44 (1996) 2437-2443.
- [94] J. Li, W. Jie, G. Yang, Y. Zhou, Solidification structure formation in undercooled Fe-Ni alloy, *Acta materialia*, 50 (2002) 1797-1807.
- [95] R.F. Cochrane, S.E. Battersby, A.M. Mullis, The mechanisms for spontaneous grain refinement in undercooled Cu-O and Cu-Sn melts, *Materials Science and Engineering: A*, 304 (2001) 262-266.
- [96] R. Wilnecker, D.M. Herlach, B. Feuerbacher, Evidence of nonequilibrium processes in rapid solidification of undercooled metals, *Physical Review Letters*, 62 (1989) 2707.
- [97] J. Walker, *The Physical Chemistry of Process Metallurgy, Part 2*, Interscience, in, New York: in: St Pierre GR (Ed), 1959.
- [98] B. Jones, G. Weston, The structural features of undercooled nickel and nickel-oxygen alloys, in, DTIC Document, 1970.
- [99] R.T. Southin, G.M. Weston, Influence of alloy additions on structure of undercooled copper ingots, *Journal of the Australian Institute of Metals*, 18 (1973) 74.
- [100] G. Powell, L. Hogan, The influence of oxygen content on the grain size of undercooled silver, *Trans Met Soc AIME*, 245 (1969) 407-412.
- [101] R. Cochrane, D. Herlach, 7th European symp on 'materials and fluid sciences under microgravity', (1989 Oxford. B H Kaldeich) 147-156.

- [102] M. Schwarz, A. Karma, K. Eckler, D.M. Herlach, Physical-mechanism of grain-refinement in solidification of undercooled melts, *Physical Review Letters*, 73 (1994) 1380–1383.
- [103] J. Lipton, W. Kurz, R. Trivedi, Effect of growth-rate dependent partition-coefficient on the dendritic growth in undercooled melts, *Acta Metallurgica*, 35 (1987) 965–970.
- [104] M. Hyman, C. McCullough, J. Valencia, C. Levi, R. Mehrabian, Microstructure evolution in TiAl alloys with B additions: conventional solidification, *Metallurgical Transactions A*, 20 (1989) 1847.
- [105] C. McCullough, J. Valencia, C. Levi, R. Mehrabian, Microstructural analysis of rapidly solidified Ti-Al-X powders, *Materials Science and Engineering: A*, 124 (1990) 83-101.
- [106] T. Broderick, A. Jackson, H. Jones, F. Froes, The effect of cooling conditions on the microstructure of rapidly solidified Ti-6Al-4V, *Metallurgical Transactions A*, 16 (1985) 1951-1959.
- [107] G. Krauss, A. Marder, The morphology of martensite in iron alloys, *Metallurgical and Materials Transactions B*, 2 (1971) 2343-2357.
- [108] O. Oloyede, T.D. Bigg, R.F. Cochrane, A.M. Mullis, Microstructure evolution and mechanical properties of drop-tube processed, rapidly solidified grey cast iron, *Materials Science and Engineering: A*, 654 (2016) 143-150.
- [109] E.-S. Lee, S. Ahn, Solidification progress and heat transfer analysis of gas-atomized alloy droplets during spray forming, *Acta metallurgica et materialia*, 42 (1994) 3231-3243.
- [110] W.F. Gale, T.C. Totemeier, *Smithells metals reference book*, Elsevier, 2003.
- [111] B. Cullity, S. Stock, *Elements of X-Ray Diffraction Third edition* Prentice Hall Upper Saddle River, in, NJ, 2001.
- [112] P.J. Goodhew, J. Humphreys, R. Beanland, *Electron microscopy and analysis*, CRC Press, 2000.
- [113] B. Fultz, J.M. Howe, *Transmission electron microscopy and diffractometry of materials*, Springer Science & Business Media, 2012.

- [114] D.B. Williams, C.B. Carter, The transmission electron microscope, in: Transmission electron microscopy, Springer, 1996, pp. 3-17.
- [115] P.E. Champness, Electron diffraction in the transmission electron microscope. RMS Microscopy handbook no. 47, Oxford.: BIOS Scientific publishers Ltd, 2001.
- [116] G. Hohne, W. Hemminger, H. Flammersheim, Differential scanning calorimetry. 2003, Berlin [etc.]: Springer.
- [117] B. Crist, J.M. Schultz, Polymer spherulites: A critical review, Progress in Polymer Science, 56 (2016) 1-63.
- [118] K. Jackson, J. Hunt, Lamellar and rod eutectic growth, AIME Met Soc Trans, 236 (1966) 1129-1142.
- [119] R. Ahmad, R. Cochrane, A. Mullis, Disorder trapping during the solidification of β -Ni₃Ge from its deeply undercooled melt, Journal of Materials Science, 47 (2012) 2411-2420.
- [120] A. Mullis, D. Walker, S. Battersby, R. Cochrane, Deformation of dendrites by fluid flow during rapid solidification, Materials Science and Engineering, A304-306 (2001) 245-249.
- [121] J. Dantzig, P. Di Napoli, J. Friedli, M. Rappaz, Dendritic Growth Morphologies in Al-Zn Alloys—Part II: Phase-Field Computations, Metallurgical and Materials Transactions A, 44 (2013) 5532-5543.
- [122] N. Haque, R.F. Cochrane, A.M. Mullis, Disorder-order morphologies in drop-tube processed Ni₃Ge: Dendritic and seaweed growth, Journal of Alloys and Compounds, (2016).
- [123] J.K. MacKenzie, The distribution of rotation axes in random aggregate of cubic crystals, Acta Metallurgica, 12 (1964) 223-225.
- [124] N. Haque, R.F. Cochrane, A.M. Mullis, Rapid solidification morphologies in Ni₃Ge: Spherulites, dendrites and dense-branched fractal structures, Intermetallics, 76 (2016) 70-77.
- [125] N. Haque, R.F. Cochrane, A.M. Mullis, Morphology of Order-Disorder Structures in Rapidly Solidified L1₂ Intermetallics, in: TMS 2017 146th Annual Meeting & Exhibition Supplemental Proceedings, Springer, 2017, pp. 729-736.

[126] A. Gupta, M. Chaturvedi, A. Jena, Microstructural characterisation and mechanical properties of Ni–Ge alloys containing Ni₃Ge, *Materials science and technology*, 9 (1993) 502-506.

Appendix

Identified phases and their crystallographic parameters

The phases involved in this project are β -Ni₃Ge, ϵ -Ni₅Ge₃ and ϵ -Ni₅Ge₃. The data of the above mentioned three phases can be obtained from the XRD diffraction database (ICCD reference patterns for β -Ni₃Ge (04-004-3112), ϵ -Ni₅Ge₃ (01-075-6729) and ϵ -Ni₅Ge₃ (04-004-7264), including the cell parameters and XRD diffraction peak list, as listed in **Table 9.1**.

Table 9.1 XRD diffraction peak list.

Ni₃Ge 04-004-3112						
(Cubic, Pm-3m, 221, a = b = c = 3.56, $\alpha = \beta = \gamma = 90^\circ$)						
No.	h	k	l	d [Å]	2Theta[deg]	I [%]
1	1	0	0	3.56600	24.950	1.4
2	1	1	0	2.52150	35.576	1.2
3	1	1	1	2.05880	43.944	100.0
4	2	0	0	1.78300	51.192	43.0
5	2	1	0	1.59480	57.764	0.7
6	2	1	1	1.45580	63.893	0.5
7	2	2	0	1.26080	75.318	17.8
8	2	2	1	1.18870	80.785	0.3
9	3	1	0	1.12770	86.168	0.2
10	3	1	1	1.07520	91.520	16.3
11	2	2	2	1.02940	96.887	4.4
12	3	2	0	0.98900	102.314	0.1
13	3	2	1	0.95310	107.842	0.3
14	4	0	0	0.89150	119.549	2.0
15	4	1	0	0.86490	125.903	0.2

16	4	1	1	0.84050	132.833	0.2
17	3	3	1	0.81810	140.634	6.2
é-Ni₅Ge₃ 01-075-6729						
(Monoclinic, C2, 5, a = 11.682, b = 6.737, c = 6.264, $\alpha = 90^\circ$, $\beta = 52.11^\circ$, $\gamma = 90^\circ$)						
No.	h	k	l	d [Å]	2Theta[deg]	I [%]
1	1	1	0	5.43940	16.283	8.4
2	2	0	1	5.43940	16.283	8.4
3	0	0	1	4.94350	17.929	0.1
4	2	0	0	4.60970	19.239	2.9
5	1	1	1	4.57550	19.384	2.5
6	0	2	0	3.37120	26.417	0.2
7	3	1	1	3.37120	26.417	0.2
8	-1	1	1	3.13620	28.436	0.8
9	2	0	2	3.11680	28.617	1.9
10	2	2	1	2.86050	31.244	10.1
11	3	1	0	2.79600	31.984	12.1
12	0	2	1	2.78370	32.129	10.2
13	3	1	2	2.77460	32.237	12.9
14	2	2	0	2.71970	32.906	6.4
15	4	0	2	2.70850	33.046	6.0
16	-2	0	1	2.65480	33.734	0.2
17	1	1	2	2.63910	33.941	2.1
18	0	0	2	2.47180	36.316	11.7
19	4	0	0	2.30480	39.050	1.4

20	2	2	2	2.28770	39.354	0.6
21	5	1	2	2.18040	41.377	5.3
22	1	3	0	2.18040	41.377	5.3
23	5	1	1	2.12080	42.595	1.9
24	1	3	1	2.11280	42.764	4.3
25	4	2	2	2.11280	42.764	4.3
26	-2	2	1	2.08510	43.361	2.9
27	4	0	3	2.07120	43.667	0.5
28	-3	1	1	2.00120	45.277	43.4
29	-1	1	2	1.99280	45.479	47.8
30	0	2	2	1.99280	45.479	47.8
31	3	1	3	1.98560	45.653	42.3
32	2	0	3	1.98560	45.653	42.3
33	6	0	2	1.94530	46.654	100.0
34	3	3	1	1.94530	46.654	100.0
35	4	2	0	1.90220	47.776	3.1
36	-1	3	1	1.89680	47.921	2.1
37	5	1	3	1.88920	48.126	1.8
38	3	3	0	1.81320	50.280	0.1
39	3	3	2	1.80730	50.455	0.4
40	6	0	3	1.80730	50.455	0.4
41	5	1	0	1.77850	51.331	2.1
42	-2	0	2	1.77180	51.539	0.5
43	1	3	2	1.76820	51.652	1.6
44	1	1	3	1.76430	51.775	1.3

45	4	2	3	1.76430	51.775	1.3
46	-4	0	1	1.72270	53.122	0.2
47	2	2	3	1.71060	53.527	1.0
48	6	2	2	1.68560	54.386	0.3
49	0	4	0	1.68560	54.386	0.3
50	0	0	3	1.64780	55.741	0.1
51	7	1	2	1.61190	57.094	0.8
52	5	3	2	1.60830	57.234	0.7
53	2	4	1	1.60830	57.234	0.7
54	6	2	1	1.59940	57.582	1.6
55	0	4	1	1.59430	57.784	2.2
56	6	2	3	1.59140	57.899	1.6
57	5	3	1	1.58390	58.199	0.2
58	2	4	0	1.58200	58.276	0.2
59	7	1	3	1.57950	58.377	0.5
60	-2	2	2	1.56810	58.843	0.5
61	4	0	4	1.55840	59.246	0.4
62	6	0	0	1.53660	60.172	2.3
63	-4	2	1	1.53220	60.363	3.7
64	-3	3	1	1.53220	60.363	3.7
65	-1	3	2	1.52920	60.494	1.1
66	3	3	3	1.52520	60.669	3.8
67	5	1	4	1.52240	60.793	3.1
68	6	0	4	1.52240	60.793	3.1
69	7	1	1	1.48940	62.288	0.5

70	-3	1	2	1.48530	62.479	1.5
71	5	3	3	1.48020	62.719	1.7
72	0	2	3	1.48020	62.719	1.7
73	3	1	4	1.47570	62.932	1.5
74	8	0	3	1.45270	64.045	0.7
75	4	4	1	1.45270	64.045	0.7
76	-1	1	3	1.43900	64.729	0.1
77	2	0	4	1.43530	64.916	0.4
78	8	0	2	1.43530	64.916	0.4
79	4	4	2	1.43030	65.171	0.7
80	5	3	0	1.42590	65.397	0.9
81	-5	1	1	1.42590	65.397	0.9
82	-2	4	1	1.42220	65.589	0.2
83	1	3	3	1.41780	65.818	0.7
84	4	2	4	1.41440	65.996	0.9
85	6	2	0	1.39800	66.871	7.1
86	0	4	2	1.39180	67.209	7.1
87	6	2	4	1.38730	67.456	6.7
88	4	4	0	1.35990	69.005	0.3
89	8	0	4	1.35420	69.336	0.1
90	1	5	0	1.33320	70.589	1.7
91	8	2	3	1.33320	70.589	1.7
92	-4	0	2	1.32740	70.944	0.1
93	2	2	4	1.32040	71.378	1.0
94	8	2	2	1.32040	71.378	1.0

95	7	3	3	1.31700	71.590	1.3
96	1	5	1	1.31700	71.590	1.3
97	1	1	4	1.31230	71.887	0.2
98	4	4	3	1.30670	72.243	0.1
99	7	1	0	1.29260	73.158	0.1
100	5	3	4	1.28230	73.843	0.2
101	9	1	3	1.27450	74.370	0.4
102	3	5	1	1.27450	74.370	0.4
103	-6	0	1	1.26280	75.178	0.4
104	7	3	1	1.26280	75.178	0.4
105	-1	5	1	1.25940	75.416	0.6
106	-3	3	2	1.25940	75.416	0.6
107	8	2	4	1.25650	75.621	0.6
108	6	0	5	1.25190	75.948	0.1
109	0	0	4	1.23590	77.111	5.9
110	6	4	1	1.23590	77.111	5.9
111	9	1	4	1.23160	77.430	1.5
112	6	4	3	1.23160	77.430	1.5
113	8	2	1	1.22500	77.926	1.0
114	5	1	5	1.22500	77.926	1.0
115	1	5	2	1.21960	78.337	0.3
116	4	0	5	1.21960	78.337	0.3
117	7	3	4	1.21730	78.513	0.5
118	7	1	5	1.21420	78.752	0.1
119	-4	4	1	1.20430	79.528	0.1

120	8	0	5	1.19700	80.110	0.1
121	-6	2	1	1.18320	81.239	0.5
122	0	4	3	1.17790	81.682	0.5
123	6	2	5	1.17350	82.054	0.5
124	10	0	3	1.16540	82.749	0.1
125	-3	1	3	1.16320	82.940	0.4
126	5	5	2	1.16320	82.940	0.4
127	0	2	4	1.16020	83.202	0.1
128	3	1	5	1.15730	83.457	0.1
129	-5	1	2	1.15520	83.643	0.3
130	5	5	1	1.15380	83.767	0.4
131	10	0	4	1.15220	83.910	0.2
132	8	0	0	1.15220	83.910	0.2
133	1	3	4	1.14940	84.161	0.2
134	4	2	5	1.14680	84.396	0.2
135	4	4	4	1.14390	84.660	0.1
136	9	1	1	1.13710	85.286	2.1
137	6	4	0	1.13510	85.472	2.4
138	7	3	0	1.13510	85.472	2.4
139	-3	5	1	1.13340	85.630	2.7
140	3	5	3	1.13050	85.903	2.9
141	6	4	4	1.12940	86.007	2.8
142	8	2	5	1.12850	86.092	2.6
143	9	1	5	1.12850	86.092	2.6
144	9	3	3	1.12380	86.541	4.3

145	0	6	0	1.12380	86.541	4.3
146	2	0	5	1.11720	87.180	0.1
147	10	0	2	1.11720	87.180	0.1
148	5	5	3	1.11180	87.711	0.1
149	10	2	3	1.10140	88.755	0.1
150	-7	1	1	1.09950	88.949	0.5
151	2	6	1	1.09950	88.949	0.5
152	0	6	1	1.09490	89.423	0.1
153	9	3	4	1.09380	89.537	0.1
154	8	4	2	1.09240	89.682	0.2
155	2	4	4	1.09240	89.682	0.2
156	5	3	5	1.09040	89.892	0.5
157	8	2	0	1.09040	89.892	0.5
158	5	5	0	1.08790	90.155	0.3
159	1	5	3	1.08460	90.505	0.4
160	10	0	5	1.08340	90.633	0.1
161	7	3	5	1.08180	90.805	0.2
162	-4	0	3	1.06600	92.540	0.1
163	2	2	5	1.06040	93.175	0.3
164	10	2	2	1.06040	93.175	0.3
165	2	6	2	1.05640	93.634	0.2
166	8	4	4	1.05540	93.750	0.3
167	-6	0	2	1.04790	94.630	1.9
168	-3	3	3	1.04540	94.927	4.3
169	4	6	1	1.04540	94.927	4.3

170	-4	4	2	1.04250	95.275	0.6
171	3	3	5	1.04090	95.468	3.8
172	11	1	3	1.04090	95.468	3.8
173	-5	3	2	1.03900	95.699	2.0
174	6	0	6	1.03900	95.699	2.0
175	7	5	3	1.03720	95.919	0.7
176	8	4	1	1.03720	95.919	0.7
177	8	0	6	1.03560	96.116	0.2
178	-2	6	1	1.03410	96.301	0.4
179	10	2	5	1.03140	96.636	0.2
180	7	1	6	1.03140	96.636	0.2
181	9	3	1	1.02620	97.291	0.6
182	0	6	2	1.02230	97.788	0.3
183	9	3	5	1.01980	98.111	0.7
184	5	5	4	1.01980	98.111	0.7
185	-4	2	3	1.01640	98.554	0.1
186	-1	3	4	1.01400	98.869	0.1
187	9	1	0	1.01270	99.041	0.3
188	5	1	6	1.01040	99.347	0.6
189	7	5	1	1.01040	99.347	0.6
190	-3	5	2	1.00910	99.521	0.4
191	4	6	0	1.00910	99.521	0.4
192	11	1	5	1.00690	99.818	0.5
193	3	5	4	1.00600	99.940	0.3
194	6	4	5	1.00480	100.103	0.3

195	9	1	6	1.00360	100.266	0.3
196	-6	2	2	1.00060	100.679	0.1
197	-2	2	4	0.99730	101.137	0.2
198	-7	3	1	0.99730	101.137	0.2
ϵ-Ni₅Ge₃ 04-004-7264						
(Hexagonal, P6 ₃ /mmc, 194, a = b = 3.92 c = 5.046, $\alpha = \beta = 90^\circ, \gamma = 120^\circ$)						
No.	h	k	l	d [Å]	2Theta[deg]	I [%]
1	1	0	0	3.39480	26.230	0.1
2	1	0	1	2.81670	31.742	18.0
3	0	0	2	2.52300	35.554	8.4
4	1	0	2	2.02500	44.716	100.0
5	1	1	0	1.96000	46.284	99.4
6	2	0	0	1.69740	53.977	0.1
7	2	0	1	1.60880	57.215	3.0
8	1	1	2	1.54780	59.692	9.0
9	1	0	3	1.50720	61.472	2.3
10	2	0	2	1.40840	66.314	21.6
11	2	1	0	1.28310	73.789	0.1
12	0	0	4	1.26150	75.269	4.9
13	2	1	1	1.24360	76.546	2.2
14	2	0	3	1.19480	80.288	0.9
15	1	0	4	1.18250	81.297	0.1
16	2	1	2	1.14370	84.678	15.8
17	3	0	0	1.13160	85.799	8.7
18	3	0	1	1.10420	88.471	0.1

19	1	1	4	1.06080	93.129	12.7
20	3	0	2	1.03250	96.499	1.6
21	2	1	3	1.02020	98.059	1.0
22	2	0	4	1.01250	99.068	0.1
23	2	2	0	0.98000	103.630	4.5
24	1	0	5	0.96740	105.548	0.4
25	3	1	0	0.94160	109.785	0.1
26	3	1	1	0.92560	112.654	0.7
27	2	2	2	0.91350	114.968	1.0
28	2	1	4	0.89960	117.801	0.1
29	3	1	2	0.88210	121.679	5.4
30	2	0	5	0.86750	125.234	0.3
31	4	0	0	0.84870	130.358	0.1
32	3	0	4	0.84240	132.244	5.6
33	4	0	1	0.83690	133.975	0.3
34	3	1	3	0.82160	139.292	0.6
35	1	0	6	0.81630	141.347	2.2
36	4	0	2	0.80440	146.515	2.1